Periodically Disturbed Oscillators

Thesis by

Brian Daffern Hong

In Partial Fulfillment of the Requirements for the
Degree of
Doctor of Philosophy

CALIFORNIA INSTITUTE OF TECHNOLOGY
Pasadena, California

2019
Defended July 17th, 2018

Brian Daffern Hong
ORCID: 0000-0001-8099-0312

For my mom and dad.

ACKNOWLEDGEMENTS

Without a doubt, attending graduate school has been the most tumultuous time of my life thus far. As a younger student, it has also served as a period of tremendous personal and academic growth. As I write this, I am still amazed by the factors and decisions that led me to where I am today, and it still feels surreal looking back on many of the events that have occurred in the past couple years.

I owe an immeasurable amount of gratitude to my advisor, Professor Ali Hajimiri. He is, of course, academically brilliant, but what sets him apart is how deeply he cares for his students on a personal level. With us, he wears many hats. As a stern academic advisor, he nurtures and motivates our intellectual growth. As a life mentor, he imparts wisdom into the non-academic aspects of our existence. As a father figure, he comforts us through the many ups and downs of our lives. As a friend, he takes us on group outings and chats with us about the myriad of topics for which he is eminently knowledgeable—from food and cinema to sports and history. More personally, I know that I was not by any means an easy student to advise. Yet, not only did Ali serve as a consistent pillar of emotional support, he also looked past my immaturity, gave me many more chances than I deserved, patiently provided me with space and time for me to work through my personal struggles, and continued to believe in me even when I had given up on myself. There are few people in the world like Ali, and working with him has been a once-in-a-lifetime opportunity.

Next, I would like to express my appreciation to Professors Azita Emami, P. P. Vaidyanathan, and Changhuei Yang for serving on my thesis committee, and also to Professor Babak Hassibi who could not make it to my defense but served on my candidacy committee. In the short amount of time they had to evaluate my work, they intently provided me with valuable feedback on how best to improve it.

It goes without saying that this work could not have been completed without the constant support from my colleagues. Aroutin Khachaturian, who has been my labmate the longest, emanates a kindness that knows no bounds and a generosity matched only by his awe-inspiring work ethic. I have treasured every single one of our many late-night journeys in search of boba and random food to snack on. Dr. Alex Pai, my “brother from another mother” and “partner in crime,” has been there for me countless times. He helped me pick myself up in the face of seeming hopelessness and taught me how to be strategic when maneuvering the real world.

It is not an understatement to say that I have learned much about life in general from him. Abhinav Agarwal is my "brother from another circuits lab." Our many dinners sampling the best Indian food LA has to offer and bonding over the difficulties of research always left me reinvigorated. My good friend Parham 'Parjom' Porsandeh Khial is driven by a fierce idealism and ambition which has never ceased to inspire me. I will miss our stress-relieving trips to Mammoth, Big Bear, and Las Vegas. Dr. Constantine 'Costis' Sideris is a caring, thoughtful, and intelligent individual. Oftentimes, a short conversation with him would enable me to make significant progress in whatever issue I was struggling with, academic or otherwise. Reza Fatemi has a rare gift: a sharp analytical mind combined with a uniquely profound insight into human behavior. His gentle encouragement and shrewd advice pulled me out of several ruts, both within and outside of research. Matan Gal-Katziri's seasoned outlook on life intermittently provided me with indispensable doses of maturity. Additionally, I am deeply grateful to him for his invaluable assistance with several critical parts of my measurement setup. Alexander 'Alex' White's fearless enthusiasm and hands-on mindset often aided my research in unexpected ways. Austin Fikes' sardonic wit, comedic comments about politics, and ability to find free food on campus served as refreshing injections into the day-to-day frustrations of grad school. The deeply compassionate David 'Elliott' Williams sympathizes with people of all plights; he connected with me during some of my darkest times. He also handled the unenviable task of coordinating with MOSIS for the fabrication and delivery of my chips. Craig Ives has been my work buddy during the numerous all-nighters I pulled in the past year, occasionally providing me with respite through impromptu conversations about philosophy and psychology. Dr. Kaushik Dasgupta's technical acumen and lightheartedness made me realize that things are not always as hard as they initially seemed. Stefan Turkowski's love of live music and ability to cook awesome food gave me a way to unwind outside of the lab. I will also never forget our transformative experience backpacking through Southeast Asia. Finally, I would like to thank Dr. Behrooz Abiri, Dr. Florian Bohn, Prof. Steve Bowers, Dr. Amirreza 'Amir' Safaripour, Dr. M. Reza Hashemi, Kuan-Chang 'Xavier' Chen, Milad Taghavi, and Aryan Hashemi for their friendship and support.

Outside of the 3rd floor of Moore, several close confidantes have kept me sane and grounded throughout my time at Caltech. My dear friends Corina Bianca Panda, Surabhi Sachdev, and Dr. Ramya Korlakai Vinayak helped me see the light when I could not on my own. Through her meticulous rationality, Corina has a way of

understanding my feelings in a way that no one else could. The sea of empathy that swells within Surabhi's heart always drowned out my feelings of emptiness and loneliness. From Ramya, I have learned not to lose hope in spite of life's unpredictability and complexity. Utkan Onur Candoğan's wry humor juxtaposed against his practical sensibilities helped me recognize when I was taking things too seriously. Katherine Rinaldi and Annalise 'Anna' Sundberg showed me the importance of maintaining balance in the midst of overwhelming stress. Lastly, I would like to mention my other friends at Caltech who have helped to relieve the burden of graduate school: Dr. Betty Ko Wong, Tahmineh 'Tami' Khazaei, Aubrey Shapero, Dr. Maria Sakovsky, Fariborz Salehi, Maxim 'Max' Budninskiy, and Armeen Taeb.

Beyond Caltech, a few lifelong confidantes deserve recognition as well. My chance encounter with Joy Dou at the Buddhist temple we go to blossomed into a friendship filled with adventures—from the turquoise waters of the Havasupai Indian Reservation to the red canyons of Zion National Park and the summit of Mount Whitney—which always rejuvenated me with happiness. Anthony Chan's humility, kindness, and humor reminded me to appreciate the small things in life. Dr. Angie Wang brightened my holidays by accompanying me to Disneyland and inviting me to her house for Christmas. I am thankful to Pak-Ling 'Leo' Szeto for providing me with a second family (IEEE) during my time as an undergraduate at UCLA and serving as a source of emotional stability throughout my graduate studies at Caltech. The many dinners I enjoyed, movies I watched, and (ironically) clinical discussions about depression I had with Michael Sechooler always left me feeling less weighed down by the world. Kamal Kajouke provided me with a shoulder to cry on whenever things were not going as expected. Finally, I am grateful to my other friends from undergrad, Calvin Cam, Justin Young, Shubham Gandhi, and Minh-Trang 'Teresa' Ha, for staying in touch and keeping it real as I slaved away in the ivory tower.

Next, I want to acknowledge the MICS lab for lending me equipment for my experiments, as well as David Hodge, Michelle Chen, Tanya Owen, Carol Sosnowski, and Christine Garske, for doing much of the work behind the scenes to ensure the smooth operation of our lab and our department. I would also like to convey my utmost appreciation to the Dean of Graduate Studies at Caltech, Professor Douglas Rees, and Assistant Dean Natalie Gilmore for their continued support in my endeavor to complete my PhD. Last but not least, I am grateful to the Admissions Office at Yale Law School for approving my belated request to defer.

In closing, I am indebted to my parents for raising me and for being an infinite source of guidance and love throughout my life. I owe them mine many times over.

This work was partially supported by the Air Force Office of Scientific Research (AFOSR), under Multidisciplinary Research Program of the University Research Initiative (MURI) grant FA9550-16-1-0566 entitled "*Universal Electromagnetic Surface:* Exploiting active electronics and active origami to generate a programmable electromagnetic response"; Northrop Grumman Corporation, under the *Space Solar Power Initiative* (SSPI) grant 8140000812; the National Institutes of Health (NIH), under City of Hope grant 51013.914960.6692; and a Rose Hills Foundation Fellowship.

ABSTRACT

By controlling the timing of events and enabling the transmission of data over long distances, oscillators can be considered to generate the "heartbeat" of modern electronic systems. Their utility, however, is boosted significantly by their peculiar tendency to synchronize to external signals that are themselves periodic in time. Although this fascinating phenomenon has been studied by scientists since the 1600s, models for describing this behavior have seen a disconnect between the rigorous, methodical approaches taken by mathematicians and the design-oriented, physically-based analyses carried out by engineers. While the analytical power of the former is often concealed by an inundation of abstract mathematical machinery, the accuracy and generality of the latter are constrained by the empirical nature of the ensuing derivations. We hope to bridge that gap here.

In this thesis, a general theory of electrical oscillators under the influence of a periodic injection is developed from first principles. Our approach leads to a fundamental yet intuitive understanding of the process by which oscillators lock to a periodic injection, as well as what happens when synchronization fails and the oscillator is instead injection pulled. By considering the autonomous and periodically time-varying nature that underlies all oscillators, we build a time-synchronous model that is valid for oscillators of any topology and periodic disturbances of any shape. A single first-order differential equation is shown to be capable of making accurate, quantitative predictions about a wide array of properties of periodically disturbed oscillators: the range of injection frequencies for which synchronization occurs, the phase difference between the injection and the oscillator under lock, stable vs. unstable modes of locking, the pull-in process toward lock, the dynamics of injection pulling, as well as phase noise in both free-running and injection-locked oscillators. The framework also naturally accommodates superharmonic injection-locked frequency division, subharmonic injection-locked frequency multiplication, and the general case of an arbitrary rational relationship between the injection and oscillation frequencies. A number of novel insights for improving the performance of systems that utilize injection locking are also elucidated. In particular, we explore how both the injection waveform and the oscillator's design can be modified to optimize the lock range. The resultant design techniques are employed in the implementation of a dual-moduli prescaler for frequency synthesis applications which features low power consumption, a wide operating range, and a small chip area.

For the commonly used inductor-capacitor (LC) oscillator, we make a simple modification to our framework that takes the oscillation amplitude into account, greatly enhancing the model's accuracy for large injections. The augmented theory uniquely captures the asymmetry of the lock range as well as the distinct characteristics exhibited by different types of LC oscillators. Existing injection locking and pulling theories in the available literature are subsumed as special cases of our model. It is important to note that even though the veracity of our theoretical predictions degrades as the size of the injection grows due to our framework's linearization with respect to the disturbance, our model's validity across a broad range of practical injection strengths are borne out by simulations and measurements on a diverse collection of integrated LC, ring, and relaxation oscillators. Lastly, we also present a phasor-based analysis of LC and ring oscillators which yields a novel perspective into how the injection current interacts with the oscillator's core nonlinearity to facilitate injection locking.

PUBLISHED CONTENT AND CONTRIBUTIONS

[1] B. Hong and A. Hajimiri, "A general theory of injection locking and pulling in electrical oscillators—Part I: Time-synchronous modeling and injection waveform design," *IEEE Journal of Solid-State Circuits*, vol. 54, no. 8, pp. 2109–2121, Aug. 2019. DOI: 10.1109/JSSC.2019.2908753,
B. Hong conceived of the project, conducted all of the research, and authored the manuscript.

[2] ——, "A general theory of injection locking and pulling in electrical oscillators—Part II: Amplitude modulation in *LC* oscillators, transient behavior, and frequency division," *IEEE Journal of Solid-State Circuits*, vol. 54, no. 8, pp. 2122–2139, Aug. 2019. DOI: 10.1109/JSSC.2019.2908763,
B. Hong conceived of the project, conducted all of the research, and authored the manuscript.

[3] ——, "A phasor-based analysis of sinusoidal injection locking in LC and ring oscillators," *IEEE Transactions on Circuits and Systems I: Regular Papers*, vol. 66, no. 1, pp. 355–368, Jan. 2019. DOI: 10.1109/TCSI.2018.2860045,
B. Hong conceived of the project, conducted all of the research, and authored the manuscript.

[4] ——, "Upper and lower bounds on a system's bandwidth based on its zero-value time constants," *Electronics Letters*, vol. 52, no. 16, pp. 1383–1385, Aug. 2016. DOI: 10.1049/el.2016.1724,
B. Hong conceived of the project, conducted all of the research, and authored the manuscript.

[5] ——, "Analysis of a balanced analog multiplier for an arbitrary number of signed inputs," *International Journal of Circuit Theory and Applications*, vol. 45, no. 4, pp. 483–501, Apr. 2017. DOI: 10.1002/cta.2243,
B. Hong conceived of the project, conducted all of the research, and authored the manuscript.

[6] A. Pai, P. Cao, E. E. White, B. Hong, M. Wang, B. Badie, A. Hajimiri, and J. M. Berlin, "Dynamically programmable magnetic fields for controlled movement of cells loaded with iron oxide nanoparticles," submitted to *Bioconjugate Chemistry*,
B. Hong used image processing algorithms to analyze cell movement data.

TABLE OF CONTENTS

LIST OF ILLUSTRATIONS

LIST OF TABLES

Chapter 1

INTRODUCTION AND BASIC DEFINITIONS

> "If I have seen further, it is by
> standing on the shoulders of giants."
>
> SIR ISSAC NEWTON, 1675

Within electronics, oscillators are employed in a wide variety of settings—the precise timing of events in microprocessors, the creation of carriers for modulating information in communication systems, the periodic control of switches in power management circuitry such as power inverters and DC-DC converters, and the generation of wireless power near the frequency limits of modern solid-state processes. In essence, almost all electronic systems require time-varying behavior of some sort and therefore need oscillators to actuate their functionality.

Oscillators exhibit a peculiar property due to their autonomous nature: the ability to synchronize to periodic disturbances. Known as *injection locking* in the electrical engineering community, this behavior has engendered a handful of applications in modern, high-speed systems. Some examples include the recovery of timing information from data streams [1], clock distribution and jitter reduction for high-density input/output (I/O) links [2], [3], frequency division [4]–[13] and frequency multiplication [14]–[18], the precise generation of quadrature or other multi-phase signals [19]–[24], and the synchronization of elements in phased arrays [25]–[29]. Beyond electronics, entrainment has also been applied to other oscillatory systems such as lasers, where it is used to clean their output spectrum and improve performance by reducing frequency chirp and nonlinear distortion [30]–[33]. Outside of electrical engineering, the phenomenon of synchronization has been studied extensively in a variety of other disciplines including physics [34], chemistry [35], neuroscience [36], and biology [37].

Despite its usefulness, the capability to lock becomes problematic when an oscillator is affected by *unwanted* disturbances in its environment. In particular, disturbances that fail to lock the oscillator will instead corrupt the oscillator's inherent periodicity or its "ability to tell time," an undesirable phenomenon known as *injection pulling*. In communication circuits, for example, the large-signal output of the power amplifier

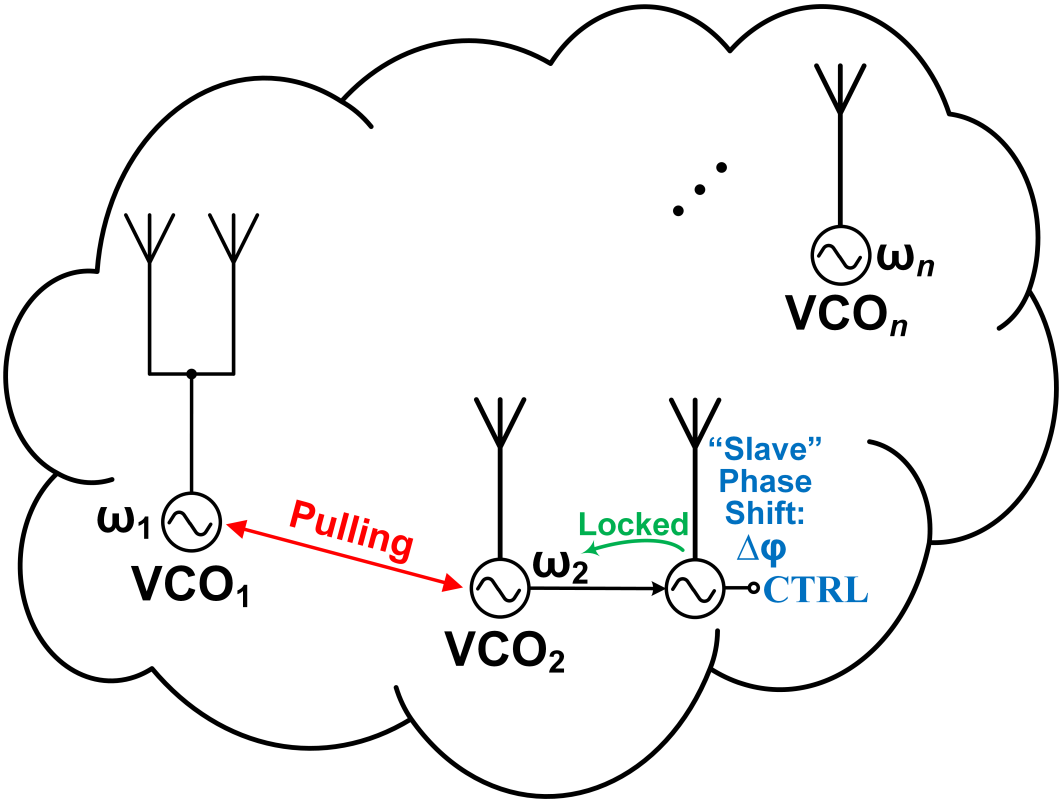

Figure 1.1: Arbitrary electromagnetic surface featuring multiple voltage-controlled oscillators (VCOs) that drive the radiating elements.

(PA) in a radio frequency (RF) transmitter can pull the oscillator generating the carrier, or pulling can occur between the receive and transmit local oscillators (LOs) in a single-chip transceiver [38]. Note that external disturbances may couple into an oscillator through any number of means: mechanically, electromagnetically, across the substrate of an integrated circuit, or through a shared supply.

An example of how both the useful applications of injection locking and the undesirable effects from injection pulling can appear in a single system is provided in Figure 1.1. In this example, an assortment of antennas is being used to engineer an arbitrary electromagnetic field pattern. The antennas are driven by a collection of voltage-controlled oscillators (VCOs). As we can see, VCO_2 is also being used to lock a "slave" VCO, whereby tuning the free-running frequency of the slave varies the phase difference $\Delta\varphi$ between them. On the other hand, oscillators in close physical proximity, such as VCO_1 and VCO_2, can pull one another, causing the signals driving the antennas to deviate from their optimal frequencies or creating unwanted interference patterns due to spurious phase relationships between the oscillators.

Given the numerous applications of injection locking on the one hand and the various settings in which unwanted pulling occurs on the other, there is a desire for a fundamental understanding of how periodic perturbations can influence an oscillator. In this thesis, we develop a general theory of injection locking and pulling in electrical oscillators that 1) leads to a deep physical understanding of the synchronization phenomenon, 2) makes accurate quantitative predictions about a myriad of different properties of periodically disturbed oscillators, and 3) yields design insights into how the implementation of systems that utilize injection locking can be optimized.

1.1 Basic Setup and Notation

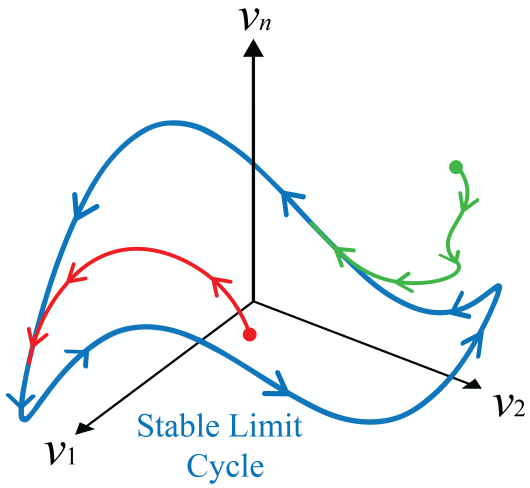

Figure 1.2: Mathematical description of an oscillator as traversing a stable limit cycle in n dimensions. Points in the state space not on the orbit will eventually converge to the limit cycle.

An oscillator is a system that is capable of self-sustaining a periodic signal. Within the dynamical systems community, oscillators are usually visualized in the state space (see Figure 1.2) [39]–[43], where they traverse a closed trajectory, a *limit cycle*, in a fixed amount of time, known as the free-running period of oscillation T_0. Although all observable signals within an electrical oscillator are periodic with this oscillation period T_0, we will focus on a particular node voltage $v_{\text{osc}}(t)$ (or set of node voltages), which we will call the ***oscillation voltage***.

We are interested in the behavior of this oscillator when it is *disturbed* by an external signal of some sort, periodic with a possibly different period T_{inj}. For our purposes, this signal will be an injection of current $i_{\text{inj}}(t)$ into one of the oscillator's nodes—

commonly (but not necessarily) the node at which the oscillation voltage is observed. This setup is depicted conceptually in Figure 1.3.

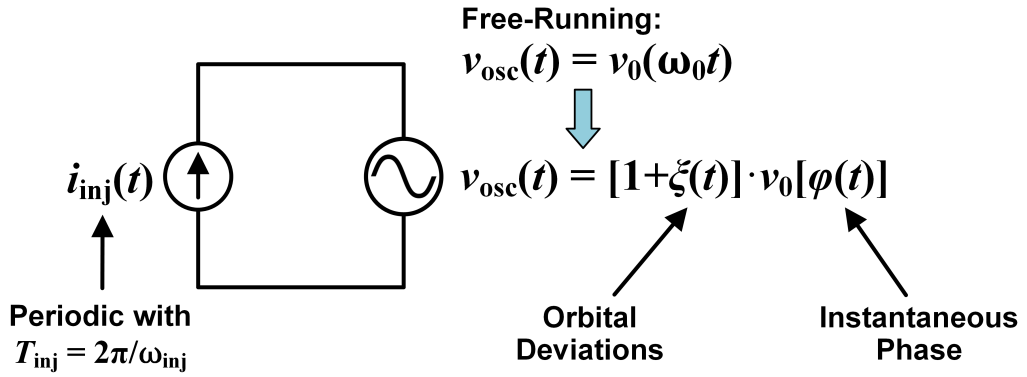

Figure 1.3: A basic cartoon of the setup and notation underlying the analysis. In the free-running case (i.e., $i_{\text{inj}} = 0$), $\xi(t) = 0$ and $\varphi(t) = \omega_0 t$. Under injection, the phase becomes $\varphi(t) \equiv \omega_0 t + \phi(t) \equiv \omega_{\text{inj}} t + \theta(t)$.

In the absence of injection—the free-running scenario—we write the oscillation voltage as

$$v_{\text{osc}}(t) = v_0(\omega_0 t),$$

where the ***oscillation waveform*** $v_0(\cdot)$ is 2π-periodic, and $\omega_0 \equiv 2\pi/T_0$ is the free-running (angular) oscillation frequency. The argument of $v_0(\cdot)$ is the ***phase*** φ of the oscillator in radians, a quantity which increases by 2π for each oscillation cycle. On the other hand, $v_0(\cdot)$ itself captures the free-running *shape* and *size* of the oscillation voltage.

In the presence of an external disturbance, two things happen:

1. The oscillator's phase may no longer increase at a constant rate equal to ω_0.
2. The oscillation voltage may deviate in size and shape from $v_0(\cdot)$.

Therefore, we write the oscillation voltage in the following form:

$$v_{\text{osc}}(t) = [1 + \xi(t)] \cdot v_0 [\varphi(t)], \tag{1.1}$$

where $\varphi(t)$ is the total, instantaneous phase of the oscillator and $\xi(t)$ represents the (fractional) deviations of the oscillator from its free-running trajectory. The

instantaneous oscillation frequency ω_{osc} is defined as the time derivative of the total phase:

$$\omega_{\text{osc}} \coloneqq \frac{d\varphi}{dt}. \tag{1.2}$$

It should be clear that when $i_{\text{inj}} = 0$ and the oscillator is free running, $\varphi(t) = \omega_0 t$ and $\xi(t) = 0$. Denoting the (angular) injection frequency $\omega_{\text{inj}} \equiv 2\pi/T_{\text{inj}}$, it will be useful to define the additional phases $\phi(t)$ and $\theta(t)$ using the following relationship:

$$\varphi(t) \equiv \omega_0 t + \phi(t) \equiv \omega_{\text{inj}} t + \theta(t). \tag{1.3}$$

Physically, $\phi(t)$ is the *phase in excess of free-running* ($\omega_0 t$), and $\theta(t)$ is the *phase referred to the injection* ($\omega_{\text{inj}} t$). Table 1.1 reiterates the physical meaning behind these important quantities. In injection locking and pulling scenarios, it is most convenient to deal with θ as the phase of interest, since we are interested in observing if or how the oscillator *synchronizes* itself to the injection frequency ω_{inj}.

Table 1.1: Oscillator Phase Definitions

φ: Total, Instantaneous Oscillator Phase	ϕ: Phase in Excess of Free-Running ($\omega_0 t$)	θ: Phase Referred to the Injection ($\omega_{\text{inj}} t$)

At this point, it should be noted from a mathematical standpoint that while the phase can be accurately represented using a single scalar variable, an oscillator in d-dimensional state space would require $(d-1)$ other scalars to fully describe its orbital deviations. However, we will see that Eq. (1.1) will prove itself to be sufficient for our purposes, while bringing in the full state-space representation of the oscillator will clutter up the analysis with a significant amount of mathematical machinery without contributing much physical insight.

1.2 Definition of Injection Locking and Pulling

The purpose of this study is to characterize the behavior of oscillators under the influence of a periodic injection. Specifically, we are interested in the scenario where the oscillator synchronizes itself to the injection and oscillates at the injection frequency: $\omega_{\text{osc}} = \omega_{\text{inj}}$.[1] We then say that the oscillator is ***injection locked*** to the injection signal. An example of injection locking is shown in Figure 1.4, where an oscillator which free-runs at $f_0 = 1$ GHz is injection locked to a sinusoidal injection

[1] The more general cases of injection-locked frequency division and multiplication will be considered in Chapter 6.

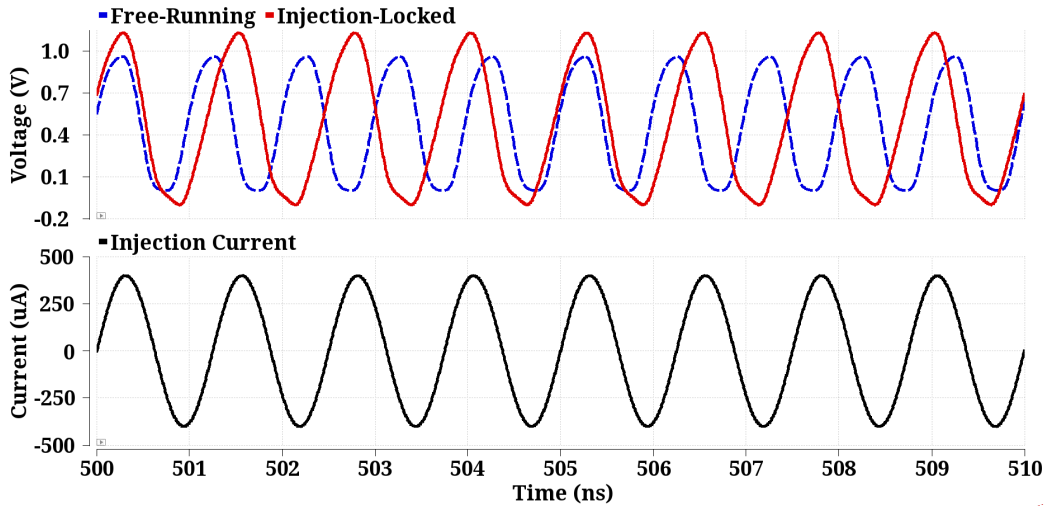

(a) Top: free-running oscillation voltage $v_0(\omega_0 t)$ (blue, dashed curve) and injection-locked oscillation voltage $v_{\text{osc}}(t)$ (red, solid curve). Bottom: injection current $i_{\text{inj}}(t)$.

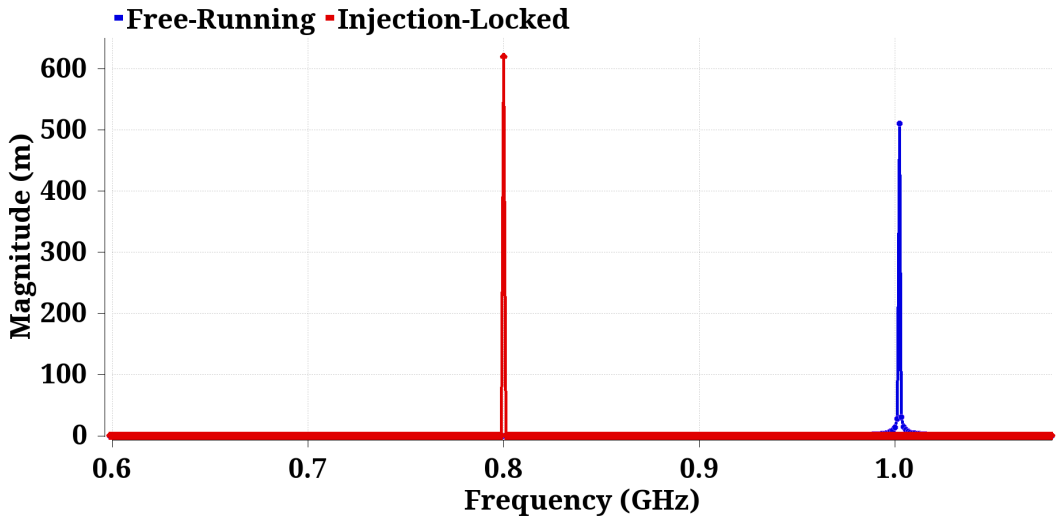

(b) Magnitude spectra of the free-running and injection-locked oscillation voltages.

Figure 1.4: An example of injection locking. Note that the oscillation voltage is observed at the node being injected into.

at $f_{\text{inj}} = 0.8\,\text{GHz}$. Consequently, while the free-running oscillation voltage traverses 10 cycles in the 10 nanosecond interval shown, both the injection current and the injection-locked oscillation voltage only undergo 8 cycles. Notice how the injection alters both the shape and the size of the oscillation voltage.

In light of Eq. (1.3), observe that the phenomenon of injection locking is mathemat-

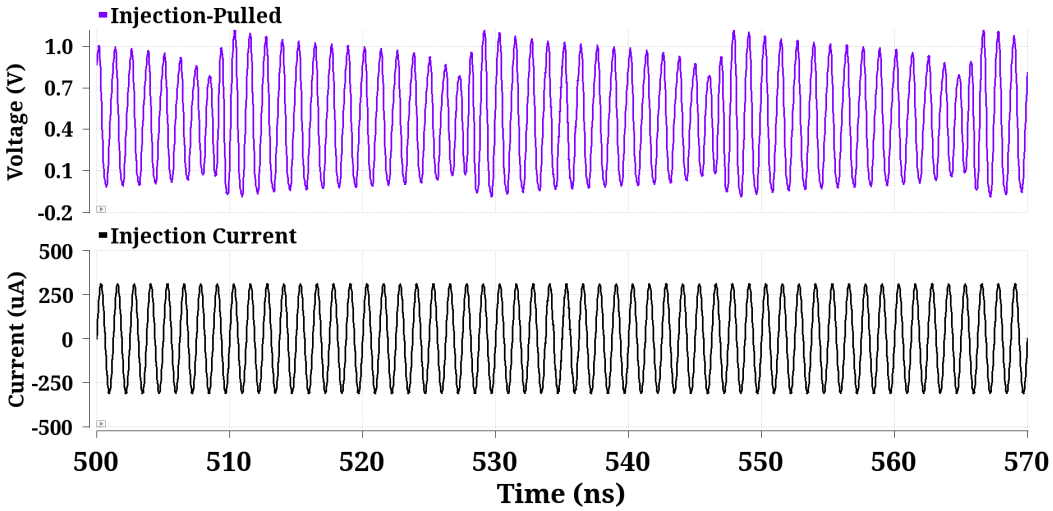

(a) Top: oscillation voltage of an injection-pulled oscillator. Bottom: injection current.

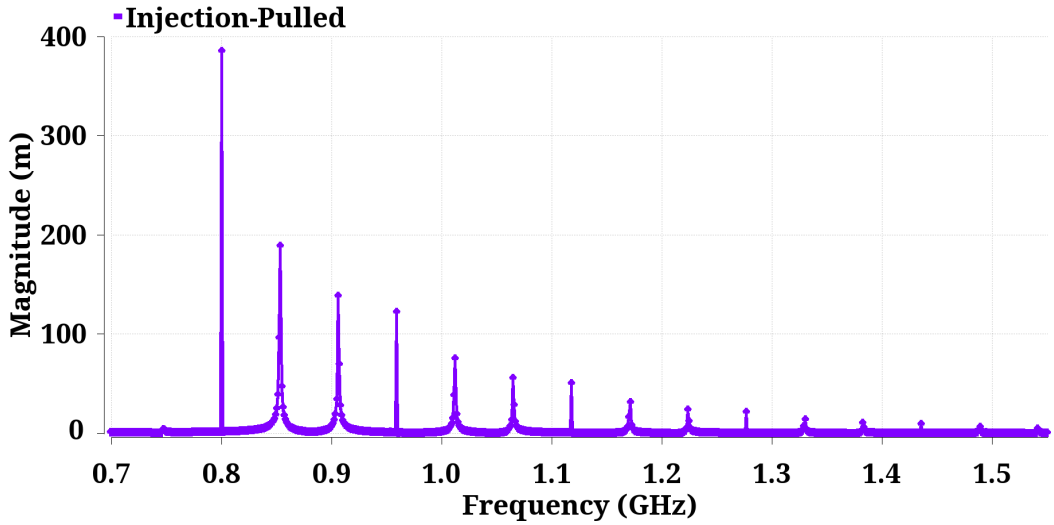

(b) Magnitude spectrum of the injection-pulled oscillation voltage.

Figure 1.5: An example of injection pulling where $f_0 = 1$ GHz and $f_{\text{inj}} = 0.8$ GHz.

ically represented by θ being constant in time:

$$\boxed{\text{Injection Locked} \iff \frac{d\theta}{dt} = 0.} \tag{1.4}$$

The value of θ for an injection-locked oscillator, which represents the phase difference between the oscillator and the injection, is not arbitrary. For a given oscillator and injection waveform, θ varies with the injection frequency in a specific manner. This relationship is known as the ***lock characteristic***.

As we will see, the oscillator is only capable of injection locking when ω_{inj} is

sufficiently close to ω_0. The range of frequencies that the oscillator can lock to is known as the ***lock range***. More precisely, the upper/lower lock range $\omega_L^{\pm}$ is defined as the maximum/minimum value of the frequency deviation $\Delta\omega \equiv \omega_{\text{inj}} - \omega_0$ for which the oscillator is capable of injection locking. The lock range depends not only on the oscillator but on the size and shape of the injection waveform as well.

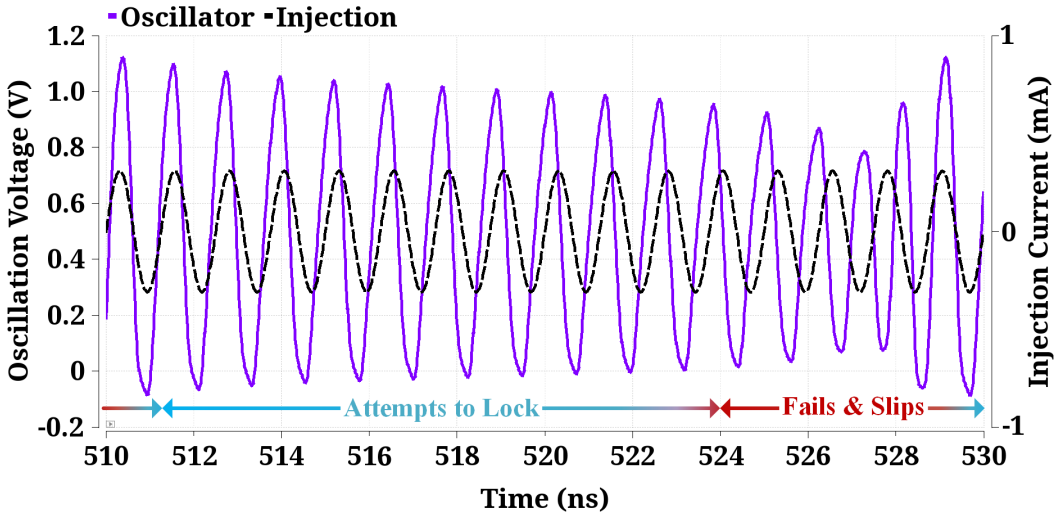

(a) Oscillation voltage and injection current.

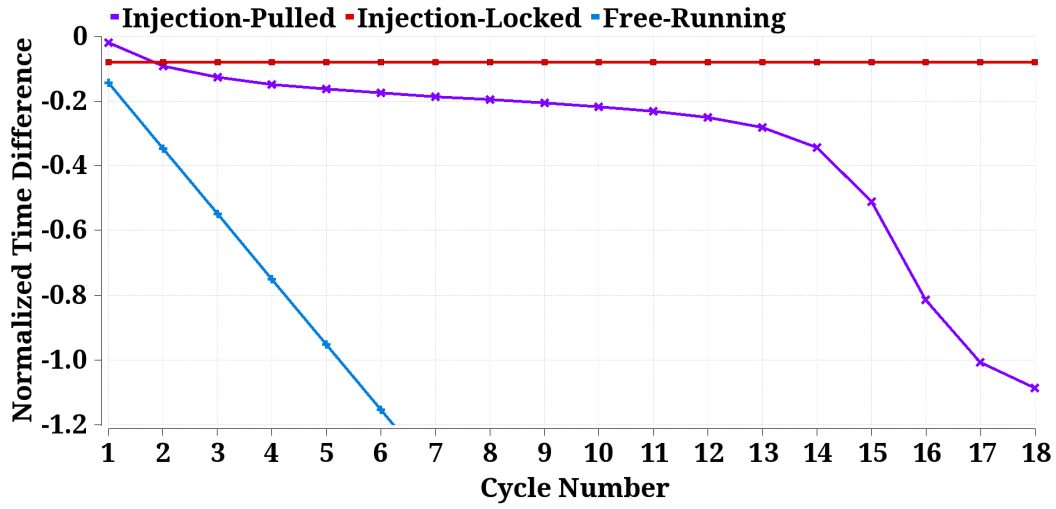

(b) Threshold-crossing difference normalized to the injection period.

Figure 1.6: Zooming into a single "beat" for the injection-pulled oscillator of Figure 1.5.

If the injection fails to lock the oscillator because it is outside of the lock range, then $d\theta/dt \neq 0$ and we instead say that the oscillator is ***injection pulled*** by the injection signal. An example of injection pulling is depicted in Figure 1.5, obtained by decreasing the injection strength, and therefore the lock range, from the injection-

locked example of Figure 1.4. The frequency of the "beats" which appear in the time-domain plot of the oscillation voltage is equal to the distance between the adjacent tones in the frequency-domain spectrum. A closer look at what happens during one of these low-frequency beats is shown in Figure 1.6. Essentially, the injection "attempts" to lock the oscillator, but is unable to effect a sufficiently large change in the oscillation frequency, causing the oscillator to eventually "slip" by an entire cycle compared to the injection signal. One way of visualizing this is to compare the threshold crossing times of the oscillator and the injection. Specifically, consider the difference between the falling-edge 0.5 V-crossing times of the oscillation voltage and the falling-edge zero-crossing times of the injection, normalized to T_{inj}. This parameter increases (or decreases) by 1 whenever the oscillator retards (or advances) by a single cycle relative to the injection. Figure 1.6b plots this parameter as a function of the number of elapsed cycles for the window under consideration and compares the result against the injection-locked and free-running scenarios. As we can see, an injection-locked oscillator features a constant threshold-crossing difference over all cycles, whereas the threshold-crossing difference must grow by a fixed amount per cycle for a free-running oscillator (at a different frequency). On the other hand, for an injection-pulled oscillator, while the injection "tries" to keep this threshold-crossing difference constant, it eventually fails and the oscillator "runs off on its own" by an entire cycle. In light of this repeated behavior, one might suspect that the oscillation voltage of an injection-pulled oscillator is periodic with this (lower) beat frequency ω_b. Unfortunately, this is not correct unless the injection frequency ω_{inj} is a *multiple* of ω_b, which is not true in general. Therefore, we surmise that the periodicity of the oscillator is corrupted by injection pulling.

1.3 Organization of Thesis

The rest of this thesis is organized as follows. Chapter 2 puts this work into context by reviewing existing injection locking and pulling models. A distinction is made between mathematical macromodeling approaches, which our theory falls under, and physically-based behavioral analyses. Chapter 3 conducts a thought experiment that examines the effect an impulse train has on an ideal LC oscillator. The understanding gleaned from this thought experiment will motivate the development of our model from a conceptual standpoint.

Chapter 4 develops, from first principles, a time-synchronous theory of oscillators that are subjected to a periodic external perturbation. We demonstrate how the oscillator's autonomy and its periodically time-varying nature combine to enable

injection locking. Chapter 5 augments the theory for the specific case of the LC oscillator by accounting for the oscillation amplitude, resulting in a model which is applicable for large injections. Novel insights into how different types of LC oscillators behave, which are uniquely captured by this model, are also provided. Chapter 6 generalizes the framework to allow for an arbitrary rational relationship between the injection and oscillation frequencies under lock.

Chapter 7 focuses on an analysis of the transient behavior of periodically disturbed oscillators. Issues such as mode stability, the pull-in process, and the dynamics of injection pulling are covered. A theoretical treatment of the effect of a *stochastic* disturbance, which illuminates the elementary connection between phase noise and injection locking, is also performed. Chapter 8 explores design insights which arise from the developed framework. Specifically, several ways of enhancing an oscillator's lock range are introduced and demonstrated. Chapter 9 uses the techniques discussed in Chapter 8 to implement a low-power injection-locked prescaler for frequency synthesis applications.

Chapter 10 takes an alternative, physical viewpoint of injection locking and carries out a phasor-based analysis of sinusoidal injection locking in LC and ring oscillators. Future research directions are suggested in Chapter 11, and other unrelated works are presented in Chapter 12.

Chapter 2

EXISTING MODELS

"All models are wrong, but some are useful."

GEORGE EDWARD PELHAM BOX, 1976

Injection locking and pulling of electrical oscillators has been studied extensively for at least the past century [44]–[85]. In this chapter, we give a brief overview of the existing models in the literature which are used more prominently in the electronics community. In general, any analysis technique can be categorized as either a *behavioral model* or a *mathematical macromodel*.

2.1 Behavioral Models

Behavioral approaches start with a *physical* model of the oscillator under injection, such as a circuit model comprising resistors, capacitors, inductors, idealized nonlinear elements, and the injection source(s). Known analysis techniques for this physical model (e.g., KCL/KVL, Ohm's Law, phasors) are then used to study the system, leading to conclusions about aspects of the system's behavior that we seek to understand. Due to their physically-based nature, such approaches tend to provide intuition more directly. But their utility is limited because the analysis is restricted to a particular oscillator topology (e.g., LC, ring, or relaxation), and their predictive power is constrained by the accuracy of the model itself. The analysis presented in Chapter 10 of this thesis is a behavioral model.

Adler's Equation

Both experimental and theoretical work on the synchronization of electrical oscillators have been conducted as early as the 1920's [44]–[46]. However, perhaps the most well-known behavioral model for injection locking is Adler's equation, developed by Robert Adler in 1946 [47]. Adler's equation describes the phase of an LC oscillator under the influence of a weak sinusoidal injection close to the free-running oscillation frequency.

We present a simplified derivation here. Consider the ideal LC oscillator shown in Figure 2.1. The loss of the LC tank, represented by the parallel resistance R_P, is restored by the nonlinear $-G_m$-transconductor which generates a current whose

fundamental component is in phase with $v_{\text{osc}}(t)$ and has an amplitude of I_{osc}. The oscillator free-runs at the LC tank's resonant frequency

$$\omega_0 = \frac{1}{\sqrt{LC}}. \tag{2.1}$$

The current consumed by the resistance is supplied by the oscillator current I_{osc}, leading to a sinusoidal oscillation amplitude of

$$V_{\text{osc}} = I_{\text{osc}} R_P. \tag{2.2}$$

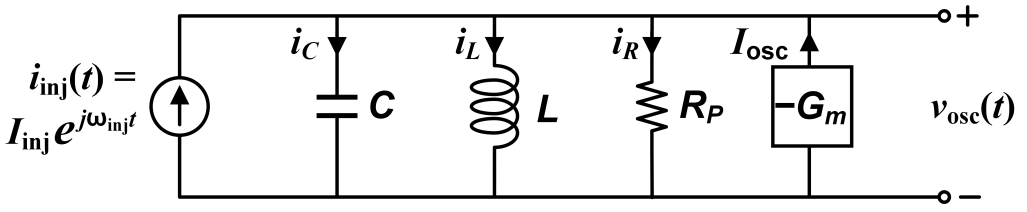

Figure 2.1: Schematic of the basic LC oscillator under injection used in the derivation of Adler's equation.

Suppose a weak sinusoidal current $i_{\text{inj}}(t)$ in the close vicinity of ω_0 is injected into the oscillator as shown. Utilizing complex exponential notation to simplify the subsequent algebra, we express the injection current as

$$i_{\text{inj}}(t) = I_{\text{inj}} e^{j\omega_{\text{inj}} t}, \tag{2.3}$$

where the injection amplitude is *small* in the sense that $I_{\text{inj}} \ll I_{\text{osc}}$, and the injection frequency is near the free-running frequency in the sense that $\left|\omega_{\text{inj}} - \omega_0\right| \ll \omega_0$. We adopt the usual convention from Eq. (1.3) of expressing the phase of the oscillation voltage as $\omega_{\text{inj}} t + \theta(t)$, where the objective of this analysis is to study the behavior of θ, the phase difference between the oscillator and the injection. Because the injection is weak compared to the oscillator current, its impact on the resistor current i_R is negligible, leaving the oscillation amplitude $V_{\text{osc}} = I_{\text{osc}} R_P$ unchanged. Therefore, we write the oscillation voltage as

$$v_{\text{osc}} = V_{\text{osc}} e^{j(\omega_{\text{inj}} t + \theta)}, \tag{2.4}$$

and we instead focus on how the injection influences the LC tank by writing KCL for the remaining currents:

$$\begin{aligned} i_{\text{inj}} &= i_C + i_L \\ \implies \frac{d i_{\text{inj}}}{dt} &= C \frac{d^2 v_{\text{osc}}}{dt^2} + \frac{v_{\text{osc}}}{L}. \end{aligned} \tag{2.5}$$

The intuition here is that the reactive current drawn by the LC tank when the oscillator operates away from resonance must be supplied by the injection current. Substituting for the injection current and the oscillation voltage, we get

$$j\omega_{\text{inj}} I_{\text{inj}} e^{j\omega_{\text{inj}} t} = \left\{ C \left[j\frac{d^2\theta}{dt^2} - \left(\omega_{\text{inj}} + \frac{d\theta}{dt} \right)^2 \right] + \frac{1}{L} \right\} I_{\text{osc}} R_P e^{j(\omega_{\text{inj}} t + \theta)}. \tag{2.6}$$

Multiplying through by $e^{-j(\omega_{\text{inj}} t+\theta)}$ and taking the real part, we get[1]

$$-\left(\omega_{\text{inj}} + \frac{d\theta}{dt} \right)^2 + {\omega_0}^2 = \frac{I_{\text{inj}}}{I_{\text{osc}}} \frac{\omega_0 \omega_{\text{inj}}}{Q} \sin\theta, \tag{2.7}$$

where we used the tank's quality factor

$$Q = \frac{R_P}{\omega_0 L} = R_P \omega_0 C. \tag{2.8}$$

To simplify the left-hand-side, we use the fact that $\left|\omega_{\text{inj}} - \omega_0\right| \ll \omega_0$ to approximate ${\omega_0}^2 - {\omega_{\text{inj}}}^2 \approx 2\omega_{\text{inj}}(\omega_0 - \omega_{\text{inj}})$, and we assume that θ varies *slowly* in comparison to the injection:

$$\left| \frac{d\theta}{dt} \right| \ll \omega_{\text{inj}}. \tag{2.9}$$

With these approximations, we obtain

$$2\omega_{\text{inj}} \left(\omega_0 - \omega_{\text{inj}} - \frac{d\theta}{dt} \right) = \frac{I_{\text{inj}}}{I_{\text{osc}}} \frac{\omega_0 \omega_{\text{inj}}}{Q} \sin\theta. \tag{2.10}$$

Rearranging, we arrive at Adler's equation:

$$\frac{d\theta}{dt} = \omega_0 - \omega_{\text{inj}} - \frac{\omega_0}{2Q} \frac{I_{\text{inj}}}{I_{\text{osc}}} \sin\theta. \tag{2.11}$$

Since θ is constant under lock, the maximum frequency deviation that the oscillator can lock to, known as the lock range, is given by

$$\omega_L = \frac{\omega_0}{2Q} \frac{I_{\text{inj}}}{I_{\text{osc}}}. \tag{2.12}$$

One of the key insights resulting from Adler's equation is that the lock range increases with the relative injection strength $I_{\text{inj}}/I_{\text{osc}}$ but varies inversely with the tank's quality factor Q.

Recall the fundamental assumptions underlying this derivation:

[1] Obviously, both the real and imaginary parts need to be satisfied. In a more detailed analysis which does not assume the transconductor and resistor currents cancel, the imaginary part of this equation would describe the oscillation amplitude.

1. The injection is much weaker than the oscillator: $I_{\text{inj}} \ll I_{\text{osc}}$.
2. The frequency deviation is small: $\left|\omega_{\text{inj}} - \omega_0\right| \ll \omega_0$.
3. The oscillator's phase varies slowly relative to the injection: $|\theta'(t)| \ll \omega_{\text{inj}}$.

In light of Adler's equation, the third assumption is implied by the first two. We will challenge the first two conditions in this thesis.

Because of the accurate conclusions about the lock range, the pull-in process, and the presence of "beats" in an unlocked oscillator that Adler's equation is able to predict, it has formed the basis for numerous other approaches to understanding injection locking and pulling in electrical oscillators.

Related Works

Many have built upon Adler's work over the years. Notable examples include generalizing the treatment to non-triode oscillator topologies (Huntoon and Weiss, 1947) [48], modifying the equation for the lock range to account for large injection currents (Paciorek, 1965) [49], focusing on the unlocked behavior of injection-pulled oscillators (Stover, 1966; Armand, 1969) [50], [51], extension of the analysis to microwave oscillators with distributed elements (Kurokawa, 1973) [52], [53], and coming up with alternative derivations of Adler's equation as well as applying Adler's equation in different settings to glean new insights (Razavi, 2004) [38]. Even recent works which focus on significantly more complicated scenarios, such as mutual pulling between VCOs residing in different PLLs [86], often use Adler's equation as a starting point for their analysis.

Mirzaei's Generalized Adler's Equation

The most powerful generalization of Adler's equation to date was proposed by Mirzaei *et al.* in 2006 [59], where they use KCL and KVL to analyze the LC oscillator without assuming a weak injection signal. Consequently, the result of their analysis, which they call "Generalized Adler's equation," accounts for how the injection can influence the *amplitude* of oscillation—not just the phase. In doing so, the term I_{osc} in Adler's equation Eq. (2.11) is replaced with $I_{\text{osc}} + I_{\text{inj}} \cos\theta$:

$$\frac{d\theta}{dt} = \omega_0 - \omega_{\text{inj}} - \frac{\omega_0}{2Q} \frac{I_{\text{inj}} \sin\theta}{I_{\text{osc}} + I_{\text{inj}} \cos\theta}. \tag{2.13}$$

They then use this equation to conduct a rather thorough analysis of the quadrature LC oscillator [21], one of the most widely used applications of injection locking in

modern high-frequency systems. The lock range associated with this more general equation can be shown to be [38], [49], [59]

$$\omega_L = \frac{\omega_0}{2Q}\frac{I_{\text{inj}}}{I_{\text{osc}}}\frac{1}{\sqrt{1-\dfrac{{I_{\text{inj}}}^2}{{I_{\text{osc}}}^2}}}. \tag{2.14}$$

In this thesis, we will demonstrate how both the time-synchronous model developed in Chapters 4 and 5 as well as our phasor-based analysis presented in Chapter 10 analytically reduce to Adler's equation and its generalization by Mirzaei *et al.*

Models for Ring Oscillators

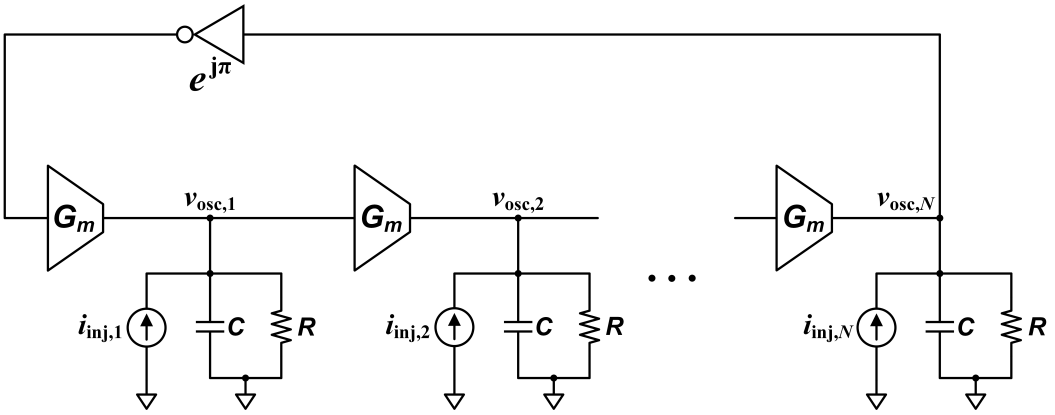

Figure 2.2: A nonlinear model of the ring oscillator often used for injection locking and pulling applications.

The most conspicuous limitation associated with Adler's equation and its surrounding body of work is, of course, the fact that the analysis pertains only to LC oscillators. Consequently a variety of behavioral approaches for modeling injection locking in ring oscillators have also been developed.[2] The approach which has gained the most traction in recent years models each stage of the ring as an *RC*-delay cell driven by an idealized, nonlinear transconductor [10], [60]–[65], as shown in Figure 2.2. In particular, this behavioral model allows for each node of the ring oscillator to be injected into, a technique which can widen the lock range significantly (see Section 6.7).

Among these approaches, several have stood out. The model proposed by Gangasani and Kinget [61], [62] is slightly more general in that it allows for an arbitrary delay

[2]The other type of non-LC electrical oscillator, the relaxation oscillator, has received much less attention in this regard because ring oscillators are far more commonly used in integrated electronics due to their ease of implementation and relatively reliable performance.

dynamic (the "d-Δ relationship") for each stage of the ring. On the more practical side, the analyses carried out by by Chien *et al.* [63] and Mirzaei *et al.* [10], [60] have led to the design of wideband CMOS ring-oscillator-based injection-locked frequency dividers.

2.2 Mathematical Macromodels

In contrast to behavioral or physically-based approaches, macromodeling techniques start with a collection of fundamental mathematical properties of the system under study (e.g., linearity, time-invariance, memory, causality). An abstract, general description of an arbitrary system that satisfies these properties is then formulated, allowing for certain *parameters*[3] of interest to be identified (e.g., impulse response, transfer function, scattering matrix, Fourier series coefficients). These parameters are then calculated analytically, simulated, or even measured for the actual system of interest (i.e., the oscillator) and then used to make conclusions about the physical properties of the system that we want to figure out.

The key to successful macromodeling lies in the choice of these parameters—they need to be sufficiently easy to ascertain, but they also need to capture enough information about the system's behavior to be useful. In effect, these parameters serve as an *intermediary* between the fundamental physics governing the system's operation and the system's characteristics that we are actually interested in, as it would be too difficult or computationally intractable to derive the latter from the former directly. As an example, it would not be feasible or necessary to perform a full-blown, brute-force analysis of the current through every branch and voltage at every node of an oscillator just to derive its phase noise or synchronization properties.

Such approaches tend to be very general in their applicability, but due to their abstract nature, care must be taken when interpreting their results to ensure that they are both physically meaningful and practically insightful. An exemplar of a mathematical macromodel which simultaneously possesses tremendous predictive power while being intuitive to understand is Hajimiri and Lee's oscillator phase noise model [87]–[90]. The core parameter at the heart of their model is a periodically time-varying impulse response of the oscillator's phase with respect to noise, embodied in a parameter they named the Impulse Sensitivity Function (ISF) $\Gamma(x)$. The ISF will be discussed extensively in Chapter 4. The model developed in the bulk of

[3]Note that a "parameter" in this context could be a function, a scalar or matrix variable, a sequence, etc.

this thesis builds upon—but greatly generalizes—Hajimiri and Lee's work, and is therefore also a mathematical macromodel.

The Perturbation Projection Vector (PPV)

A theoretical framework based on Floquet theory, pioneered mostly by Demir and Roychowdhury, has been developed over the past couple decades for modeling oscillators in the presence of external disturbances. The framework, originally developed to model phase noise [91]–[93], is based on a parameter known as the Perturbation Projection Vector (PPV) $\mathbf{v}_1(t)$. A key advantage of the PPV is that it can be readily extracted from the steady-state solution of the oscillator, whereas the ISF requires a collection of (possibly time-consuming) transient simulations. As a result, this framework is particularly useful for performing efficient phase noise simulations of large circuits with numerous noise sources. The PPV-based framework has recently been extended to the modeling of injection locking and pulling in oscillators [66]–[71], and has shown success in being able to capture both the steady-state locked, as well as transient unlocked, behavior of an arbitrary oscillator under injection. Recently, the PPV has also been used to model the effect of weak coupling between oscillators [74] as well as injection-locked frequency dividers by Maffezzoni [75], [76].

At its core, the PPV-based framework approaches the analysis problem from a dynamical systems standpoint—situated more closely to the mathematics rather than the engineering community—leading to an overtly abstract and complicated formulation. Furthermore, the PPV has not been demonstrated to offer more accuracy or predictive power for electrical oscillators than other macromodeling approaches; in fact, the PPV and the ISF are actually the same in many practical scenarios [94]. Consequently, while this body of work is mathematically rigorous, it has not found mainstream usage within the circuit design community.

The Single-Period Injection Response (SPIR)

The Single-Period Injection Response (SPIR) was first utilized within the neuroscience community to model neural oscillators [36]. It was later introduced within the context of electrical oscillators by Dunwell and Carusone in 2013 [77], albeit given a much less insightful name: the Phase Domain Response (PDR). The PDR, which they denote as $P(\phi)$, measures the response of a free-running oscillator to a *single period* of the external injection as the relative timing ϕ between the oscillator and the injection is varied. This parameter is then used to determine properties such

as the lock range, the lock time, and the jitter tracking bandwidth of the oscillator. Although seemingly intuitive, simple to implement, and unconstrained by the type of oscillator or the shape or size of the injection, we will show in Appendix B that this framework is fundamentally flawed from a mathematical standpoint. This error can be intuitively understood by noting that the PDR or SPIR captures the *transient* behavior of a *free-running* oscillator, which is different from the *steady-state* behavior of an *injection-locked* oscillator. With that said, the PDR has found some usage within the electronics community for designing oscillators injection locked by short, tall pulses [18], [78].

Other Works

There are a few other macromodeling approaches in the literature which have found some prominence. In 2008, Maffezzoni used the ISF to derive expressions for the lock range of an arbitrary oscillator subjected to a periodic injection signal [72]. His analysis made no assumptions about the shape of the injection or to the relative harmonic between the injection and oscillation (i.e., the injection-locked oscillation frequency ω_{osc} satisfies $N\omega_{\text{osc}} = M\omega_{\text{inj}}$ where M and N are coprime integers). Consequently, Maffezzoni's work comes the closest to our model—but, it exposes only the tip of the iceberg in terms of the wide array of properties and behaviors that can be predicted using the ISF. Other, more design-oriented mathematical macromodels have focused on analyzing the nonlinear frequency mixing effects that occur within the oscillator and between the oscillator and the injection [4], [6], [79]. These approaches have led to several useful insights for designing integrated injection-locked frequency dividers and prescalers for frequency synthesizer applications.

Chapter 3

A THOUGHT EXPERIMENT: SYNCHRONIZING AN LC OSCILLATOR TO AN IMPULSE TRAIN

3.1 Introduction

In this chapter, we explore the possibility of using a current impulse train to entrain a harmonic electrical oscillator. In doing so, our calculations will lead to an understanding of how the concept of the impulse response can be used to model the phenomenon of injection locking.

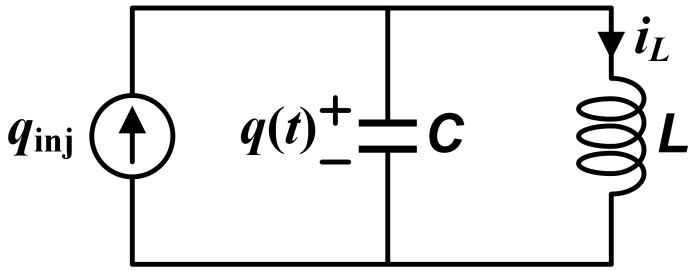

(a) Parallel LC tank with a charge injection source.

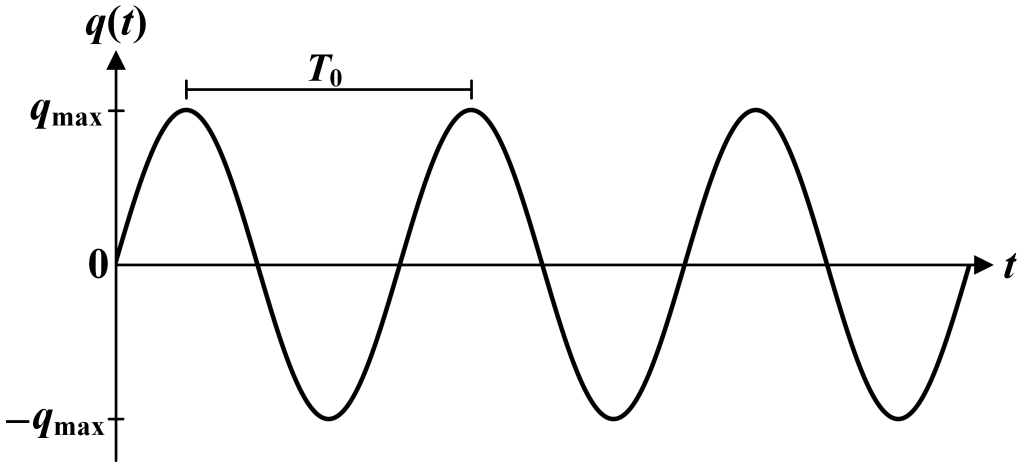

(b) Unperturbed charge swing.

Figure 3.1: Idealized conceptual setup for our thought experiment.

3.2 A Thought Experiment

Consider the parallel LC tank shown in Figure 3.1a, where some amount of energy resonates back and forth between the inductor L and the capacitor C, leading to the

charge swing $q(t)$ shown in Figure 3.1b. The period of oscillation is $T_0 = 2\pi\sqrt{LC}$, the tank's resonant period. In parallel with the tank is a current source which *periodically* injects an impulse of current. The area under each impulse is a discrete amount of charge, whose (absolute) amount we will denote as q_{inj}. Note that this charge is deposited entirely onto the capacitor.

Let us restrict ourselves to the scenario where each injection does not change the amount of energy in the tank; therefore, it merely switches the *polarity* of the instantaneous charge swing $q(t)$. Two such examples are shown in Figure 3.2. Observe how positive (or negative) injections of charge at rising (or falling) edges of the oscillation waveform will advance the phase, whereas the opposite arrangement will retard the phase. We would like to derive a relationship between the amount of injected charge q_{inj}, the maximum charge swing $q_{\max}$, and the change in the oscillation frequency $\Delta\omega \coloneqq \omega_{\text{inj}} - \omega_0$.

Let us compute the phase shift caused by each injection. If we adopt a sine reference, meaning that $q(t) = q_{\max} \sin\varphi(t)$, then each injection takes the instantaneous phase from $-\phi$ to ϕ or vice versa, for some phase $\phi > 0$. The amount of charge needed to advance the phase by $\Delta\varphi = \pm 2\phi$ is (the negative of) twice the capacitor charge at the instant of injection:

$$q_{\text{inj}} = 2q_{\max}\sin(\phi) = 2q_{\max}\sin\left(\frac{\pm\Delta\varphi}{2}\right). \tag{3.1}$$

Solving for the phase shift $\Delta\varphi$ and assuming the injected charge is much less than the maximum charge swing, $q_{\text{inj}} \ll q_{\max}$, we can approximate

$$\Delta\varphi = \pm 2\sin^{-1}\left(\frac{q_{\text{inj}}}{2q_{\max}}\right) \approx \pm\frac{q_{\text{inj}}}{q_{\max}}, \tag{3.2}$$

where the sign depends on the polarity of the injections and on whether they are applied at rising or falling edges.

Next, this phase shift $\Delta\varphi$ corresponds to a period difference $\Delta T \coloneqq T_{\text{inj}} - T_0$ of and a frequency shift $\Delta\omega$ of

$$\frac{\Delta\varphi}{2\pi} = -\frac{\Delta T}{T_0} = \frac{\Delta\omega}{\omega_{\text{inj}}}. \tag{3.3}$$

Thus, we obtain the following relationship:

$$\boxed{\Delta\omega = \frac{\Delta\varphi}{T_{\text{inj}}}.} \tag{3.4}$$

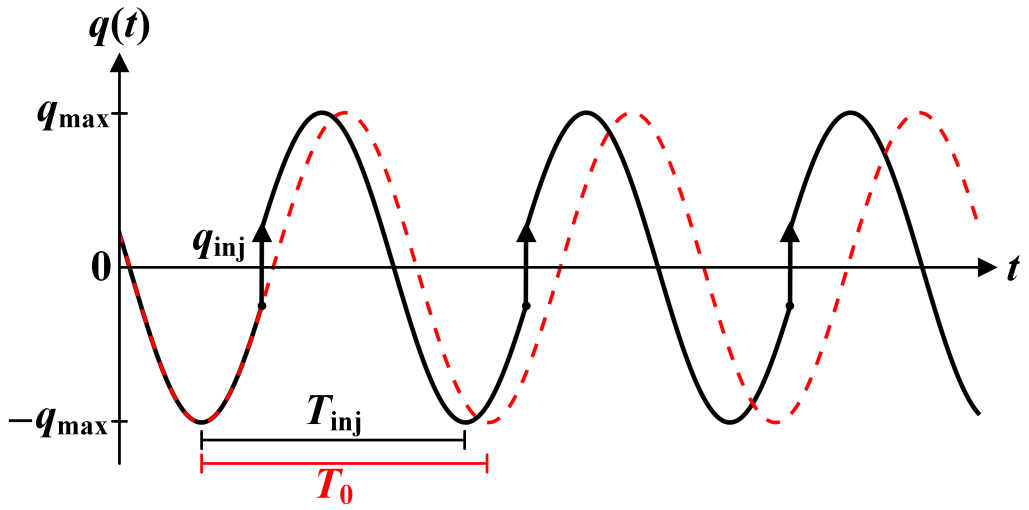

(a) Injections which speed up the oscillation.

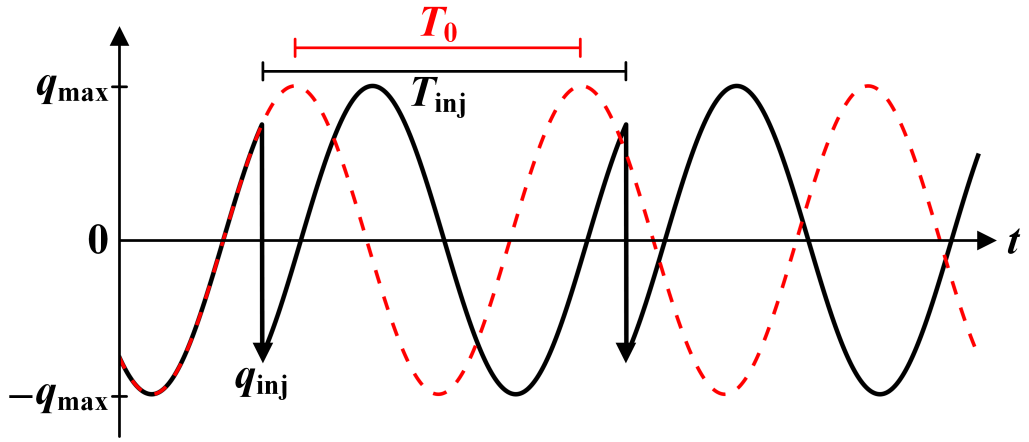

(b) Injections which slow down the oscillation.

Figure 3.2: Synchronizing an LC tank to an impulse train of current injections which leave the amount of energy in the tank unchanged.

Combining this result with Eq. (3.2), we get

$$\Delta\omega = \pm\frac{1}{T_{\text{inj}}}\frac{q_{\text{inj}}}{q_{\text{max}}}. \tag{3.5}$$

One might have noticed that our analysis thus far has really only dealt with an LC *tank*. To extend our reasoning to an LC *oscillator*, which features nonlinear amplitude restoration, we augment the setup of Figure 3.1 to the more complete circuit of Figure 3.3. The current exchanged between the inductor and the capacitor has a peak value of $\omega_0 q_{\text{max}}$, whereas the "oscillator current" consumed by the loss resistance R_P and replenished by the active $-G_m$ transconductor has an amplitude

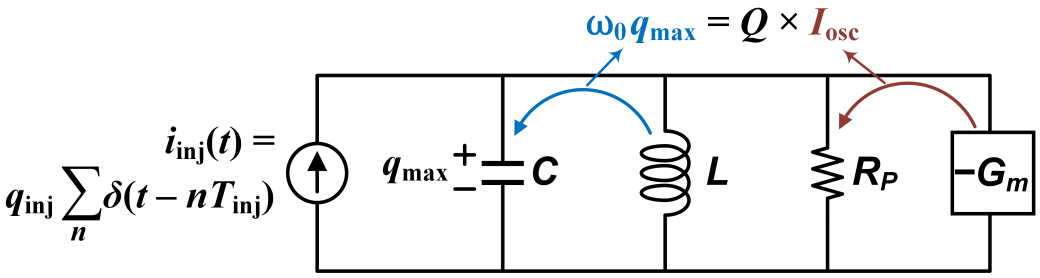

Figure 3.3: Applying an impulse train current injection to an LC oscillator. We are interested in the steady-state behavior of this circuit.

of I_{osc}. Because the LC tank and the resistor are in parallel and therefore experience the same voltage swing, these currents must be related through

$$\omega_0 q_{\max} \cdot \omega_0 L = \frac{\omega_0 q_{\max}}{\omega_0 C} = I_{\text{osc}} R_P. \tag{3.6}$$

In other words, as indicated in Figure 3.3, the amplitude of the current sloshing within the LC tank is Q times the oscillator current:

$$\boxed{\omega_0 q_{\max} = Q I_{\text{osc}},} \tag{3.7}$$

where Q is the tank's quality factor:

$$Q = \frac{R_P}{\omega_0 L} = R_P \omega_0 C. \tag{3.8}$$

For the sake of argument, let us look at the *fundamental component* of the impulse train $i_{\text{inj}}(t)$. Its amplitude, which we shall denote by I_{inj}, is given by

$$\begin{aligned} I_{\text{inj}} &= \frac{2}{T_{\text{inj}}} \int_{T_{\text{inj}}} q_{\text{inj}} \sum_{n=-\infty}^{\infty} \delta(t - nT_{\text{inj}})\, e^{-j\omega_{\text{inj}} t}\, dt \\ &= \frac{2q_{\text{inj}}}{T_{\text{inj}}}. \end{aligned} \tag{3.9}$$

Combining Eqs. (3.5), (3.7), and (3.9), we get

$$\Delta\omega = \pm \frac{\omega_0}{2Q} \frac{I_{\text{inj}}}{I_{\text{osc}}}, \tag{3.10}$$

which yields a remarkable result: the frequency difference is equal to the lock range obtained from Adler's equation Eq. (2.12)!

One way of interpreting this result is that the current setup is poised at the "edge" of the lock range. In other words, "all" of the injection current is being used to

change the oscillation frequency. Mathematically, this follows from the fact that the impulse train's fundamental component is in quadrature with the oscillation. The delineation of the injection's "in-phase" and "quadrature-phase" components will be discussed in great detail in Chapter 10.

3.3 Varying the Time of Injection

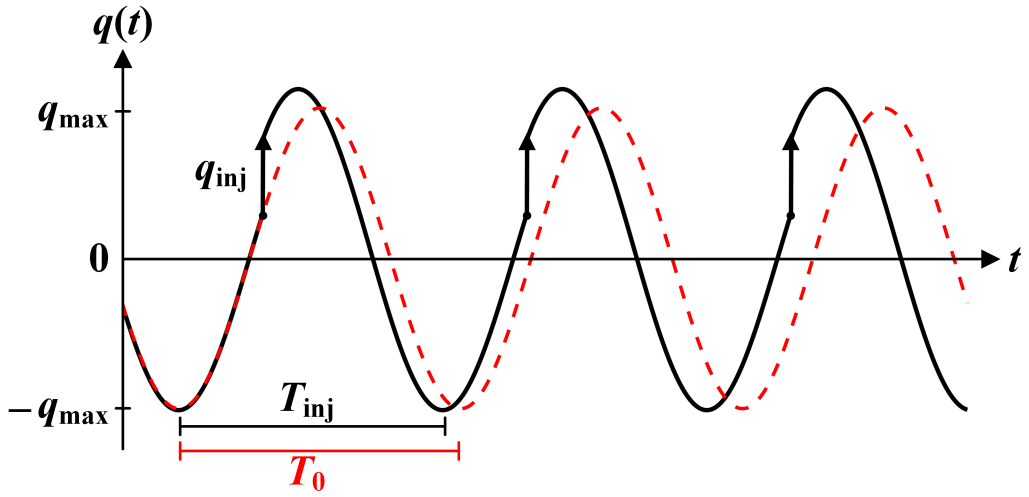

Figure 3.4: Varying the time at which the injections are applied.

Based on the preceding analysis, it should be apparent that for a fixed relative injection strength $q_{\text{inj}}/q_{\text{max}}$, there are only two instants during each cycle when the injection can be applied so as to leave the tank's energy unchanged. Specifically, notice how the fundamental components of $i_{\text{inj}}(t)$ and $q(t)$ are $\pm 90°$ out-of-phase. But what if we vary the time of injection, thereby allowing the injections to instantaneously change the tank's energy? An example of this is shown in Figure 3.4.

To describe this situation precisely, we must characterize the point along the oscillation cycle at which the injection is applied. Specifically, let θ represent the phase difference between the *fundamental components* of the injection current and the charge swing. This is illustrated in Figure 3.5, where $q_{\text{fund}}(t)$ is the fundamental component of the actual charge swing $q(t)$, and $i_{\text{fund}}(t)$ is the fundamental component of the impulse train injection current. Notice how θ has two possible interpretations. As the phase difference between the fundamental components, the difference between their rising (or falling) edge zero-crossing times is equal to $-\theta/\omega_{\text{inj}}$. Equivalently, for positive or negative injections of charge respectively, the value of $q_{\text{fund}}(t)$ at the time of injection is equal to $\pm q_{\text{max}} \cos\theta$, where q_{max} is the amplitude of $q_{\text{fund}}(t)$. In other words, θ can be thought of as a generalized definition

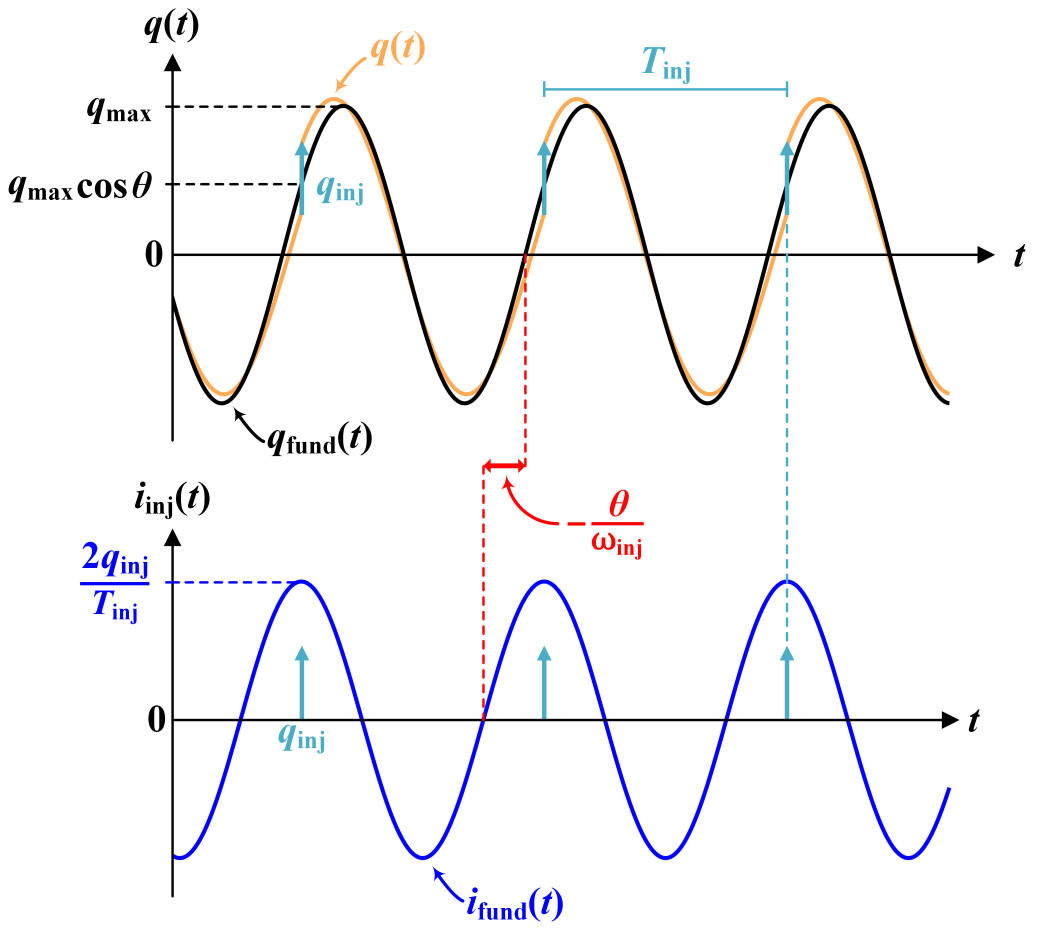

Figure 3.5: Defining the phase θ using the fundamental components of the waveforms from Figure 3.4.

of the phase of oscillation at the time of injection. In particular, $\theta = 0$ or $\theta = \pi$ correspond to peak/trough injections that respectively *increase* or *decrease* the tank energy, whereas $\theta = \pm\pi/2$ correspond to zero-crossing injections that respectively retard or advance the oscillation.

By dealing with fundamental components, observe how θ automatically accounts for the *polarity* of the injection. For example, reversing the injection polarity has the same effect on the oscillator as delaying the injections by half of a cycle. Likewise, negating an impulse train delays its fundamental component by half of a period, thereby shifting θ by π.

Next, we will assume for now that the oscillation amplitude is quickly and completely restored by the oscillator's inherent nonlinearities within a single injection period—but the phase perturbation remains. Now, in order for the oscillator to synchronize

to the impulse train, the relationship between the frequency difference $\Delta\omega$ and the injection strength must involve the phase θ. To quantify this relationship, we need to calculate the phase shift induced by the injection as a function of θ.

The Phase and Amplitude Response of an LC Oscillator

This treatment parallels that found in Appendix C of [88]. Let us assume the injection is applied at time $t = 0$. With this time reference, we can see from Figure 3.5 that the capacitor charge and the inductor current before the injection ($t < 0$) can be written as

$$\begin{aligned} q(t) &= q_{\max}\cos(\omega_0 t + \theta) \\ i_L(t) &= -q'(t) = \omega_0 q_{\max}\sin(\omega_0 t + \theta). \end{aligned} \tag{3.11}$$

After the injection, both the phase and the amplitude change. Therefore, for $t \geq 0^+$, the capacitor charge and inductor current become

$$\begin{aligned} q(t) &= (q_{\max} + \Delta q_{\max})\cos(\omega_0 t + \theta + \Delta\varphi) \\ i_L(t) &= -q'(t) = \omega_0\,(q_{\max} + \Delta q_{\max})\sin(\omega_0 t + \theta + \Delta\varphi), \end{aligned} \tag{3.12}$$

where amplitude restoration (i.e., the decay of $\Delta q_{\max}$ with time) is irrelevant since we are only interested in the immediate effect of the injection in this analysis.

But we also know that the capacitor charge changes instantaneously by q_{inj} after the injection, whereas the inductor current remains the same. Therefore, using Eq. (3.11) gives

$$\begin{aligned} q(0^+) &= q_{\max}\cos\theta + q_{\text{inj}} \\ i_L(0^+) &= \omega_0 q_{\max}\sin\theta. \end{aligned} \tag{3.13}$$

Comparison with Eq. (3.12) at $t = 0$ therefore yields

$$\begin{aligned} (q_{\max} + \Delta q_{\max})\cos(\theta + \Delta\varphi) &= q_{\max}\cos\theta + q_{\text{inj}} \\ (q_{\max} + \Delta q_{\max})\sin(\theta + \Delta\varphi) &= q_{\max}\sin\theta. \end{aligned} \tag{3.14}$$

Assuming the amount of injected charge is small, $q_{\text{inj}} \ll q_{\max}$, we linearize the equations above with respect to *both* $\Delta\varphi$ and $\Delta q_{\max}$ to get

$$\begin{aligned} \Delta q_{\max}\cos\theta - \Delta\varphi q_{\max}\sin\theta &= q_{\text{inj}} \\ \Delta q_{\max}\sin\theta + \Delta\varphi q_{\max}\cos\theta &= 0. \end{aligned} \tag{3.15}$$

Now, we can easily solve for $\Delta\varphi$ and $\Delta q_{\max}$:

$$\begin{aligned} \Delta\varphi &= -\frac{q_{\text{inj}}}{q_{\max}}\sin\theta \\ \Delta q_{\max} &= q_{\text{inj}}\cos\theta. \end{aligned} \tag{3.16}$$

Adler's Solution

With this result, the frequency difference $\Delta\omega$ is now related to θ through

$$\Delta\omega = -\frac{1}{T_{\text{inj}}}\frac{q_{\text{inj}}}{q_{\text{max}}}\sin\theta. \tag{3.17}$$

Using Eqs. (3.7) and (3.9) to once again transform the charge quantities q_{inj} and q_{max} into the respective currents I_{inj} and I_{osc}, we arrive at

$$\Delta\omega = -\frac{\omega_0}{2Q}\frac{I_{\text{inj}}}{I_{\text{osc}}}\sin\theta, \tag{3.18}$$

which is the *steady-state solution* to Adler's equation, as we can see from Eq. (2.11)!

3.4 Accounting for Changes in the Maximum Charge Swing

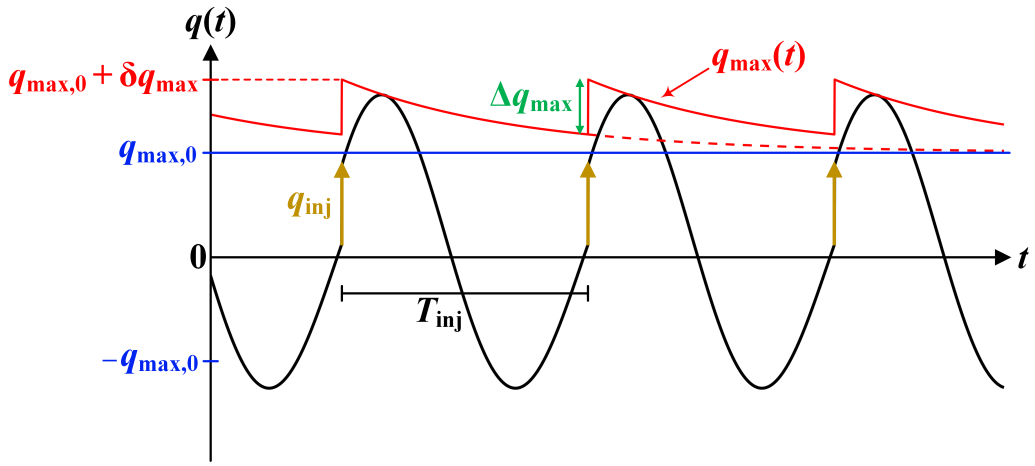

Figure 3.6: Depiction of how the oscillation amplitude $q_{\text{max}}(t)$ evolves with time in steady-state when the injections change the amount of energy stored in the tank.

We can take this thought experiment slightly further by assuming a realistic decay dynamic for the tank's energy in between consecutive injections. This is important because as we can see from Eq. (3.16), the phase shift induced by an injection is inversely proportional to the maximum charge swing. Although Eq. (3.16) already gives the instantaneous change in q_{max} caused by an injection, we will also need to quantify how q_{max} changes with time throughout the entire period.

The unperturbed or free-running amplitude satisfies $\omega_0\, q_{\text{max,0}} = QI_{\text{osc}}$, as this charge swing $q_{\text{max,0}}$ is sustained by an energetic balance between the transconductor, which supplies I_{osc}, and the tank loss, which sets Q. Therefore, we will assume that any deviation of the amplitude from $q_{\text{max,0}}$ decays exponentially with the relaxation time constant of the parallel RLC circuit: $\tau_0 = 2R_PC = 2Q/\omega_0$. Consequently,

even though each injection instantaneously changes the amount of energy stored in the LC tank, the oscillator also continuously attempts to restore this energy to the free-running amount. Eventually, this process reaches an equilibrium, an example of which is shown in Figure 3.6. Let $\delta q_{\max}$ denote the maximum charge swing *in excess* (positive or negative) of $q_{\max,0}$ immediately after an injection. In steady state, the oscillator must return to the same amplitude over each period, and so we require

$$\delta q_{\max} e^{-T_{\text{inj}}/\tau_0} = \delta q_{\max} - \Delta q_{\max}. \tag{3.19}$$

Solving for $\delta q_{\max}$, we get

$$\delta q_{\max} = \frac{\Delta q_{\max}}{1 - e^{-T_{\text{inj}}/\tau_0}}. \tag{3.20}$$

We know that between successive injections, the maximum charge swing as a function of time is given by

$$q_{\max}(t) = q_{\max,0} + \delta q_{\max} e^{-t/\tau_0}. \tag{3.21}$$

For the sake of argument, let us consider the *time-average* of the maximum charge swing:

$$\langle q_{\max} \rangle \coloneqq \frac{1}{T_{\text{inj}}} \int_0^{T_{\text{inj}}} q_{\max}(t)\, dt = q_{\max,0} + \frac{\tau_0}{T_{\text{inj}}} \delta q_{\max} \left(1 - e^{-T_{\text{inj}}/\tau_0}\right). \tag{3.22}$$

Substituting for $\delta q_{\max}$ from Eq. (3.20), we get

$$\langle q_{\max} \rangle = q_{\max,0} + \frac{\tau_0}{T_{\text{inj}}} \Delta q_{\max}. \tag{3.23}$$

This equation makes sense: the longer it takes to dissipate energy (a larger τ_0), or the more frequent the injections (a smaller T_{inj}), the more influence the injections will have on the average amplitude in steady state.

Replacing $q_{\max}$ with $\langle q_{\max} \rangle$ in Eq. (3.17), our frequency shift becomes

$$\Delta\omega = -\frac{1}{T_{\text{inj}}} \frac{q_{\text{inj}}}{\langle q_{\max} \rangle} \sin\theta = -\frac{\dfrac{q_{\text{inj}}}{T_{\text{inj}}} \sin\theta}{q_{\max,0} + \dfrac{\tau_0}{T_{\text{inj}}} q_{\text{inj}} \cos\theta}. \tag{3.24}$$

Using Eqs. (3.9) and (3.7) to eliminate q_{inj} and $q_{\max,0}$ respectively, and relating τ_0 to the quality factor Q, we get

$$\Delta\omega = -\frac{\omega_0}{2Q} \frac{I_{\text{inj}} \sin\theta}{I_{\text{osc}} + I_{\text{inj}} \cos\theta}. \tag{3.25}$$

Interestingly, this is the steady-state solution to Eq. (2.13), which is Mirzaei's Generalized Adler's equation [21].

3.5 Concluding Thoughts

By making simple physical arguments about the behavior of an ideal LC oscillator injected with an impulse train, we arrived at results which originally came from behavioral analyses carried out by Adler [47] and Mirzaei [21]. Therefore, it may be fruitful to use the concept of the *impulse response* to model the phenomenon of injection locking and pulling. We conclude this chapter by pointing out that the relationship between this thought experiment and the general model introduced in this thesis will be established rigorously in Section 5.9.

Chapter 4

A TIME-SYNCHRONOUS MODEL

4.1 Introduction

In this chapter, we develop from first principles a general model for the behavior of an electrical oscillator subjected to a periodic disturbance. As we stated in Section 1.1, within the context of electronics, the disturbance is usually taken to be an injection of current into one or more of the oscillator's nodes. The model makes no assumptions about the topology of the oscillator or the shape of the injection. We will see that our analysis leads to a single, first-order ordinary differential equation for the oscillator's phase which accurately predicts the phenomenon of injection locking and pulling under a variety of scenarios. A distinguishing feature of this model is its time synchronicity—its mathematical structure reveals how the autonomy of the oscillator fundamentally facilitates injection locking and pulling behavior.

4.2 The Impulse Sensitivity Function (ISF)

Here, we construct the fundamental differential equation that governs the behavior of the oscillator's phase. Let us begin by describing the effect that the injection $i_{\text{inj}}(t)$ has on the oscillator's *excess* phase ϕ. Naively reasoning from a perturbation-based perspective, we can attempt to model how fast $\phi(t)$ changes in response to an injection of charge $i_{\text{inj}}(t) \equiv dq_{\text{inj}}/dt$ by using the chain rule:

$$\frac{d\phi}{dt} = \frac{d\phi}{dq_{\text{inj}}} \cdot \frac{dq_{\text{inj}}}{dt}. \tag{4.1}$$

The first derivative represents the rate of change of the oscillator's (excess) phase with respect to injected charge. In other words, it characterizes the sensitivity of the oscillator's phase to an injection of an infinitesimally small impulse of current. However, due to the periodically time-varying nature of the oscillator, this term is not a constant but is instead dependent upon the point along the trajectory the oscillator is at—the oscillator's phase—when the injection occurs. This phase-dependent derivative is known as the oscillator's ***Impulse Sensitivity Function*** or ***ISF*** [87], [88]:

$$\boxed{\tilde{\Gamma}(\varphi) \coloneqq \frac{\partial \phi}{\partial q_{\text{inj}}},} \tag{4.2}$$

with units of [radians/Coulomb]. Note that the ISF defined by Hajimiri and Lee [87], which is denoted by $\Gamma(x)$ *without* the overhead tilde '$\sim$', has been normalized by an additional factor—the inverse of the maximum charge swing $q_{\max}$ across the injection terminals:

$$\tilde{\Gamma}(x) \equiv \frac{\Gamma(x)}{q_{\max}}. \tag{4.3}$$

However, our definition of the ISF will be more convenient for us to work with. Being a function of the oscillator's phase, the ISF is periodic with period 2π.

The second derivative in Eq. (4.1) is simply the injection current $i_{\text{inj}}(t)$. Therefore, we can write

$$\frac{d\phi}{dt} = \tilde{\Gamma}(\varphi) \cdot i_{\text{inj}}(t). \tag{4.4}$$

Before proceeding, we want to very carefully note that this model, by construction, inherently assumes that the injection-to-phase relationship is a linear one. We will discuss the justification for and the implications of this assumption shortly.

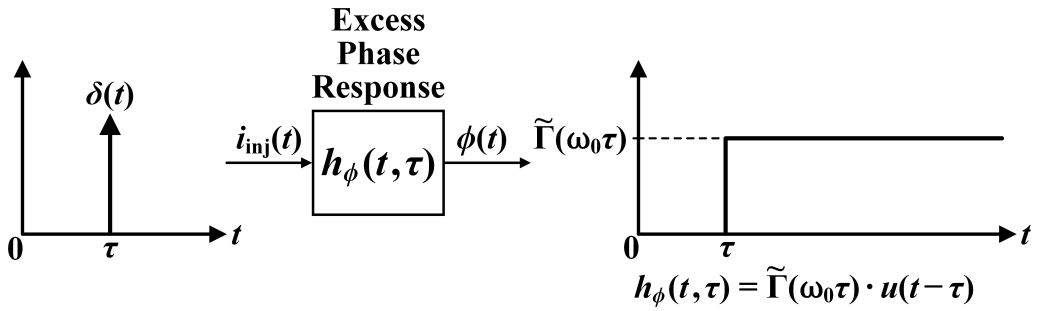

Figure 4.1: Relating the time-varying impulse response for the oscillator's excess phase to the ISF.

Although this reasoning makes sense intuitively, we must make the analysis rigorous. Given the set of observations and assumptions we have just made, we are essentially adopting a linear, periodically time-varying (LPTV) dynamical system model. Now, the ISF appears within the time-varying impulse response of this system. Specifically, the oscillator's excess phase ϕ at time t due to a unit impulse of current injected at time τ is

$$h_\phi(t, \tau) = \tilde{\Gamma}[\varphi(\tau)]\, u(t - \tau). \tag{4.5}$$

The unit-step function in the impulse response signifies the fact that an oscillator has no absolute time reference—any resultant perturbation in its phase appears immediately and will persist indefinitely [87]. This interpretation of the ISF is depicted in Figure 4.1.

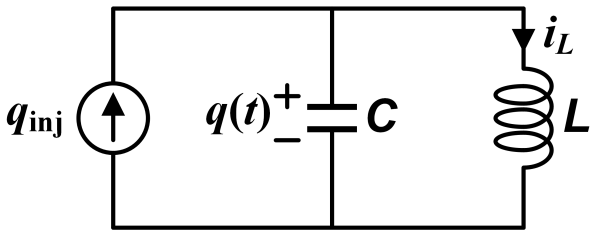

(a) Ideal LC oscillator. Amplitude limiting nonlinearities are not shown.

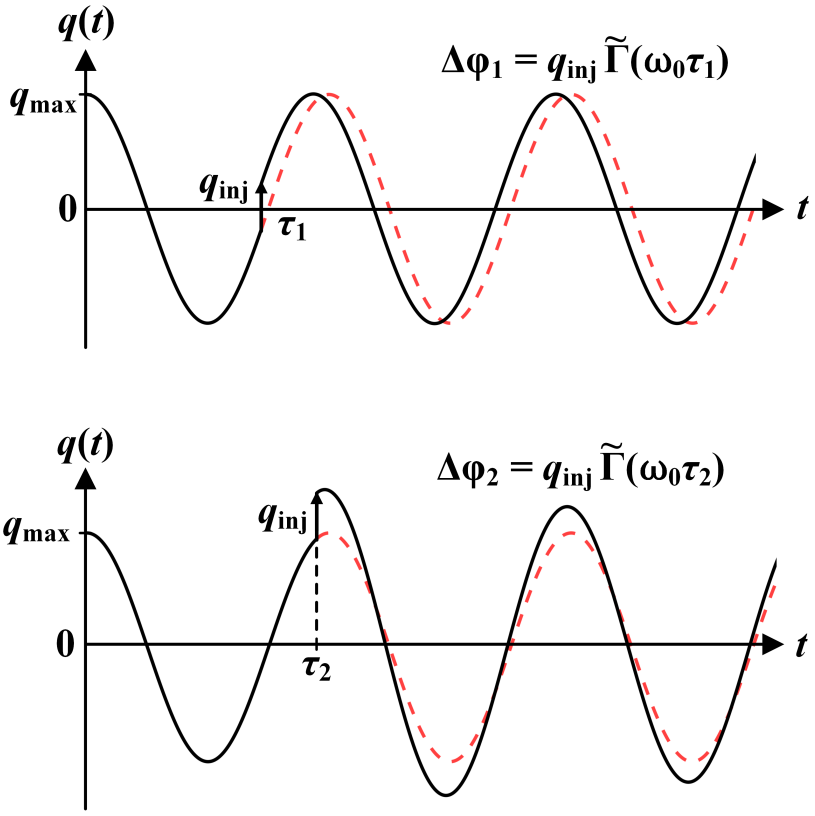

(b) The charge swing $q(t)$ across the capacitor responding to an injection of charge q_{inj} at two different times. The red, dashed curve is the unperturbed version of $q(t)$.

Figure 4.2: The impulse sensitivity function (ISF) captures the dependence of the incurred phase shift on the time of injection.

An example of how time variance arises is given in Figure 4.2, which shows the response of an ideal LC oscillator to an instantaneous injection of charge at two different times. Notice that injecting near a zero-crossing ($t = \tau_1$) results in a large phase shift, whereas injecting near one of the waveform's peaks ($t = \tau_2$) results in almost no phase shift.

The two equivalent viewpoints of the ISF that we have just described are reiterated in Table 4.1. Methods for simulating or calculating the ISF are discussed extensively

Table 4.1: Two Equivalent Viewpoints of the ISF

The ***gradient*** of the phase *along* the limit cycle w.r.t. injected charge: $\tilde{\Gamma} := \frac{\partial \varphi}{\partial q_{\text{inj}}}$	The kernel of the ***time-varying impulse response*** of the (excess) phase w.r.t. the injected current: $h_\phi(t, \tau) = \tilde{\Gamma}[\varphi(\tau)]\, u(t - \tau)$

elsewhere [87], [88], [95].

An Aside: The ISF for Orthogonal States

It is worth noting that a closed-form formula for the ISF exists if the oscillator has an orthogonal state-space representation. Consider a d-dimensional oscillator where the d state variables are node voltages $V_1, \ldots, V_d$ with respective node capacitances $C_1, \ldots, C_d$. Writing the free-running state variables in terms of their oscillation waveforms $v_1(\omega_0 t), \ldots, v_d(\omega_0 t)$ respectively, the ISF due to an injection at the i^{th} node can be computed as [87], [88]

$$\tilde{\Gamma}_i(\varphi) = \frac{v_i'(\varphi)}{\sum_{n=1}^{d} C_n \left[v_n'(\varphi)\right]^2}, \tag{4.6}$$

where the derivatives with respect to the phase φ. If the n^{th} state variable is a branch current I_n instead, simply replace $V_n \to I_n$ and $C_n \to L_n$ (the branch inductance). Notable oscillators with orthogonal state variables are the LC oscillator (using the capacitor voltage and the inductor current) and instantaneously switching relaxation oscillators (using the voltage across the timing capacitor and a binary hysteresis state). Keep in mind, however, that most oscillator representations do not have orthogonal states, and so this formula is only useful in limited circumstances.

Why Linear?

The system we have just described—whose input is the injection current $i_{\text{inj}}(t)$ and output is the excess phase $\phi(t)$—is in general nonlinear; most systems in nature are. Interestingly, the mathematical construction of our model is itself incompatible with true linearity due to its phase-variant nature: suppose we inject some charge q_{inj} into an oscillator at a phase φ. The incurred phase shift is equal to

$$\Delta\phi_0 = q_{\text{inj}} \tilde{\Gamma}(\varphi). \tag{4.7}$$

We can also decompose this injection into two consecutive injections, each of size $q_{\text{inj}}/2$. If the system were truly linear, we could use superposition to say that the

incurred phase shift is also equal to

$$\Delta\phi_1 = \frac{q_{\text{inj}}}{2}\left[\tilde{\Gamma}(\varphi) + \tilde{\Gamma}\left(\varphi + \frac{\Delta\phi_0}{2}\right)\right]. \tag{4.8}$$

As we can see, these two approaches lead to different results in general ($\Delta\phi_0 \neq \Delta\phi_1$) unless q_{inj} is infinitesimally small.

However, we also know that fundamentally, any functional dependence $f(x)$ in nature will exhibit linear behavior provided that the stimulus x is small enough (assuming the first derivative $f'(x)$ is nonzero). This is justified mathematically by looking at a first-order Taylor series expansion of the dependence, and in electrical engineering contexts is frequently referred to as the "small-signal" regime. In particular, it has been empirically observed on a variety of electrical oscillators that when they are injected with a discrete amount of charge which is sufficiently small, the incurred phase shift scales proportionally with the amount of charge [87], [88]. (This proportionality constant is equal to the ISF.) Specifically, the amount of injected charge can typically be considered to be "sufficiently small" when it is much smaller than the maximum charge swing at the injection node. Let us call this regime where linearity holds the "Linear Response Region" [82]–[85] of the oscillator's charge-to-phase relationship.

Let us now use this concept to discuss the linearity of the oscillator's *current*-to-phase relationship[1], which is what we truly care about. Since the ISF is the gradient of the oscillator's phase along the limit cycle, we argue that as long as the oscillator's operation is close enough to its free-running trajectory such that it does not exhibit *qualitatively* different behavior, linearity prevails. Furthermore, we reason that this condition is achieved when the total amount of excess charge accumulated at the injection node, q_{inj}, is within the Linear Response Region defined above.[2] Since the Linear Response Region corresponds to the injected charge being small in comparison to the (free-running) maximum charge swing $q_{\text{max},0}$, this reveals the rather intuitive result that linearity simply requires $q_{\text{inj}} \ll q_{\text{max},0}$, as this preserves the oscillator's "operating point" (along its limit cycle).

We can crudely quantify the condition for current-to-phase linearity, or the "small-injection condition," a bit more precisely. For many oscillators, such as ring and

[1] Note that the current-to-phase relationship subsumes the charge-to-phase relationship since the latter stimulus is merely an impulsive current waveform.

[2] For the more mathematically inclined, note that this is a physical argument—not a rigorous proof. We are not claiming that a system which exhibits linearity with respect to impulses will be linear in general with respect to all inputs.

relaxation oscillators, strong amplitude-limiting mechanisms are in place and the excess injected charge q_{inj} decays very rapidly. Let us examine this dynamic using a first-order, linear, time-invariant model via the following differential equation:

$$\frac{dq_{\text{inj}}}{dt} + \frac{q_{\text{inj}}}{\tau_d} = i_{\text{inj}}(t), \tag{4.9}$$

where τ_d is the time constant at which the excess charge decays. This is equivalent to an impulse response equal to $h_q(t) = e^{-t/\tau_d}u(t)$. For a sinusoidal injection current of amplitude I_{inj}, it is easy to show that the *amplitude* Q_{inj} of the excess charge $q_{\text{inj}}(t)$ is equal to

$$Q_{\text{inj}} = \frac{I_{\text{inj}}}{\sqrt{{\omega_{\text{inj}}}^2 + 1/{\tau_d}^2}} < I_{\text{inj}}\tau_d, \tag{4.10}$$

where the bound holds for any nonzero injection frequency $\omega_{\text{inj}} > 0$. Next, note that this decay usually takes place within a tiny fraction of the oscillation period, and so $\tau_d \ll 1/\omega_0$. Thus, we further have that $Q_{\text{inj}} < I_{\text{inj}}/\omega_0$. Hence, a sufficient condition to maintain linearity is given by

$$I_{\text{inj}} \ll \omega_0 q_{\text{max},0}. \tag{4.11}$$

The right-hand-side is a rough estimate of the amplitude of the (free-running) current flowing across the injection node's capacitance.[3] (In fact, for a sinusoidal swing, they would be equal.) Defining this quantity as the ***oscillation current***,

$$I_{\text{max}} \coloneqq \omega_0 q_{\text{max},0}, \tag{4.12}$$

we can rewrite our small-injection condition as

$$\boxed{I_{\text{inj}} \ll I_{\text{max}}.} \tag{4.13}$$

Note that the time-invariance underlying this analysis can actually lead to woefully inaccurate results—for an LC oscillator, for example, the periodically time-varying nature of the oscillator plays a crucial role in the effect that the injection has on the oscillation amplitude (see Chapter 5). A thorough analysis reveals that the true small-injection condition is $I_{\text{inj}} \ll I_{\text{max}}/Q$, where Q is the tank's quality factor.

Closing this discussion, it is worth mentioning that the range of injection strengths for which linearity holds already covers a wide range of practical scenarios in injection locking and pulling applications.

[3] Carefully note here that $q_{\text{max},0}$ is technically defined as the amplitude of the charge displacement from a DC operating point, which can be approximated as *half* of the peak-to-peak swing.

4.3 A Differential Equation for the Oscillator's Phase

Now, we can calculate the oscillator's excess phase $\phi(t)$ in response to an arbitrary injection of current $i_{\text{inj}}(t)$ using a superposition integral:

$$\phi(t) = \int_{-\infty}^{\infty} h_\phi(t,\tau) i_{\text{inj}}(\tau)\, d\tau = \int_{-\infty}^{t} \tilde{\Gamma}[\varphi(\tau)]\, i_{\text{inj}}(\tau)\, d\tau. \tag{4.14}$$

Differentiating with respect to time,

$$\frac{d\phi}{dt} = \tilde{\Gamma}[\varphi(t)]\, i_{\text{inj}}(t), \tag{4.15}$$

which is exactly what we expected intuitively from Eq. (4.1), but now established rigorously. Next, we make use of Eq. (1.3) to write this differential equation in terms of θ:

$$\frac{d\theta}{dt} = \omega_0 - \omega_{\text{inj}} + \tilde{\Gamma}\left(\omega_{\text{inj}} t + \theta\right) i_{\text{inj}}(t). \tag{4.16}$$

As it stands, this equation has a subtle problem, best illustrated with a simple example. If the oscillator is injection-locked, θ should be constant in time. However, this outcome is not a solution of Eq. (4.16): if θ is constant, then both $\tilde{\Gamma}\left(\omega_{\text{inj}} t + \theta\right)$ and $i_{\text{inj}}(t)$ are periodic with a frequency of ω_{inj}. Hence, their product can, in general, exhibit infinitely many harmonics at DC, ω_{inj}, $2\omega_{\text{inj}}$, etc. Thus, the right-hand-side of Eq. (4.16) will not be equal to zero (or any constant for that matter), as is required by the steady-state solution where $d\theta/dt = 0$. Therefore, we postulate that Eq. (4.16) also captures *intra*-period dynamics that we are not interested in. Instead, the physical behavior we seek to describe is actually encapsulated in the *time-average* of the oscillator's phase, which would eliminate the aforementioned higher-order harmonics.

Time-Averaging and Spectral Decomposition

In order to enforce this conjecture, we need to appeal to the theory of averaging for differential equations. The fundamental theorem governing this technique will be briefly introduced here. Consider the following ordinary differential equation:

$$\frac{du}{dt} = \varepsilon f(u,t), \tag{4.17}$$

where f is periodic in t with period T, and the parameter $\varepsilon > 0$ is assumed to be "small." Now, calculate the time-average of f:

$$\langle f(u) \rangle \coloneqq \frac{1}{T} \int_T f(u,t)\, dt, \tag{4.18}$$

where u is assumed to be a constant within this averaging integral. Then, it is possible to prove that the solution to the averaged differential equation

$$\frac{dv}{dt} = \varepsilon \langle f(v) \rangle \tag{4.19}$$

is ε-close to $u(t)$ on the time scale $1/\varepsilon$ [96].

Within our setting, the averaging period is clearly T_{inj}. The "amplitude" of the injection signal $i_{\text{inj}}(t)$ takes the place of the parameter ε, in the sense that doubling the injection current both doubles the error and halves the time scale over which the error is bounded.[4] Therefore, we obtain[5]

$$\boxed{\frac{d\theta}{dt} = \omega_0 - \omega_{\text{inj}} + \frac{1}{T_{\text{inj}}} \int_{T_{\text{inj}}} \tilde{\Gamma}\big(\omega_{\text{inj}} t + \theta\big)\, i_{\text{inj}}(t)\, dt.} \tag{4.20}$$

Once again, θ is to be treated as a *constant* within the averaging integral on the right-hand-side. This is the basic differential equation that governs the oscillator's phase θ in the presence of a periodic external injection of current $i_{\text{inj}}(t)$. We will refer to this important equation as the ***pulling equation***.

The averaging operation is independent of the time scale. In other words, only the *size* and *shape* of the injection current (and ISF) can directly affect the result—there is no explicit dependence on the averaging period T_{inj} itself. To that end, let us define the ***injection waveform*** $i_{\text{inj},0}(x)$ as the injection current normalized in scale to a period of 2π:

$$i_{\text{inj}}(t) \equiv i_{\text{inj},0}(\omega_{\text{inj}} t). \tag{4.21}$$

The injection waveform only captures the size and shape of the injection current, properties which are independent of the injection period T_{inj}—in much the same way that the oscillation *waveform* $v_0(x)$ contains no information about the free-running oscillation period T_0.

We can now use the injection waveform to rewrite the pulling equation in the following equivalent manner:

$$\frac{d\theta}{dt} = \omega_0 - \omega_{\text{inj}} + \left\langle \tilde{\Gamma}(x + \theta)\, i_{\text{inj},0}(x) \right\rangle_{2\pi}, \tag{4.22}$$

where $\langle \cdot \rangle$ is the averaging operation:

$$\langle \cdot \rangle_T \equiv \frac{1}{T} \int_T \cdot\, dt. \tag{4.23}$$

[4] In Section 7.6 where we discuss phase noise, we will deal with the *non-periodic* case of averaging.

[5] Excuse the abuse of notation—we have reused the variable θ as the solution to the averaged equation.

Figure 4.3 shows a block diagram to help visualize the process described by the pulling equation. Note that since θ is a constant variable with respect to the averaging integral, we can shift it into the argument of the injection current. If the process reaches a static equilibrium for θ, the oscillator becomes injection locked.

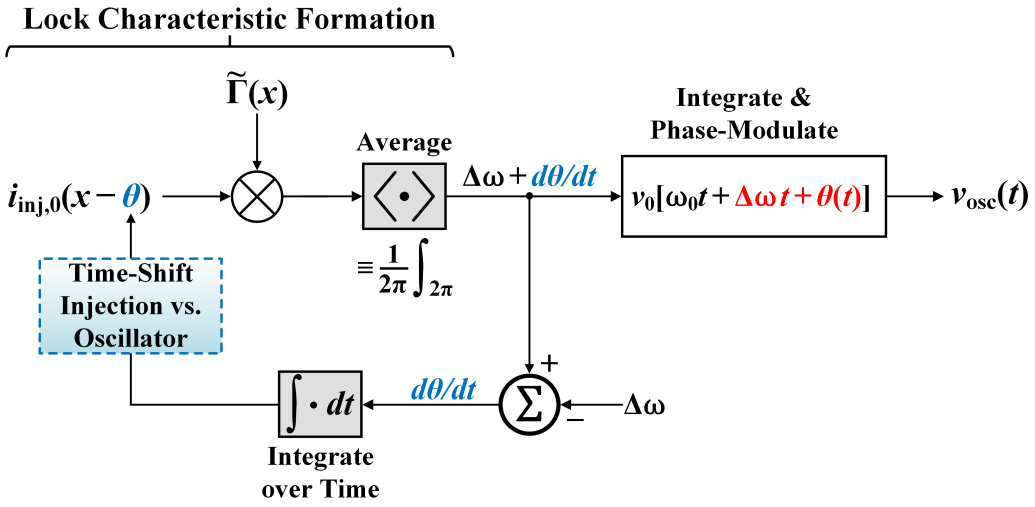

Figure 4.3: Block diagram depicting what happens to the phase of a periodically disturbed oscillator.

The result of the averaging operation can also be expressed in a more insightful way by utilizing Fourier analysis to expose the periodicity of the ISF and the injection. Specifically, let us expand these two functions in terms of their Fourier series:

$$\begin{aligned} \tilde{\Gamma}(x) &= \frac{\tilde{\Gamma}_0}{2} + \sum_{n=1}^{\infty} \left|\tilde{\Gamma}_n\right| \cos(nx + \angle\tilde{\Gamma}_n) \\ i_{\text{inj}}(t) &= \frac{I_{\text{inj},0}}{2} + \sum_{n=1}^{\infty} \left|I_{\text{inj},n}\right| \cos(n\omega_{\text{inj}} t + \angle I_{\text{inj},n}), \end{aligned} \tag{4.24}$$

where the Fourier series coefficients are given by

$$\begin{aligned} \tilde{\Gamma}_n &= \frac{1}{\pi}\int_{2\pi} \tilde{\Gamma}(x) e^{-jnx}\, dx \\ I_{\text{inj},n} &= \frac{2}{T_{\text{inj}}}\int_{T_{\text{inj}}} i_{\text{inj}}(t) e^{-jn\omega_{\text{inj}} t}\, dt. \end{aligned} \tag{4.25}$$

Because θ is constant within the averaging integral, we can evaluate the integral directly in terms of the Fourier series coefficients of the ISF and the injection. This

yields

$$\boxed{\frac{d\theta}{dt} = \omega_0 - \omega_{\text{inj}} + \frac{1}{2}\left[\frac{I_{\text{inj},0}\tilde{\Gamma}_0}{2} + \sum_{n=1}^{\infty}\left|I_{\text{inj},n}\tilde{\Gamma}_n\right|\cos\left(n\theta + \angle\tilde{\Gamma}_n - \angle I_{\text{inj},n}\right)\right].} \tag{4.26}$$

This formulation is often more convenient to deal with, both analytically and conceptually. A block diagram depicting the spectral decomposition of the ISF is given in Figure 4.4.

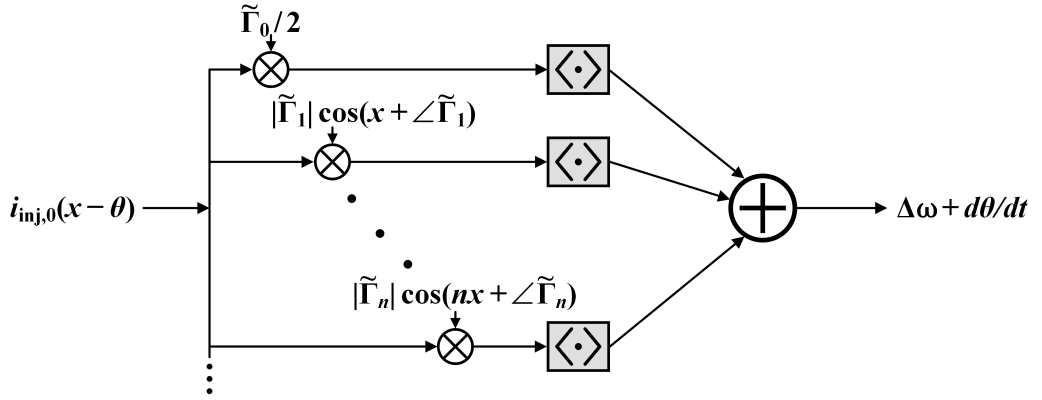

Figure 4.4: Decomposing the ISF into its spectral components, emphasizing how the injection waveform is filtered in the formation of the lock characteristic.

The Lock Range

The lock range is perhaps the most important parameter associated with the phenomenon of injection locking. It is defined as the range of frequencies that the oscillator is capable of locking to for a given injection waveform. Because the oscillator's phase relative to the injection, θ, is constant in time for a locked oscillator, the frequency deviation $\Delta\omega \equiv \omega_{\text{inj}} - \omega_0$ is given by

$$\Delta\omega = \frac{1}{T_{\text{inj}}}\int_{T_{\text{inj}}} \tilde{\Gamma}\left(\omega_{\text{inj}}t + \theta\right) i_{\text{inj}}(t)\, dt. \tag{4.27}$$

Because of the importance of this relationship, let us define the following function $\Omega(\theta)$ of the oscillator's phase θ:

$$\boxed{\begin{aligned}\Omega(\theta) &\coloneqq \frac{1}{T_{\text{inj}}}\int_{T_{\text{inj}}} \tilde{\Gamma}\left(\omega_{\text{inj}}t + \theta\right) i_{\text{inj}}(t)\, dt \\ &= \left\langle \tilde{\Gamma}(x+\theta)\, i_{\text{inj},0}(x)\right\rangle_{2\pi} \\ &= \frac{1}{2}\left[\frac{I_{\text{inj},0}\tilde{\Gamma}_0}{2} + \sum_{n=1}^{\infty}\left|I_{\text{inj},n}\tilde{\Gamma}_n\right|\cos\left(n\theta + \angle\tilde{\Gamma}_n - \angle I_{\text{inj},n}\right)\right].\end{aligned}} \tag{4.28}$$

Notice that this function is periodic with a period of 2π. Since $\Delta\omega = \Omega(\theta)$ for an injection-locked oscillator, $\Omega(\theta)$ dictates the relationship between the frequency deviation $\Delta\omega$ and the locked oscillator's phase θ. Therefore, we will call $\Omega(\theta)$ the ***lock characteristic***, which was first introduced in Section 1.2. As we will see, the lock characteristic captures practically all of the essential information about an oscillator's injection locking and pulling behavior.

By definition, the lock range is equal to the maximum frequency deviation achievable under lock:

$$\begin{aligned} \omega_L^{\pm} \coloneqq \max_{\theta}/\min \quad & \Delta\omega \\ \text{s.t.} \quad & \frac{d\theta}{dt} = 0. \end{aligned} \tag{4.29}$$

Therefore, the lock range can be calculated by extremizing the lock characteristic:

$$\boxed{\omega_L^{\pm} = \max_{\theta}/\min\ \Omega(\theta).} \tag{4.30}$$

It should be apparent at this point that the lock range is only defined for an "oscillator-injection pair", as varying either fundamentally alters the lock characteristic. On a final note, observe that if $\theta = \theta^*$ is an optimal solution to the above optimization problem (upper or lower), then basic differential calculus dictates $\Omega'(\theta^*) = \left\langle \tilde{\Gamma}'(x + \theta^*)\, i_{\text{inj},0}(x) \right\rangle_{2\pi} = 0$, assuming differentiability. In other words, at the edge of the lock range, the derivative of the ISF and the injection current must be *orthogonal* to one another (in the L^2 sense, over the appropriate period).

Sinusoidal Lock Range: Of particular importance and interest is the case of a sinusoidal injection current

$$i_{\text{inj}}(t) = I_{\text{inj}} \cos(\omega_{\text{inj}} t),$$

due to its mathematical simplicity and the bandpass nature of many electronic systems and devices. It is straightforward to see that the lock characteristic for a sinusoidal injection is given by

$$\Delta\omega = \frac{1}{2} I_{\text{inj}} \left|\tilde{\Gamma}_1\right| \cos\left(\theta + \angle\tilde{\Gamma}_1\right), \tag{4.31}$$

and so the lock range is equal to [72]

$$\omega_L = \frac{1}{2} I_{\text{inj}} \left|\tilde{\Gamma}_1\right|. \tag{4.32}$$

4.4 Example: The Bose Relaxation Oscillator

In this section, we will derive a closed-form expression for the ISF of a comparator- or Schmitt trigger-based relaxation oscillator, also known as a Bose oscillator. The schematic of this oscillator is shown in Figure 4.5. The simple exponential-discharge dynamic which governs the operation of this oscillator makes it a particularly suitable candidate for demonstrating the concepts discussed in this chapter. The key insight

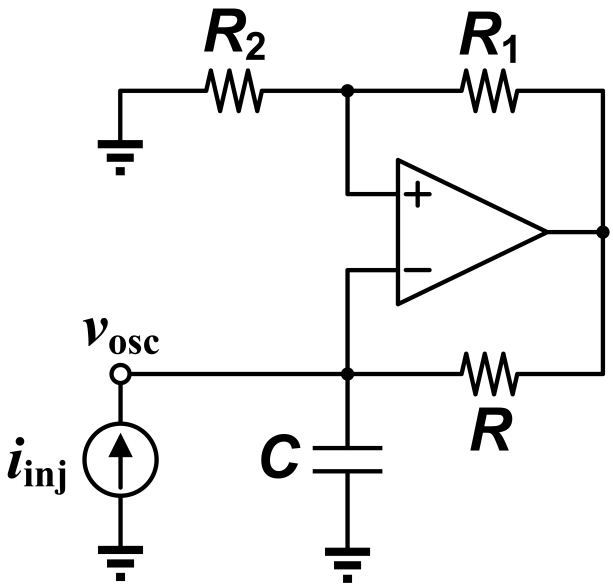

Figure 4.5: Schematic of the comparator-based relaxation oscillator.

here is that the time shift induced by a small injection of charge is equal to the amount of time it would take the original waveform to travel to the perturbed point. This is because the oscillator simply continues to charge or discharge from the perturbed point; the injection cannot "knock" the oscillator off of its limit cycle.

Assume the op amp's positive and negative supplies are at $V_{\mathrm{DD}} > 0$ and $-V_{\mathrm{SS}} < 0$, respectively. Further assume an equal resistive divider straddling the non-inverting input ($R_1 = R_2$), and define the time constant $\tau = RC$. We allow for the general case of $V_{\mathrm{DD}} \neq V_{\mathrm{SS}}$ which results in asymmetric charge/discharge times. The capacitor charges and discharges between

$$q^{+}_{\mathrm{max}} = \frac{CV_{\mathrm{DD}}}{2} \qquad \text{and} \qquad q^{-}_{\mathrm{max}} = -\frac{CV_{\mathrm{SS}}}{2}.$$

The free-running oscillation period is $T_0 = T_C + T_D$, where T_C and T_D are the charge/discharge times respectively. It is easy to see that

$$T_C = \tau \cdot \ln\left(\frac{q^-_{\max}}{q^+_{\max}} + 2\right) \qquad T_D = \tau \cdot \ln\left(\frac{q^+_{\max}}{q^-_{\max}} + 2\right).$$

Thus,

$$T_0 = \tau \cdot \ln\left[2\left(\frac{q^-_{\max}}{q^+_{\max}} + \frac{q^+_{\max}}{q^-_{\max}}\right) + 5\right]. \tag{4.33}$$

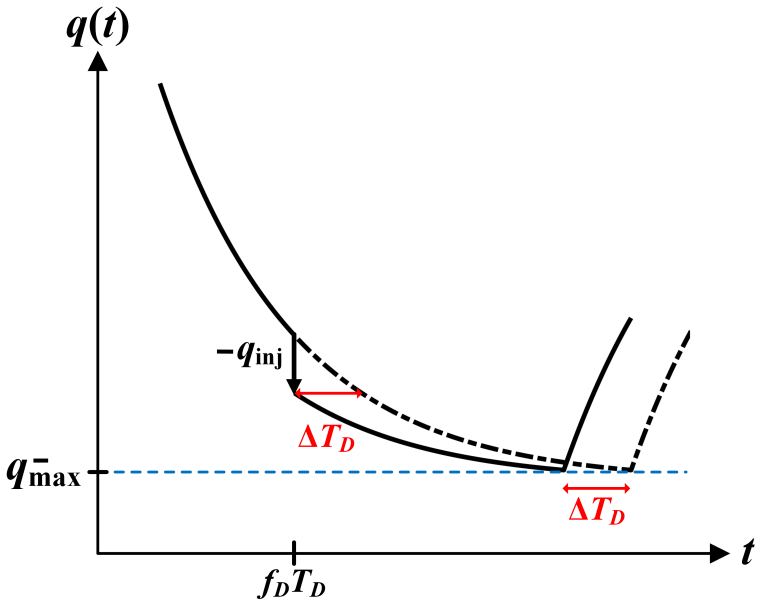

Figure 4.6: Time shift ΔT_D induced by an injection into a Bose oscillator while it is discharging.

Let us analyze the discharge scenario. Say some amount of negative charge $-q_{\text{inj}}$ is injected onto the capacitor when the oscillator is some fraction $0 \le f_D \le 1$ of the way through the discharge process (see Figure 4.6). The injection will speed up the discharge by ΔT_D, which obeys

$$(q^+_{\max} + 2q^-_{\max}) \exp\left(-\frac{f_D T_D}{\tau}\right) \exp\left(-\frac{\Delta T_D}{\tau}\right) = (q^+_{\max} + 2q^-_{\max}) \exp\left(-\frac{f_D T_D}{\tau}\right) - q_{\text{inj}}.$$

But since $q^+_{\max} + 2q^-_{\max} = q^-_{\max} \exp(T_D \tau)$, we can rewrite this as

$$q^-_{\max} \exp\left[\frac{(1-f_D)T_D}{\tau}\right] \exp\left(-\frac{\Delta T_D}{\tau}\right) = q^-_{\max} \exp\left[\frac{(1-f_D)T_D}{\tau}\right] - q_{\text{inj}}.$$

Solving for ΔT_D, we get

$$\Delta T_D = -\tau \cdot \ln\left(1 - \frac{q_{\text{inj}}}{q^-_{\max}} \exp\left[\frac{(f_D - 1)T_D}{\tau}\right]\right). \tag{4.34}$$

The *linear* phase shift induced with respect to only the discharge process is

$$\Delta\phi_D \equiv \frac{\Delta T_D}{T_D} = -\frac{\tau}{T_D}\cdot\ln\left(1-\frac{q_{\text{inj}}}{q^-_{\max}}\exp\left[\frac{(f_D-1)T_D}{\tau}\right]\right). \tag{4.35}$$

Therefore, the discharge ISF, in units of *fraction of the discharge period*, can be calculated by differentiating the phase shift with respect to the injected charge:

$$\boxed{P_D(f_D) \equiv \left.\frac{\partial\Delta\phi_D}{\partial(-q_{\text{inj}})}\right|_{q_{\text{inj}}=0} = -\frac{1}{q^-_{\max}}\cdot\frac{\left(e^{T_D/\tau}\right)^{f_D-1}}{T_D/\tau} = -\frac{\left(\frac{q^+_{\max}}{q^-_{\max}}+2\right)^{f_D-1}}{q^-_{\max}\ln\left(\frac{q^+_{\max}}{q^-_{\max}}+2\right)},} \tag{4.36}$$

where we have also given an equivalent form solely in terms of the charge swings. Similarly, for the charging scenario, it is analogous to show that

$$\boxed{P_C(f_C) \equiv \left.\frac{\partial\Delta\phi_C}{\partial q_{\text{inj}}}\right|_{q_{\text{inj}}=0} = \frac{1}{q^+_{\max}}\cdot\frac{\left(e^{T_C/\tau}\right)^{f_C-1}}{T_C/\tau} = \frac{\left(\frac{q^-_{\max}}{q^+_{\max}}+2\right)^{f_C-1}}{q^+_{\max}\ln\left(\frac{q^-_{\max}}{q^+_{\max}}+2\right)}.} \tag{4.37}$$

Notice the exponential dependence of the ISF upon the phase (f_D and f_C).

Symmetric Charge and Discharge

In the case where $q^+_{\max} = q^-_{\max} = q_{\max}$ and so $T_C = T_D = \tau\ln 3$, we get $T_0 = 2\tau\ln 3$. Furthermore, we can combine the charging and discharging ISFs into a single ISF. Denoting $f \in [0,1]$ again as the *fraction* of the charge/discharge period,

$$\tilde{\Gamma}_{C/D}(f) = \pi P_{C/D}(f) = \pm\pi\frac{3^{f-1}}{q_{\max}\ln 3}. \tag{4.38}$$

Let us assume the reference for our oscillation charge waveform $q_0(\varphi) = Cv_0(\varphi)$ starts at $-q_{\max}$ (the beginning of the charging event) when $\varphi = 0$. Then

$$\frac{q_0(\varphi\equiv\omega_0 t)}{q_{\max}} = \begin{cases} 2-3e^{-t/\tau} = 3\left(\dfrac{2}{3}-3^{-\varphi/\pi}\right), & 0\le\varphi\le\pi \\ -2+3e^{-(t-T_0/2)/\tau} = -3\left(\dfrac{2}{3}-3^{-(\varphi-\pi)/\pi}\right), & \pi\le\varphi\le 2\pi \end{cases} \tag{4.39}$$

where we made use of the fact that $T_0 = 2\tau\ln 3$. Knowing that $f = \varphi/\pi$ during charging and $f = (\varphi-\pi)/\pi$ during discharging, the ISF can therefore be written as

$$\boxed{\tilde{\Gamma}(\varphi) = \begin{cases} \dfrac{\pi\cdot 3^{\varphi/\pi}}{3\ln 3\, q_{\max}}, & 0<\varphi<\pi \\ -\dfrac{\pi\cdot 3^{(\varphi-\pi)/\pi}}{3\ln 3\, q_{\max}}, & \pi<\varphi<2\pi. \end{cases}} \tag{4.40}$$

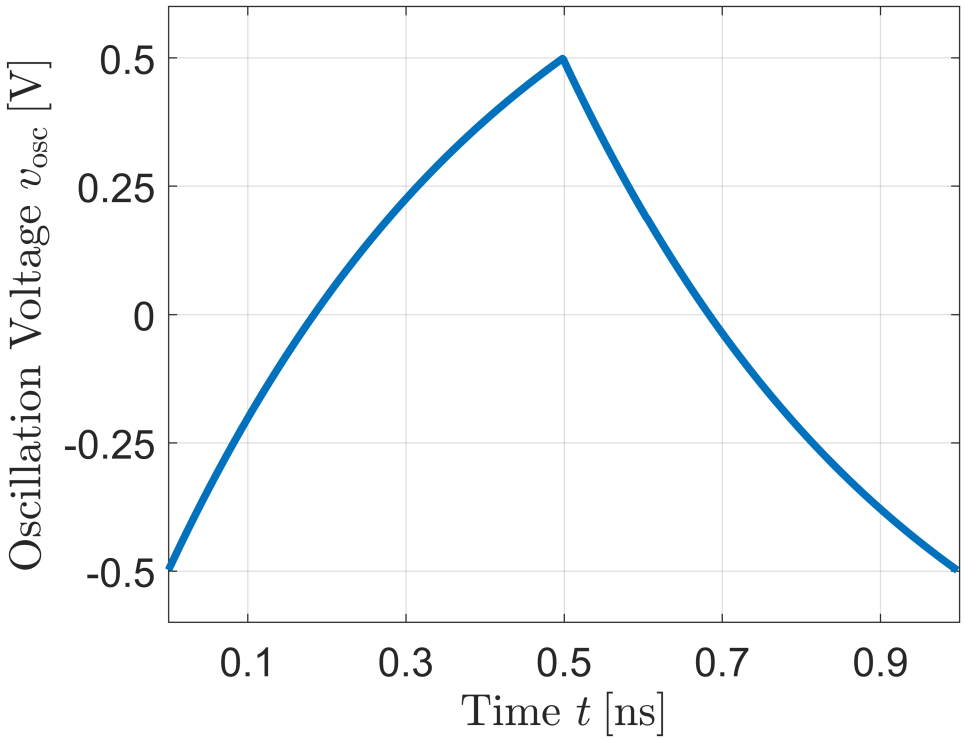

Figure 4.7: One period of the free-running oscillation voltage of an ideal, symmetric 1 GHz Bose oscillator with $V_{\mathrm{DD}} = V_{\mathrm{SS}} = 1$ V.

Note that this oscillator actually has two states: one of them is the voltage across the capacitor C, while the other is represented by the hysteresis within the op amp. However, the latter is a binary state, which toggles only when the oscillator transitions between the charging and discharging phases. Therefore, only the first state is changing at all but two points in a cycle. We thus refer to this oscillator as a "quasi-single-state" oscillator, and the ISF can also be very simply computed from the waveform directly using the orthogonal state-space calculation of Eq. (4.6):

$$\tilde{\Gamma}(\varphi) = \frac{1}{C \cdot v_0'(\varphi)} = \frac{1}{q_0'(\varphi)}. \tag{4.41}$$

One can easily verify that taking the derivative of $q_0(\varphi)$ from Eq. (4.39) and substituting the result into Eq. (4.41) yields Eq. (4.40).

Figure 4.7 shows the free-running oscillation voltage of a symmetric 1 GHz Bose oscillator implemented with an ideal comparator. Note that $C = 9.1$ pF. Figure 4.8 compares the simulated ISF against the closed-form formula of Eq. (4.40) and by numerically differentiating the waveform in Figure 4.7 in accordance with (4.41).

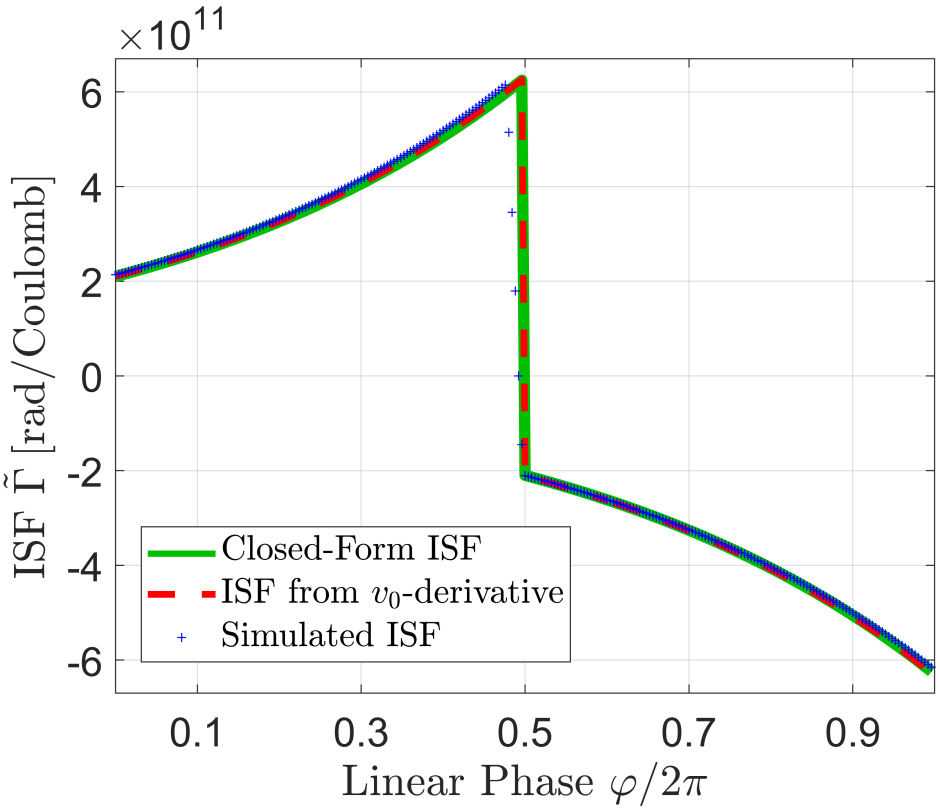

Figure 4.8: The impulse sensitivity function of the ideal Bose oscillator (whose oscillation voltage is shown in Figure 4.7) obtained several different ways.

Notice the near identical match between the different approaches. The discrepancy in the simulated ISF near the transition point is due to the fact that actual injections of charge cannot be infinitesimally small in simulation, even though the ISF is defined as a derivative evaluated at $q_{\text{inj}} = 0$. For our simulation, we injected positive amounts of charge. Thus, near the transition point from charging to discharging, there are a few simulation points for which the injection pushes the capacitor voltage beyond the positive supply rail, introducing a simulation "error" which causes deviations from the true ISF.

The Sinusoidal Lock Range of the Bose Oscillator

The magnitude of the fundamental component of the ISF is

$$\left|\tilde{\Gamma}_1\right| = \frac{1}{\pi}\left|\int_0^{2\pi} \tilde{\Gamma}(x)e^{-jx}dx\right| = \frac{8\pi}{3\ln 3\sqrt{\pi^2 + (\ln 3)^2}} \cdot \frac{1}{q_{\max}}. \tag{4.42}$$

For a general Bose oscillator with a peak-to-peak voltage swing of $V_{\max}$ across a timing capacitor C, the charge amplitude $q_{\max}$ is simply half of the peak-to-peak

charge swing: $q_{\max} = CV_{\max}/2$. Thus,

$$\left|\tilde{\Gamma}_1\right| = \frac{16\pi}{3\ln 3\sqrt{\pi^2 + (\ln 3)^2}} \cdot \frac{1}{CV_{\max}} \approx \frac{4.582}{CV_{\max}}. \tag{4.43}$$

Therefore, for a sinusoidal injection current, the linear lock range is given by

$$\boxed{f_L = \frac{1}{4\pi} I_{\text{inj}} \left|\tilde{\Gamma}_1\right| = \frac{4}{3\ln 3\sqrt{\pi^2 + (\ln 3)^2}} \frac{I_{\text{inj}}}{CV_{\max}} \approx 0.3647 \frac{I_{\text{inj}}}{CV_{\max}}.} \tag{4.44}$$

4.5 Linearity Case Study: Injecting a DC Current into an Oscillator

What happens if the current injected into the oscillator is constant in time: $i_{\text{inj}}(t) = I_{\text{DC}}$? In steady state, the pulling equation Eq. (4.20) predicts a *constant* shift in the oscillation frequency given by

$$\begin{aligned} \Delta\omega &= \frac{1}{T_{\text{inj}}} \int_{T_{\text{inj}}} \tilde{\Gamma}\left(\omega_{\text{inj}} t + \theta\right) I_{\text{DC}}\, dt \\ &= \tilde{\Gamma}_{\text{DC}} \cdot I_{\text{DC}}, \end{aligned} \tag{4.45}$$

where $\tilde{\Gamma}_{\text{DC}} = \tilde{\Gamma}_0/2$ is the average value, or DC component, of the ISF. Thus, according to our model, a constant injection of current induces a frequency shift proportional to the current level. Let us examine if this is true in reality.

Figure 4.9a shows the simulated oscillation voltage for a 17-stage ring oscillator where a DC current of ±5 mA is injected into one of the stages. In steady state, we observe that the oscillator indeed oscillates at a constant frequency. Figure 4.9b shows a plot of the oscillation frequency as a function of the injection current. As we can see, the line generated by the ISF model does not accurately predict the oscillation frequency. This is because the injection of DC current also introduces a significant offset in the output voltage (see Figure 4.9a), and so the amount of excess charge introduced by the injection is appreciable compared to the free-running maximum charge swing. However, since the ISF model is equivalent to a *linearization* of this behavior, notice that the line $\Delta\omega = \tilde{\Gamma}_{\text{DC}} \cdot I_{\text{DC}}$ serves as a *tangent line* to the simulated data at the point $I_{\text{DC}} = 0$.

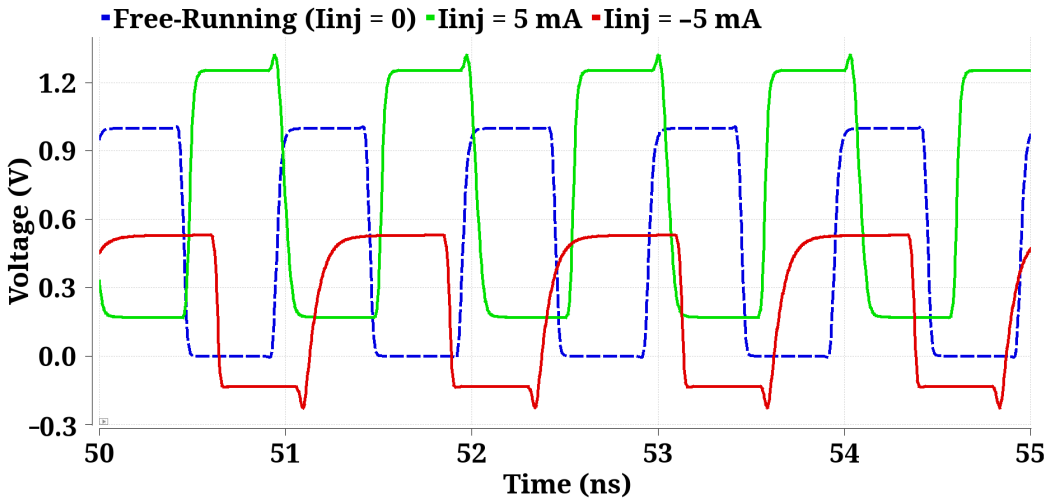

(a) Free-running oscillation voltage (blue dashed curve), and the oscillation voltages with $I_{\text{DC}} = 5$ mA (green curve) and $I_{\text{DC}} = -5$ mA (red curve).

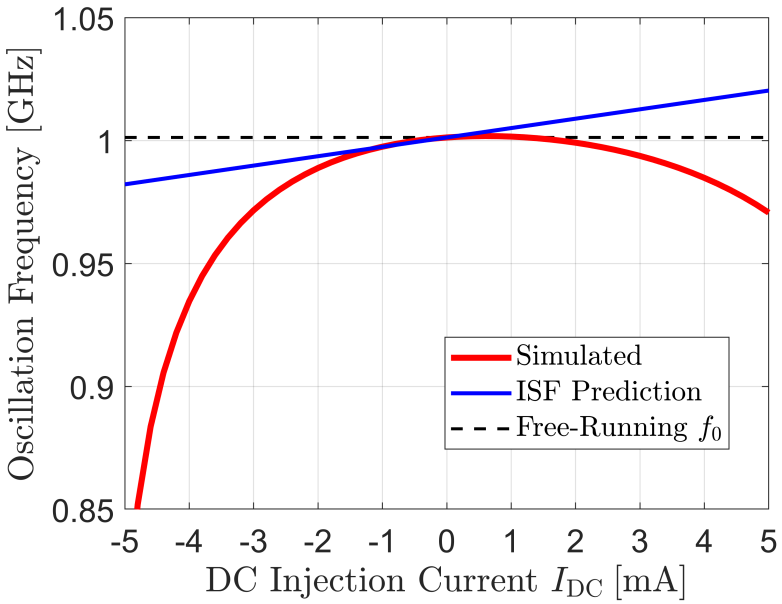

(b) Oscillation frequency f_{osc} for -5 mA $\leq I_{\text{DC}} \leq 5$ mA.

Figure 4.9: Exploring the effect of injecting a DC current into one of the stages of a 1 GHz 17-stage ring oscillator.

4.6 Simulation Results

In this section, we will simulate the lock characteristics for a collection of canonical ring and relaxation oscillators[6] injected with sinusoidal currents[7] of various amplitudes and compare them against the theoretical lock characteristics obtained from the ISF. All the oscillators free-run at roughly $f_0 = 1$ GHz. Because the injection is sinusoidal, only the fundamental component of the ISF, $\tilde{\Gamma}_1$, is relevant. To decide what range of injection amplitudes to use, we calculated the oscillation current $I_{\max}$ defined in Section 4.2 and chose values of I_{inj} that ranged from being much smaller than $I_{\max}$ to being comparable to $I_{\max}$. This allows us to observe how the predictive power of our model begins to falter as the assumption of linearity fails. Table 4.2 lists the magnitude of the ISF's fundamental component $\left|\tilde{\Gamma}_1\right|$ and the oscillation current $I_{\max}$ for each oscillator.

Table 4.2: $\left|\tilde{\Gamma}_1\right|$ and $I_{\max}$ of the Simulated Ring and Relaxation Oscillators

Oscillator	$\left\|\tilde{\Gamma}_1\right\|$	$I_{\max}$
3-Stage Ring	7.84×10^{12} rad/C	0.54 mA
17-Stage Ring	2.24×10^{11} rad/C	0.72 mA
6-Stage Differential Ring	6.51×10^{11} rad/C	3.0 mA
Ideal Bose	5.05×10^{11} rad/C	29 mA
Astable Multivibrator	2.02×10^{13} rad/C	1.2 mA

Because of the periodicity of the lock characteristic, there are at least two solutions for the phase θ at each injection frequency. However, as we will show in Section 7.2, only the solution where the lock characteristic has a negative slope is stable. This will be reflected in our figures by plotting the stable and unstable parts of the lock characteristic using solid and dashed lines, respectively. Note that the simulated lock characteristic was obtained through repeated transient simulations: the lock range was determined by inspection (to a 1 MHz accuracy), and then the injection frequency was swept over the lock range and θ was computed for each sweep point. It should be apparent from the setup of our analysis (see Figure 1.3) that θ is calculated by comparing the phase of the *fundamental component* of the oscillation voltage to the phase of the injection current; this will be explained in more detail in Section 6.8.

[6] LC oscillators will be considered in much more detail in Chapter 5.

[7] Non-sinusoidal injection currents will be explored in Chapter 8.

3-Stage Single-Ended Ring Oscillator

The schematic, free-running oscillation voltage, and ISF of this oscillator are shown in Figure 4.10.

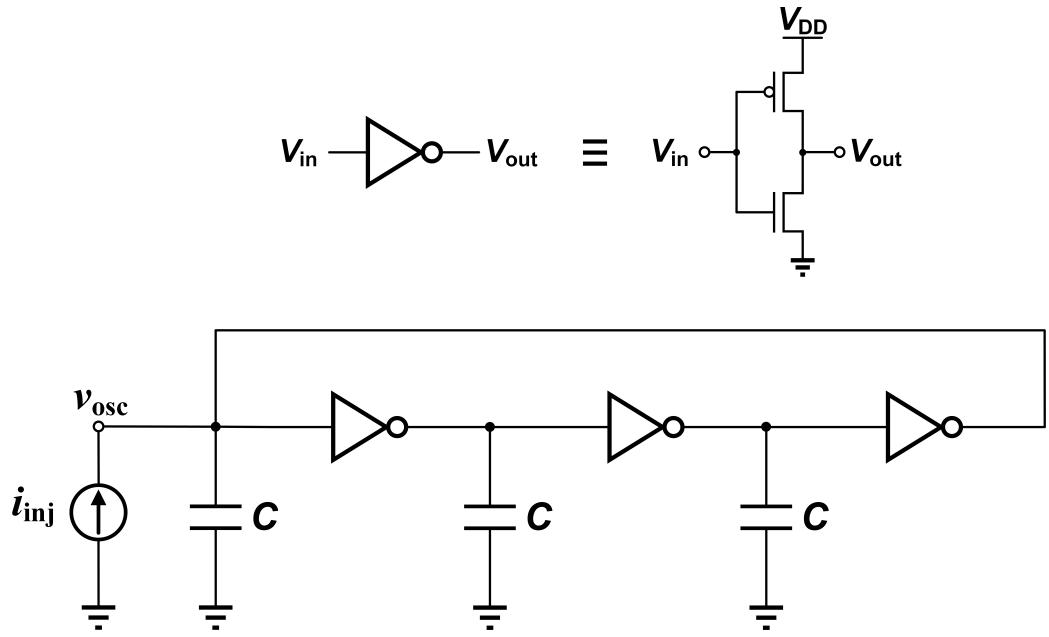

(a) Oscillator schematic. Note that each stage is loaded with an additional external capacitance C.

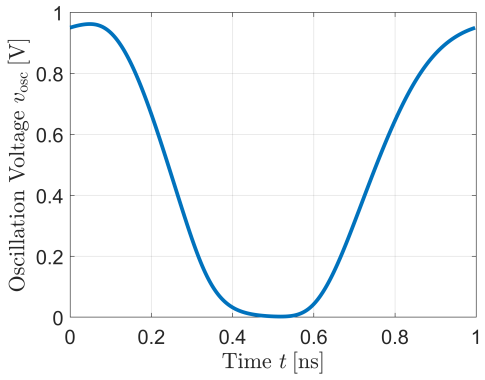

(b) Free-running oscillation voltage.

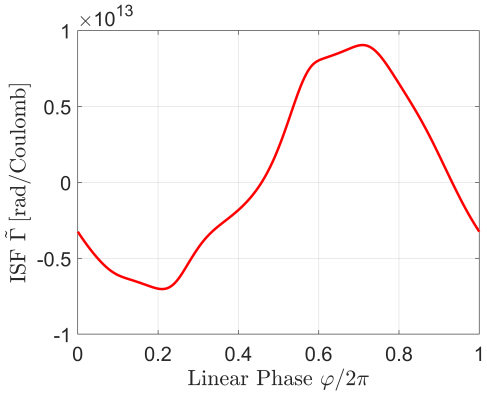

(c) Impulse sensitivity function.

Figure 4.10: 3-stage single-ended inverter-chain ring oscillator.

The sinusoidal lock characteristics for several different injection strengths are shown in Figure 4.11. Notice how the upper edge of the lock characteristic deviates from the ISF prediction as the injection amplitude grows.

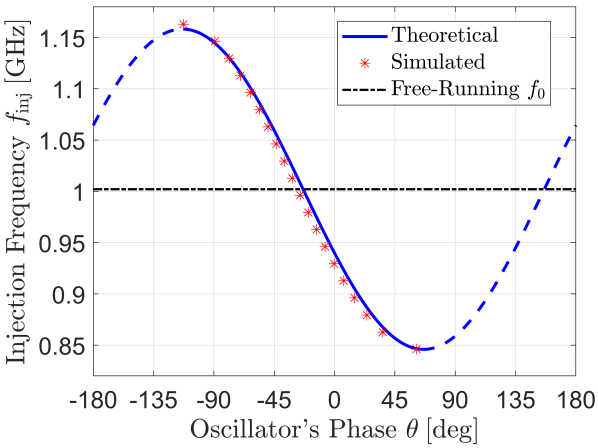

(a) I_{inj} = 0.25 mA

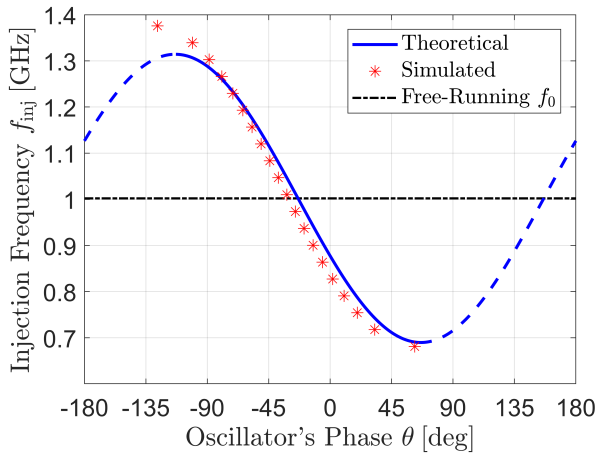

(b) I_{inj} = 0.5 mA

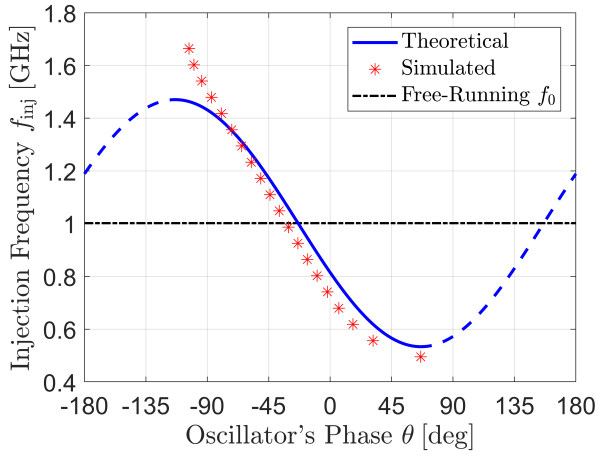

(c) I_{inj} = 0.75 mA

Figure 4.11: Lock characteristic of the 3-stage ring oscillator for sinusoidal injections of varying amplitude I_{inj}.

17-Stage Single-Ended Ring Oscillator

The schematic, free-running oscillation voltage, and ISF of this oscillator are shown in Figure 4.12.

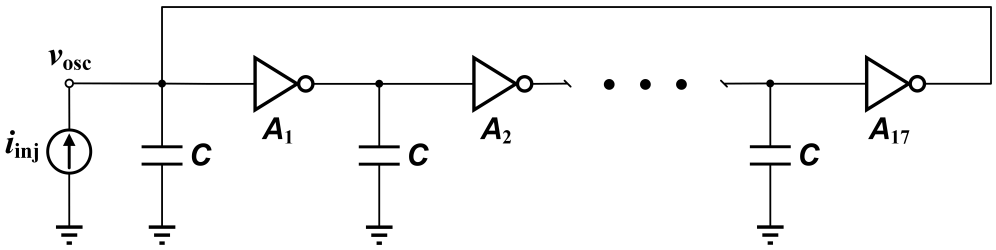

(a) Oscillator schematic.

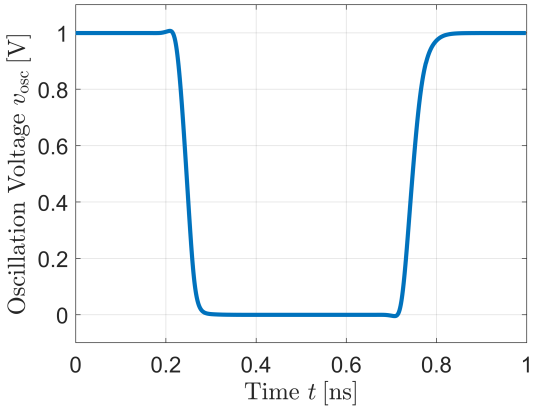

(b) Free-running oscillation voltage.

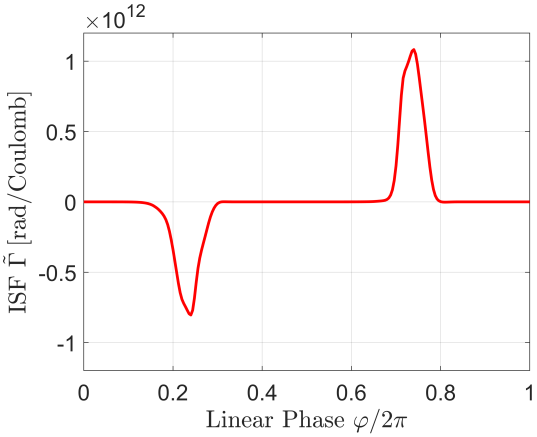

(c) Impulse sensitivity function.

Figure 4.12: 17-stage single-ended inverter-chain ring oscillator.

The sinusoidal lock characteristics for several different injection strengths are shown in Figure 4.13. Unlike the 3-stage ring oscillator, it is the *lower* edge of the lock characteristic which deviates from theory as I_{inj} increases. Interestingly, the assumption of linearity is still reasonable when $I_{inj} > I_{max}$ for this oscillator.

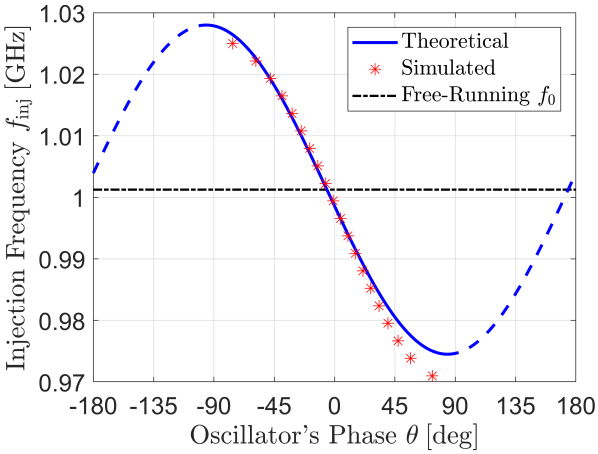

(a) I_{inj} = 1.5 mA

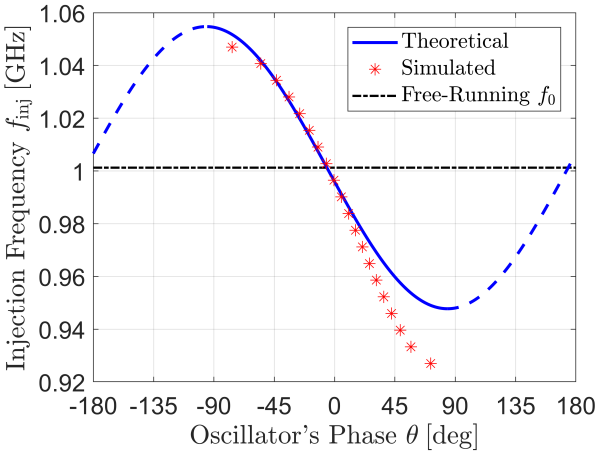

(b) I_{inj} = 3 mA

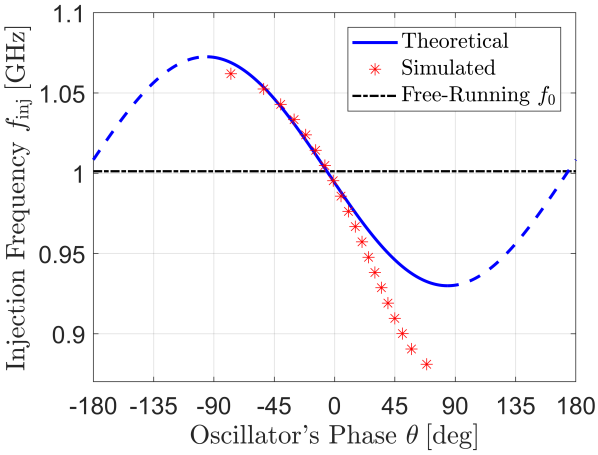

(c) I_{inj} = 4 mA

Figure 4.13: Lock characteristic of the 17-stage ring oscillator for sinusoidal injections of varying amplitude I_{inj}.

6-Stage Differential Ring Oscillator

The schematic, free-running oscillation voltage, and ISF of this oscillator are shown in Figure 4.14.

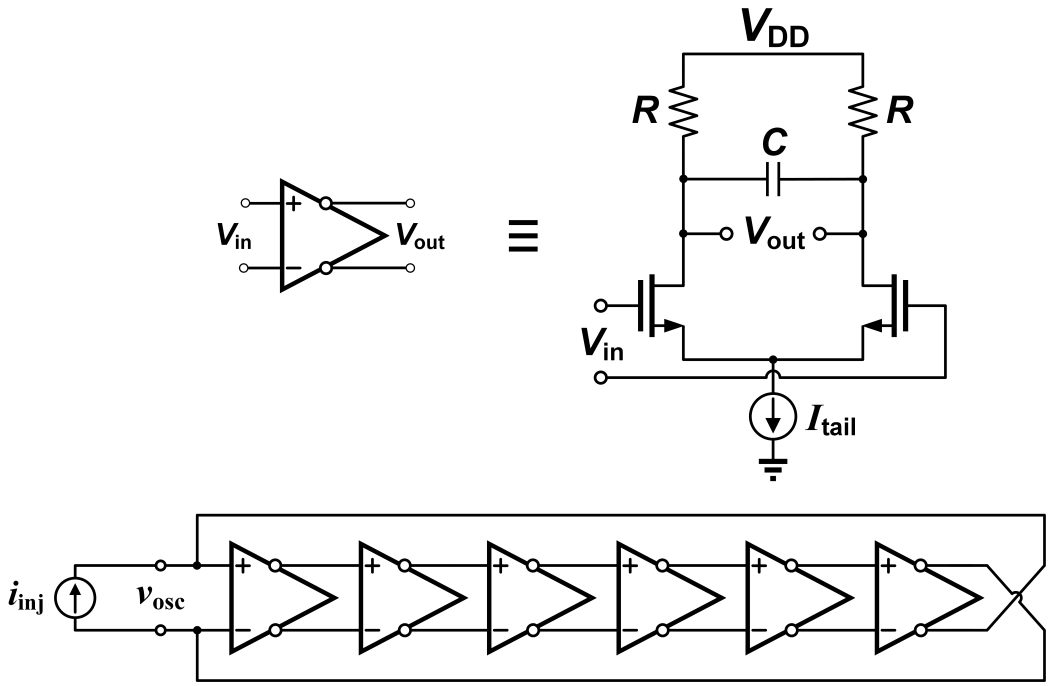

(a) Oscillator schematic. A single resistively biased current mirror was used to set the same tail current I_{tail} for all the stages.

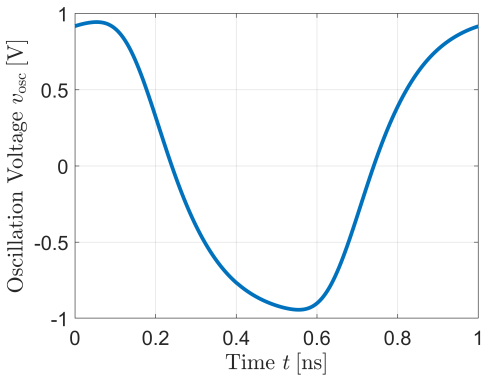

(b) Free-running oscillation voltage.

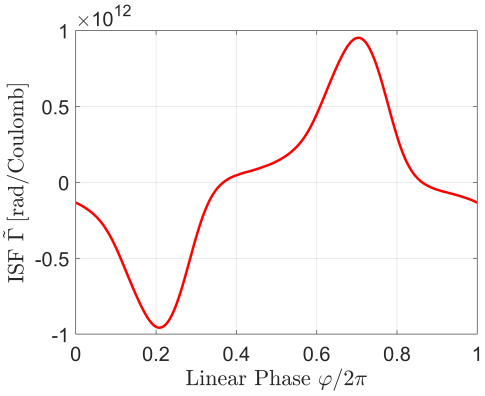

(c) Impulse sensitivity function.

Figure 4.14: 6-stage differential ring oscillator.

The sinusoidal lock characteristics for several different injection strengths are shown in Figure 4.15.

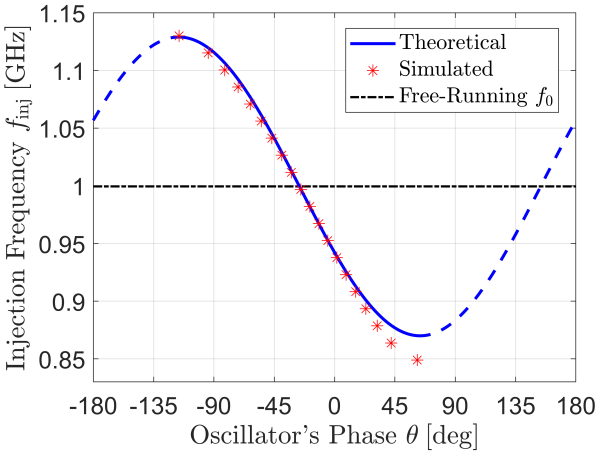

(a) I_{inj} = 2.5 mA

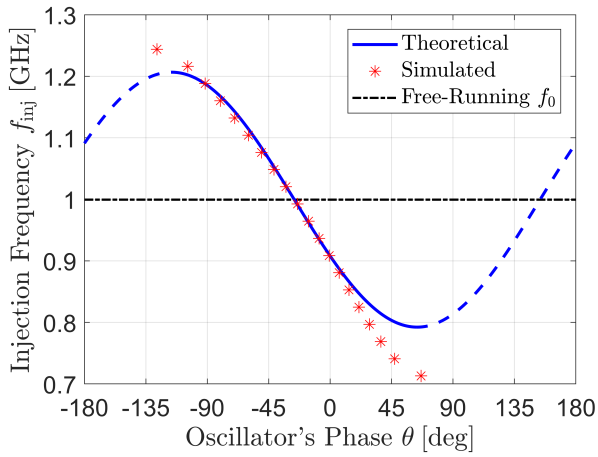

(b) I_{inj} = 4 mA

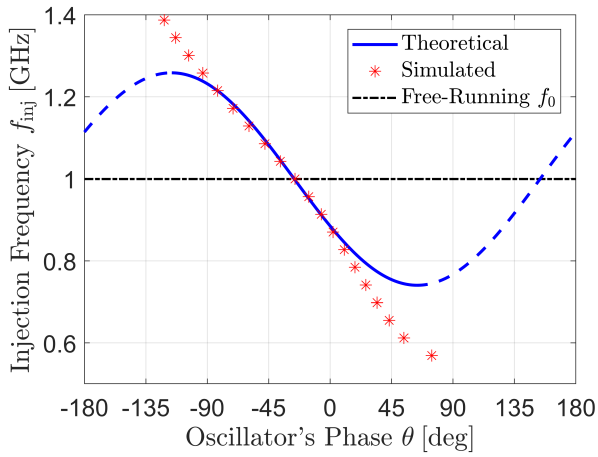

(c) I_{inj} = 5 mA

Figure 4.15: Lock characteristic of the 6-stage ring oscillator for sinusoidal injections of varying amplitude I_{inj}.

Ideal, Symmetric Bose Relaxation Oscillator

This is the same oscillator which was analyzed in Section 4.4 and whose schematic, free-running oscillation voltage, and ISF are shown in Figures 4.5, 4.7, and 4.8 respectively. The sinusoidal lock characteristics for several different injection strengths are shown in Figure 4.16.

Note that the only way the charge on the capacitor C can be considered to be in "excess" of free-running is if v_{osc} has exceeded what is allowed by the supply rails ($V_{\text{DD}}/2$ and $-V_{\text{SS}}/2$), in which case the dissipation of this excess charge will not be governed by the simplified analysis conducted in Section 4.2. In other words, for this oscillator, the oscillation current I_{max} carries less physical significance with respect to the linearity of the current-to-phase relationship.

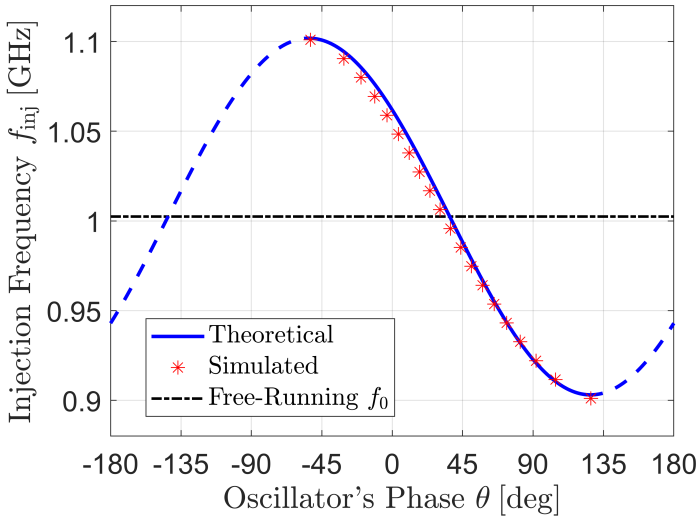

(a) I_{inj} = 2.5 mA

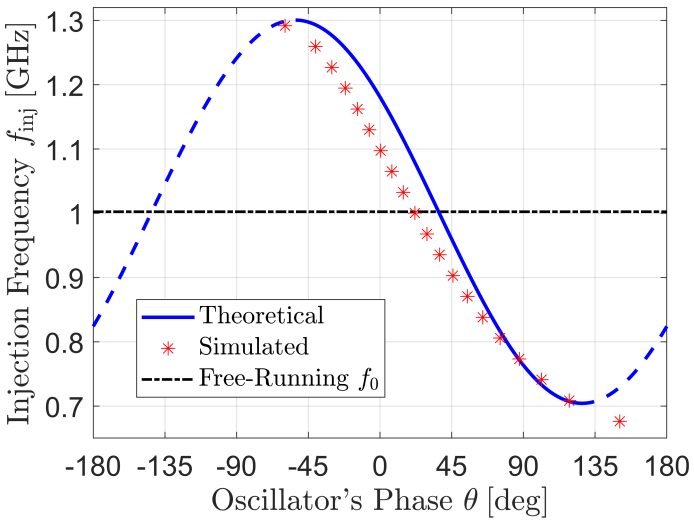

(b) I_{inj} = 7.5 mA

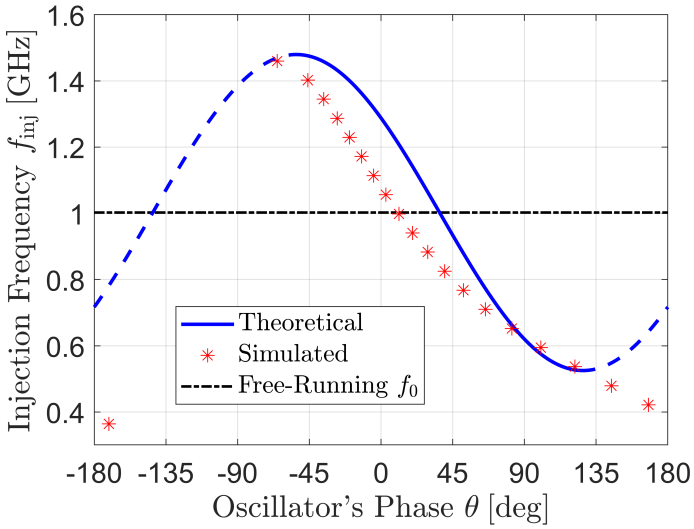

(c) I_{inj} = 12 mA

Figure 4.16: Lock characteristic of the ideal Bose oscillator for sinusoidal injections of varying amplitude I_{inj}.

NMOS Differential Astable Multivibrator

The schematic, free-running oscillation voltage, and ISF of this oscillator are shown in Figure 4.17. Note that this oscillator is also a type of relaxation oscillator.

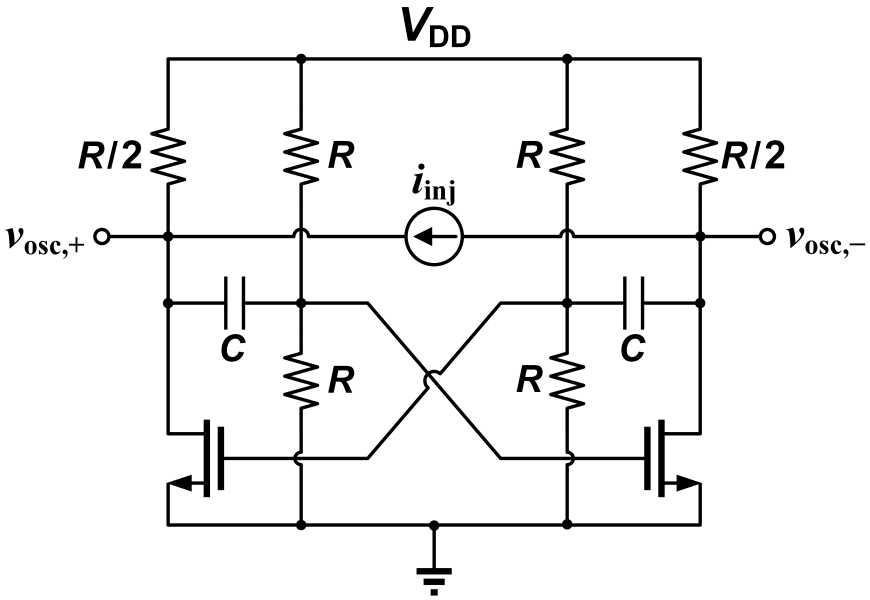

(a) Oscillator schematic.

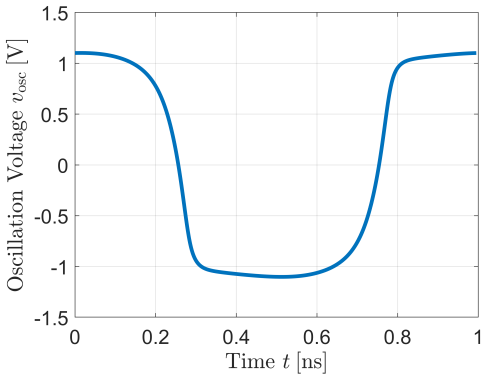

(b) Free-running oscillation voltage.

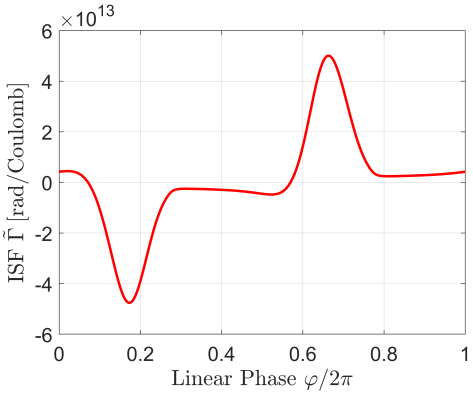

(c) Impulse sensitivity function.

Figure 4.17: NMOS differential astable multivibrator.

The sinusoidal lock characteristics for several different injection strengths are shown in Figure 4.18. This oscillator is known to be particularly sensitive—small changes in its component values or in the bias point of the transistor can drastically alter the oscillation frequency or shape of the oscillation waveform. Consequently, the threshold for linearity on I_{inj} is much lower than what is dictated by I_{max}.

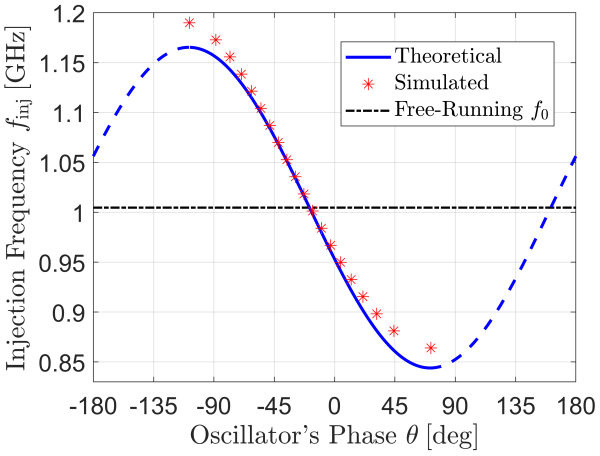

(a) I_{inj} = 0.1 mA

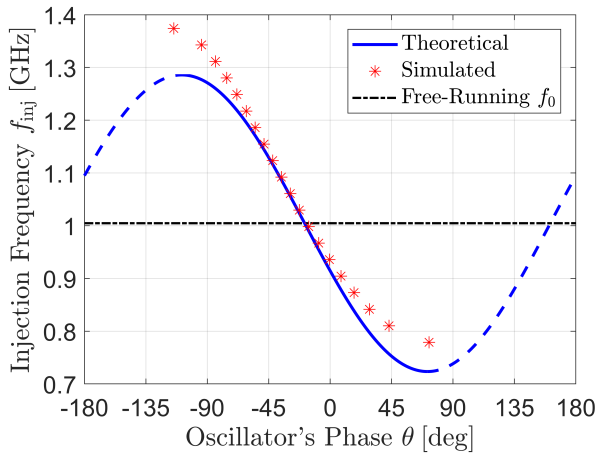

(b) I_{inj} = 0.175 mA

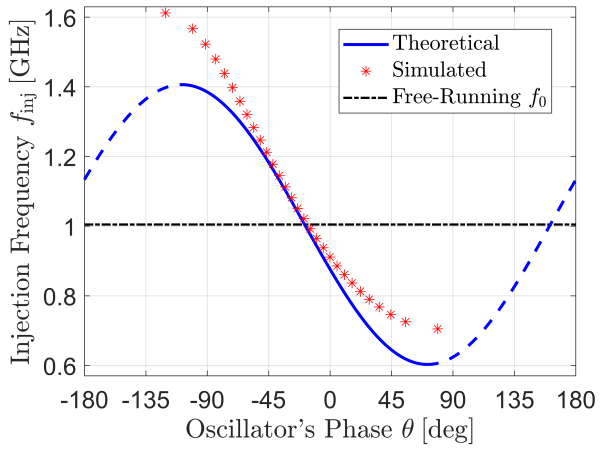

(c) I_{inj} = 0.25 mA

Figure 4.18: Lock characteristic of the astable multivibrator oscillator for sinusoidal injections of varying amplitude I_{inj}.

4.7 Experimental Results

We conclude this chapter by presenting lock range measurements on integrated versions of the oscillators considered in the previous section, fabricated in a 65-nm bulk CMOS process. All but one of the oscillators were designed to oscillate at around 1 GHz. The measurements are compared against the theoretical predictions made by our model, where the ISFs were obtained through simulation of the post-layout extracted oscillators.

For each oscillator, we measured the lock range at various sinusoidal injection amplitudes. The predicted lock range is therefore given in Eq. (4.32) to be equal to

$$\omega_L^{\pm} = \pm\frac{1}{2} I_{\text{inj}} \left|\tilde{\Gamma}_1\right|.$$

To account for possible measurement error, each oscillator was measured three separate times. Error bars depicting the entire range of measurements for each data point are shown in black. (The error bars for most data points are not noticeable.) Note that the injection amplitude I_{inj} is shown both on an absolute scale (top axis) and as an injection strength normalized to the oscillation current I_{max} (bottom axis). Likewise, the lock range f_L is also shown both on an absolute scale (right axis) and as a fractional lock range normalized to the free-running oscillation frequency f_0 (left axis). The simulated ISF for each oscillator will also be shown for reference.

The measurement setup, including the implementation of the sinusoidal injection current source, is detailed in Appendix A. Note that experimental results for LC oscillators will be presented separately in Chapter 5. A die micrograph of the fabricated chip is shown in Figure 4.19, where the locations of the oscillators measured in this section are specified.

Ring Oscillators

The first set of experiments was performed on 3-stage and 17-stage inverter-chain single-ended ring oscillators, as well as a 6-stage differential ring oscillator. In order to tune the oscillation frequency to be around 1 GHz, identically sized MIM capacitors were used to load each stage of the ring. Table 4.3 summarizes the design parameters of the ring oscillators. All listed parameters were obtained from extracted simulation or from the design kit directly, with the exception of the oscillation frequency which was measured. The current consumption is the core current drawn by the oscillator alone, neglecting bias circuitry.

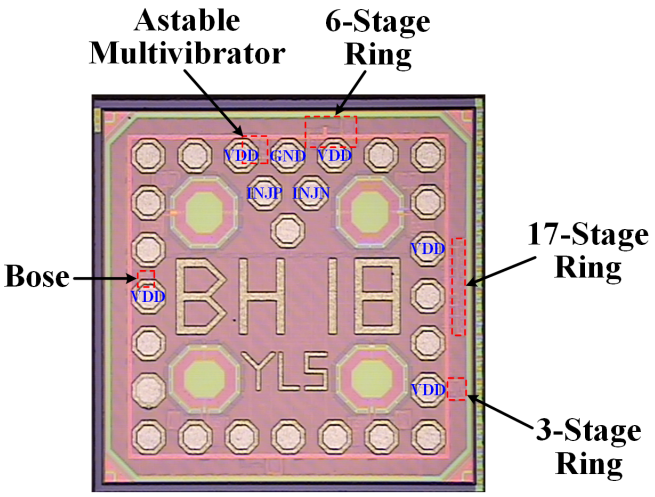

Figure 4.19: Die photo of the measured oscillators. Pads for the supply ('VDD') of each oscillator, ground ('GND'), and the injections ('INJP','INJN') are labeled.

Table 4.3: Characteristics of the Measured Ring Oscillators

Parameter	3-Stage	17-Stage	6-Stage Differential
Schematic	Figure 4.10a	Figure 4.12a	Figure 4.14a
Load Capacitance C (per stage) [fF]	135	111	350
Current Consumed [mA]	1.1	4.6	25
Supply V_{DD} [V]	1	1	1
Peak-to-Peak Voltage Swing V_{max} [V]	0.88	1.0	1.0
ISF Fundamental Magnitude $\lvert\tilde{\Gamma}_1\rvert$ [rad/pC]	8.83	0.346	1.88
Measured Oscillation Frequency f_0 [GHz]	1.085	1.092	1.316

Figures 4.20, 4.21, and 4.22 present the measurement results. Decent agreement is observed between theory and experiment. The deviation between the measured and predicted lock ranges at higher injection amplitudes is reminiscent of the nonlinear behavior seen in the simulation results of Figures 4.11, 4.13, and 4.15. It is noteworthy that our theoretical predictions seem to fare well even when I_{inj} is comparable to or greater than I_{max}, although this may simply be indicative of the fact that I_{max} is not a terribly robust metric for determining when linearity fails.

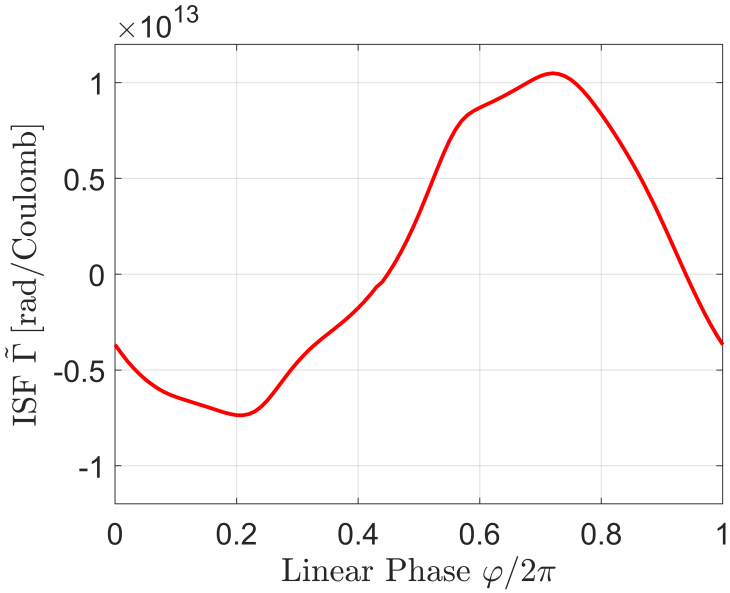

(a) Simulated ISF.

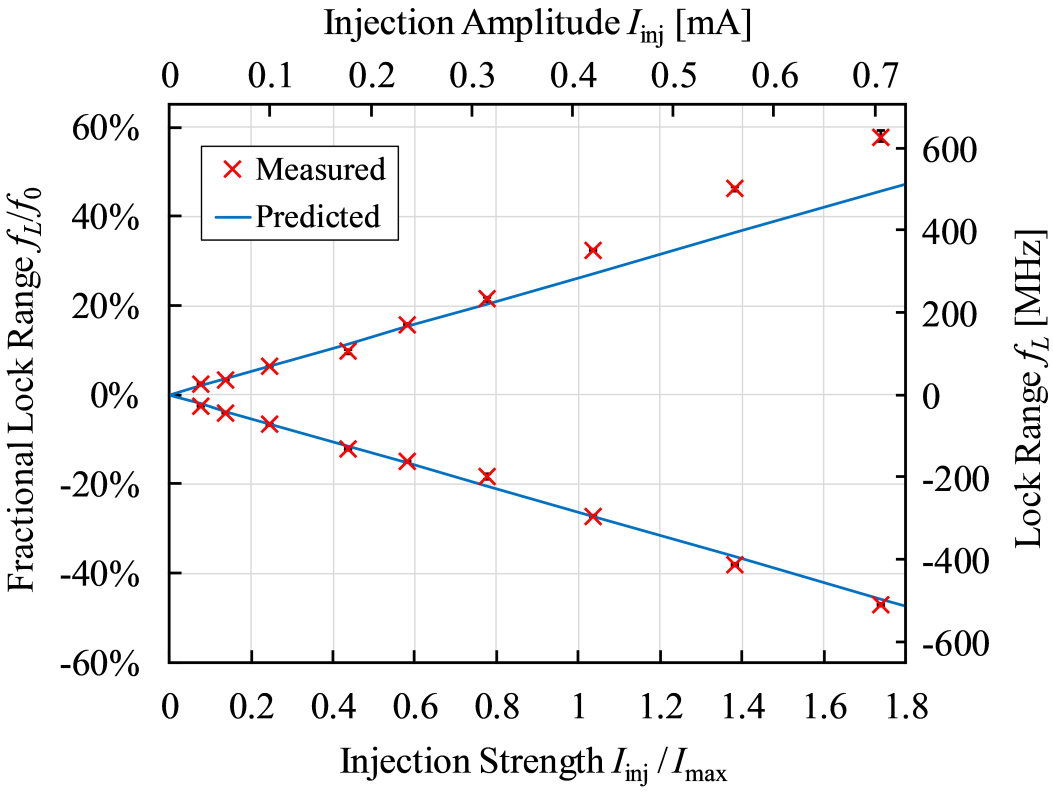

(b) Measured lock range.

Figure 4.20: Measurement results for the 3-stage single-ended ring oscillator.

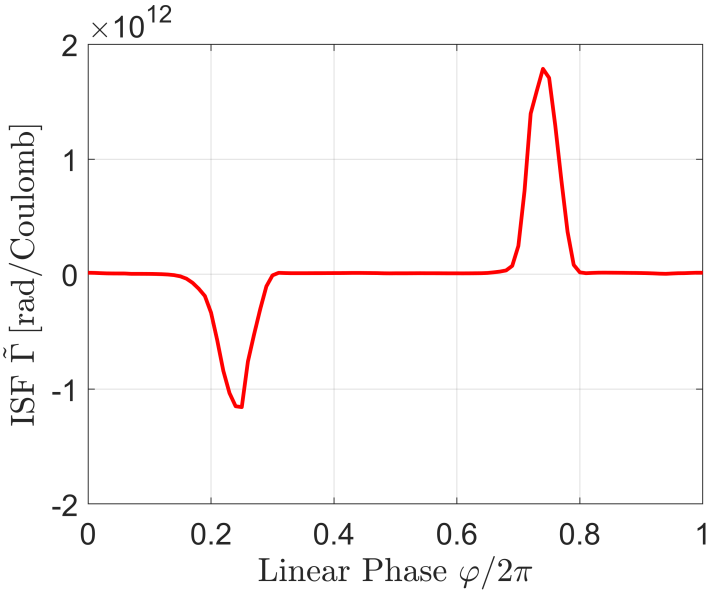

(a) Simulated ISF.

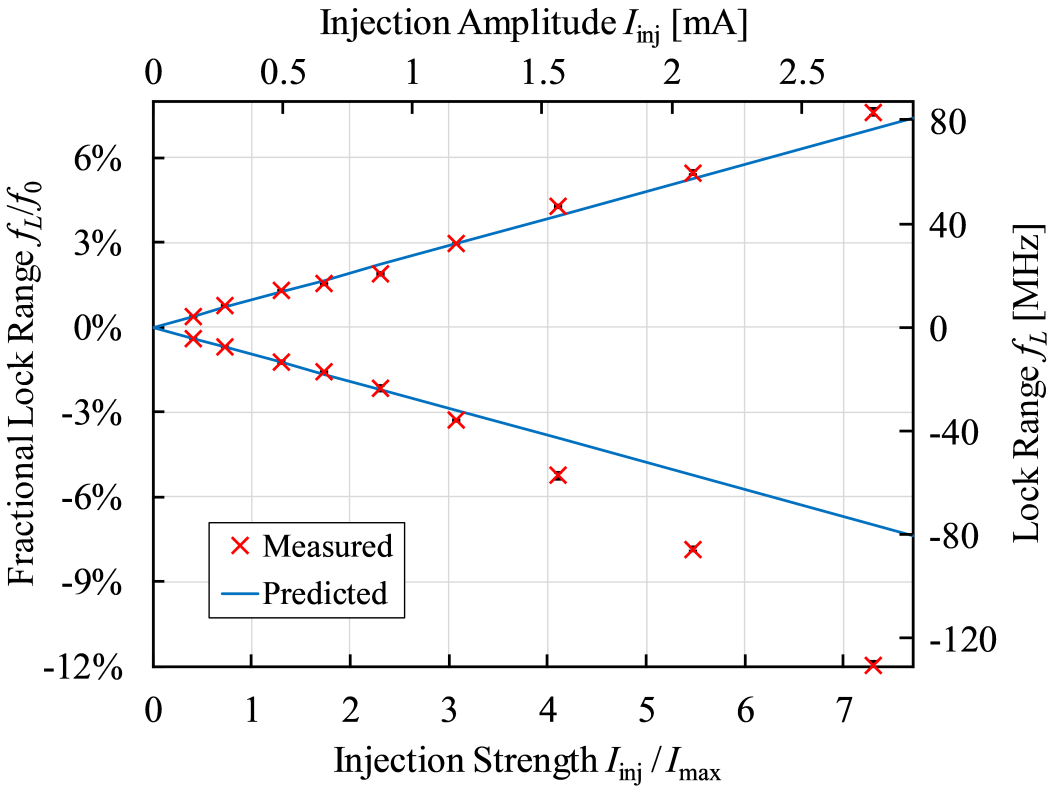

(b) Measured lock range.

Figure 4.21: Measurement results for the 17-stage single-ended ring oscillator.

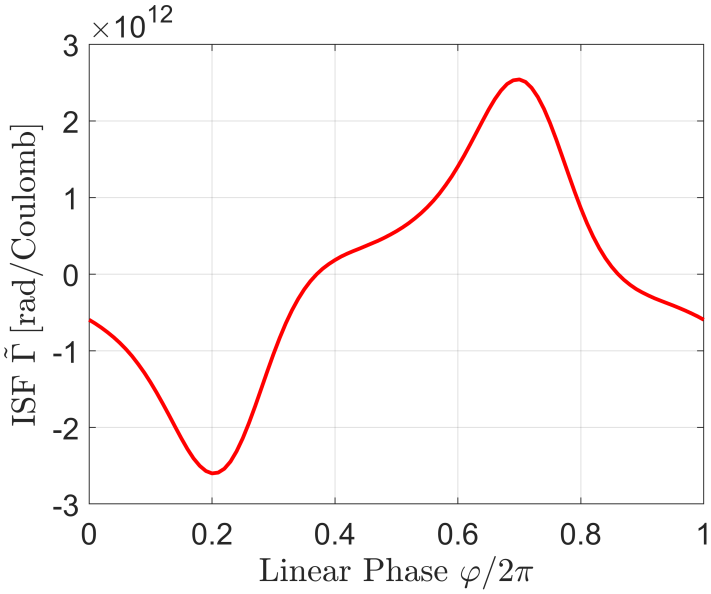

(a) Simulated ISF.

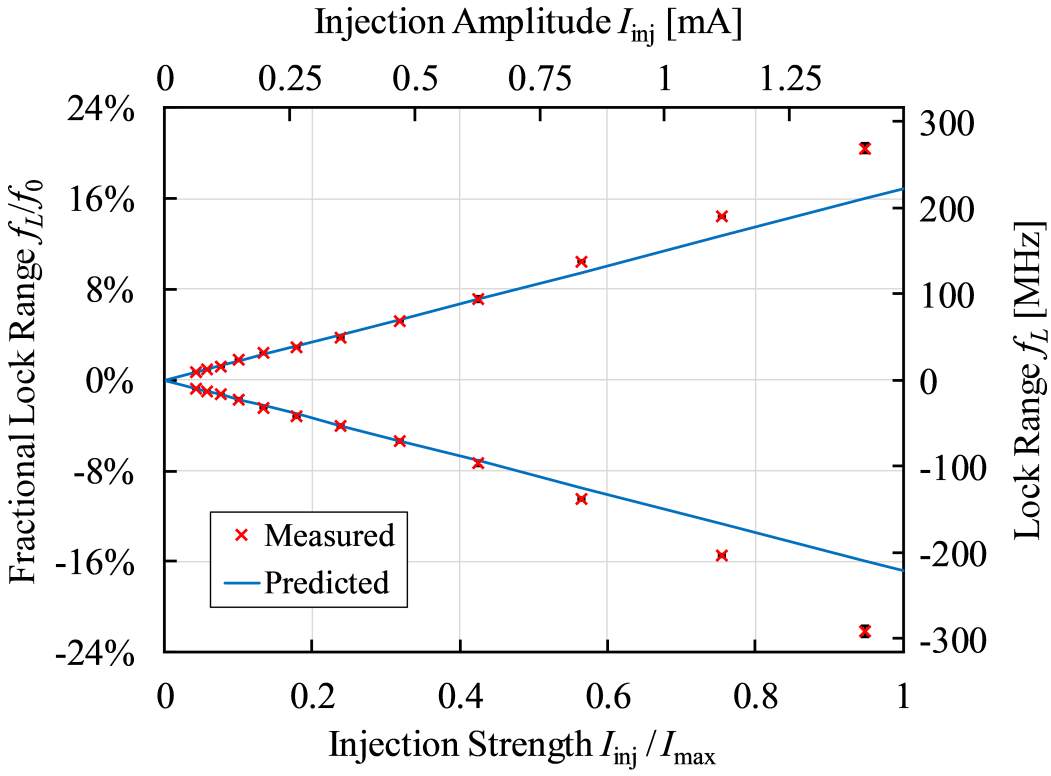

(b) Measured lock range.

Figure 4.22: Measurement results for the 6-stage differential ring oscillator.

Relaxation Oscillators

The next two experiments were performed on a comparator-based Bose oscillator and a differential NMOS astable multivibrator.

The Bose oscillator was designed to oscillate at around 10 MHz, as the bandwidth of the comparator[8] used did not exceed 100 MHz. The negative rail of the comparator was biased to ground. The resistive divider of the Bose oscillator (see Figure 4.5) featured resistances of $R_1 = 5\ \text{k}\Omega$ and $R_2 = 50\ \text{k}\Omega$ to enhance the voltage swing at the output. Because of the low operation frequency, a Rigol Function Generator (DG4202) and Rigol Digital Oscilloscope (DS4032) were used to provide the injection signal and observe the oscillation voltage directly.

Table 4.4 summarizes the design parameters of the two relaxation oscillators. Again, the only listed parameter which was measured is the oscillation frequency. Note that using Eq. (4.43) to calculate $\left|\tilde{\Gamma}_1\right|$ for the Bose oscillator gives 8.56 rad/pC.

Table 4.4: Characteristics of the Measured Relaxation Oscillators

Parameter	Bose	Astable Multivibrator
Schematic	Figure 4.5	Figure 4.17a
Timing Capacitor C [fF]	820	597
Charging Resistor R [kΩ]	25	1
Current Consumed [mA]	0.47	6.5
Supply V_{DD} [V]	1.2	2
Peak-to-Peak Voltage Swing V_{max} [V]	0.653	2.17
ISF Fundamental Magnitude $\left\|\tilde{\Gamma}_1\right\|$ [rad/pC]	9.09	4.23
(Average) *Measured* Oscillation Frequency f_0 [MHz]	11.85	873.8

Figures 4.23 and 4.24 present the measurement results. Reasonable agreement is observed between theory and experiment. It is noteworthy that the astable multivibrator appeared to be extremely noisy—its free-running spectrum was usually very visibly spread out over several megahertz. It also exhibited the most short-term drift, often necessitating repeated monitoring of the free-running oscillation frequency in between measurements of the lock range.

[8]The comparator was designed by Matan Gal-Katziri.

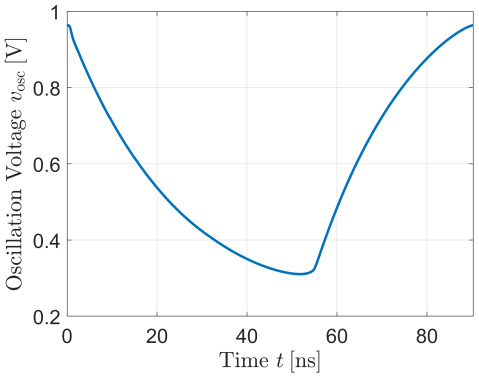

(a) Simulated oscillation voltage.

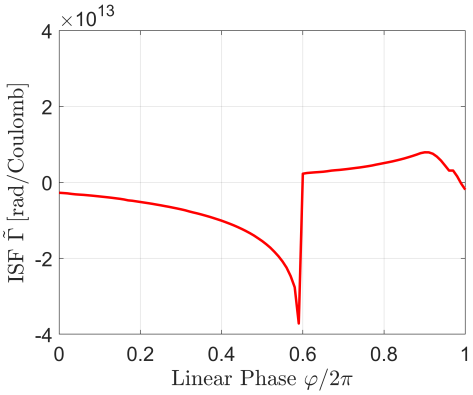

(b) Simulated ISF.

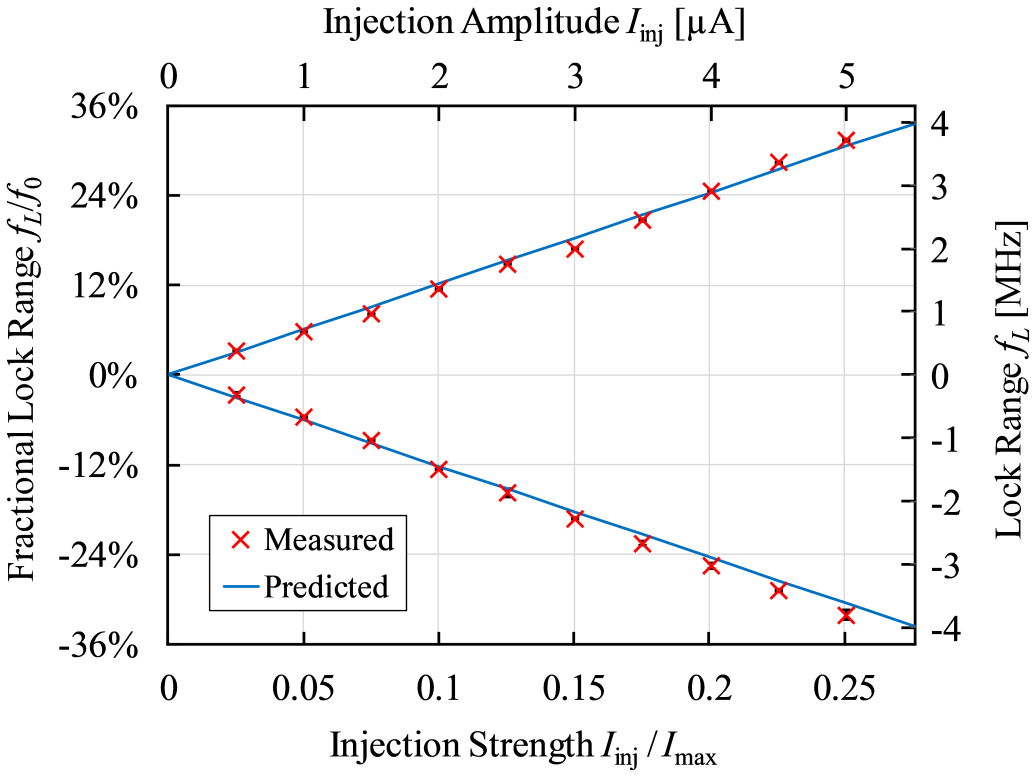

(c) Measured lock range.

Figure 4.23: Measurement results for the Bose oscillator.

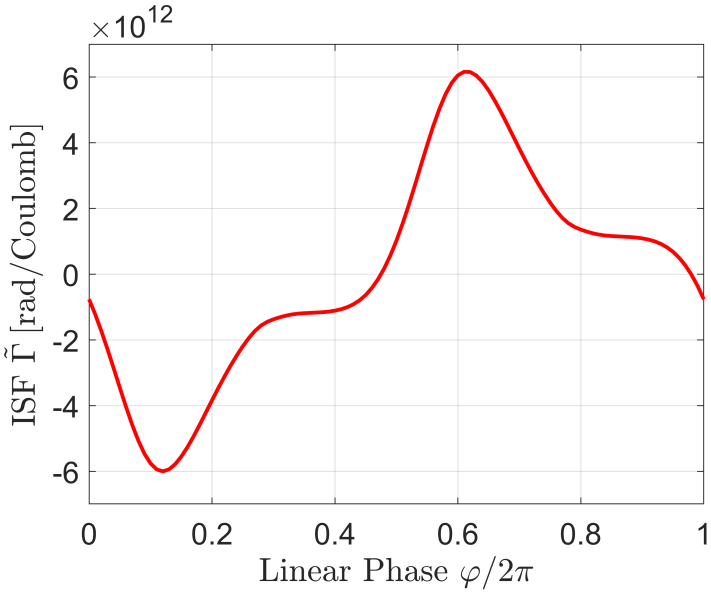

(a) Simulated ISF.

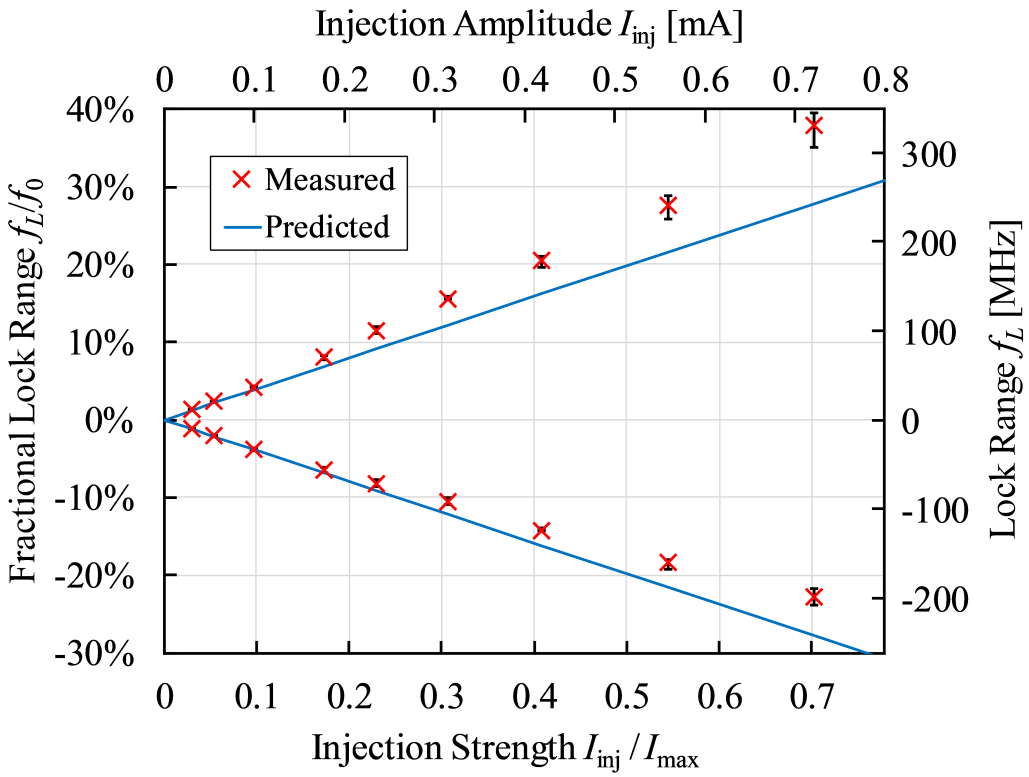

(b) Measured lock range.

Figure 4.24: Measurement results for the differential astable multivibrator.

4.8 The Sinusoidal Injection Compliance

Based on the preceding measurement results, it is apparent that having a uniform metric which quantifies how "easy" it is to lock a particular oscillator would be useful. To that end, we define a ***Sinusoidal Injection Compliance*** as the fractional, two-sided, sinusoidal lock range normalized to the injection strength:[9]

$$\boxed{\eta := \frac{2\omega_L/\omega_0}{I_{\text{inj}}/I_{\text{max}}}.} \tag{4.46}$$

In the linear regime, this quantity is independent of the size of the injection and can be simplified to

$$\boxed{\eta = q_{\text{max},0}\left|\tilde{\Gamma}_1\right|,} \tag{4.47}$$

where $q_{\text{max},0}$ is the maximum (free-running) charge swing across the injection terminals. (Recall that this quantity is defined as *half* of the peak-to-peak charge swing.) Calculated from Eq. (4.47), Table 4.5 lists the compliances of all the schematic-level oscillators simulated in Section 4.6 and the laid-out, extracted oscillators measured in Section 4.7. Two things are worth noting: relaxation oscillators tend to boast a much wider fractional lock range than ring oscillators for the same injection strength, and the compliance of the ring oscillator decreases as the number of stages increases.

Table 4.5: Compliances of Various Ring and Relaxation Oscillators

Topology	Version	Sinusoidal Injection Compliance η
3-Stage Ring	Section 4.6	67.8%
	Section 4.7	52.6%
6-Stage Ring	Section 4.6	30.7%
	Section 4.7	33.6%
17-Stage Ring	Section 4.6	2.6%
	Section 4.7	1.9%
Ideal Bose Oscillator	Sections 4.4 and 4.6	226.9%
Bose Oscillator	Section 4.7	243.3%
Astable Multivibrator	Section 4.6	396.9%
	Section 4.7	79.2%

[9]For LC oscillators, a slightly more general definition involving the quality factor will be introduced in the next chapter.

Chapter 5

LC OSCILLATORS: AMPLITUDE DEPENDENCE

5.1 Introduction

The primary limitation of the model developed in Chapter 4 is its inability to deal with injections that are large enough to cause *qualitative* deviations from the oscillator's free-running behavior. This was due to our assumption that the injection-to-phase relationship is a linear one. In this chapter, we overcome this shortcoming for the specific—but widely utilized—case of the LC oscillator by making several crucial observations about the dependence of the injection-to-phase relationship upon the oscillation amplitude. Through this insight, we show that a simple modification to the framework from Chapter 4 enables its usage for accurately modeling the nonlinear behavior of the oscillator under large injection currents.

On a more fundamental level, this analysis owes its success to the fact that an LC oscillator has only two states: the capacitor voltage and the inductor current. Therefore, an equivalent two-state representation of the LC oscillator given by the phase and the amplitude—which has a well-defined correspondence with the total energy stored in the LC tank—also forms a mathematically complete description of the state space.

5.2 Inverse Dependence on Amplitude

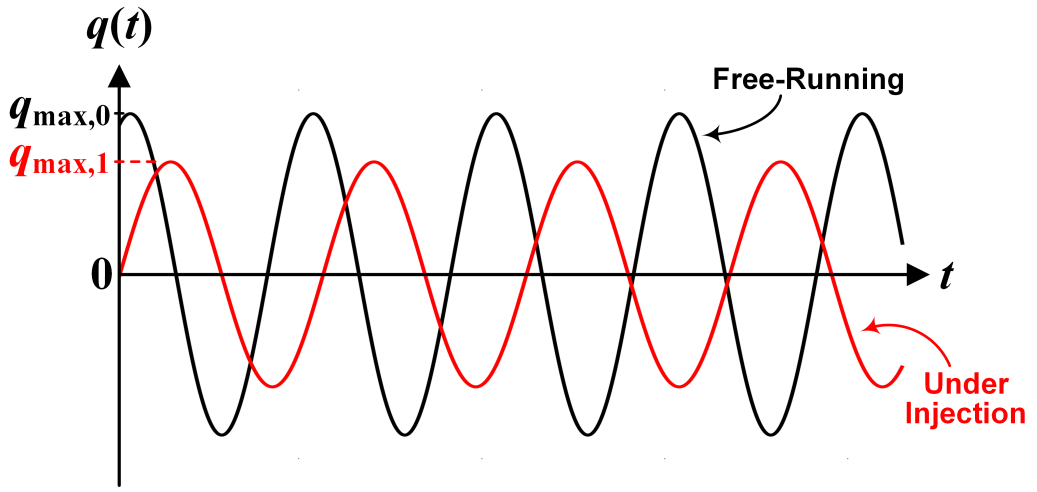

Figure 5.1: An example of how the injection could alter the oscillation amplitude.

Other than influencing the phase, the external injection is also capable of changing the size and shape of the oscillation waveform. These so-called orbital deviations were encapsulated in the term $\xi(t)$ from Eq. (1.1) and Figure 1.3. Due to the narrowband nature of the LC tank, however, we will assume that the shape of the output voltage remains fairly sinusoidal—only its size, or amplitude, can be modulated by the injection on average. A hypothetical example is shown in Figure 5.1.

Next, recall from our calculations in Chapter 3 that the phase shift induced by injecting a small, discrete amount of charge into an LC tank is inversely proportional to the maximum charge swing $q_{\max}$:

$$\Delta\varphi \propto \frac{q_{\text{inj}}}{q_{\max}} \tag{5.1}$$

for $q_{\text{inj}} \ll q_{\max}$. This is demonstrated in Figure 5.2, where the same amount of charge q_{inj} is injected at the same time τ into two identical LC tanks containing different amounts of energy. Because $q_{\max,1} > q_{\max,2}$, we see that $\Delta\varphi_1 < \Delta\varphi_2$.

We therefore conjecture that the ISF of an LC oscillator is inversely proportional to the oscillation amplitude. We can prove this by returning to the orthogonal state-space description of the ISF given by Eq. (4.6). Since the two state variables are the capacitor voltage $v(\varphi)$ and the inductor current $i(\varphi)$, the ISF is given by

$$\tilde{\Gamma}(\varphi) = \frac{v'(\varphi)}{Cv'(\varphi)^2 + Li'(\varphi)^2}. \tag{5.2}$$

Since both the capacitor voltage and the inductor current scale with the oscillation amplitude[1], increasing the amplitude by a factor of $A > 0$ decreases the ISF by a factor of $1/A$.

Consequently, we model the *effective* ISF of the LC oscillator with the following *inverse* dependence on the amplitude:

$$\boxed{\tilde{\Gamma}_{\text{eff}} = \frac{\tilde{\Gamma}}{1+\xi},} \tag{5.3}$$

where ξ is equal to the fractional change in the oscillation amplitude. With this idea in mind, our next step will be to relate ξ to the injection current.

[1] In case this is not obvious, note that the oscillation amplitude is proportional to the square root of the total amount of energy stored in the LC tank, which periodically alternates between being stored entirely in the capacitor and entirely in the inductor. Therefore, $E = CV_0{}^2/2 = LI_0{}^2/2$, where V_0 and I_0 are the amplitudes of the capacitor voltage and the inductor current, respectively.

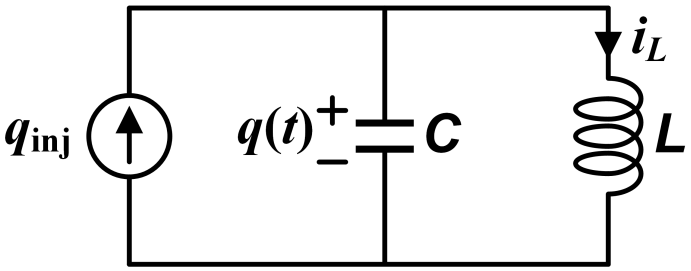

(a) LC oscillator perturbed by an injection of charge.

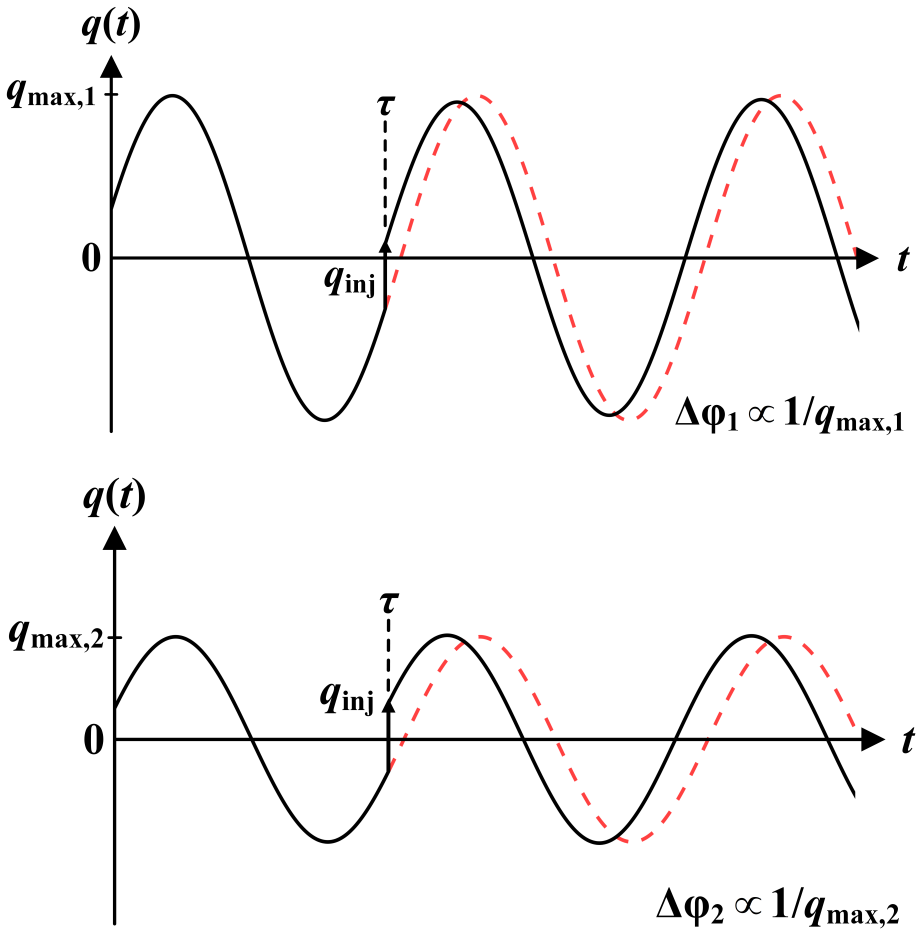

(b) Note that the time of injection τ is the same in both examples.

Figure 5.2: The phase shift $\Delta\varphi$ induced by the injection of charge q_{inj} depends inversely on the maximum charge swing q_{max} across the capacitor.

5.3 Modeling the Amplitude: The Amplitude Perturbation Function (APF)

To calculate the orbital deviation $\xi(t)$ in response to the injection current $i_{\text{inj}}(t)$, we will once again appeal to a linear, periodically time-varying (LPTV) model. However, unlike the permanent nature of phase perturbations, amplitude distur-

bances must decay to 0 eventually in any stable oscillator. We therefore write the time-varying impulse response for $\xi(t)$ as

$$h_\xi(t,\tau) = D\big(t-\tau, \omega_{\text{inj}}\tau + \theta\big) \cdot u(t-\tau), \tag{5.4}$$

where $D(\Delta t, \varphi)$ is a ***decay function*** which physically represents the fractional change in the oscillation amplitude due to a unit impulse applied at a phase φ after time Δt has passed since the application of the impulse. For oscillators which possess a stable limit cycle, $D(\Delta t, \varphi) \to 0$ as $\Delta t \to \infty$ for all φ.

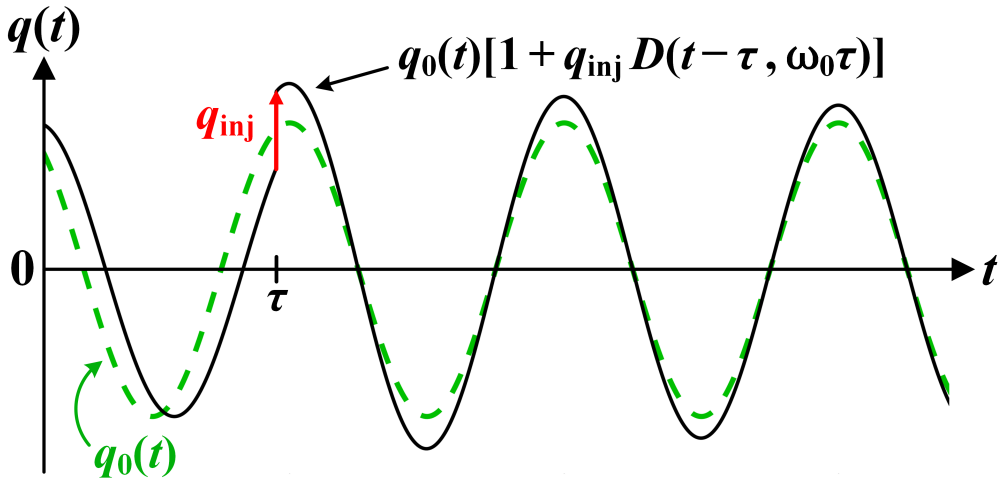

(a) Decay of the excess amplitude of the charge waveform after an injection.

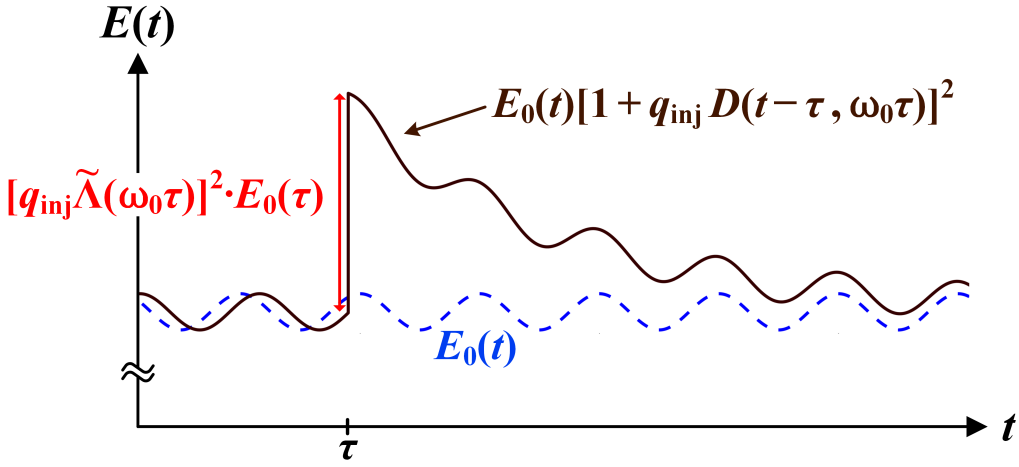

(b) Decay of the excess energy stored in the oscillator after an injection.

Figure 5.3: The dynamic by which the oscillator dissipates excess energy is captured by the decay function $D(\cdot,\cdot)$.

How does one compute the orbital deviation $\xi(t)$ of an actual LC oscillator for

the purposes of simulating the decay function? First and foremost, note that the voltage (and current) waveforms of interest [e.g., the $v(\varphi)$ and $i(\varphi)$ referenced in Eq. (5.2)] have a zero DC value; they only correspond to variations about the bias voltage (or current).[2] This is because the peak values of the voltage and current must correspond to the total amount of energy in the tank being exchanged back and forth between the capacitor and the inductor. Therefore, comparing only the voltage (or the current) waveform between the perturbed and free-running cases is problematic, as one would run into the numerical issue of dealing with zero-crossings. Instead, both the voltage and the current should be used to calculate the instantaneous oscillation amplitude:

$$[1 + \xi(t)] \cdot V_{\text{osc}} = \sqrt{\frac{2E(t)}{C}} = \sqrt{v(t)^2 + \frac{L}{C} i(t)^2}. \tag{5.5}$$

Consequently, for LC oscillators, the orbital deviation ξ also represents the fractional change in the *square root* of the energy E stored in the oscillator's tank. If this tank consists of a network containing multiple capacitors and inductors, then

$$E = \frac{1}{2} \sum_k C_k {v_k}^2 + \frac{1}{2} \sum_k L_k {i_k}^2 + \sum_{p<q} M_{pq} i_p i_q, \tag{5.6}$$

where M_{pq} represents the mutual inductance between inductors L_p and L_q (assuming i_p and i_q both leave/enter the dotted terminal). It is worth noting, however, that at RF and mm-wave frequencies, integrated inductors are typically modeled using scattering parameters obtained from electromagnetic simulation, making the energy stored in the tank considerably more cumbersome to calculate. Fortunately, lumped-element models for on-chip inductors [97]–[99] usually provide sufficient accuracy for our purposes.

Once the energy has been ascertained, we can calculate the orbital deviation by

$$\xi = \sqrt{\frac{E}{E_0}} - 1, \tag{5.7}$$

where E_0 is the amount of tank energy stored by the free-running oscillator in steady state. The concept of the decay function is shown in Figure 5.3 from the perspective of both the oscillation amplitude and the stored energy.

[2] This is obviously a moot point for the voltage in differential LC oscillators.

Given the impulse response, we can use a superposition integral to calculate the orbital deviation:

$$\begin{aligned}\xi(t) &= \int_{-\infty}^{\infty} i_{\text{inj}}(\tau) \cdot h_\xi(t,\tau)\, d\tau \\ &= \int_{-\infty}^{t} i_{\text{inj}}(\tau) \cdot D\big(t-\tau, \omega_{\text{inj}}\tau + \theta\big)\ d\tau \\ &= \int_{0}^{\infty} i_{\text{inj}}(t-\tau) \cdot D\big(\tau, \omega_{\text{inj}}(t-\tau) + \theta\big)\ d\tau.\end{aligned} \tag{5.8}$$

The change of variables in the last step allows us to see that $\xi(t)$ is itself periodic with frequency ω_{inj}. Thus, we once again appeal to the theory of time-averaging [96] and replace ξ with its time-average over an injection period:

$$\begin{aligned}\implies \xi &= \frac{1}{T_{\text{inj}}} \int_{T_{\text{inj}}} \int_{0}^{\infty} i_{\text{inj}}(t-\tau) \cdot D\big(\tau, \omega_{\text{inj}}(t-\tau) + \theta\big)\ d\tau\, dt \\ &= \frac{1}{T_{\text{inj}}} \int_{0}^{\infty} \int_{T_{\text{inj}}} i_{\text{inj}}(t-\tau) \cdot D\big(\tau, \omega_{\text{inj}}(t-\tau) + \theta\big)\ dt\, d\tau.\end{aligned} \tag{5.9}$$

Due to the periodicity of the integrand with respect to t, the inner integral is invariant to the specific period being integrated over, so long as it has a length of T_{inj}. Therefore, this integral is also independent of τ. Hence,

$$\begin{aligned}\xi &= \frac{1}{T_{\text{inj}}} \int_{0}^{\infty} \int_{T_{\text{inj}}} i_{\text{inj}}(t) \cdot D\big(\tau, \omega_{\text{inj}} t + \theta\big)\ dt\, d\tau \\ &= \frac{1}{T_{\text{inj}}} \int_{T_{\text{inj}}} i_{\text{inj}}(t) \int_{0}^{\infty} D\big(\tau, \omega_{\text{inj}} t + \theta\big)\ d\tau\, dt.\end{aligned} \tag{5.10}$$

To conceptually decouple the instantaneous change in the amplitude induced by the impulse from the subsequent decay dynamic, we decompose the decay function as

$$D(\tau,\varphi) \equiv \tilde{\Lambda}(\varphi) \cdot d(\tau,\varphi), \tag{5.11}$$

where we normalize

$$d(0,\varphi) \equiv 1 \qquad \forall \varphi. \tag{5.12}$$

Let us refer to $d(\tau,\varphi)$ as the oscillator's ***characteristic decay function***. Like the decay function $D(\tau,\varphi)$, it also represents the fractional change in the oscillation amplitude due to a unit impulse applied at a phase φ after time τ has elapsed, but normalized to the *initial* amplitude change immediately after application of the impulse. It is then easy to see that $\tilde{\Lambda}(\varphi)$ is the ***Amplitude ISF*** first introduced by Hajimiri and Lee [88], [100] (up to a normalization factor of $q_{\max}$—i.e., $\Lambda = q_{\max} \cdot \tilde{\Lambda}$).

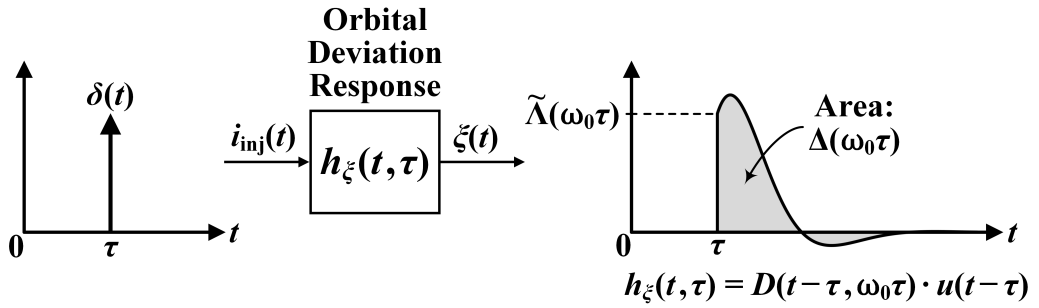

Figure 5.4: Relating the time-varying impulse response for orbital deviations to the amplitude ISF and the APF.

We will now define the ***Amplitude Perturbation Function*** or ***APF*** $\Delta(\varphi)$ by

$$\boxed{\Delta(\varphi) \coloneqq \int_0^\infty D(\tau,\varphi)\,d\tau = \tilde{\Lambda}(\varphi)\int_0^\infty d(\tau,\varphi)\,d\tau.} \tag{5.13}$$

The Amplitude Perturbation Function Δ has units of $[1/\text{Ampere}]$; multiplying it by a current yields a unit-less quantity. In practice, one need only integrate up to some observation time T_{obs}, beyond which the decay functions D or d are negligibly small. Notice that the APF is equal to the area under the orbital deviation impulse response $h_\xi(t,\tau)$, as shown in Figure 5.4.

With this definition, the average orbital deviation becomes

$$\xi = \frac{1}{T_{\text{inj}}}\int_{T_{\text{inj}}} \Delta\big(\omega_{\text{inj}}t + \theta\big)\, i_{\text{inj}}(t)\,dt. \tag{5.14}$$

It should be apparent that the oscillation amplitude of an injection-locked LC oscillator is therefore given by

$$V_{\text{osc}} = (1+\xi)\,V_{\text{osc},0}, \tag{5.15}$$

where $V_{\text{osc},0}$ is the free-running oscillation amplitude.

Note that the APF is a measure of both how much the oscillation amplitude changes *and* how long it takes for the perturbation to decay. More importantly, its spectral components give us a sense for how malleable the oscillator's amplitude is to a current injection at that harmonic. A block diagram summarizing the process by which the APF filters the injection to create amplitude modulation is shown in Figure 5.5.

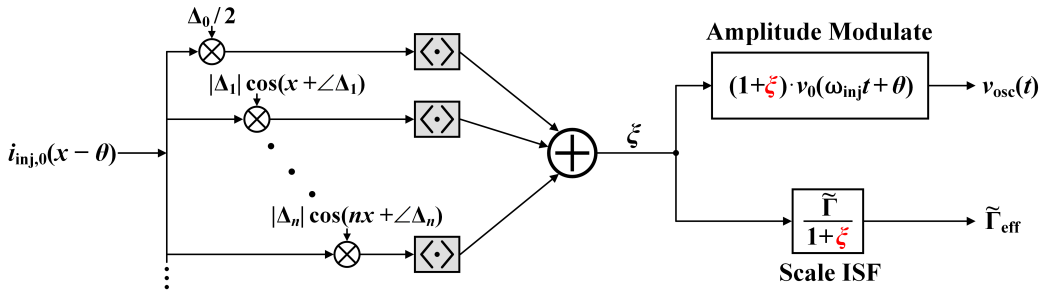

Figure 5.5: The APF captures the perturbation in the oscillation amplitude caused by the injection—for which the ISF of an LC oscillator has an inverse dependence.

5.4 A Modified Differential Equation for the Phase

We start with the original pulling equation for the phase $\theta(t)$, which was given in Eq. (4.20) as

$$\begin{aligned}\frac{d\theta}{dt} &= \omega_0 - \omega_{\text{inj}} + \frac{1}{T_{\text{inj}}}\int_{T_{\text{inj}}} \tilde{\Gamma}_{\text{eff}}\left(\omega_{\text{inj}}t+\theta\right) i_{\text{inj}}(t)\,dt \\ &= \omega_0 - \omega_{\text{inj}} + \frac{1}{T_{\text{inj}}}\int_{T_{\text{inj}}} \frac{\tilde{\Gamma}\left(\omega_{\text{inj}}t+\theta\right)}{1+\xi} i_{\text{inj}}(t)\,dt.\end{aligned} \tag{5.16}$$

Notice that we used the effective ISF for LC oscillators from Eq. (5.3). In light of our expression for the average orbital deviation, Eq. (5.14), we can rewrite this as:

$$\boxed{\frac{d\theta}{dt} = \omega_0 - \omega_{\text{inj}} + \frac{\dfrac{1}{T_{\text{inj}}}\displaystyle\int_{T_{\text{inj}}} \tilde{\Gamma}\left(\omega_{\text{inj}}t+\theta\right) i_{\text{inj}}(t)\,dt}{1+\dfrac{1}{T_{\text{inj}}}\displaystyle\int_{T_{\text{inj}}} \Delta\left(\omega_{\text{inj}}t+\theta\right) i_{\text{inj}}(t)\,dt}.} \tag{5.17}$$

We can also express the APF in terms of its Fourier series expansion:

$$\Delta(x) = \frac{\Delta_0}{2} + \sum_{n=1}^{\infty} |\Delta_n|\cos(nx+\angle\Delta_n) \tag{5.18}$$

where

$$\Delta_n = \frac{1}{\pi}\int_{2\pi} \Delta(x)e^{-jnx}\,dx. \tag{5.19}$$

This allows us to rewrite Eq. (5.17) as

$$\begin{aligned}\frac{d\theta}{dt} &= \omega_0 - \omega_{\text{inj}} + \frac{\left\langle \tilde{\Gamma}(x+\theta)\, i_{\text{inj},0}(x)\right\rangle_{2\pi}}{1+\left\langle \Delta(x+\theta)\, i_{\text{inj},0}(x)\right\rangle_{2\pi}} \\ &= \omega_0 - \omega_{\text{inj}} + \frac{\dfrac{1}{2}\left[\dfrac{I_{\text{inj},0}\tilde{\Gamma}_0}{2} + \displaystyle\sum_{n=1}^{\infty}\left|I_{\text{inj},n}\tilde{\Gamma}_n\right|\cos\left(n\theta+\angle\tilde{\Gamma}_n-\angle I_{\text{inj},n}\right)\right]}{1+\dfrac{1}{2}\left[\dfrac{I_{\text{inj},0}\Delta_0}{2} + \displaystyle\sum_{n=1}^{\infty}\left|I_{\text{inj},n}\Delta_n\right|\cos\left(n\theta+\angle\Delta_n-\angle I_{\text{inj},n}\right)\right]}.\end{aligned} \tag{5.20}$$

In essence, this model can be viewed as a "quasi-nonlinear" approach, as it models the nonlinear behavior within the injection-to-phase relationship by decomposing it into separate quantities, each of which is assumed to have a linear dependence on the injection current input.

Since the ISF and APF of an LC oscillator are usually fairly sinusoidal, it is often the case that only the fundamental component of the injection is relevant. Therefore, we present the simplified case of a sinusoidal injection current here. Assuming that $i_{\text{inj}}(t) = I_{\text{inj}} \cos(\omega_{\text{inj}} t)$, the pulling equation becomes

$$\frac{d\theta}{dt} = \omega_0 - \omega_{\text{inj}} + \frac{\frac{1}{2} I_{\text{inj}} \left|\tilde{\Gamma}_1\right| \cos\left(\theta + \angle\tilde{\Gamma}_1\right)}{1 + \frac{1}{2} I_{\text{inj}} \left|\Delta_1\right| \cos(\theta + \angle\Delta_1)}, \tag{5.21}$$

which also results in the following lock characteristic:

$$\Omega(\theta) = \frac{\frac{1}{2} I_{\text{inj}} \left|\tilde{\Gamma}_1\right| \cos\left(\theta + \angle\tilde{\Gamma}_1\right)}{1 + \frac{1}{2} I_{\text{inj}} \left|\Delta_1\right| \cos(\theta + \angle\Delta_1)}. \tag{5.22}$$

This lock characteristic can be optimized over θ to obtain the lock range:

$$\omega_L^{\pm} = \frac{\frac{1}{2} I_{\text{inj}} \left|\tilde{\Gamma}_1\right|}{\frac{1}{2} I_{\text{inj}} \left|\Delta_1\right| \cos\beta \pm \sqrt{1 - \left(\frac{1}{2} I_{\text{inj}} \left|\Delta_1\right| \sin\beta\right)^2}}, \tag{5.23}$$

where $\beta \equiv \angle\tilde{\Gamma}_1 - \angle\Delta_1$. This lock range is generally asymmetric, meaning $\omega_L^+ \neq -\omega_L^-$. In particular, the lower lock range is wider when $|\beta| < \pi/2$, whereas the upper lock range is wider when $\pi/2 < |\beta| < \pi$. If, however, $\beta = \pm\pi/2$, indicating that the ISF and APF are in perfect quadrature with respect to one another, the upper and lower lock ranges become symmetric:

$$\omega_L^{\pm} = \pm \frac{\frac{1}{2} I_{\text{inj}} \left|\tilde{\Gamma}_1\right|}{\sqrt{1 - \left(\frac{1}{2} I_{\text{inj}} \left|\Delta_1\right|\right)^2}}. \tag{5.24}$$

Another thing to observe is how the lock characteristic becomes unbounded when $I_{\text{inj}} \left|\Delta_1\right| \geq 2$, resulting in an infinite lock range! Physically, this is because the fractional amplitude change ξ is able to dip below -1 for certain values of θ,

corresponding to the nonphysical scenario of an oscillation amplitude which is zero or negative. Consequently, it may be necessary in these situations to constrain the range of phases θ to be a subset of $[-\pi, \pi)$. Note that this downside of our model only manifests for rather large injection strengths, and it is a property of other large-injection models for LC oscillators as well.[3] As we will see empirically from the simulation results of the next section, restricting $\theta \in [-110°, 110°]$ for very large injection amplitudes usually results in reliable estimates of the lock range.

5.5 Simulation Results

In this section, we present simulation results for two differential LC oscillators and a bipolar Colpitts oscillator, all implemented in a bulk CMOS process. The injection will be applied across the tank's effective capacitance. For each oscillator, we will show (1) the free-running oscillation voltage, inductor current, and tank energy over a single period; (2) the ISF, Amplitude ISF, APF, and characteristic decay function; and (3) the theoretical and simulated lock characteristic for several different sinusoidal injection amplitudes. The theoretical lock characteristic which does not incorporate the APF is also shown for comparison. To further demonstrate the validity of our model, a plot of the oscillation amplitude as a function of the injection frequency is also shown. The theoretical oscillation amplitude was calculated using Eq. (5.15). For each injection frequency, there are two solutions for the phase θ and therefore also two possible oscillation amplitudes. As we will see, the stable mode corresponds to the larger oscillation amplitude. Again, the unstable portions of all theoretical curves are delineated with dashed lines.

CMOS Differential LC Oscillator

The schematic, free-running oscillation voltage, and free-running inductor current of this oscillator are shown in Figure 5.6. The tank's parameters are $L = 6$ nH and $C = 4.15$ pF with a quality factor of $Q = 15$. The oscillation frequency is around $f_0 = 1$ GHz, and the oscillator is biased at $I_{\text{tail}} = 1$ mA.

[3] For example, both Mirzaei's Generalized Adler's equation [21] and the model in Chapter 10 predict an infinite lock range when $I_{\text{inj}} \geq I_{\text{osc}}$.

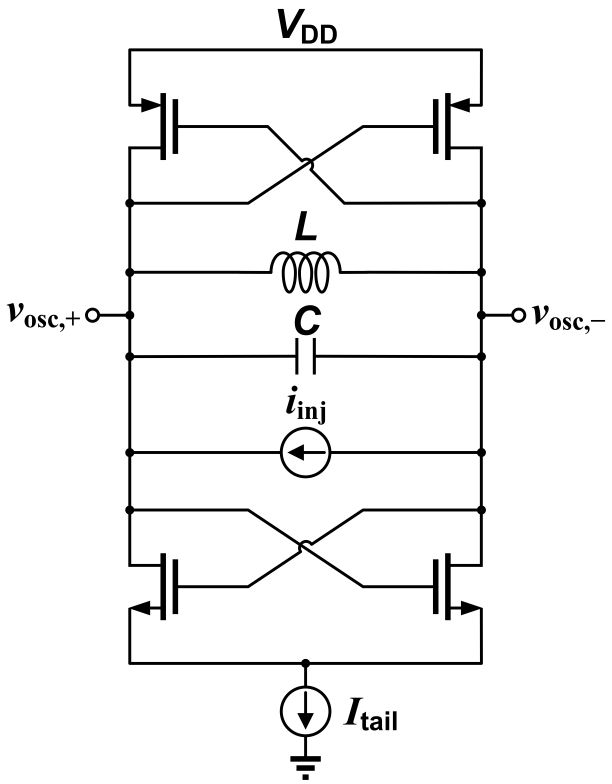

(a) Oscillator schematic. I_{tail} is implemented with a resistively biased current mirror.

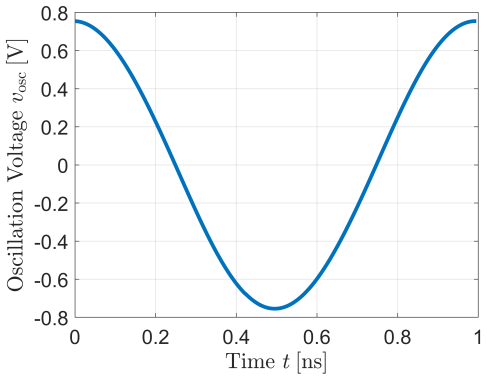

(b) Free-running oscillation voltage.

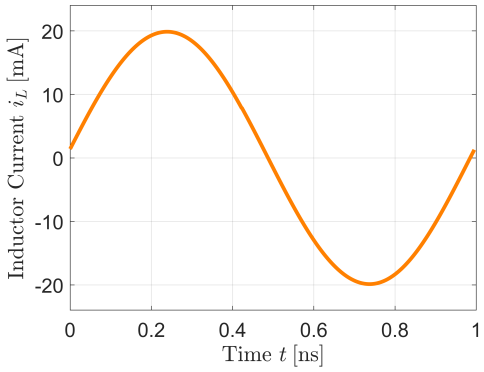

(c) Free-running inductor current.

Figure 5.6: Cross-coupled CMOS differential LC oscillator.

The free-running tank energy, sensitivity functions, and characteristic decay function are shown in Figure 5.7. Note that the tank energy is not necessarily constant, as the transistors do not merely present a negative linear resistance to the tank. The characteristic decay function $d(t, \varphi)$ quite closely follows the same exponential decay over all phases φ. The associated time constant is roughly $\tau = 5\,\text{ns}$, which is slightly longer than that of a linear RLC tank with the same quality factor: $2Q/\omega_0 = 4.8\,\text{ns}$.

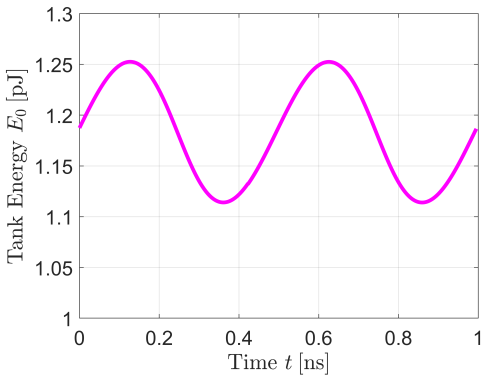

(a) Free-running tank energy.

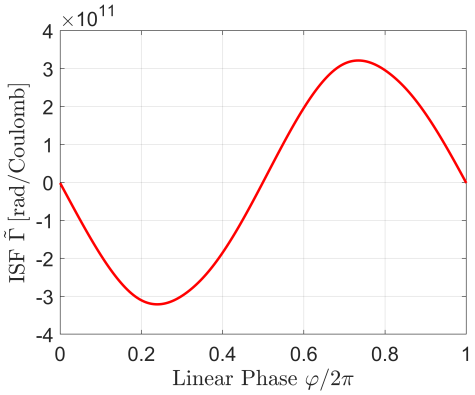

(b) Impulse sensitivity function.

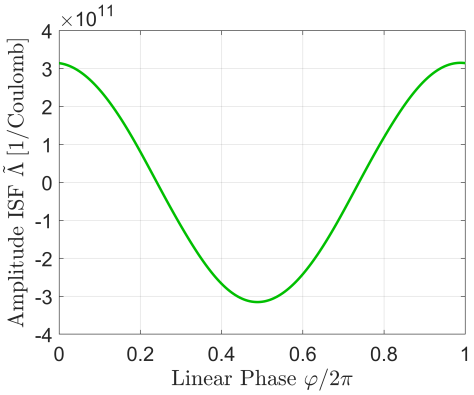

(c) Amplitude ISF.

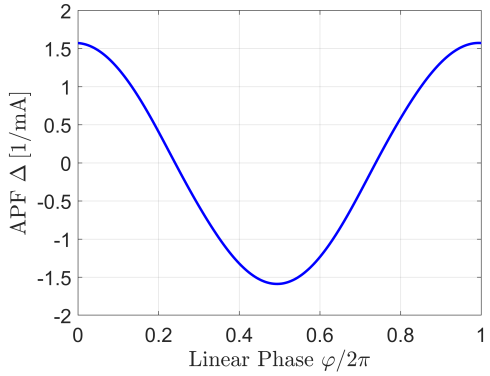

(d) Amplitude perturbation function.

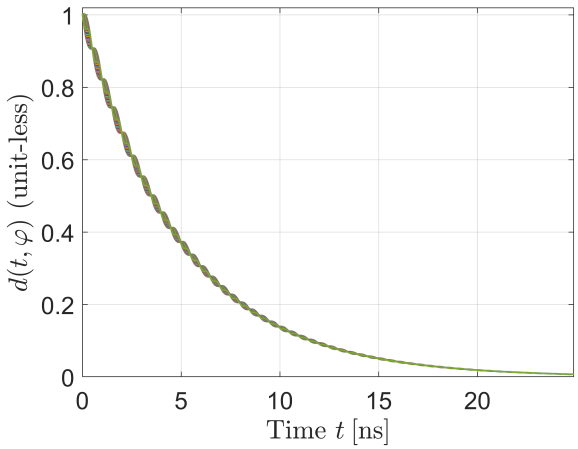

(e) Characteristic decay function. Each curve corresponds to a different phase φ.

Figure 5.7: Other properties of the cross-coupled CMOS differential LC oscillator.

The lock characteristic and the oscillation amplitude as a function of the injection frequency for an injection amplitude of $I_{\text{inj}} = 0.5$ mA are shown in Figure 5.8.

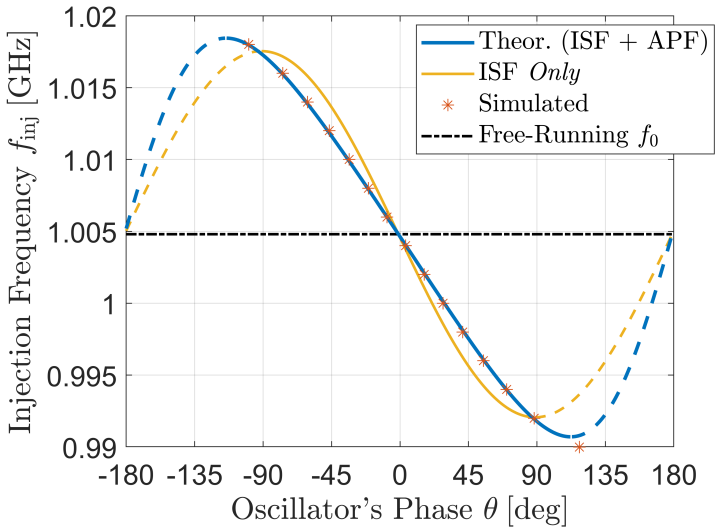

(a) Sinusoidal lock characteristic.

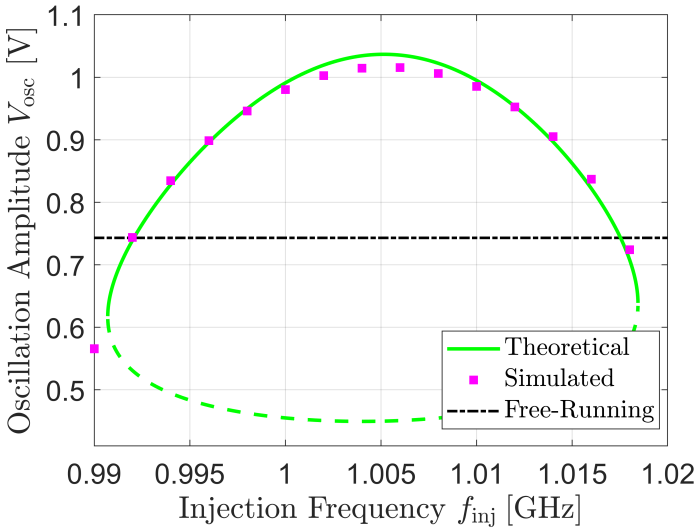

(b) Oscillation amplitude vs. injection frequency under lock.

Figure 5.8: Predicted and simulated behavior of a sinusoidally injection-locked CMOS differential LC oscillator with an injection amplitude of $I_{\text{inj}} = 0.5$ mA.

Figure 5.9 shows the same plots for $I_{\text{inj}} = 0.75$ mA. Again, good agreement is observed between simulation and theory. The error incurred from neglecting the APF and using the ISF alone to predict the lock characteristic is much more evident for this injection amplitude.

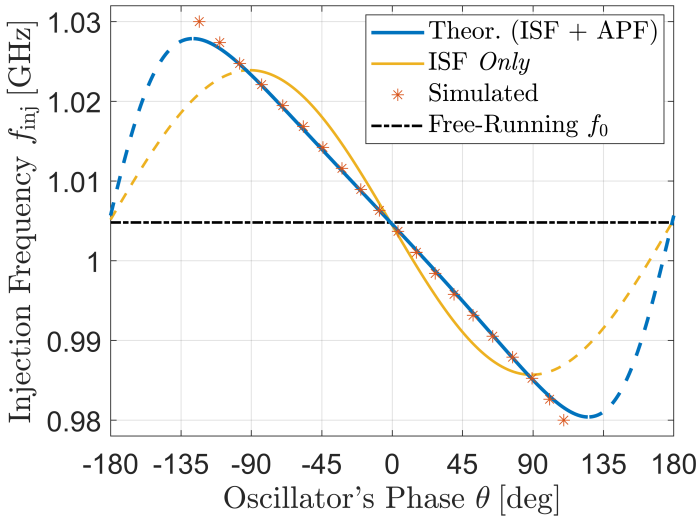

(a) Sinusoidal lock characteristic.

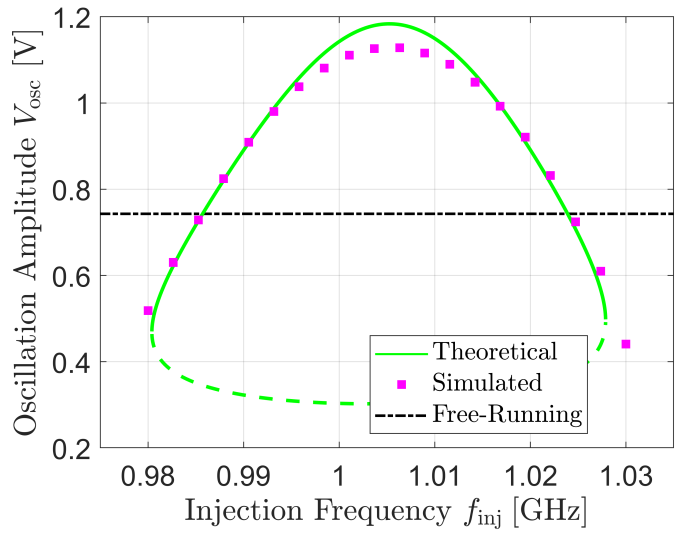

(b) Oscillation amplitude vs. injection frequency under lock.

Figure 5.9: Predicted and simulated behavior of a sinusoidally injection-locked CMOS differential LC oscillator with an injection amplitude of $I_{\text{inj}} = 0.75$ mA.

Figure 5.10 shows the same plots for $I_{\text{inj}} = 1$ mA. Notice that the simulated lock range is narrower (on both ends) than its theoretical prediction. This is because the edges of the lock range correspond to the smallest oscillation amplitudes, and the oscillator fails to stably oscillate at such small amplitudes. Unfortunately, our model fails to capture this dynamic, but this issue is discussed to some extent in Chapter 10.

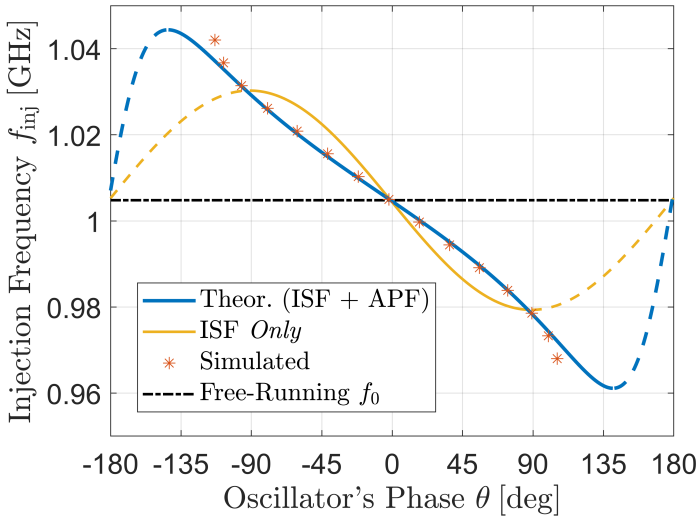

(a) Sinusoidal lock characteristic.

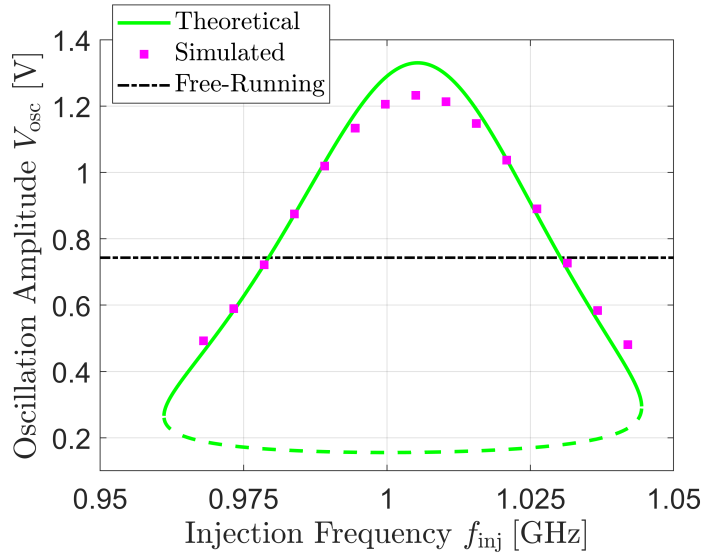

(b) Oscillation amplitude vs. injection frequency under lock.

Figure 5.10: Predicted and simulated behavior of a sinusoidally injection-locked CMOS differential LC oscillator with an injection amplitude of $I_{\text{inj}} = 1$ mA.

Figure 5.11 shows the same plots for $I_{\text{inj}} = 2$ mA. Since $I_{\text{inj}}\,|\Delta_1| = 3.2 > 2$, the range of phases θ portrayed in the lock characteristic is between $-115°$ and $110°$.

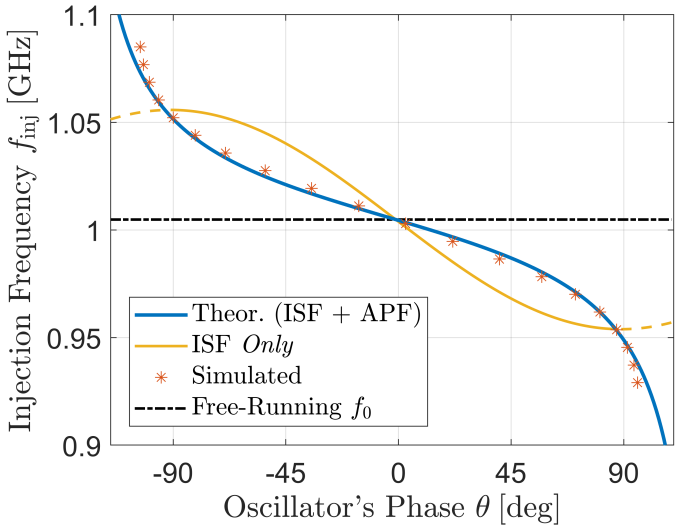

(a) Sinusoidal lock characteristic.

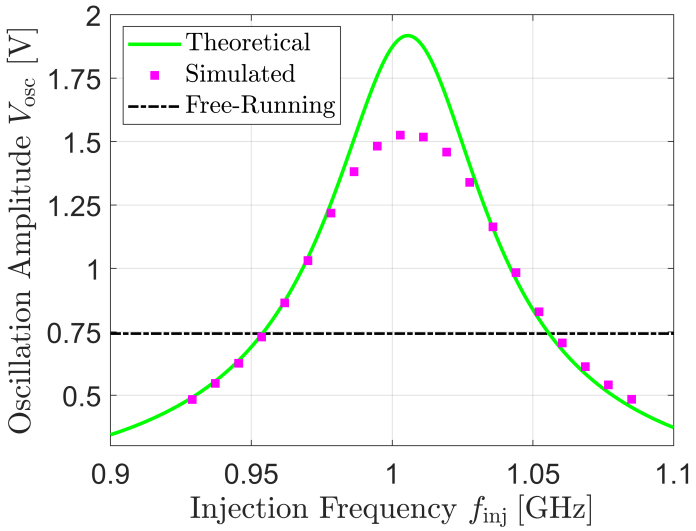

(b) Oscillation amplitude vs. injection frequency under lock.

Figure 5.11: Predicted and simulated behavior of a sinusoidally injection-locked CMOS differential LC oscillator with an injection amplitude of $I_{\text{inj}} = 2$ mA.

Notice the deviation between theory and simulation near the center of the oscillation amplitude plot for larger injection strengths. This occurs since nonlinear amplitude restoring effects, which are not captured by the APF, are more prominent at larger oscillation amplitudes. Fortunately, as we can see, this deviation does not affect the accuracy of the predicted lock characteristic, since the size of $\tilde{\Gamma}_{\text{eff}}$ becomes increasingly less relevant for injection frequencies close to f_0.

NMOS-Only Differential LC Oscillator

A differential LC oscillator with only the NMOS cross-coupled pair has different amplitude properties than one utilizing complementary pairs (PMOS and NMOS). In particular, even though the former has half the voltage swing for the same bias current in the current-limited regime, it features a maximum differential swing of $2V_{\mathrm{DD}}$, which is twice that of the CMOS LC oscillator [89]. Here, we consider an NMOS-only differential LC oscillator with the same tank parameters as the CMOS oscillator of Figures 5.6 and 5.7, but biased at $I_{\mathrm{tail}} = 2$ mA to maintain the same voltage swing. The schematic, free-running oscillation voltage, and free-running inductor current are shown in Figure 5.12, while the free-running tank energy, sensitivity functions, and characteristic decay function are shown in Figure 5.13.

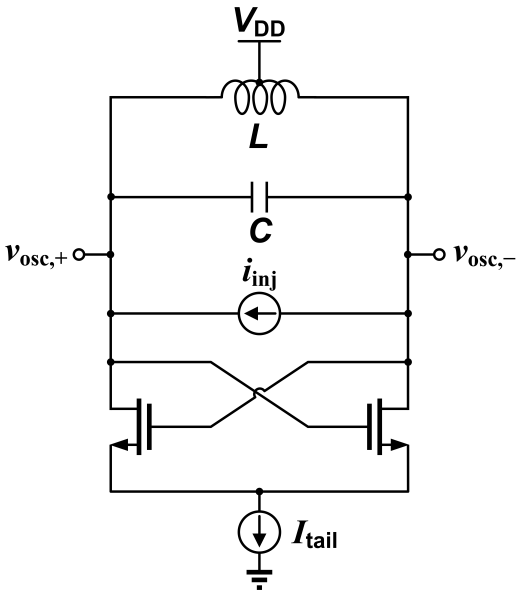

(a) Oscillator schematic. I_{tail} is implemented with a resistively biased current mirror.

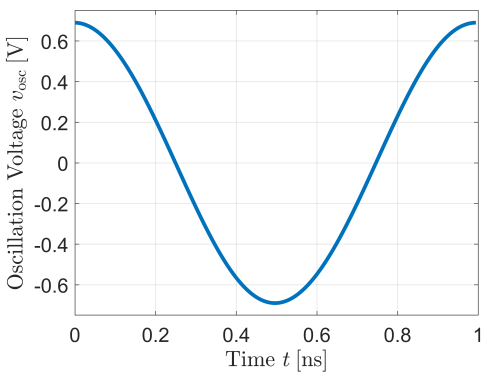

(b) Free-running oscillation voltage.

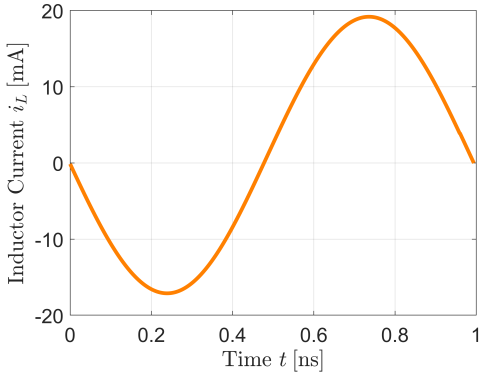

(c) Free-running inductor current.

Figure 5.12: Cross-coupled NMOS-only differential LC oscillator.

Notice how the tank energy only iterates through a single cycle per oscillation period, while the tank energy in the presence of complementary pairs oscillates at twice the oscillation frequency. The characteristic decay is also slower with a time constant of roughly $\tau = 7.2$ ns. This leads to a larger APF compared to a CMOS LC oscillator with the same voltage swing.

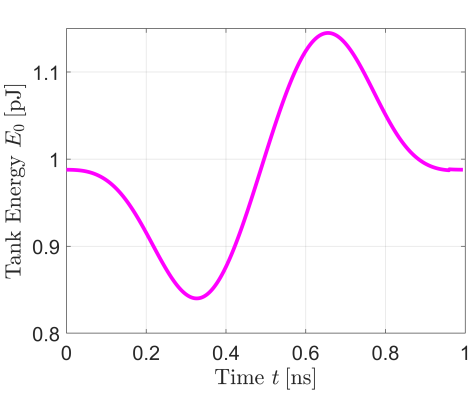

(a) Free-running tank energy.

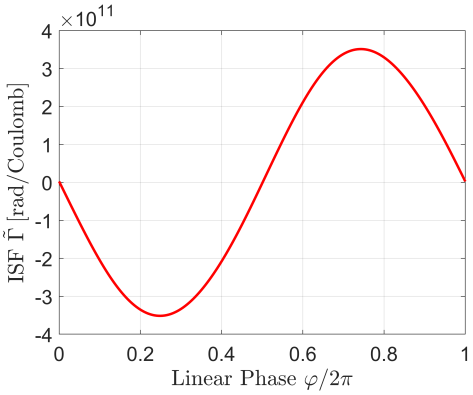

(b) Impulse sensitivity function.

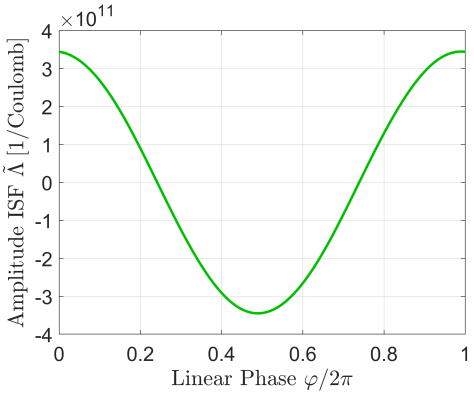

(c) Amplitude ISF.

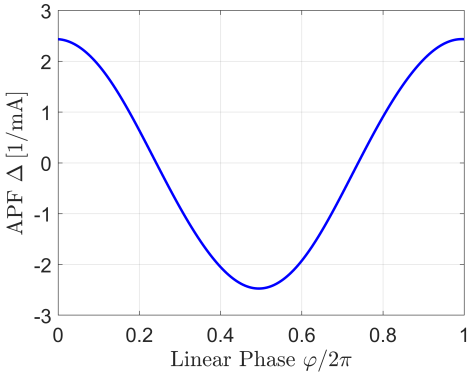

(d) Amplitude perturbation function.

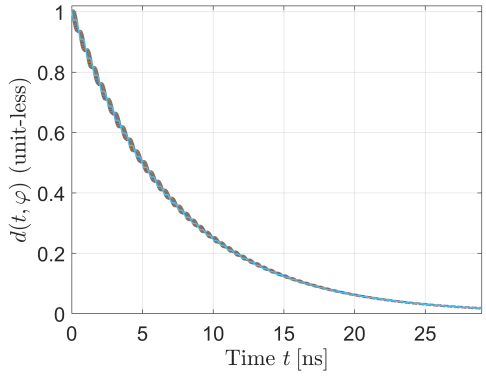

(e) Characteristic decay function. Each curve corresponds to a different phase φ.

Figure 5.13: Other properties of the NMOS-only differential LC oscillator.

The lock characteristic and the oscillation amplitude as a function of the injection frequency for an injection amplitude of $I_{\text{inj}} = 0.5$ mA are shown in Figure 5.14.

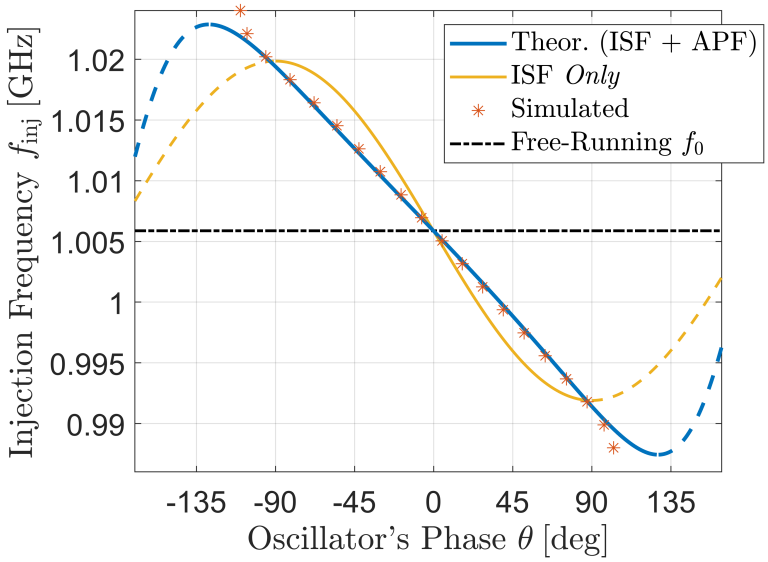

(a) Sinusoidal lock characteristic.

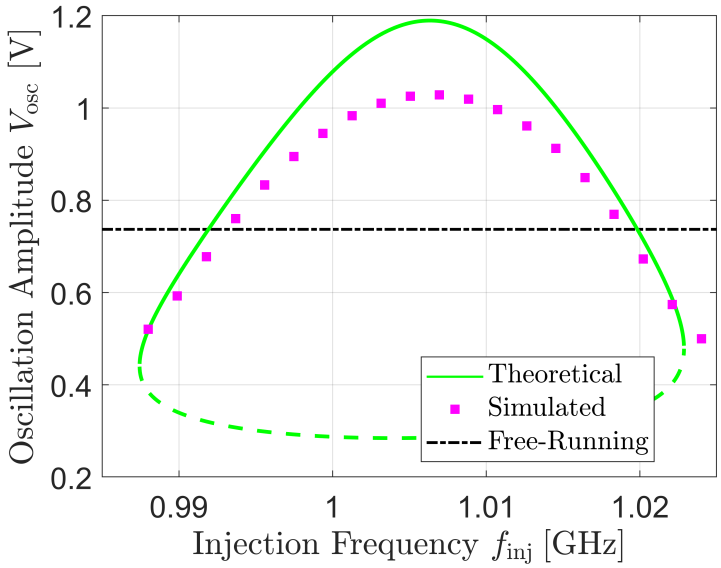

(b) Oscillation amplitude vs. injection frequency under lock.

Figure 5.14: Predicted and simulated behavior of a sinusoidally injection-locked NMOS-only differential LC oscillator with an injection amplitude of $I_{\text{inj}} = 0.5$ mA.

Figure 5.15 shows the same plots for $I_{\text{inj}} = 0.75$ mA. Because of the larger APF compared to the CMOS oscillator, the overestimation of the lock range occurs for lower injection strengths.

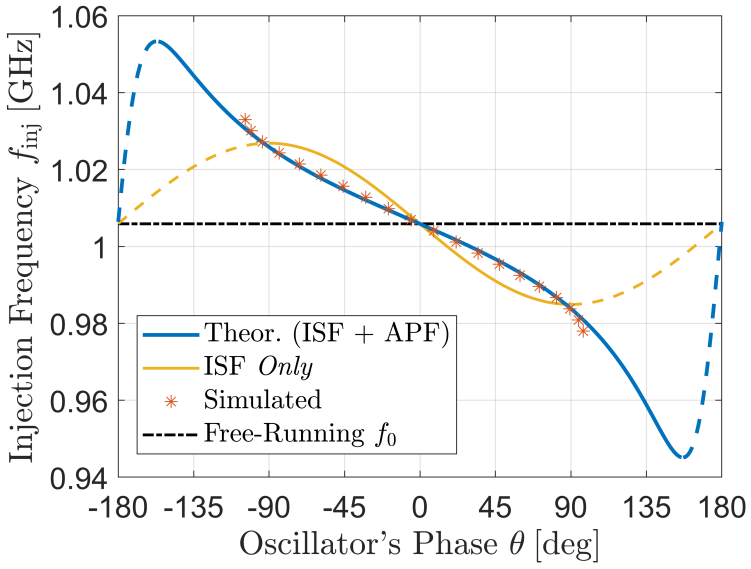

(a) Sinusoidal lock characteristic.

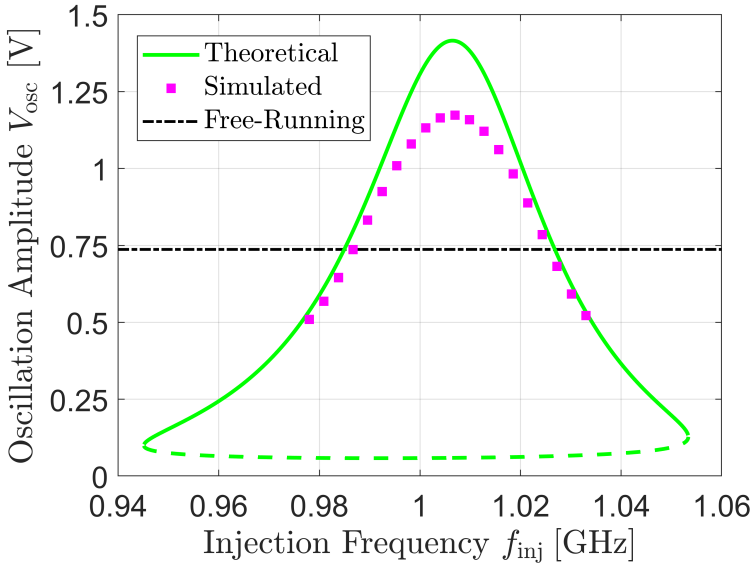

(b) Oscillation amplitude vs. injection frequency under lock.

Figure 5.15: Predicted and simulated behavior of a sinusoidally injection-locked NMOS-only differential LC oscillator with an injection amplitude of $I_{\text{inj}} = 0.75$ mA.

Figures 5.16 and 5.17 show the same plots for $I_{\text{inj}} = 1$ mA and $I_{\text{inj}} = 2$ mA, respectively. Because $2/|\Delta_1| = 0.81$ mA, the range of values for the phase θ was confined for both of these injection amplitudes.

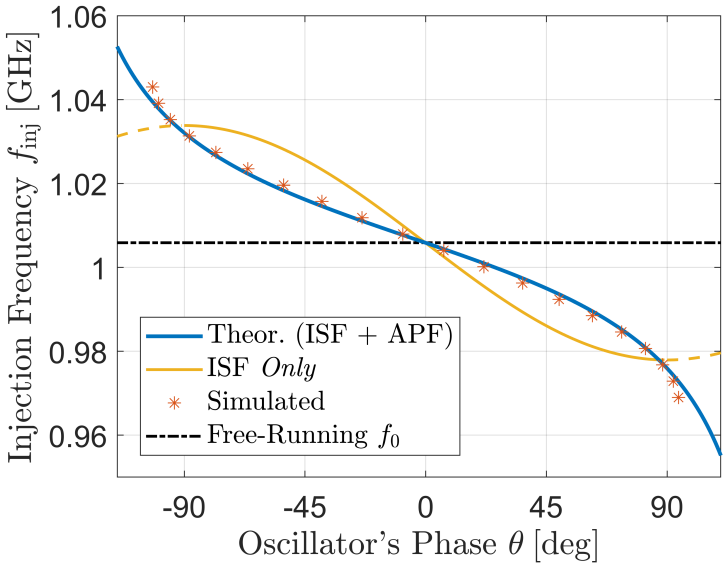

(a) Sinusoidal lock characteristic.

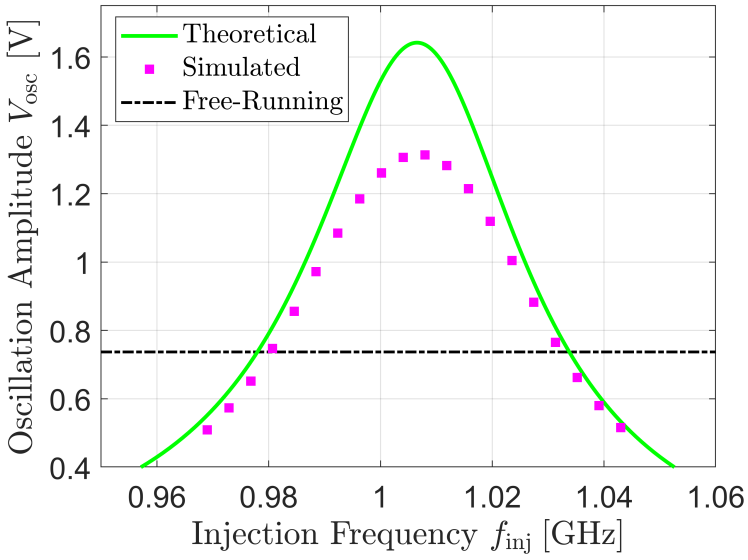

(b) Oscillation amplitude vs. injection frequency under lock.

Figure 5.16: Predicted and simulated behavior of a sinusoidally injection-locked NMOS-only differential LC oscillator with an injection amplitude of $I_{\text{inj}} = 1$ mA.

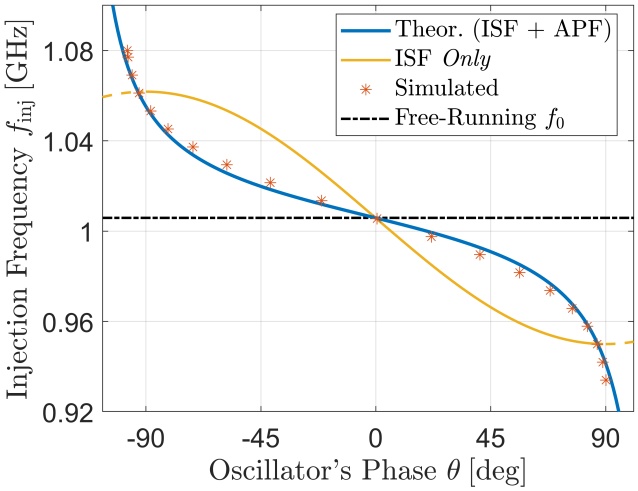

(a) Sinusoidal lock characteristic.

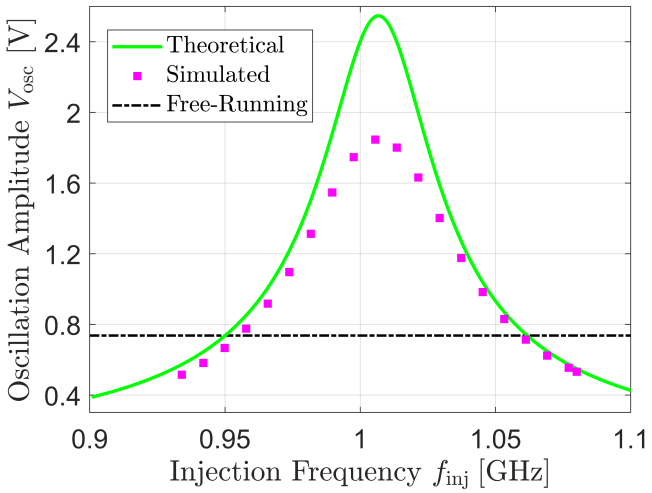

(b) Oscillation amplitude vs. injection frequency under lock.

Figure 5.17: Predicted and simulated behavior of a sinusoidally injection-locked NMOS-only differential LC oscillator with an injection amplitude of $I_{inj} = 2$ mA.

One may wonder how the lock ranges of the NMOS-only and the CMOS differential LC oscillator compare for the same tank Q, free-running swing q_{max}, and injection amplitude I_{inj}. There are two competing factors at play here. While the slower decay and larger APF of the former translate into a bigger $\tilde{\Gamma}_{eff}$ (for certain θ values) and correspondingly wider lock range, one must also be mindful of the limitation imposed by the inability to oscillate at very small amplitudes. Since the latter only becomes an issue for rather large injection strengths near I_{tail}, we conclude that for injections which are weak in comparison to the tail bias current, differential LC oscillators with only the NMOS cross-coupled pair boast a wider lock range.

Bipolar Colpitts Oscillator

The schematic, free-running oscillation voltage, and free-running inductor current of this oscillator are shown in Figure 5.18. The tank's parameters are $L = 6$ nH and $C = 8$ pF with a quality factor of $Q = 15$. The oscillation frequency is around $f_0 = 1$ GHz, and the oscillator is biased at $I_{\text{bias}} = 10$ mA.

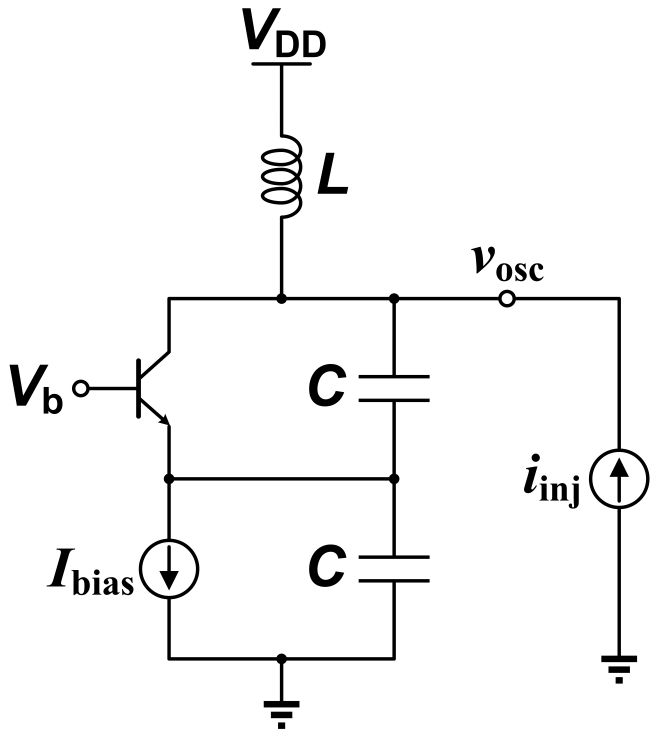

(a) Oscillator schematic. V_{b} is set with a resistive divider, and I_{bias} is implemented using a resistively biased current mirror.

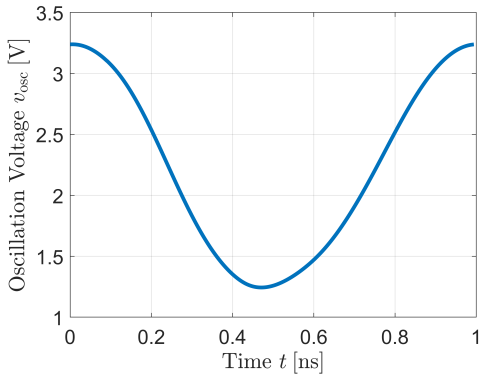

(b) Free-running oscillation voltage.

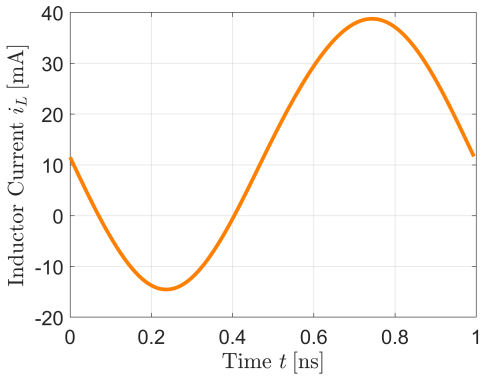

(c) Free-running inductor current.

Figure 5.18: Common-base bipolar Colpitts oscillator.

The free-running tank energy, sensitivity functions, and characteristic decay function are shown in Figure 5.19. Notice the rather unusual characteristic decay function:

the energy does not necessarily decay monotonically with time, and the decay dynamic can vary significantly based on when the injection was applied. While a *physical* analysis of how these traits affects the oscillator's behavior under injection might be difficult to perform, it is readily captured by the APF.

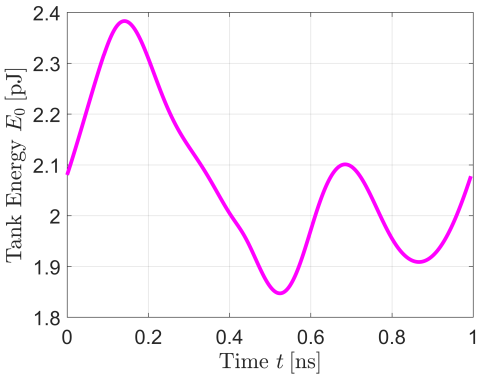

(a) Free-running tank energy.

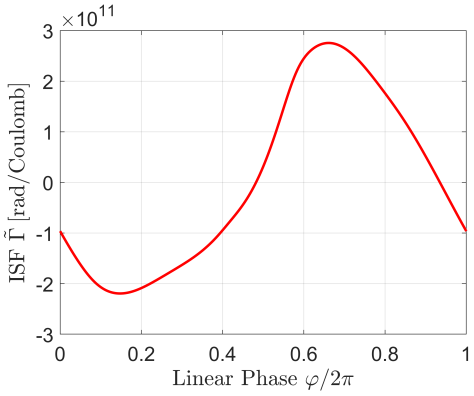

(b) Impulse sensitivity function.

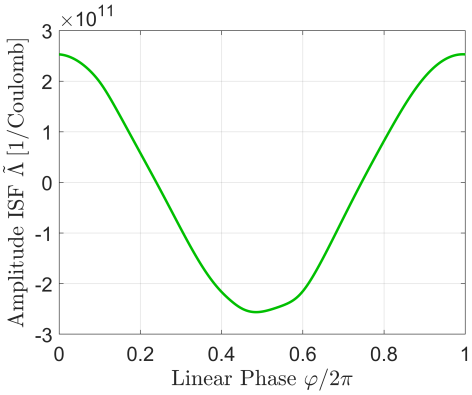

(c) Amplitude ISF.

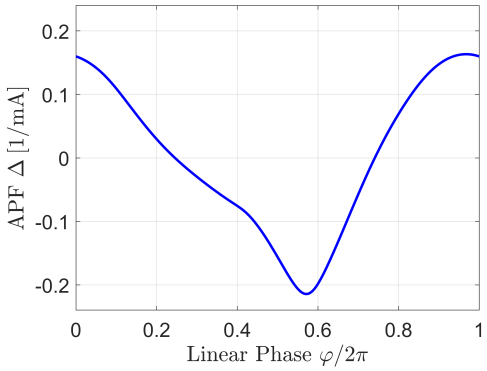

(d) Amplitude perturbation function.

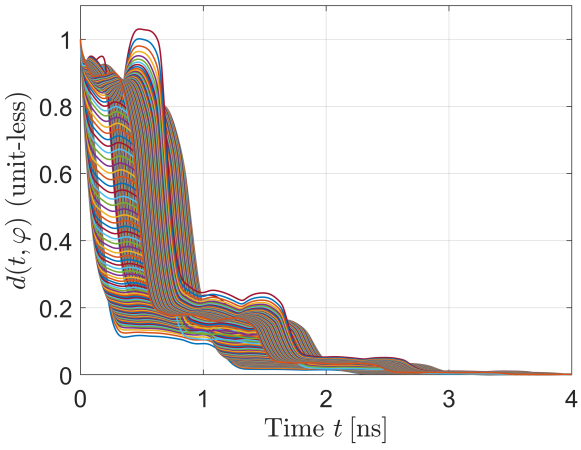

(e) Characteristic decay function. Each curve corresponds to a different phase φ.

Figure 5.19: Other properties of the common-base bipolar Colpitts oscillator.

The lock characteristic and the oscillation amplitude as a function of the injection frequency for an injection amplitude of $I_{\text{inj}} = 2.5$ mA are shown in Figure 5.20.

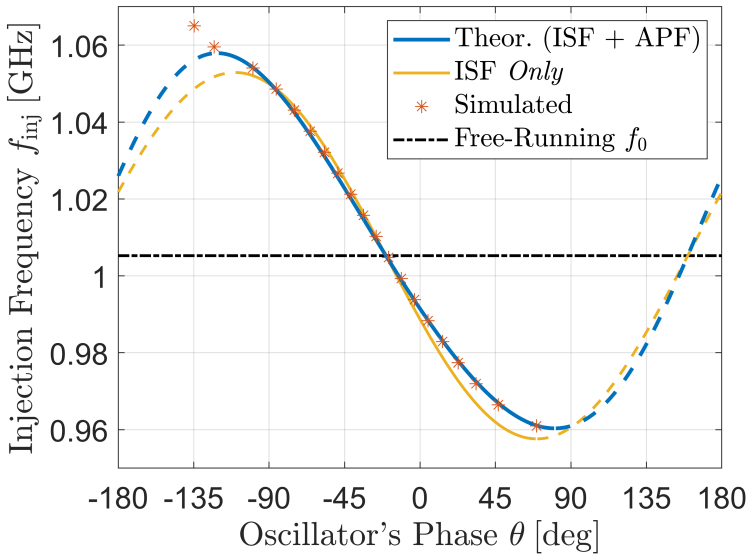

(a) Sinusoidal lock characteristic.

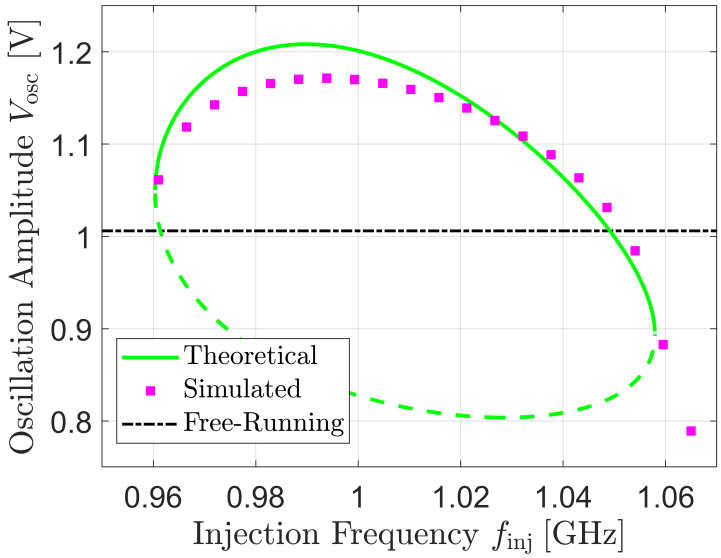

(b) Oscillation amplitude vs. injection frequency under lock.

Figure 5.20: Predicted and simulated behavior of a sinusoidally injection-locked Colpitts oscillator with an injection amplitude of $I_{\text{inj}} = 2.5$ mA.

Figure 5.21 shows the same plots for $I_{\text{inj}} = 5$ mA, whereas Figure 5.22 shows them for $I_{\text{inj}} = 10$ mA. The upper edge of the lock range is overestimated by our model at the latter injection strength, again due to energetic stability issues associated with smaller oscillation amplitudes.

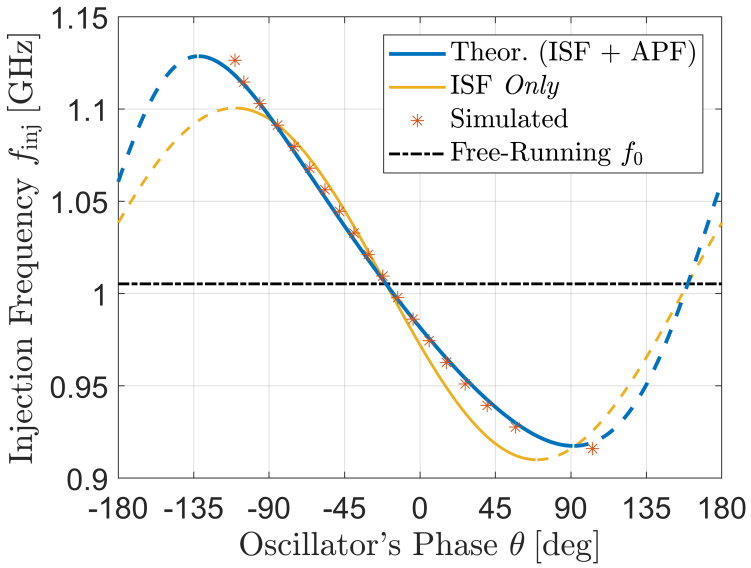

(a) Sinusoidal lock characteristic.

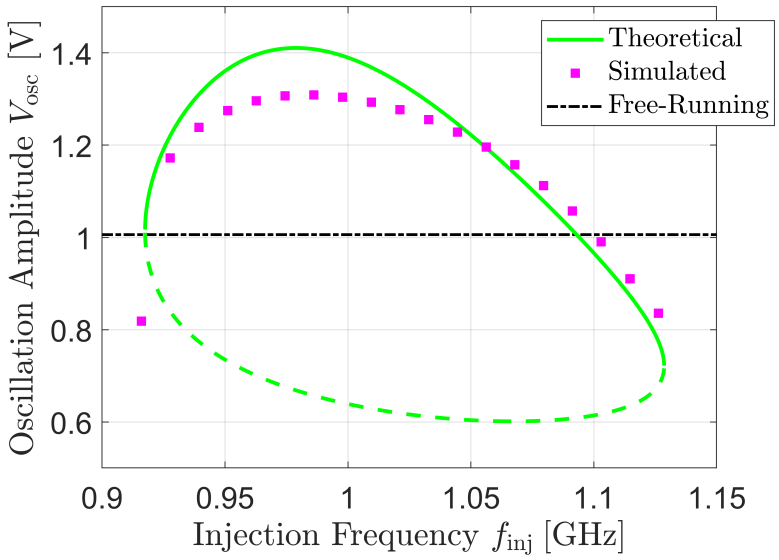

(b) Oscillation amplitude vs. injection frequency under lock.

Figure 5.21: Predicted and simulated behavior of a sinusoidally injection-locked Colpitts oscillator with an injection amplitude of $I_{\text{inj}} = 5$ mA.

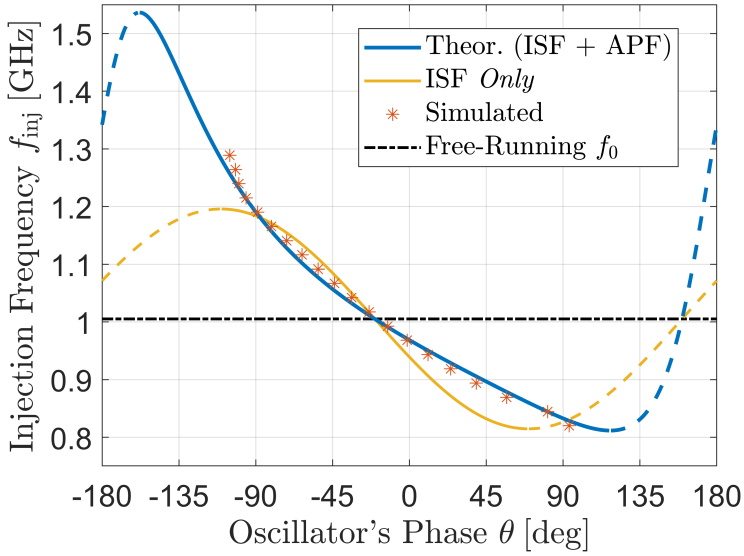

(a) Sinusoidal lock characteristic.

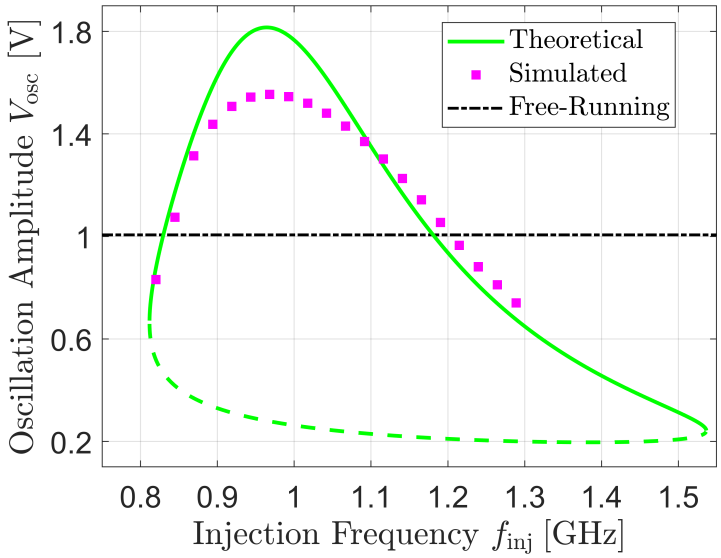

(b) Oscillation amplitude vs. injection frequency under lock.

Figure 5.22: Predicted and simulated behavior of a sinusoidally injection-locked Colpitts oscillator with an injection amplitude of $I_{\text{inj}} = 10$ mA.

Notice how the Colpitts oscillator exhibits the starkest asymmetry in its lock range, since its ISF and APF are the least in quadrature ($\beta \equiv \angle\tilde{\Gamma}_1 - \angle\Delta_1 = 113°$). This asymmetry is uniquely captured by our model, since Adler's equation [47] neglects amplitude modulation, and as we will show in Section 5.7, Mirzaei's analysis [21] implicitly assumes the ISF and APF are exactly 90° out-of-phase.

5.6 Experimental Results

We now present lock range measurements as a function of the injection amplitude for the same types of LC oscillators considered in the previous section: cross-coupled CMOS and NMOS-only differential LC oscillators, as well as a MOS common-gate Colpitts oscillator. Implemented in a 65-nm bulk CMOS process, the LC tanks were constructed using Metal-Insulator-Metal (MIM) capacitors and 50-μm-radius planar spiral symmetric inductors with 6 turns.

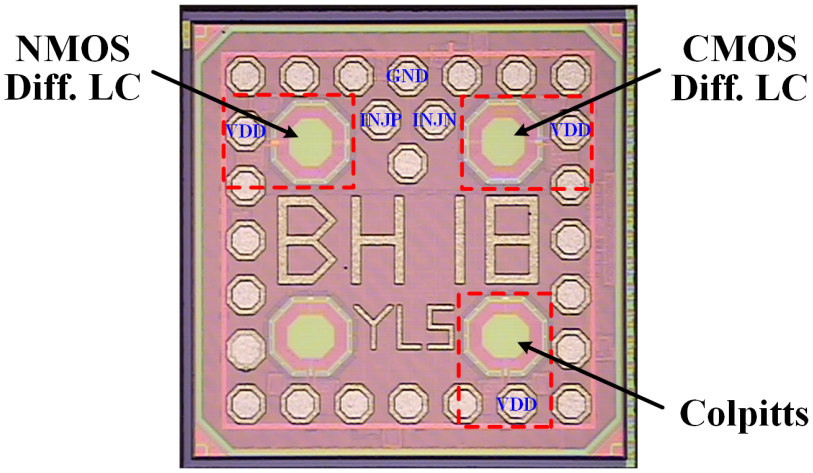

Figure 5.23: Die photo of the measured oscillators. The supply ('VDD') pads for each oscillator as well as the ground ('GND') and injection ('INJP','INJN') pads are labeled.

The details of the measurement setup can be found in Appendix A. Figure 5.23 shows a die micrograph of the fabricated chip, where the locations of the measured LC oscillators are indicated.[4]

For each oscillator, we also show the ISF and APF, which were obtained through simulation of the extracted oscillator. As discussed in Section 5.3, to calculate the tank energy for determining the APF, we used the lumped-element networks shown in Figure 5.24 to model the on-chip inductor. Specifically, the CMOS differential and Colpitts oscillators utilized Figure 5.24a, whereas the center-tapped version of Figure 5.24b was used in the NMOS-only differential oscillator. Note that mutual inductance played a significant role in the center-tapped inductor; however, the total differential inductance is simply $(1 + k)L_s$.

[4]The lower-left inductor corresponds to a bipolar Colpitts oscillator which did not oscillate. The BJTs in this process are not well-modeled and have extremely low gains.

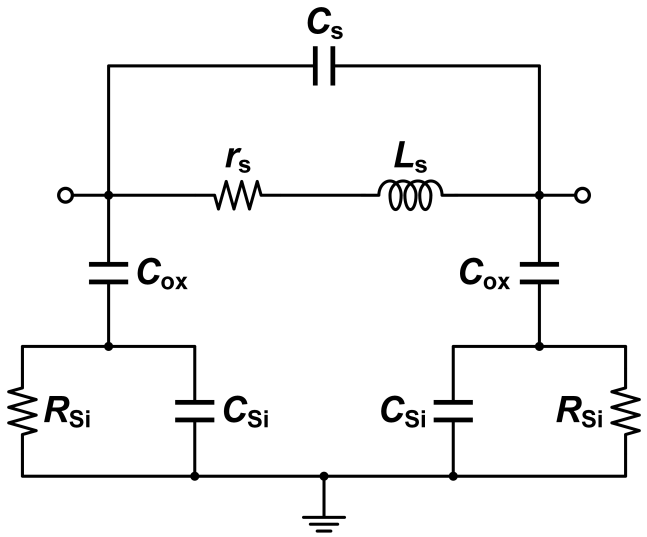

(a) Two-terminal inductor (with substrate grounded).

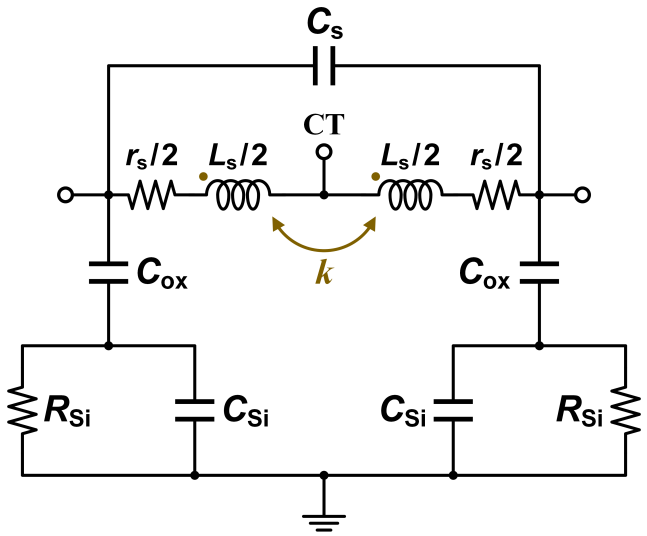

(b) Center-tapped inductor (with substrate grounded).

Figure 5.24: Lumped-element model for an on-chip symmetric spiral inductor [97]–[99]. C_s and r_s are the series capacitance and resistance, C_{ox} is the capacitance across the oxide, and C_{Si}, and R_{Si} are the capacitance and resistance of the silicon substrate.

The component values in the lumped-element model were chosen through a combination of: (1) matching the limiting behavior of the network at DC and at very high frequencies to the S-parameters provided by the design kit, and (2) using numerical optimization to directly minimize the element-wise error between the scattering matrices. For each oscillator, replacing the kit inductor with its lumped-element model incurred a less than 5% change in the oscillation frequency, voltage swing, power dissipation, and the ISF (at all simulated phases).

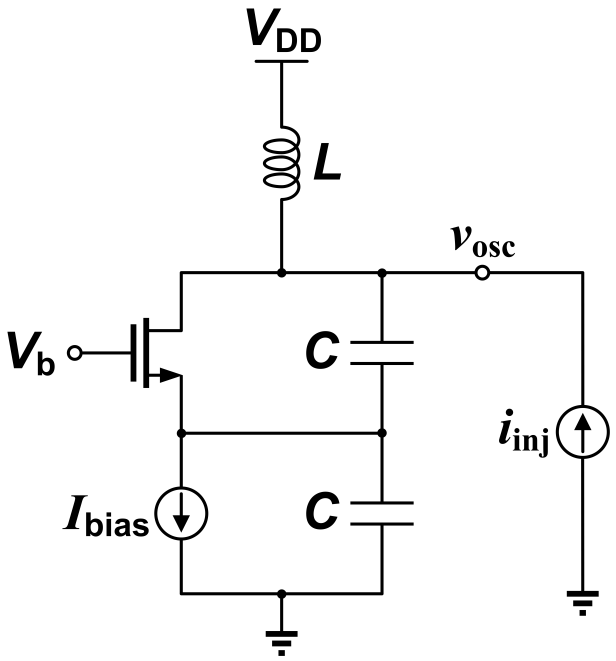

Figure 5.25: Schematic of the common-gate MOS Colpitts oscillator. A resistively biased current mirror and a resistive divider generate I_{bias} and V_b, respectively.

Table 5.1: Characteristics of the Measured LC Oscillators

Parameter	CMOS Differential	NMOS-Only Differential	MOS Colpitts
Schematic	Figure 5.6a	Figure 5.12a	Figure 5.25
Tank Capacitance C [pF]	2.75	2.75	5.5
Tank Inductance L [nH]	7.37	6.91	7.36
Inductor Q	8.07	7.83	8.04
Current Consumed [mA]	3.1	7.6	9.2
Supply V_{DD} [V]	1.5	1.5	2
Voltage Swing $V_{osc,0}$ [V]	1.0	0.48	1.3
ISF Fundamental Harmonic $\tilde{\Gamma}_1$ [rad/nC]	369 $\angle$92.3°	759 $\angle$91.5°	243 $\angle$107.4°
APF Fundamental Harmonic Δ_1 [1/mA]	0.515 $\angle$1.5°	3.17 $\angle$8.3°	0.47 $\angle$3°
Measured Oscillation Frequency f_0 [GHz]	1.0917	1.099	1.0923

Table 5.1 summarizes the design parameters of the LC oscillators. The only measured parameter is the oscillation frequency; everything else was obtained from extracted simulation or listed directly in the design kit. Note that the current consumption does not include bias circuitry, and the tank capacitance C only pertains to the MIM capacitors and does not account for the parasitics of the active devices.

The predicted lock range was calculated from Eq. (5.23). For comparison purposes, our plots will also show the linear prediction of the lock range based on the ISF alone. To demonstrate the superiority of our model over the state-of-the-art, we will also include the theoretical lock range from the best previously available model for LC oscillators, which is the generalization of Adler's lock range for large injection currents. Given in Eq. (2.14), this expression was derived separately by Paciorek [49], Razavi [38], and Mirzaei [21]. The various approaches for modeling the lock range of an LC oscillator are summarized in Table 5.2.

Table 5.2: Various Models for the Lock Range of an LC Oscillator

Model	Formula	Diverges?
Ours	$\omega_L^{\pm} = \dfrac{\frac{1}{2} I_{\text{inj}} \left\lvert \tilde{\Gamma}_1 \right\rvert}{\frac{1}{2} I_{\text{inj}} \lvert \Delta_1 \rvert \cos\beta \pm \sqrt{1 - \left(\frac{1}{2} I_{\text{inj}} \lvert \Delta_1 \rvert \sin\beta \right)^2}}$	Diverges for $I_{\text{inj}} \geq \dfrac{2}{\lvert \Delta_1 \rvert}$
ISF Only	$\omega_L^{\pm} = \pm \frac{1}{2} I_{\text{inj}} \left\lvert \tilde{\Gamma}_1 \right\rvert$	No
Best Prior	$\omega_L^{\pm} = \pm \dfrac{\omega_0}{2Q} \dfrac{I_{\text{inj}}}{I_{\text{osc}}} \dfrac{1}{\sqrt{1 - \frac{{I_{\text{inj}}}^2}{{I_{\text{osc}}}^2}}}$	Diverges for $I_{\text{inj}} \geq I_{\text{osc}}$
Adler	$\omega_L^{\pm} = \pm \dfrac{\omega_0}{2Q} \dfrac{I_{\text{inj}}}{I_{\text{osc}}}$	No

Notice that utilization of the best prior model requires I_{osc}, the oscillator current. For the three LC oscillators under consideration, the topology-dependent relationship between I_{osc} and the current consumption is given in Table 5.3, assuming operation in the current-limited regime [89], [101].

In differential LC oscillators, the tail current is commutated into a square wave which is delivered to the tank, whose fundamental component gives rise to the $4/\pi$ factor [89]. However, since the differential amplitude of the square wave is $I_{\text{tail}}/2$ per cross-coupled pair, the NMOS-only oscillator only sees half of this current [21].

The analysis of the Colpitts oscillator is slightly more involved; a describing function analysis which approximates the current delivered by the transistor as consisting of short, tall pulses [102] results in the expression given in the table, where C_1 and C_2 are the top and bottom capacitors, respectively [88].

Also, because the layout can often de-Q the tank significantly, instead of using the inductor Q, we calculated an effective quality factor based on the simulated voltage swing of the extracted oscillator using the relationship $V_{\text{osc},0} = I_{\text{osc}} Q_{\text{eff}} \omega_0 L$.

Table 5.3: Oscillator Currents for Various LC Oscillators

CMOS Differential	NMOS-Only Differential	MOS Colpitts
$I_{\text{osc}} = \frac{4}{\pi} I_{\text{tail}}$	$I_{\text{osc}} = \frac{2}{\pi} I_{\text{tail}}$	$I_{\text{osc}} = 2I_{\text{bias}} \frac{C_2}{C_1 + C_2}$ $= I_{\text{bias}} \quad \text{for} \quad C_1 = C_2$

Table 5.4 lists the computed oscillator current I_{osc} and effective quality factor Q_{eff} of the measured LC oscillators. Again, the current consumption and voltage swing used in the calculations were obtained from post-layout simulation.

Table 5.4: Simulated I_{osc} and Q_{eff} of the Measured LC Oscillators

Parameter	CMOS Differential	NMOS-Only Differential	MOS Colpitts
I_{osc} [mA]	3.95	4.84	9.2
Q_{eff}	5.01	2.09	2.88

Figures 5.26, 5.27, and 5.28 present the measurement results. Again, error bars covering the entire range of the three measurements that were taken for each data point are also shown. Excellent agreement is observed between theory and experiment, indicating the usefulness of our model for practical LC oscillator design applications. In particular, the APF is shown to accurately capture the asymmetric deviation of the lock range from the linear ISF-only model—something which is not captured by the best prior model. As shown in Table 5.2, both our model and the best prior model diverge for sufficiently large injections due to the possibility of having a zero oscillation amplitude.

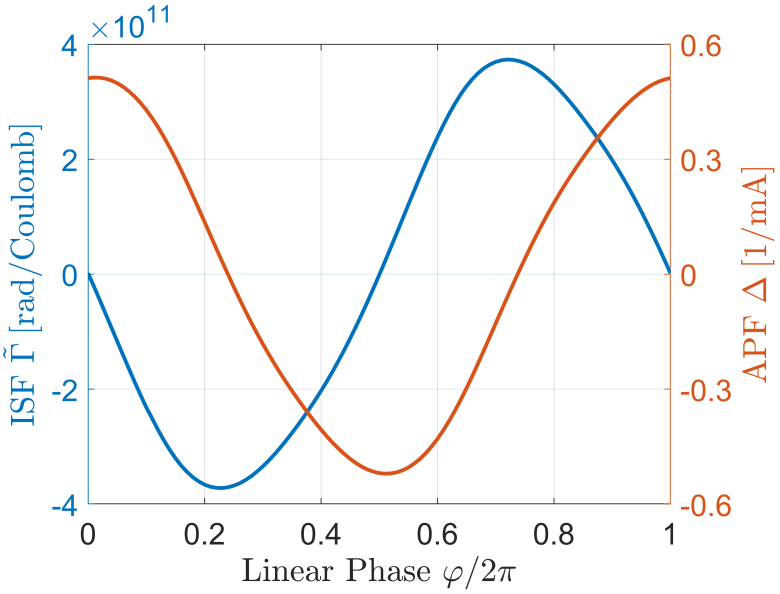

(a) Simulated ISF (left axis) and APF (right axis).

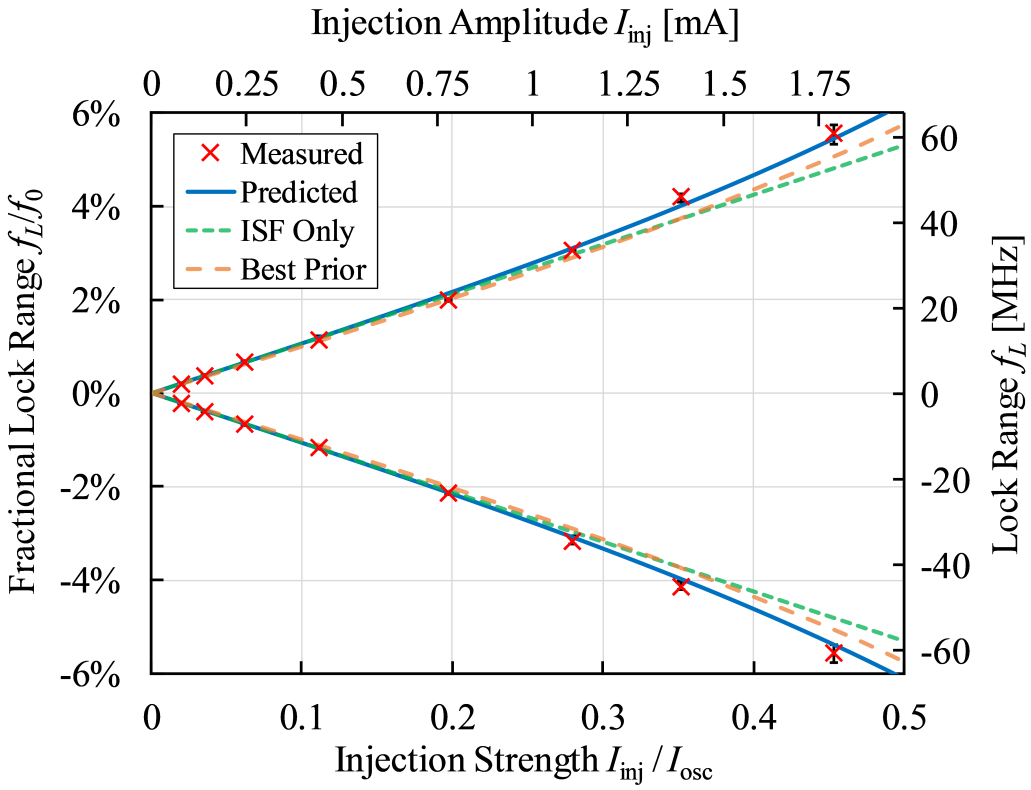

(b) Measured lock range.

Figure 5.26: Measurement results for the CMOS differential LC oscillator.

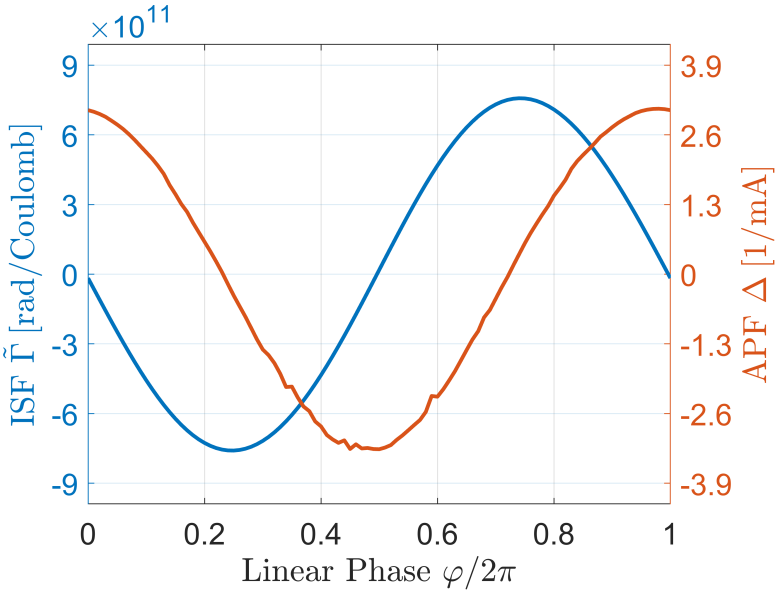

(a) Simulated ISF (left axis) and APF (right axis).

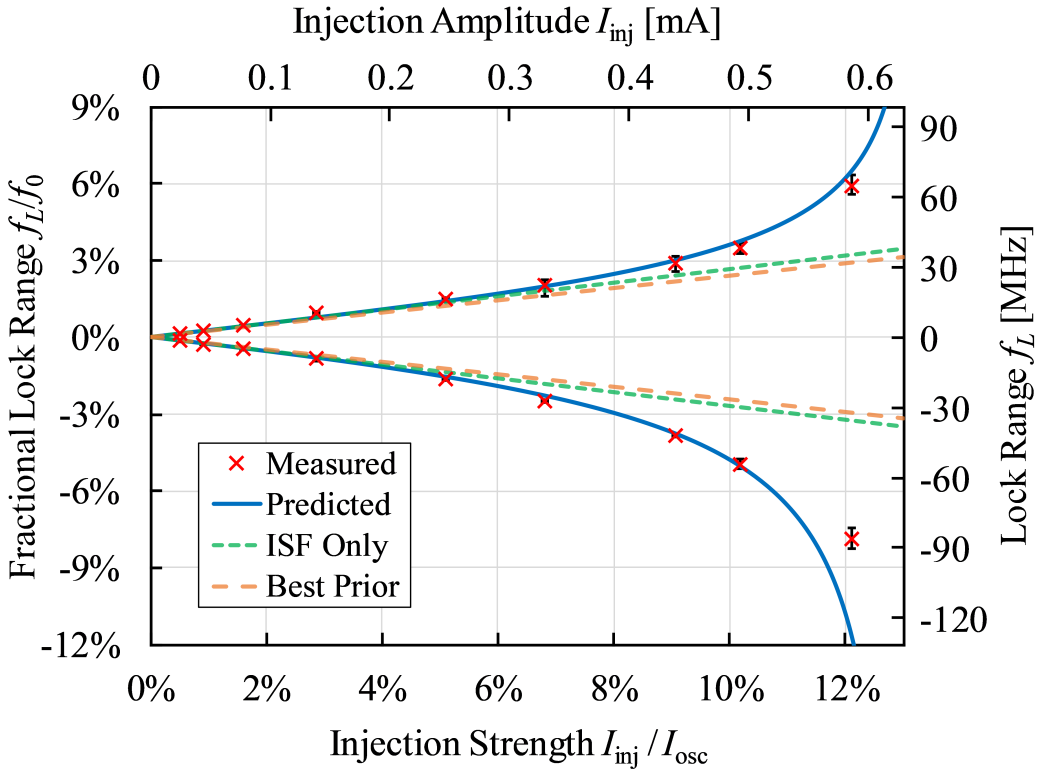

(b) Measured lock range.

Figure 5.27: Measurement results for the NMOS-only differential LC oscillator.

Notice how the NMOS-only differential LC and the Colpitts oscillators exhibit wider lower and upper lock ranges as the injection strength increases, respectively. This is because the phase difference β between the ISF and the APF for these two oscillators are 83.2° and 110.4°, which are below and above 90° respectively.

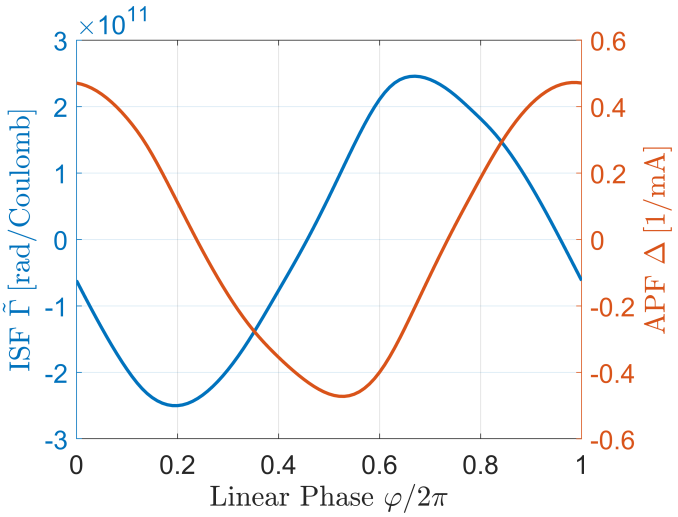

(a) Simulated ISF (left axis) and APF (right axis).

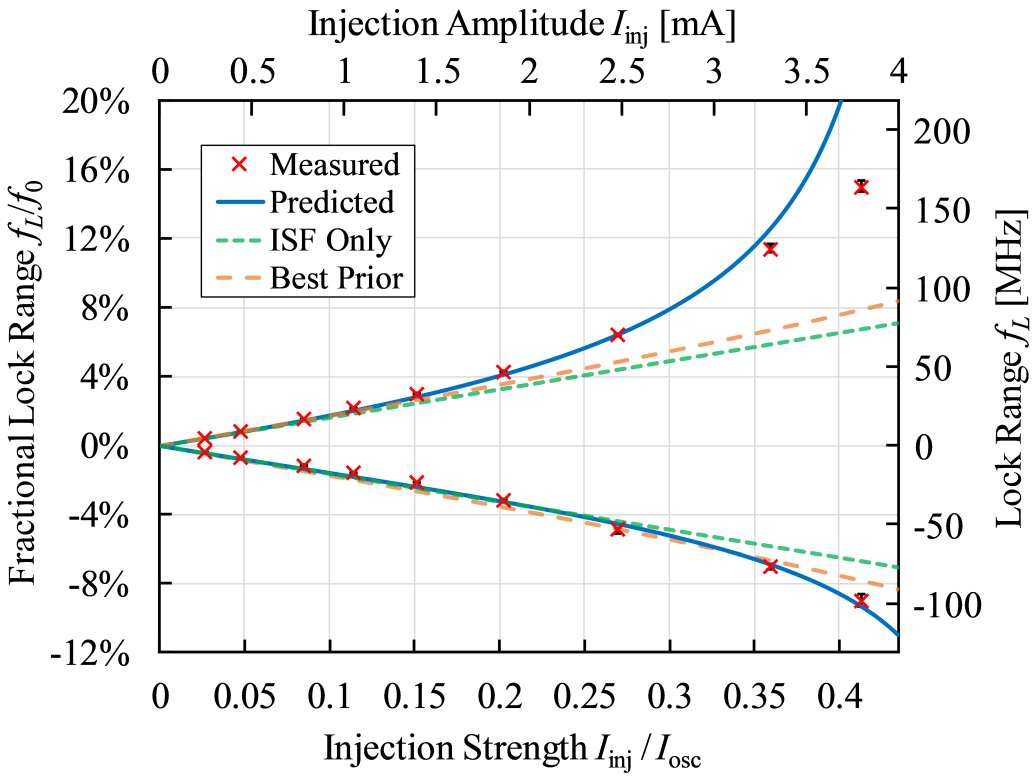

(b) Measured lock range.

Figure 5.28: Measurement results for the MOS Colpitts oscillator.

5.7 Reduction to Mirzaei's Generalized Adler's Equation

In this section, we show how our quasi-nonlinear model for LC oscillators, namely Eq. (5.17), reduces to the so-called "Generalized Adler's equation" by Mirzaei *et al.* [21]. Their work, which is based on a behavioral analysis (i.e., KVL/KCL) of current-limited LC oscillators under a large sinusoidal injection, results in the most accurate and general model currently found in the literature. Furthermore, it reduces to Adler's original equation [47] for small injection currents.

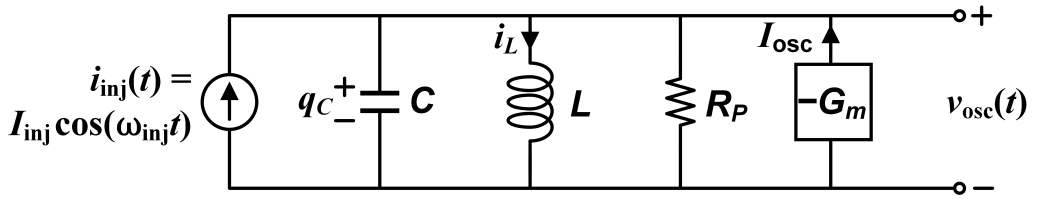

Figure 5.29: Behavioral model of an ideal, current-biased LC oscillator with a sinusoidal injection.

We start by computing the sensitivity functions of the ideal, current-biased LC oscillator depicted in Figure 5.29. In response to a periodic tank voltage, the $-G_m$-transconductor generates a periodic current whose fundamental component has an amplitude of I_{osc}. The other harmonics are irrelevant from the perspective of the oscillation voltage due to the tank's narrowband nature. Although these calculations were already performed in Section 3.3, we present simpler and more academically mature derivations here.

The ISF of an Ideal LC Oscillator

An ideal LC oscillator features a perfectly sinusoidal free-running output voltage. Without loss of generality, assume

$$v_0(\varphi) = V_{\text{osc},0} \sin \varphi. \tag{5.25}$$

The key insight for calculating the ISF is that the phase can be uniquely determined once the capacitor charge and inductor current are known. In the free-running case,

$$\begin{aligned} q_C(t) &= q_{\text{max},0} \sin(\omega_0 t) \\ i_L(t) &= -i_C(t) = -q_C'(t) = -\omega_0\, q_{\text{max},0} \cos(\omega_0 t), \end{aligned} \tag{5.26}$$

where $q_{\text{max},0} = CV_{\text{osc},0}$ is the free-running maximum charge swing across the capacitor. Thus, the free-running phase is

$$\varphi = \tan^{-1}\left(-\frac{\omega_0\, q_C}{i_L}\right) = \omega_0 t, \tag{5.27}$$

as expected. An injection of charge instantaneously changes q_C but leaves the inductor current invariant. The *change* in the oscillator's phase due to an injection q_{inj} applied at an initial phase $\varphi = \omega_0 t$ is therefore given by

$$\begin{aligned}\Delta\varphi &= \tan^{-1}\left(\frac{q_{\max,0}\sin\varphi + q_{\text{inj}}}{q_{\max,0}\cos\varphi}\right) - \tan^{-1}\left(\frac{q_{\max,0}\sin\varphi}{q_{\max,0}\cos\varphi}\right) \\ &= \tan^{-1}\left(\tan\varphi + \frac{q_{\text{inj}}}{q_{\max,0}\cos\varphi}\right) - \varphi.\end{aligned} \tag{5.28}$$

Taking a linear approximation with respect to q_{inj}, we obtain

$$\Delta\varphi = \left.\frac{\partial\Delta\varphi}{\partial q_{\text{inj}}}\right|_{q_{\text{inj}}=0} q_{\text{inj}} = \frac{1}{1+\tan^2\varphi}\cdot\frac{1}{q_{\max,0}\cos\varphi}\cdot q_{\text{inj}} = \frac{q_{\text{inj}}}{q_{\max,0}}\cos\varphi. \tag{5.29}$$

The derivative above is actually the ISF, which is defined as the phase shift normalized to the injected charge:

$$\tilde{\Gamma}(\varphi) \equiv \lim_{q_{\text{inj}}\to 0}\frac{\Delta\varphi}{q_{\text{inj}}} = \frac{1}{q_{\max,0}}\cos\varphi. \tag{5.30}$$

Note that we could also have computed the ISF using its state-space decomposition, Eq. (5.2), and the state variable expressions given in Eq. (5.26). Specifically,

$$\tilde{\Gamma}(\varphi) = \frac{q_C'(\varphi)}{q_C'(\varphi)^2 + LCi_L'(\varphi)^2} = \frac{1}{q_{\max,0}}\cos\varphi, \tag{5.31}$$

where we made use of the fact that the oscillator free-runs at the tank's resonant frequency: $\omega_0 = 1/\sqrt{LC}$.

One might have noticed that there are always two values of $\varphi \in [0, 2\pi)$ that result in the same value of $\tilde{\Gamma}(\varphi)$, since $\cos(2\pi - x) = \cos(x)$. That is, there are two different points in a cycle where the same injection results in the same phase shift. This can be understood intuitively by noting that the phase can be unambiguously determined by the time until the next peak or trough in the oscillation voltage. Physically, this is the amount of time needed for the inductor to fully de-energize or "de-flux." An abrupt injection of charge changes this time by altering the voltage across the inductor, which controls the rate at which the inductor de-fluxes (since $v = L\cdot di/dt$). By way of physical analogy, notice that the amount of time saved by driving slightly faster is given by $\Delta t \approx (\Delta v/v)\cdot t_0$, which is the fractional change in the speed, $\Delta v/v$, multiplied by the original amount of time needed to complete the trip, t_0. Although the inductor does not de-flux at a constant rate, we can still roughly intuit that the phase shift induced by the injection is proportional to the fractional change in

$-di/dt$, which scales with $-q_{\text{inj}}/q_{\text{max},0}$, multiplied by the amount of current flowing through the inductor at the time of injection, $i_L(\varphi)$. Therefore, the phase ISF is oblivious to the amount of charge on the capacitor and depends only on how *fast* that charge is changing—which is equal to the current flowing through the inductor.

The Amplitude ISF of an Ideal LC Oscillator

To calculate the effect that an injection of charge has on the oscillation amplitude, observe that the energy stored in the tank is a unique determinant of the oscillation amplitude:

$$E = \frac{{q_{\text{max}}}^2}{2C}. \tag{5.32}$$

At any instant in time, however, the tank energy is also equal to

$$E = \frac{{q_C}^2}{2C} + \frac{1}{2}L{i_L}^2, \tag{5.33}$$

and so the maximum charge swing can be expressed as

$$q_{\text{max}} = \sqrt{{q_c}^2 + (i_L/\omega_0)^2}. \tag{5.34}$$

Therefore, the oscillation amplitude after an injection of charge q_{inj} is applied at an initial phase φ is

$$\begin{aligned} q_{\text{max}} &= \sqrt{\left(q_{\text{max},0}\sin\varphi + q_{\text{inj}}\right)^2 + \left(q_{\text{max},0}\cos\varphi\right)^2} \\ &= \sqrt{{q_{\text{max},0}}^2 + 2q_{\text{inj}}q_{\text{max},0}\sin\varphi + {q_{\text{inj}}}^2}. \end{aligned} \tag{5.35}$$

Taking a linear approximation with respect to q_{inj}, we get

$$\begin{aligned} q_{\text{max}} &= q_{\text{max},0} + \left.\frac{\partial q_{\text{max}}}{\partial q_{\text{inj}}}\right|_{q_{\text{inj}}=0} q_{\text{inj}} \\ &= q_{\text{max},0} + q_{\text{inj}}\sin\varphi. \end{aligned} \tag{5.36}$$

The derivative above essentially gives the amplitude ISF, which is defined as the fractional change in the oscillation amplitude, normalized to the injected charge:

$$\tilde{\Lambda}(\varphi) \equiv \lim_{q_{\text{inj}}\to 0} \frac{1}{q_{\text{inj}}}\frac{\Delta q_{\text{max}}}{q_{\text{max},0}} = \frac{1}{q_{\text{max},0}}\sin\varphi. \tag{5.37}$$

Although this derivation is perfectly sound, it is more insightful—and much simpler—to note that the work done by an infinitesimal injection of charge dq_{inj} on the oscillator is given by

$$dE = v_C(\varphi)\,dq_{\text{inj}} = \frac{q_C(\varphi)}{C}dq_{\text{inj}} = \frac{q_{\text{max},0}\sin\varphi}{C}dq_{\text{inj}}. \tag{5.38}$$

By definition,

$$\tilde{\Lambda}(\varphi) \equiv \frac{1}{q_{\max}} \frac{\partial q_{\max}}{\partial q_{\text{inj}}}\bigg|_{q_{\text{inj}}=0}. \tag{5.39}$$

Applying the chain rule and using Eq. (5.32), we calculate

$$\begin{aligned}\tilde{\Lambda}(\varphi) &= \frac{1}{q_{\max}} \frac{\partial q_{\max}}{\partial E} \frac{\partial E}{\partial q_{\text{inj}}}\bigg|_{q_{\text{inj}}=0} \\ &= \frac{1}{q_{\max,0}} \cdot \frac{C}{q_{\max,0}} \cdot \frac{q_{\max,0} \sin\varphi}{C} \\ &= \frac{1}{q_{\max,0}} \sin\varphi.\end{aligned} \tag{5.40}$$

Again, observe how there are always two values of $\varphi \in [0, 2\pi)$ that result in the same value of $\tilde{\Lambda}(\varphi)$, since $\sin(\pi - x) = \sin(x)$. That is, there are two different points in a cycle where the same injection results in the same amplitude change. This is easy to understand. As mentioned above, the oscillation amplitude is tied unambiguously to the amount of energy stored in the tank. But, the amount by which the tank's energy changes due to the injection depends only on the electric potential across which the charge was injected. Therefore, the amplitude ISF is impervious to the inductor current and depends only on the capacitor voltage.

We summarize our results, including what the expressions would be if we had adopted a cosine reference for v_0, in Table 5.5. Again, we reiterate the fact that for

Table 5.5: The Impulse Sensitivity Functions (ISFs) of an Ideal LC Oscillator

Phase Convention	Phase ISF	Amplitude ISF
$v_0(\varphi) = V_{\text{osc},0} \sin\varphi$	$\tilde{\Gamma}(\varphi) = \frac{1}{q_{\max,0}} \cos\varphi$	$\tilde{\Lambda}(\varphi) = \frac{1}{q_{\max,0}} \sin\varphi$
$v_0(\varphi) = V_{\text{osc},0} \cos\varphi$	$\tilde{\Gamma}(\varphi) = -\frac{1}{q_{\max,0}} \sin\varphi$	$\tilde{\Lambda}(\varphi) = \frac{1}{q_{\max,0}} \cos\varphi$

an LC oscillator, the phase ISF depends only on the slope of the voltage waveform and not on its polarity, whereas the amplitude ISF depends only on the value of the voltage waveform and not on the direction of the inductor current.

The APF of an Ideal LC Oscillator

Finally, let us analyze how excess energy in the oscillator decays. Since the transconductor only acquiesces the current consumed by the parallel resistance R_P up to the

free-running oscillation amplitude, we can assume that any excess energy simply decays in accordance with the LTI dynamics of a damped LC resonator. In other words, the characteristic decay function is

$$d(t, \varphi) = e^{-t/\tau_0}, \tag{5.41}$$

where $\tau_0 = 2Q/\omega_0$ is the characteristic time constant and $Q = R_P/\omega_0 L = R_p \omega_0 C$ is the tank's quality factor. Since $\int_0^\infty d(t, \varphi)\, dt = \tau_0$, this leads to an Amplitude Perturbation Function (APF) equal to

$$\boxed{\Delta(\varphi) = \tau_0 \cdot \tilde{\Lambda}(\varphi).} \tag{5.42}$$

Generalized Adler's Equation

Now, we can put everything together. As detailed in Section 6.8, we will use the same phase reference for (the fundamental components of) the free-running oscillation voltage $v_0(\varphi)$ and the injection current $i_{\text{inj}}(t)$. With this in mind, one can easily verify that

$$\frac{1}{T_{\text{inj}}} \int_{T_{\text{inj}}} \tilde{\Gamma}\big(\omega_{\text{inj}} t + \theta\big)\, i_{\text{inj}}(t)\, dt = -\frac{1}{2} \frac{I_{\text{inj}}}{q_{\text{max},0}} \sin\theta \tag{5.43}$$

and

$$\frac{1}{T_{\text{inj}}} \int_{T_{\text{inj}}} \Delta\big(\omega_{\text{inj}} t + \theta\big)\, i_{\text{inj}}(t)\, dt = \frac{1}{2} \tau_0 \frac{I_{\text{inj}}}{q_{\text{max},0}} \cos\theta. \tag{5.44}$$

Substituting these expressions into Eq. (5.17), we obtain the pulling equation for ideal LC oscillators:

$$\frac{d\theta}{dt} = \omega_0 - \omega_{\text{inj}} - \frac{\dfrac{1}{2} \dfrac{I_{\text{inj}}}{q_{\text{max},0}} \sin\theta}{1 + \dfrac{1}{2} \tau_0 \dfrac{I_{\text{inj}}}{q_{\text{max},0}} \cos\theta}. \tag{5.45}$$

Recall that the peak current which flows within the LC tank is Q times larger than the oscillator current I_{osc} which flows through the loss resistance R_P. Therefore, we can see that $\omega_0\, q_{\text{max},0} = Q I_{\text{osc}}$. Using this relationship to eliminate the maximum charge swing $q_{\text{max},0}$, we can rewrite Eq. (5.45) as

$$\boxed{\frac{d\theta}{dt} = \omega_0 - \omega_{\text{inj}} - \frac{\omega_0}{2Q} \frac{I_{\text{inj}} \sin\theta}{I_{\text{osc}} + I_{\text{inj}} \cos\theta},} \tag{5.46}$$

which is Mirzaei's Generalized Adler's equation [21]. It is apparent that assuming the injection to be small ($I_{\text{inj}} \ll I_{\text{osc}}$) yields Adler's original equation [47].

5.8 The Injection Compliance for LC Oscillators

Recall from Section 4.8 that we defined the sinusoidal injection compliance as the ratio of the fractional lock range to the injection strength. As we can see from the measurement and analysis results of this chapter, the injection strength for LC oscillators is more appropriately obtained by normalizing the injection amplitude I_{inj} to the oscillator current $I_{\text{osc}} = I_{\max}/Q$. Physically, this is due to the current "recycling" capabilities of the LC tank. Consequently, we define the sinusoidal injection compliance for LC oscillators as

$$\boxed{\eta_{\text{LC}} \coloneqq \frac{2\omega_L/\omega_0}{I_{\text{inj}}/I_{\text{osc}}}.} \tag{5.47}$$

This definition reflects the fact that for the same power consumption, an LC oscillator with a higher tank Q will have a narrower lock range. In the small-injection regime (where amplitude modulation can be neglected), this can be simplified to

$$\boxed{\eta_{\text{LC}} = \frac{q_{\max,0}}{Q}\left|\tilde{\Gamma}_1\right|.} \tag{5.48}$$

Table 5.6 lists the sinusoidal injection compliances for the various LC oscillators we encountered in this chapter, calculated from Eq. (5.48). The parameters for the (simulated) LC oscillators in Section 5.5 were obtained from schematic-level simulation, whereas the parameters for the (measured) LC oscillators in Section 5.6 were obtained from extracted simulation. The ideal LC oscillator is technically a mathematical construct—one whose sensitivity functions conform exactly to that of a parallel LC tank and whose excess energy decays via a first-order dynamic.

5.9 Relation to the Thought Experiment from Chapter 3

In Chapter 3, we conducted a thought experiment that involved "locking" an ideal LC oscillator to an injection current which took on the form of an impulse train—essentially a periodic injection of discrete amounts of charge that instantaneously change the phase of oscillation. Specifically, for a maximum charge swing across the capacitor of $q_{\max}$ and amount of injected charge per impulse q_{inj}, we determined that the resultant frequency shift can be expressed as

$$\Delta\omega = \frac{\Delta\varphi}{T_{\text{inj}}} = -\frac{1}{T_{\text{inj}}}\frac{q_{\text{inj}}}{q_{\max}}\sin\theta, \tag{5.49}$$

where $\Delta\varphi$ is the phase shift caused by *each* injection and the phase θ characterized the time of injection during the oscillation cycle. More precisely, we needed to define

Table 5.6: Compliances of Various LC Oscillators

Topology	Version	Sinusoidal Injection Compliance η_{LC}
Ideal LC	Section 5.7	$\frac{1}{Q}$
CMOS Differential LC	Section 5.5	6.62%
	Section 5.6	21.2%
NMOS-Only Differential LC	Section 5.5	6.63%
	Section 5.6	53.3%
Bipolar Colpitts	Section 5.5	6.29%
MOS Colpitts	Section 5.6	32.5%

θ as the phase difference between the *fundamental components* of the oscillation voltage and the impulse train. This result should be straightforward to see in light of the ISF of an ideal LC oscillator, since $\tilde{\Gamma}(\theta) \equiv \Delta\varphi/q_{\text{inj}}$ by definition.

In our thought experiment, we somewhat arbitrarily decided to "convert" the *injected charge* q_{inj} to an *injection current* using the *fundamental amplitude* of the impulse train: $I_{\text{inj}} = 2q_{\text{inj}}/T_{\text{inj}}$. We also argued that the amplitude of the tank current at resonance, $\omega_0\, q_{\text{max}}$, is Q times as large as the oscillator current I_{osc} supplied by the active circuitry. This allowed us to arrive at the steady-state solution to Adler's equation:

$$\Delta\omega = -\frac{1}{T_{\text{inj}}}\frac{q_{\text{inj}}}{q_{\text{max}}}\sin\theta \qquad \Longrightarrow \qquad \Delta\omega = -\frac{\omega_0}{2Q}\frac{I_{\text{inj}}}{I_{\text{osc}}}\sin\theta. \tag{5.50}$$

We then generalized the experiment by accounting for how the impulses altered the amplitude of oscillation as well. By denoting the free-running maximum charge swing as $q_{\text{max},0}$ and assuming an exponential decay of the amplitude in between injections with a time constant of $\tau_0 = 2Q/\omega_0$, we calculated the time-averaged maximum charge swing:

$$\langle q_{\text{max}}\rangle = q_{\text{max},0} + \frac{\tau_0}{T_{\text{inj}}} q_{\text{inj}}\cos\theta. \tag{5.51}$$

Again, this expression makes sense in light of the amplitude ISF and APF of an ideal LC oscillator, since $\Delta(\theta) = \tau_0\cos\theta/q_{\text{max},0}$. Substituting $\langle q_{\text{max}}\rangle$ for q_{max} in Eq. (5.49) then yielded the steady-state solution to Mirzaei's Generalized Adler's

equation:

$$\Longrightarrow \Delta\omega = -\frac{\omega_0}{2Q}\frac{I_{\text{inj}}\sin\theta}{I_{\text{osc}} + I_{\text{inj}}\cos\theta}. \tag{5.52}$$

We are now in a position to rigorously explain why this procedure relating the impulse train to its fundamental component, which may have seemed somewhat contrived at first, led to meaningful results. Note that what our thought experiment actually shows is the following statement:

An ideal LC oscillator injection locked by an impulse train behaves in the same way as an ideal LC oscillator injection locked by a sinusoidal injection current equal to the fundamental component of the impulse train.

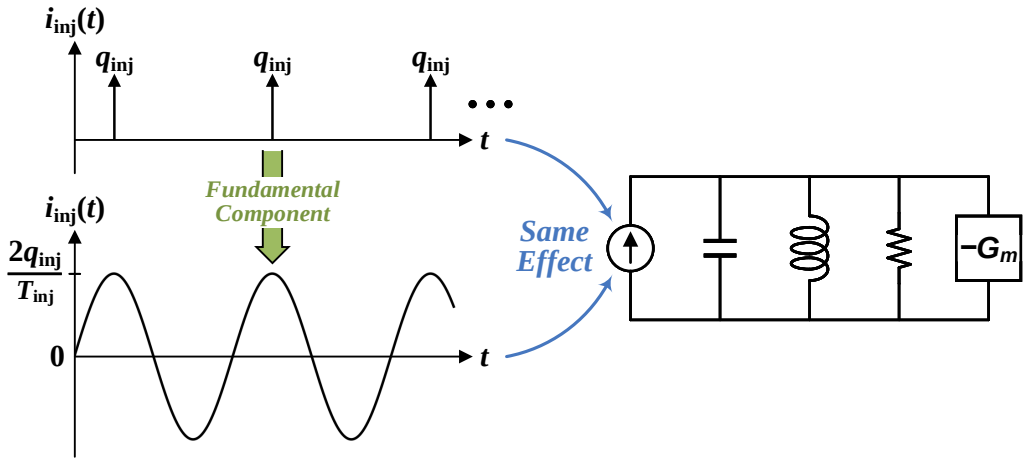

Figure 5.30: Equivalence between the thought experiment of Chapter 3 and the time-synchronous model of Chapters 4 and 5.

This equivalence, shown in Figure 5.30, is not surprising. After all, the ISF and the APF of an ideal LC oscillator are perfectly sinusoidal and therefore only contain the fundamental harmonic. As a result, only the fundamental component of the injection matters anyways, since the rest are *filtered out* by the averaging depicted in the block diagrams of Figures 4.4 and 5.5. Therefore, our model subsumes, justifies, and illuminates the fundamental physics behind our thought experiment.

Chapter 6

SUPERHARMONIC AND SUBHARMONIC INJECTION LOCKING AND PULLING

In this chapter, we generalize our framework to accommodate synchronization scenarios where the injection and oscillation frequencies are not equal to each other. Instead, we will see how the injection frequency can be a multiple N of the oscillation frequency, the oscillation frequency can be a multiple M of the injection frequency, and the most general case where ratio between the two is an arbitrary rational number. Injection-locked frequency dividers and frequency multipliers are often used as building blocks in frequency synthesizers.

6.1 Superharmonic Injection

It is well-known that oscillators are also capable of locking onto an injection at a harmonic of the oscillation frequency, giving rise to what is known as injection-locked frequency division [6], [8], [11]–[13]. This is readily captured by our model as well: Eq. (4.20) merely requires that $i_{\text{inj}}(t)$ be periodic with T_{inj}, and a function which has a period of T_{inj}/N for any positive integer N is also periodic with T_{inj}. In other words, our framework never required the *fundamental* period of $i_{\text{inj}}(t)$ to be equal to the interval being averaged over. However, for the purposes of analyzing *superharmonic* locking onto an injection current $i_{\text{inj}}(t)$ whose fundamental frequency ω_{inj} is "near" $N\omega_0$ for some positive integer N, it makes much more sense to define the oscillator's phase θ via

$$\varphi(t) \equiv \frac{\omega_{\text{inj}}}{N} t + \theta(t). \tag{6.1}$$

Then, the phase pulling equation can be rewritten as

$$\frac{d\theta}{dt} = \omega_0 - \frac{\omega_{\text{inj}}}{N} + \frac{1}{NT_{\text{inj}}} \int_{NT_{\text{inj}}} \tilde{\Gamma}\left(\frac{\omega_{\text{inj}}}{N} t + \theta\right) i_{\text{inj}}(t)\, dt, \tag{6.2}$$

and so the lock characteristic $\Omega(\theta)$ is now redefined as the steady-state solution for the frequency deviation $\Delta\omega := \omega_{\text{inj}}/N$. It is instructive to look at the "frequency domain" expansion of this lock characteristic:

$$\begin{aligned} \Delta\omega &:= \frac{\omega_{\text{inj}}}{N} - \omega_0 \\ &= \frac{1}{2}\left[\frac{I_{\text{inj},0}\tilde{\Gamma}_0}{2} + \sum_{n=1}^{\infty} \left|I_{\text{inj},n}\tilde{\Gamma}_{nN}\right| \cos\left(nN\theta + \angle\tilde{\Gamma}_{nN} - \angle I_{\text{inj},n}\right)\right]. \end{aligned} \tag{6.3}$$

Carefully note that the lock characteristic is now periodic with a period of $2\pi/N$. The key insight to be had here is that the only harmonics of the ISF which matter here are those that are multiples of N. In particular, a sinusoidal injection current must "utilize" the N^{th} harmonic of the ISF to lock the oscillator. This explains why, for example, the injection current is usually applied at the tail node of LC oscillators implemented as divide-by-2 circuits.

6.2 Simulation Results

Here, we compare a few examples of the simulated superharmonic lock characteristic against the theoretical one predicted by Eq. (6.3). All injections are sinusoidal.

Differential LC Oscillator – Tail Injection: The first example is an injection at the 2^{nd} harmonic into the tail node of a 1 GHz CMOS differential LC oscillator. Note that this is the same oscillator from Figure 5.6 (with a different injection site). The schematic, free-running positive and negative oscillation voltages, voltage at the tail node, and ISF are shown in Figure 6.1.

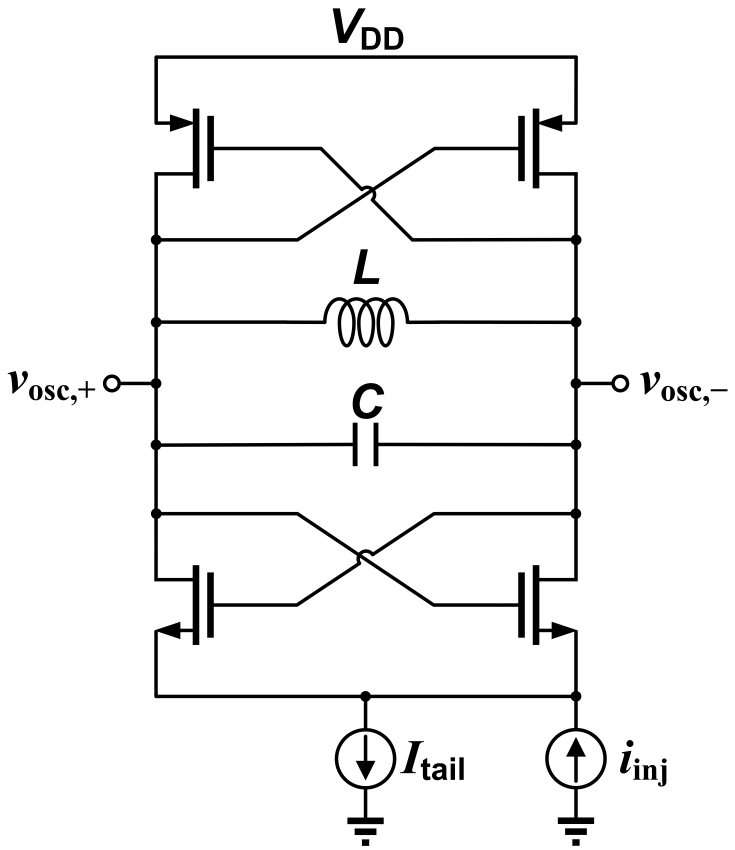

(a) Oscillator schematic.

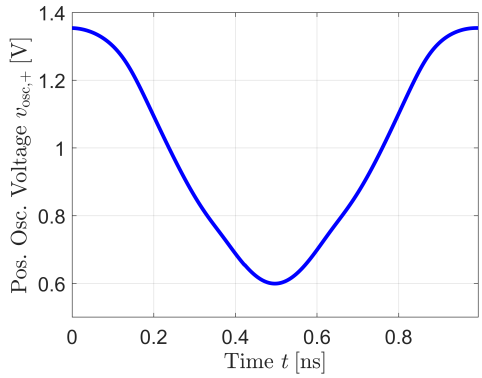

(b) Free-running positive osc. voltage.

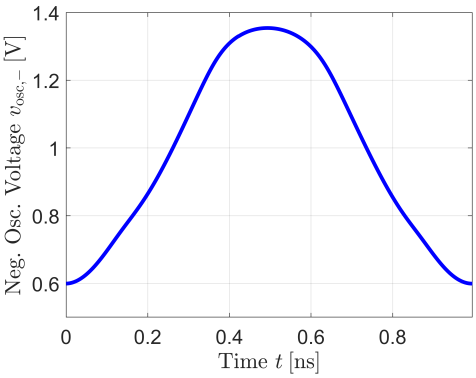

(c) Free-running negative osc. voltage.

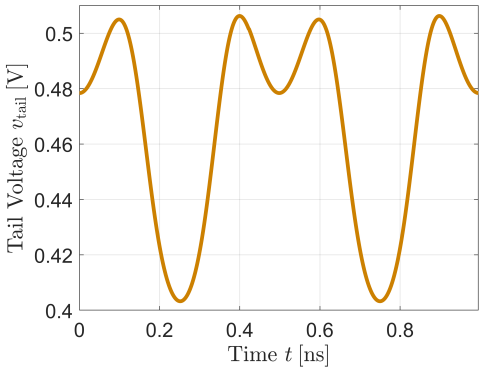

(d) Free-running tail voltage.

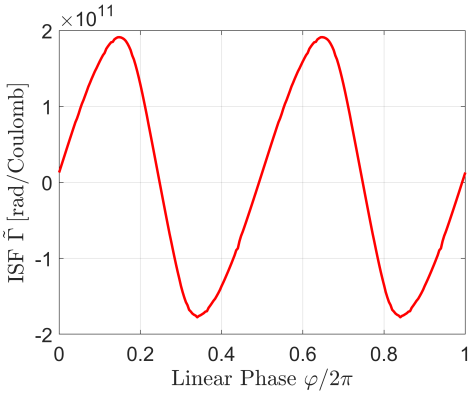

(e) Impulse sensitivity function.

Figure 6.1: Injection into the tail node of a CMOS differential LC oscillator.

Notice how the tail voltage and the ISF both iterate through two cycles over the course of a single oscillation period, indicating that $\tilde{\Gamma}(x)$ actually has a fundamental period of π as opposed to 2π. Therefore, this ISF contains no odd harmonics. Physically, this is a consequence of the fact that the tail node cannot distinguish between the two arms of the oscillator due to symmetry. As we can see, the tail voltage v_{tail} rises with both the positive and negative single-ended oscillation voltages. As a result, the sensitivity at the tail is the same regardless of whether the differential oscillation voltage across the capacitor, $v_{\text{osc}} \equiv v_{\text{osc},+} - v_{\text{osc},-}$, is increasing or decreasing.

The sinusoidal lock characteristics for two different injection strengths are shown in Figure 6.2.

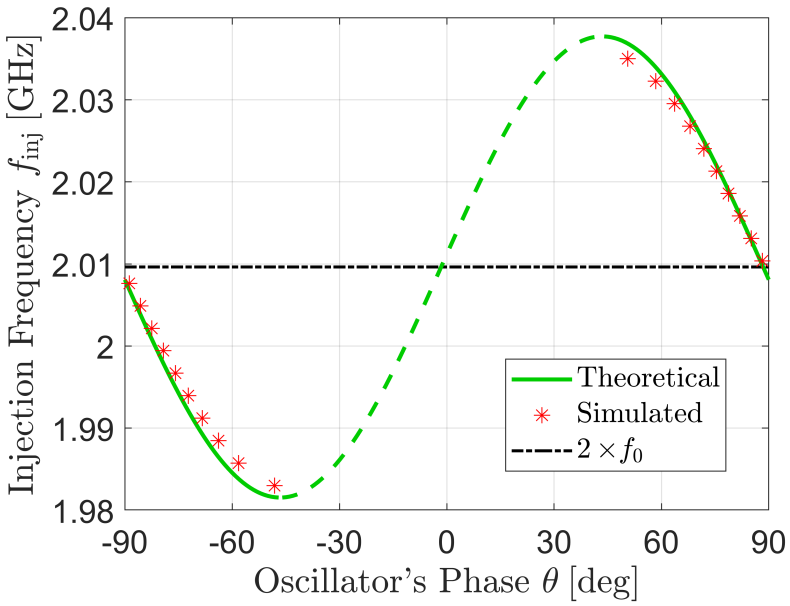

(a) I_{inj} = 1 mA

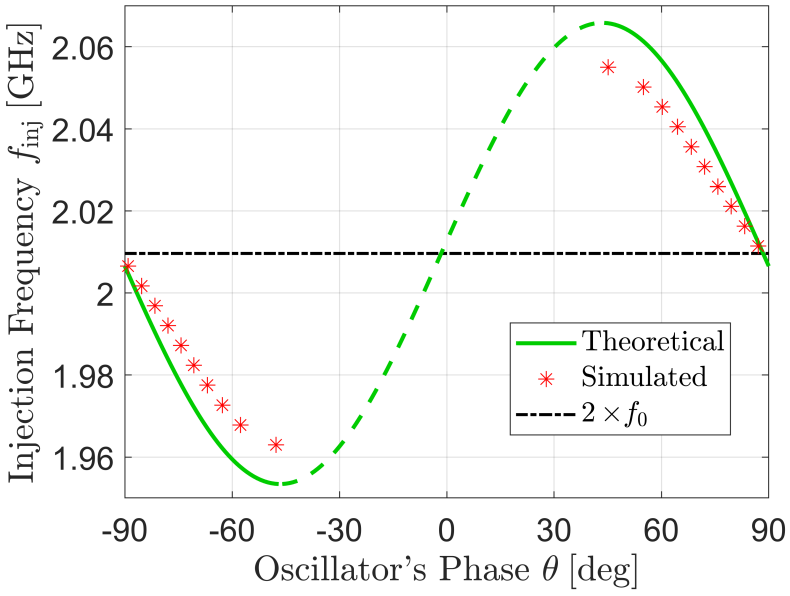

(b) I_{inj} = 2 mA

Figure 6.2: Lock characteristic of the differential LC oscillator for a sinusoidal injection at the 2nd harmonic into the tail node.

Ring Oscillator: In the following example, we again consider the 17-stage single-ended ring oscillator of Figure 4.12, but the injection is sinusoidal at the third and fifth harmonics. The resultant lock characteristics are shown in Figure 6.3.

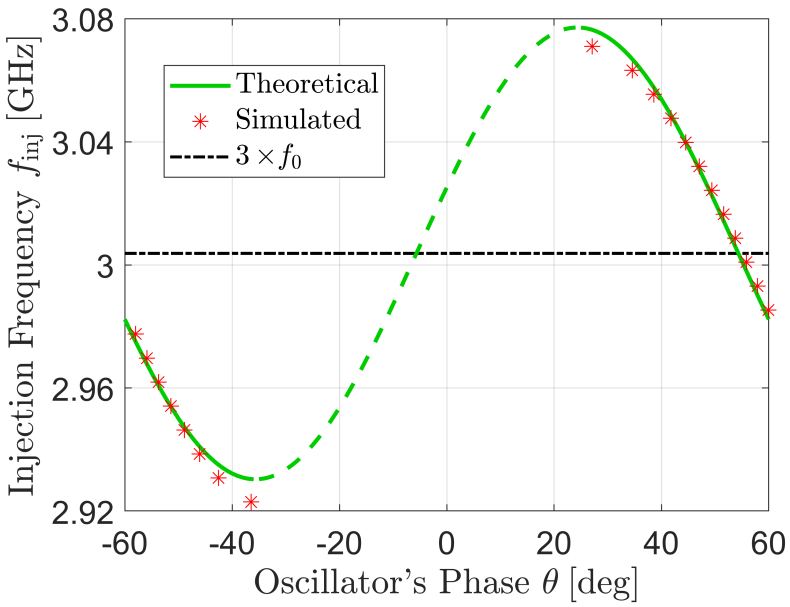

(a) Divide by $N = 3$ with $I_{\text{inj}} = 1.5$ mA.

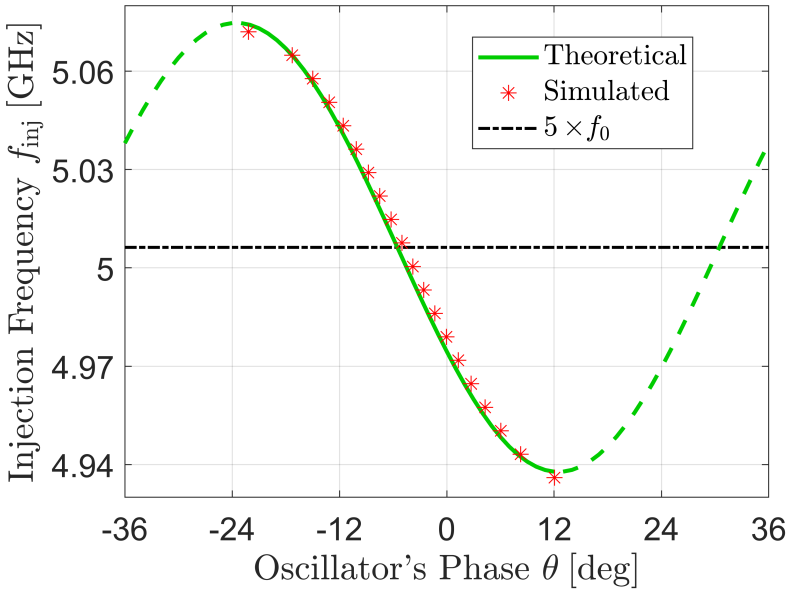

(b) Divide by $N = 5$ with $I_{\text{inj}} = 1$ mA.

Figure 6.3: Lock characteristic of the 17-stage single-ended ring oscillator for a sinusoidal injection at the 3$^{\text{rd}}$ and 5$^{\text{th}}$ harmonics.

The next example is injection at the first five harmonics into one stage of a 7-stage single-ended ring oscillator constructed using "asymmetric" inverters with unequal rise and fall times.[1] The free-running oscillation voltage and ISF for this scenario are shown in Figure 6.4. As we can see, the fall time is much shorter than the rise time, due to the size of the NMOS transistors being triple that of the PMOS devices.

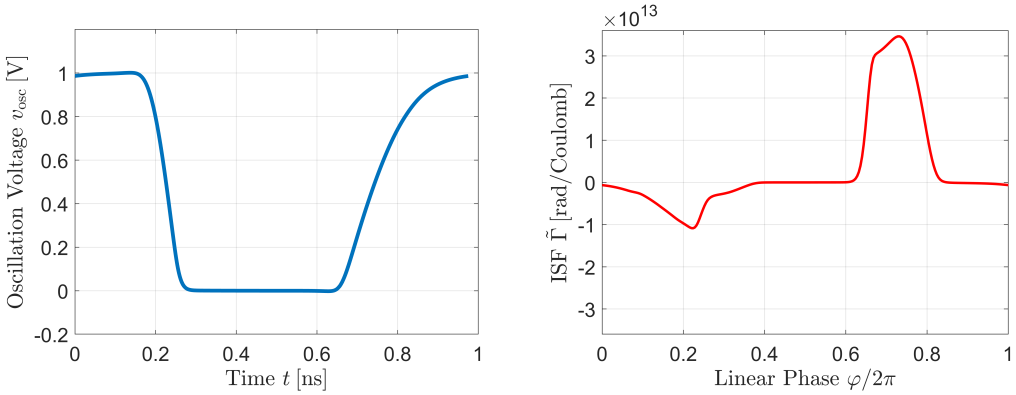

(a) Free-running oscillation voltage. (b) Impulse sensitivity function.

Figure 6.4: 7-stage asymmetric ring oscillator with $W_N/W_P = 3$.

The sinusoidal lock characteristics for the first five harmonics are shown in Figure 6.5. Despite the relatively weak injection amplitude compared to our other examples, deviations between simulation and theory due to nonlinear behavior are apparent. Note that $I_{\max} = 89\ \mu$A for this oscillator.

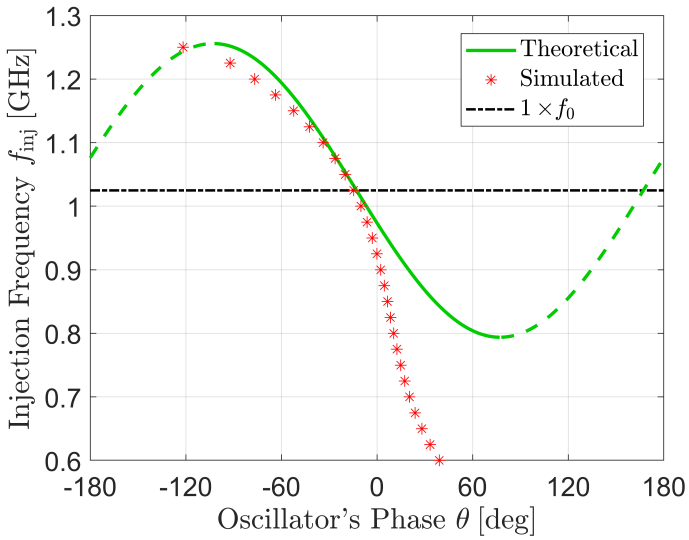

(a) $N = 1$ (fundamental harmonic)

[1] The reason for making the inverters asymmetric will be discussed in Section 8.5.

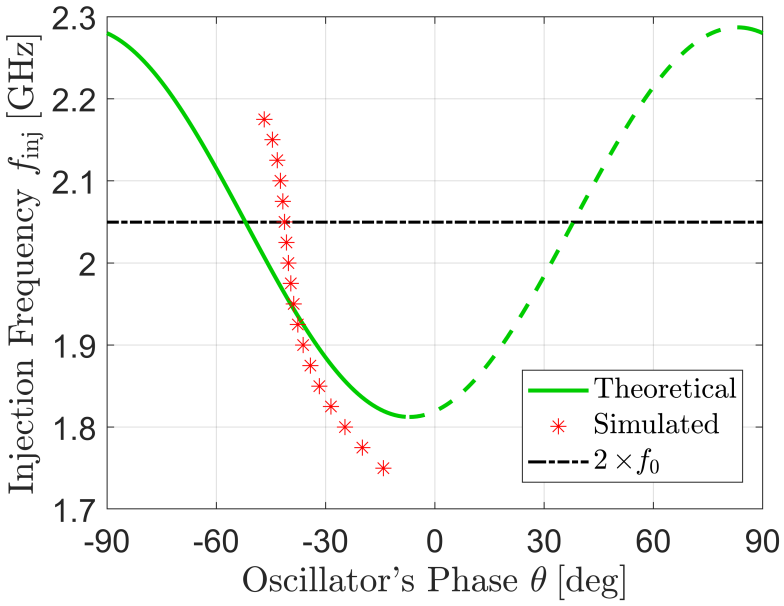

(b) Divide by $N = 2$

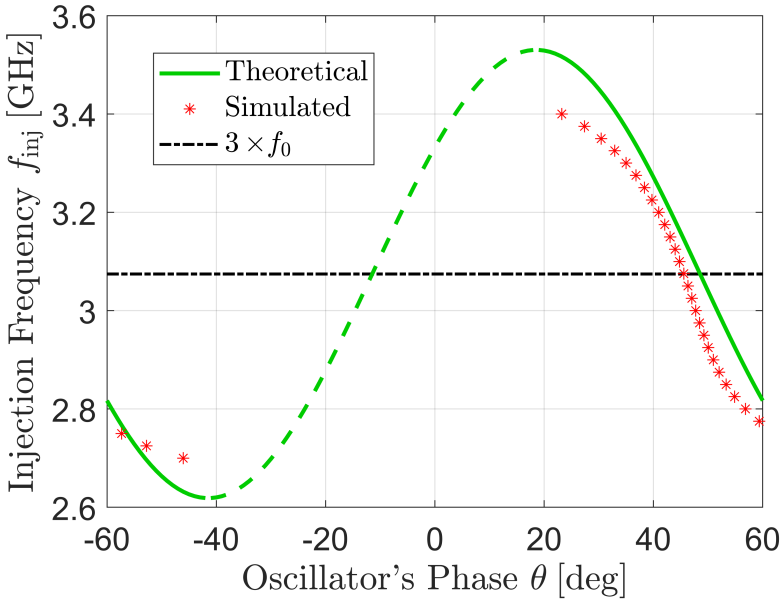

(c) Divide by $N = 3$

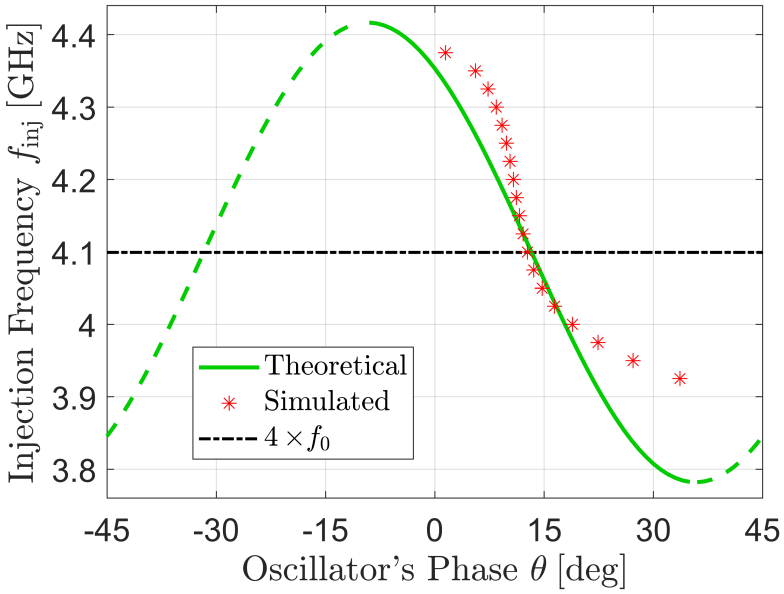

(d) Divide by $N = 4$

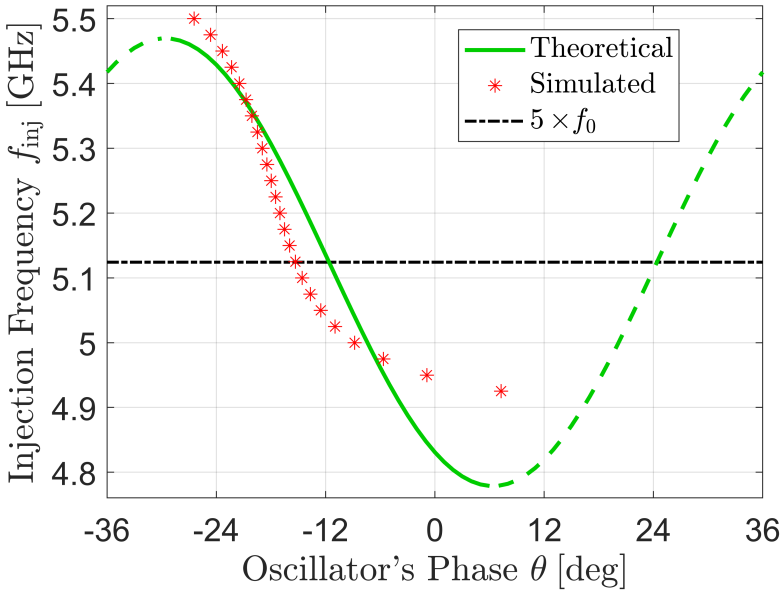

(e) Divide by $N = 5$

Figure 6.5: Lock characteristic of the 7-stage single-ended asymmetric ring oscillator for a $I_{inj} = 0.25$ mA sinusoidal injection at the first 5 harmonics.

Relaxation Oscillator: The final example involves using the ideal Bose oscillator from Section 4.4 in a divide-by-3 configuration. Note that the ISF of the Bose oscillator contains no even harmonics; therefore, dividing by even ratios is impossible. The lock characteristic is shown in Figure 6.6.

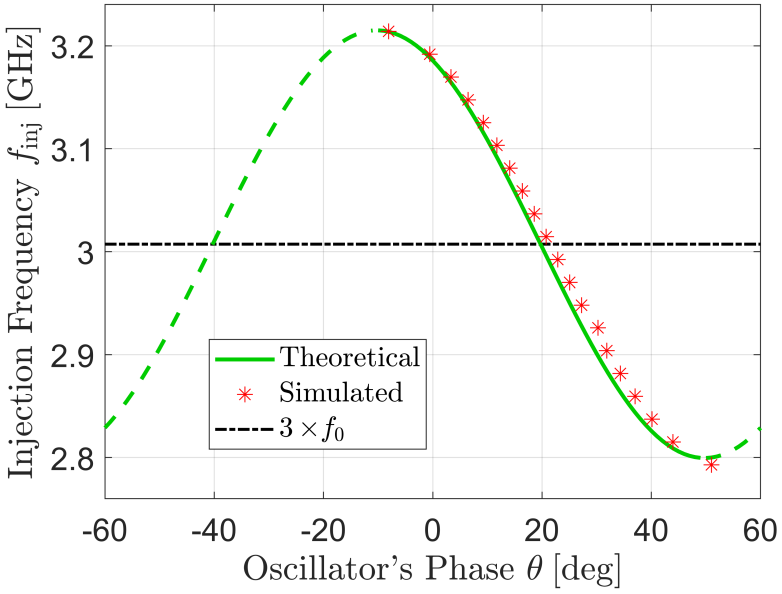

Figure 6.6: Lock characteristic of the ideal Bose oscillator for a 5 mA sinusoidal injection at the 3$^{\text{rd}}$ harmonic.

6.3 Experimental Results

A collection of measurement results are also provided here to accommodate the simulations of the previous section. Specifically, the same set of integrated oscillators from Section 4.7 was subjected to sinusoidal injections at various higher-order harmonics, and second harmonic sinusoidal injections were applied to the tail nodes of the two differential LC oscillators from Section 5.6. Again, each set of lock range measurements was repeated twice, and error bars that encompass all three trials are shown for each data point. Note that the absolute lock range is referred to the injection frequency—it corresponds to the maximum and minimum values of $f_{\text{inj}} - N f_0$ for which the oscillator is locked, where N is the division ratio. Therefore, the predicted lock range that the measurements are compared against is equal to [72]

$$N\omega_L^{\pm} = \pm\frac{1}{2} N I_{\text{inj}} \left|\tilde{\Gamma}_N\right|. \tag{6.4}$$

Table 6.1 lists the magnitudes of the relevant harmonics of the ISFs of these oscillators. Appendix A explains the details of the measurement setup. A die micrograph of the fabricated chip is shown in Figure 6.7, where the locations of the measured oscillators are specified.

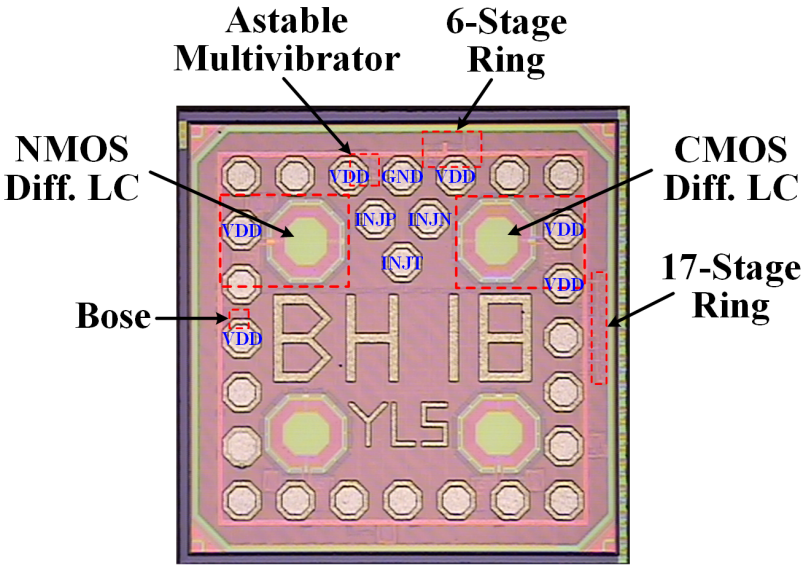

Figure 6.7: Die photo of the measured oscillators. The supply ('VDD') pads for each oscillator, the ground ('GND') pad, the differential injection ('INJP','INJN') pads, and the tail injection ('INJT') pad are labeled.

Table 6.1: Higher-Order ISF Harmonics of the Measured Oscillators

Oscillator	Schematic	Magnitudes of Relevant ISF Harmonics
17-Stage Ring	Figure 4.12a	$\lvert\tilde{\Gamma}_2\rvert$ = 55.5 rad/nC $\lvert\tilde{\Gamma}_3\rvert$ = 316 rad/nC $\lvert\tilde{\Gamma}_5\rvert$ = 266 rad/nC
6-Stage Differential Ring	Figure 4.14a	$\lvert\tilde{\Gamma}_3\rvert$ = 606 rad/nC
Bose Oscillator	Figure 4.5	$\lvert\tilde{\Gamma}_2\rvert$ = 4.95 rad/pC $\lvert\tilde{\Gamma}_3\rvert$ = 1.96 rad/pC $\lvert\tilde{\Gamma}_4\rvert$ = 3.14 rad/pC $\lvert\tilde{\Gamma}_5\rvert$ = 2.01 rad/pC
Astable Multivibrator	Figure 4.17a	$\lvert\tilde{\Gamma}_3\rvert$ = 1.73 rad/pC $\lvert\tilde{\Gamma}_5\rvert$ = 0.29 rad/pC
CMOS Differential LC Tail	Figure 6.1a	$\lvert\tilde{\Gamma}_2\rvert$ = 38.8 rad/nC
NMOS Differential LC Tail	Figure 6.11	$\lvert\tilde{\Gamma}_2\rvert$ = 2.45 rad/nC

Ring Oscillators

The first set of experiments measured the second, third, and fifth harmonic lock ranges of the 17-stage ring oscillator, as well as the third harmonic lock range of the 6-stage differential ring oscillator. As will be discussed in Section 8.5, the 17-stage ring oscillator is able to divide by $N = 2$, albeit with a rather limited lock range, due to the asymmetry between the rising and falling edges of the oscillation. The 6-stage ring oscillator features no such asymmetry because of its differential nature and can therefore only divide by odd ratios. The measurement results are presented in Figure 6.8.

Compared to the fundamental harmonic, nonlinear behavior appears at smaller injection amplitudes. This may be attributed to the fact that the oscillator's nodes are comparatively more perturbed from their free-running operating point since the injections occur on a time scale that is N times faster, leaving less time for the excess charge deposited by the injection to dissipate.

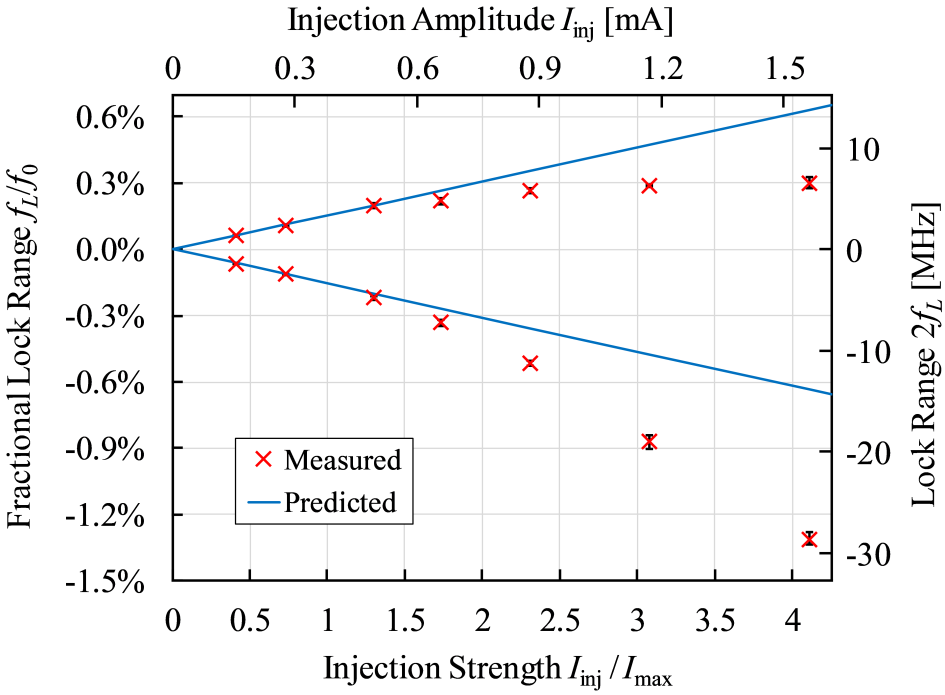

(a) Measured 2nd harmonic lock range for the 17-stage ring oscillator.

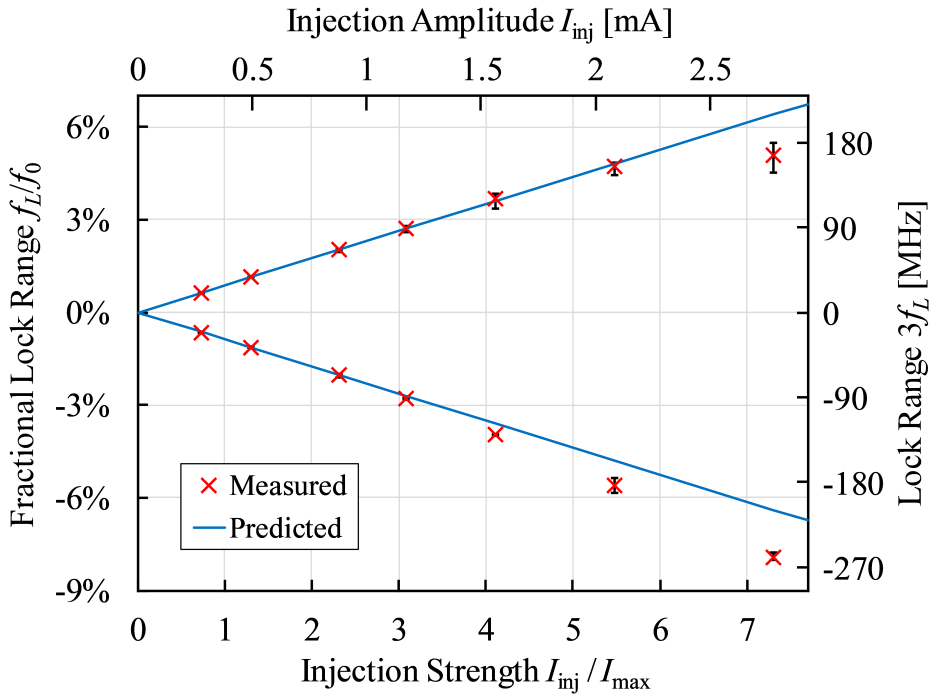

(b) Measured 3rd harmonic lock range for the 17-stage ring oscillator.

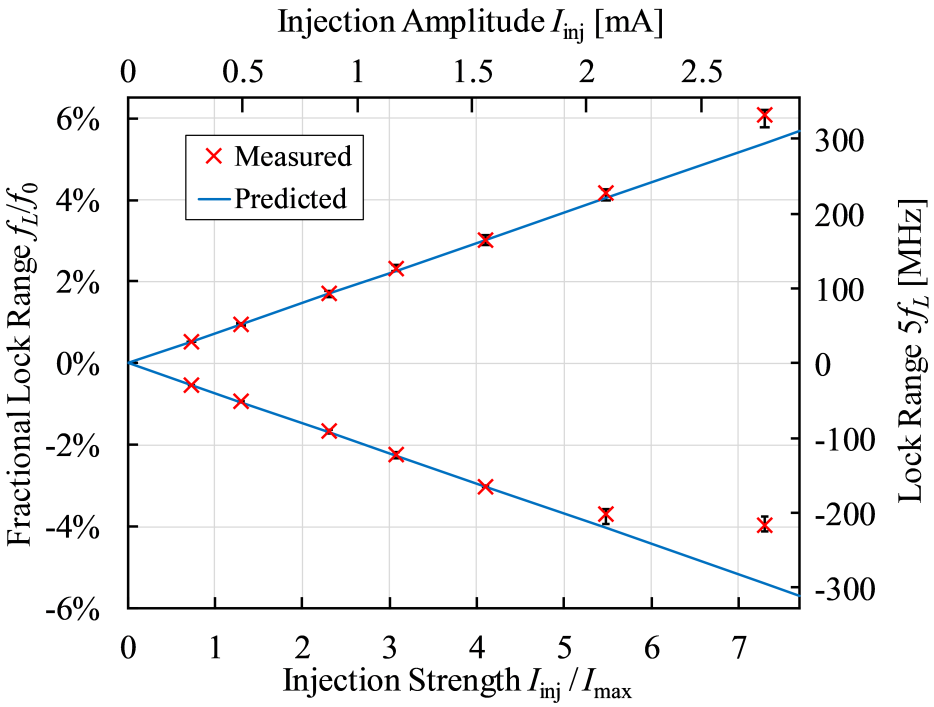

(c) Measured 5th harmonic lock range for the 17-stage ring oscillator.

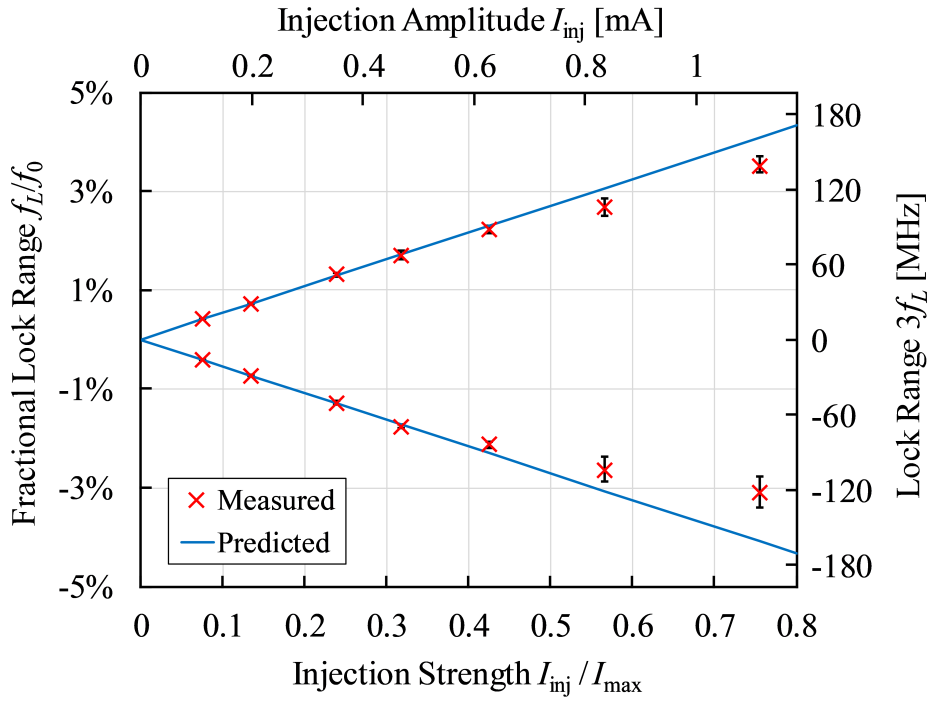

(d) Measured 3rd harmonic lock range for the 6-stage differential ring oscillator.

Figure 6.8: Superharmonic lock range measurement results for two different ring oscillators.

Relaxation Oscillators

The second set of experiments measured the second, third, fourth, and fifth harmonic lock ranges of the 10 MHz Bose oscillator, as well as the third and fifth harmonic lock ranges of the NMOS astable multivibrator. The measurement results for the Bose oscillator are presented in Figure 6.9. Observe how the ISF of the fabricated Bose oscillator (Figure 4.23b) features a single sharp peak. In the frequency domain, this impulse-like waveform translates into more equally distributed energy across all harmonics, leading to the ability to divide by both even and odd ratios.

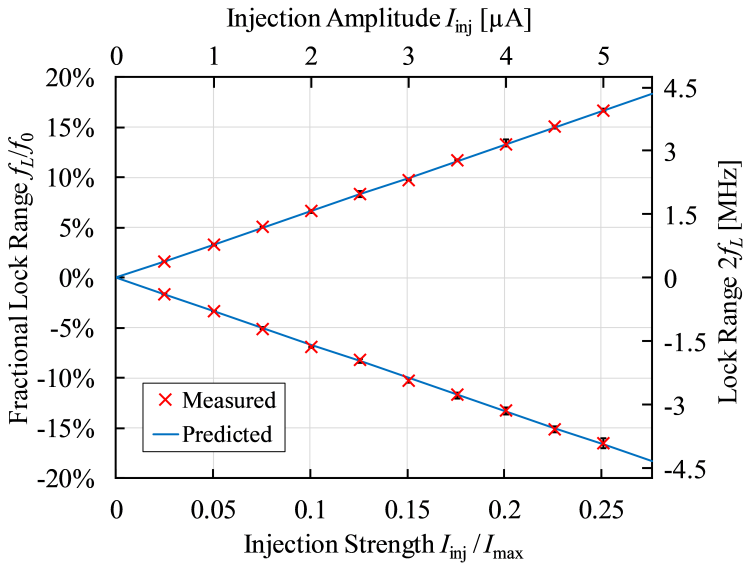

(a) Measured 2nd harmonic lock range.

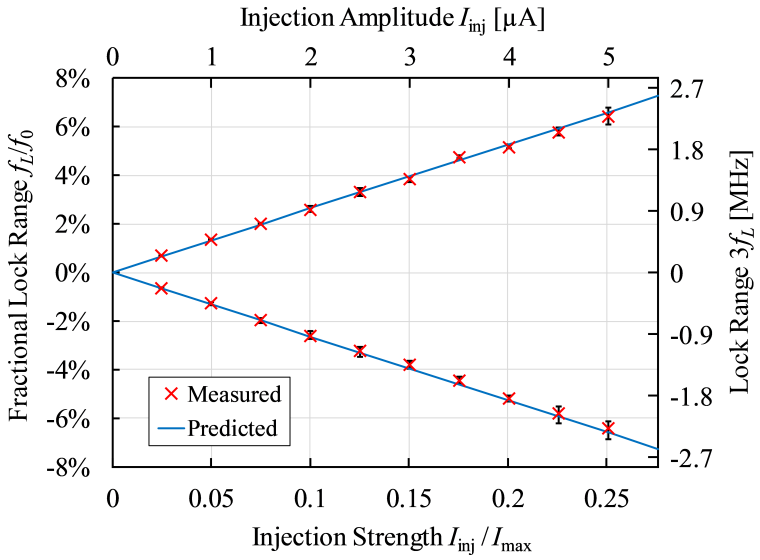

(b) Measured 3rd harmonic lock range.

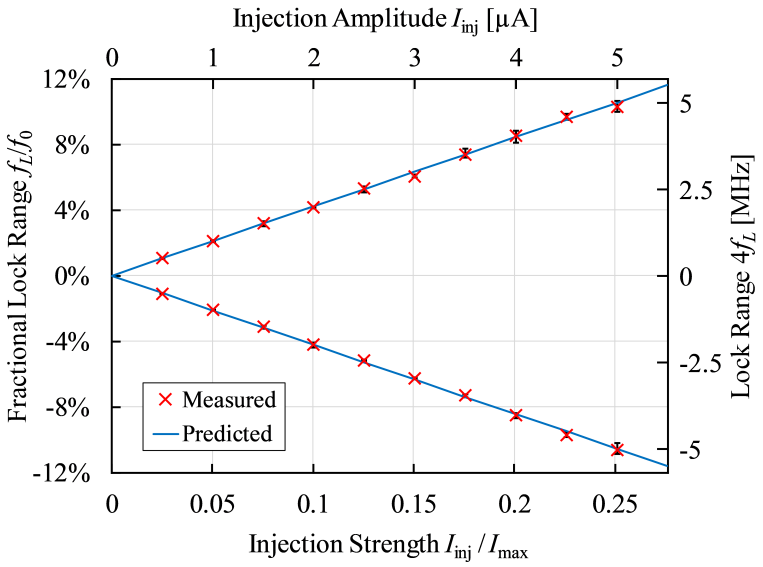

(c) Measured 4th harmonic lock range.

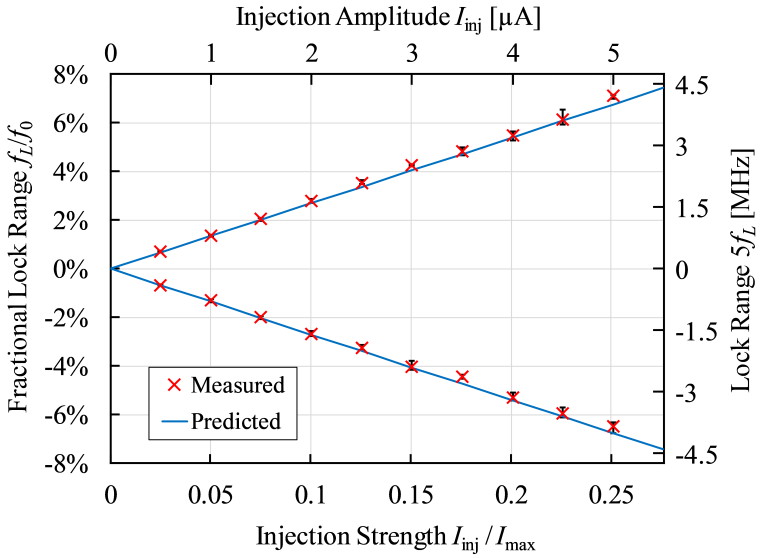

(d) Measured 5th harmonic lock range.

Figure 6.9: Superharmonic lock range measurement results for the 10 MHz Bose relaxation oscillator.

The Bose oscillator is rather "well-behaved" with respect to being faithful to the theoretically predicted lock range. This is due to its relatively simple "quasi-single-state" nature, which corresponds to a comparatively more linear lock characteristic with respect to the injection.

The measurement results for the astable multivibrator are presented in Figure 6.10.

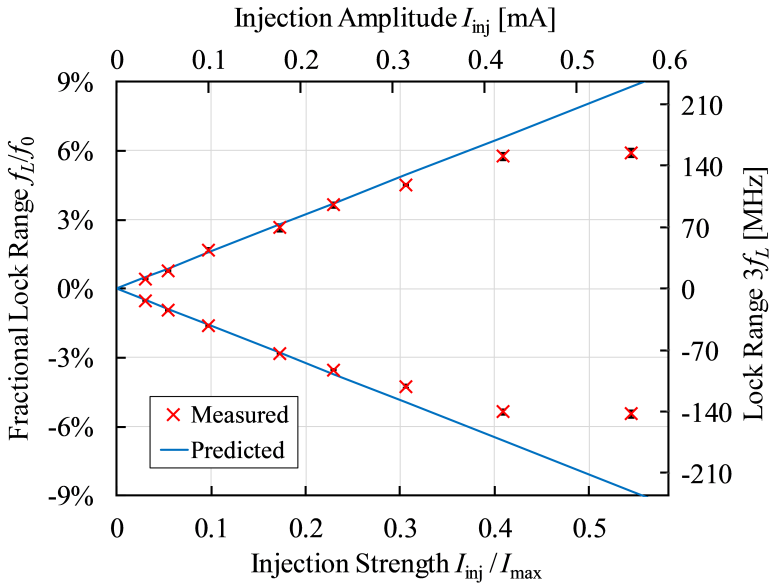

(a) Measured 3rd harmonic lock range.

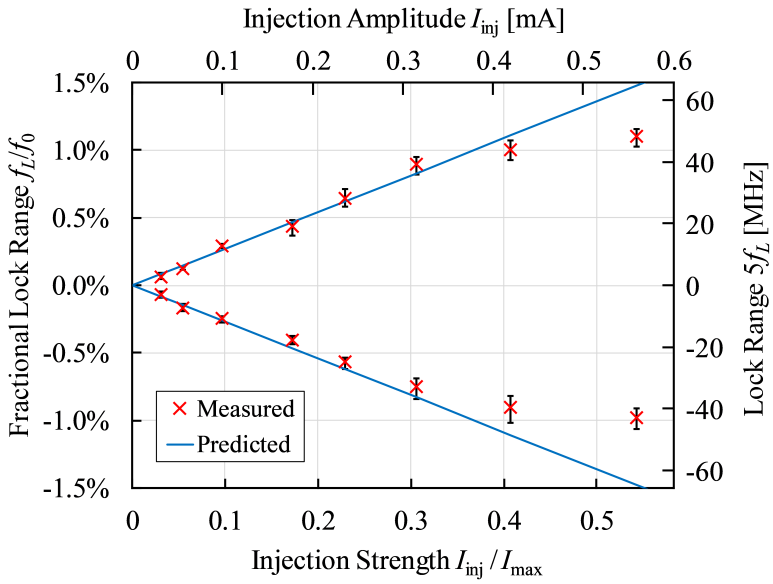

(b) Measured 5th harmonic lock range.

Figure 6.10: Superharmonic lock range measurement results for the NMOS differential astable multivibrator.

Interestingly, higher-order lock ranges for the astable multivibrator appear to approach some limit as the injection amplitude grows.

Differential LC Oscillator Tail Injections

The final set of experiments measured the second harmonic lock ranges associated with injecting into the tail nodes of the CMOS and NMOS-only differential LC oscillators. The schematic for the latter is given in Figure 6.11. The simulated tail-injection ISFs and the measurement results are presented in Figures 6.12 and 6.13 for the CMOS and NMOS-only oscillators, respectively. Note that the bottom axis normalizes the injection amplitude to the tail bias current, I_{tail}.

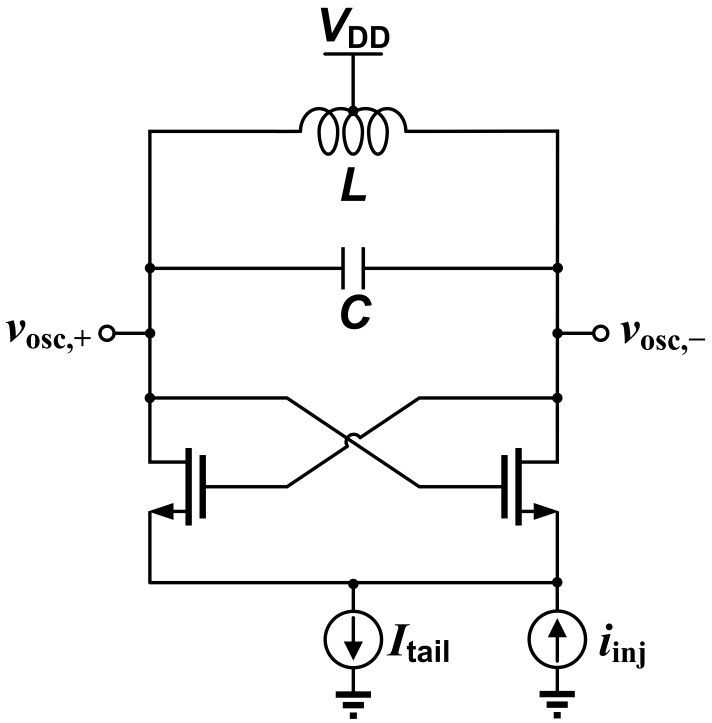

Figure 6.11: Schematic of the NMOS-only differential LC oscillator with a tail injection. I_{tail} is implemented with a resistively biased current mirror.

Notice how the NMOS-only version has a considerably narrower lock range for the same injection amplitude due to its much smaller $\left|\tilde{\Gamma}_2\right|$. We can explain this physically by noting that the voltage swing of the NMOS-only oscillator is both lower (see Table 5.1) *and* occurs at nodes that have an elevated DC operating point, specifically the supply V_{DD}. Thus, the drain voltage of the tail transistor is significantly less affected by the oscillation and therefore fluctuates much less over a single period. This, in turn, translates into a diminished effect that an injection into the tail has on the phase of oscillation.

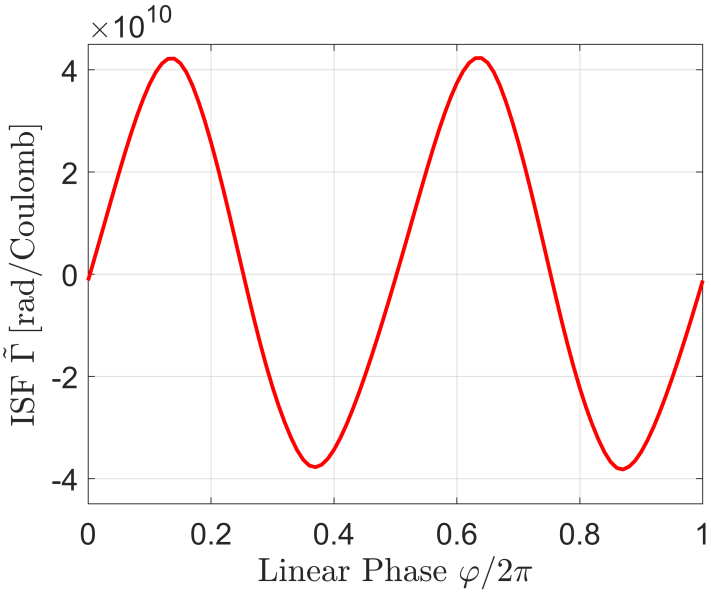

(a) Simulated ISF.

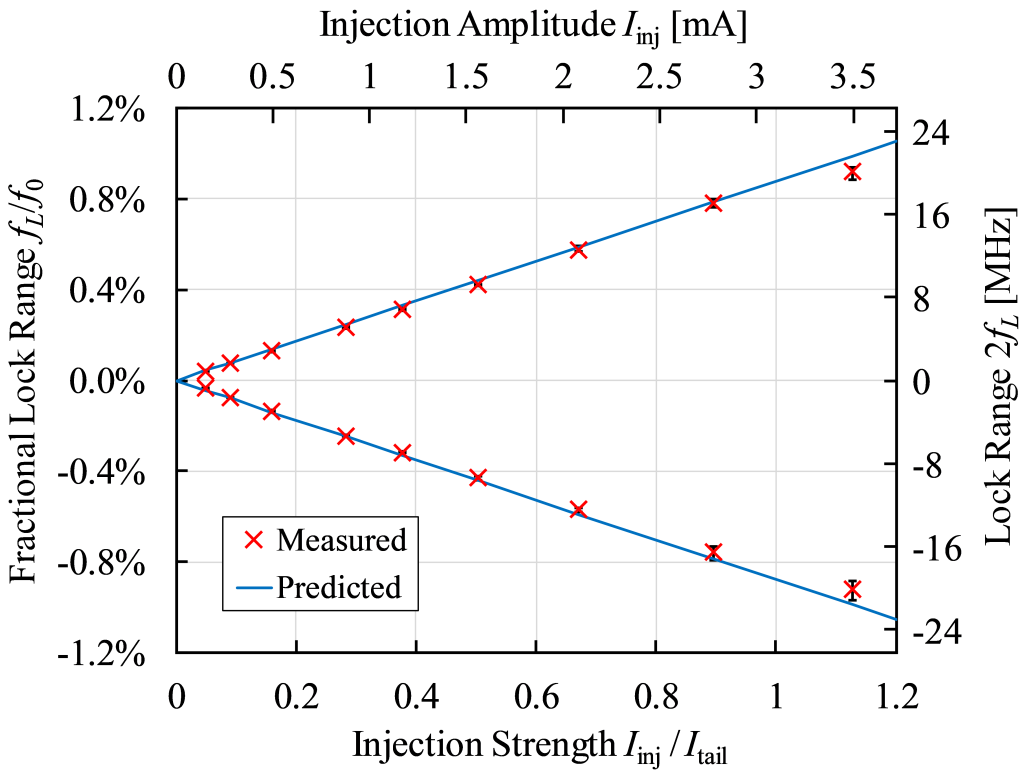

(b) Measured lock range.

Figure 6.12: Measurement results for injecting into the tail of the CMOS differential LC oscillator.

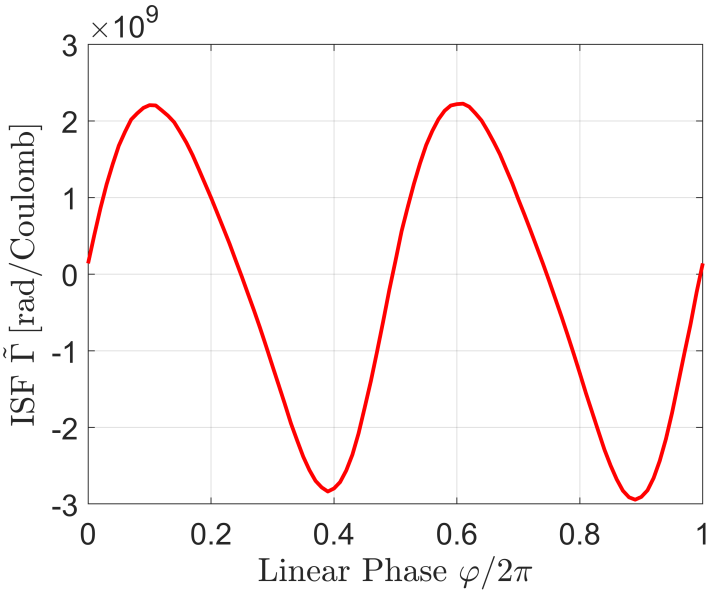

(a) Simulated ISF.

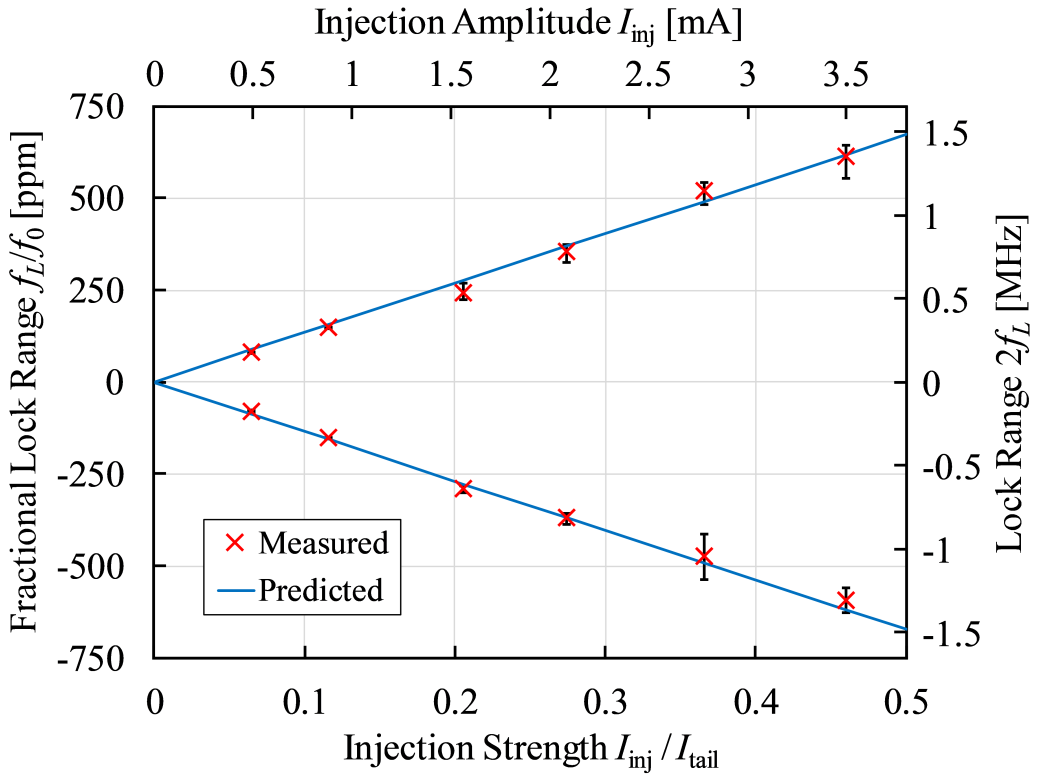

(b) Measured lock range.

Figure 6.13: Measurement results for injecting into the tail of the NMOS-only differential LC oscillator.

6.4 Higher-Order Sinusoidal Injection Compliances

We can generalize the concept of the sinusoidal injection compliance introduced in Section 4.8 to include injection-locked frequency division. Specifically, the compliance for sinusoidal injections that are not large enough to violate linearity is given by

$$\boxed{\eta_N \coloneqq \frac{2\omega_L/\omega_0}{I_{\text{inj}}/I_{\max}} = q_{\max,0}\left|\tilde{\Gamma}_N\right|.} \tag{6.5}$$

For differential oscillator tail injections, we calculated the injection strength via normalization to the tail bias current. Therefore,

$$\boxed{\eta_{\text{tail},2} \coloneqq \frac{2\omega_L/\omega_0}{I_{\text{inj}}/I_{\text{tail}}} = \frac{q_{\max,0}}{\kappa_{\text{tail}}}\left|\tilde{\Gamma}_2\right|,} \tag{6.6}$$

where $q_{\max,0}$ is still the charge amplitude across the oscillation terminals (not at the tail), and κ_{tail} is a conversion factor from the tail current to the oscillation current $I_{\max} \coloneqq \omega_0 q_{\max,0}$. For CMOS and NMOS-only differential LC oscillators, κ_{tail} is equal to $4Q/\pi$ and $2Q/\pi$, respectively. For differential ring oscillators (see Figure 4.14a), the charge swing is given by $q_{\max,0} = I_{\text{tail}}RC$, which leads to a conversion factor of $\kappa_{\text{tail}} = \omega_0 RC$. Estimating the period of oscillation as twice the number of stages K multiplied by the RC-delay per stage, we can approximate $\kappa_{\text{tail}} \approx \pi/K$. Table 6.2 lists the higher-order sinusoidal injection compliances based on Eqs. (6.5) and (6.6) for the various oscillators simulated and measured in this chapter. Again, Sections 6.2 and 6.3 contain schematic-level and extracted oscillators, respectively.

6.5 Subharmonic Injection

Now consider the possibility of locking onto an injection which is at a *subharmonic* of the oscillation frequency: $\omega_{\text{osc}} = M\omega_{\text{inj}}$ for some positive integer M under lock [14]–[17]. Again, Eq. (4.20) can also predict locking if $\tilde{\Gamma}(\omega_{\text{osc}}t)$ has a fundamental period of T_{inj}/M, since this still implies periodicity with respect to the averaging interval T_{inj}. To that end, it again makes sense to redefine the oscillator's phase θ so that

$$\varphi(t) \equiv M\omega_{\text{inj}}t + \theta(t). \tag{6.7}$$

With this definition, the phase pulling equation becomes

$$\frac{d\theta}{dt} = \omega_0 - M\omega_{\text{inj}} + \frac{1}{T_{\text{inj}}}\int_{T_{\text{inj}}} \tilde{\Gamma}\left(M\omega_{\text{inj}}t + \theta\right) i_{\text{inj}}(t)\,dt, \tag{6.8}$$

Table 6.2: Higher-Order Compliances of Various Oscillators

Oscillator	Version	Sinusoidal Injection Compliance η_N
6-Stage Differential Ring	Section 6.3	$\eta_3 = 10.83\%$
7-Stage Asymmetric Ring	Section 6.2	$\eta_1 = 17.03\%$ $\eta_2 = 8.75\%$ $\eta_3 = 11.20\%$ $\eta_4 = 5.85\%$ $\eta_5 = 5.09\%$
17-Stage Ring	Section 6.2	$\eta_3 = 2.34\%$ $\eta_5 = 1.97\%$
	Section 6.3	$\eta_2 = 0.31\%$ $\eta_3 = 1.75\%$ $\eta_5 = 1.48\%$
Ideal Bose	Section 6.2	$\eta_3 = 79.02\%$
Bose	Section 6.3	$\eta_2 = 132.63\%$ $\eta_3 = 52.53\%$ $\eta_4 = 84.14\%$ $\eta_5 = 53.84\%$
Astable Multivibrator	Section 6.3	$\eta_3 = 32.31\%$ $\eta_5 = 5.43\%$
CMOS Diff. LC Tail	Section 6.2	$\eta_{\text{tail},2} = 2.87\%$
	Section 6.3	$\eta_{\text{tail},2} = 1.76\%$
NMOS-Only Diff. LC Tail	Section 6.3	$\eta_{\text{tail},2} = 0.27\%$

and so the lock characteristic $\Omega(\theta)$, which is now the steady-state solution for the modified frequency deviation $\Delta\omega \coloneqq M\omega_{\text{inj}} - \omega_0$, admits the following frequency domain representation:

$$\begin{aligned}\Delta\omega &\coloneqq M\omega_{\text{inj}} - \omega_0 \\ &= \frac{1}{2}\left[\frac{I_{\text{inj},0}\tilde{\Gamma}_0}{2} + \sum_{n=1}^{\infty}\left|I_{\text{inj},nM}\tilde{\Gamma}_n\right|\cos\left(n\theta + \angle\tilde{\Gamma}_n - \angle I_{\text{inj},nM}\right)\right].\end{aligned} \tag{6.9}$$

We see that for subharmonic injection locking to occur, the oscillator must lock onto the M^{th}-multiple harmonics of the injection current. However, it is important to note

that the higher-order harmonics required of the injection current are typically generated within the oscillator itself as byproducts of mixing [14]–[17]. Unfortunately, this nonlinear phenomenon is not explicitly captured by our model.

6.6 Generalized M:N Sub-/Super-Harmonic Injection

It is not hard to extend the aforementioned concepts of superharmonic and subharmonic injection locking to a more general scenario. Assume M and N are two positive, coprime integers such that $M\omega_{\text{inj}} = N\omega_{\text{osc}}$ under lock [34], [72]. Then, the oscillator's phase θ should now satisfy

$$\varphi(t) \equiv \frac{M}{N}\omega_{\text{inj}}t + \theta(t), \tag{6.10}$$

which means the phase pulling equation becomes

$$\frac{d\theta}{dt} = \omega_0 - \frac{M}{N}\omega_{\text{inj}} + \frac{1}{NT_{\text{inj}}}\int_{NT_{\text{inj}}} \tilde{\Gamma}\left(\frac{M}{N}\omega_{\text{inj}}t + \theta\right) i_{\text{inj}}(t)\,dt. \tag{6.11}$$

Again, we redefine the lock characteristic $\Omega(\theta)$ as the steady-state solution for the generalized frequency deviation $\Delta\omega \coloneqq (M/N)\,\omega_{\text{inj}} - \omega_0$, which can therefore be expressed in the frequency domain as:[2]

$$\begin{aligned}\Delta\omega &\coloneqq \frac{M}{N}\omega_{\text{inj}} - \omega_0 \\ &= \frac{1}{2}\left[\frac{I_{\text{inj},0}\tilde{\Gamma}_0}{2} + \sum_{n=1}^{\infty}\left|I_{\text{inj},nM}\tilde{\Gamma}_{nN}\right|\cos\left(nN\theta + \angle\tilde{\Gamma}_{nN} - \angle I_{\text{inj},nM}\right)\right].\end{aligned} \tag{6.12}$$

Therefore, for locking to take place, the M^{th}-multiple harmonics of the injection need to interact with the N^{th}-multiple harmonics of the oscillator's ISF. A block diagram of this generalized fractional harmonic injection process, as well as its frequency domain decomposition, is shown in Figure 6.14.

Notice that it is mathematically feasible for modes corresponding to different sub-/super-harmonics of the injection to exist simultaneously, leading to more than one possibility for the oscillation frequency that the locked oscillator can assume. That is, for a given injection signal $i_{\text{inj}}(t)$ at a particular injection frequency ω_{inj}, there could be multiple pairs of positive, coprime integers M and N that satisfy the

[2] If M and N have any common factors besides one, then the representation of Eq. (6.12) would be missing components of the injection waveform and the ISF that can actually contribute to locking. Specifically, it is not hard to see from the averaging in Eq. (6.11) that M and N in Eq. (6.12) should generally be replaced with $M/\gcd(M,N)$ and $N/\gcd(M,N)$, respectively (where gcd stands for *greatest common divisor*).

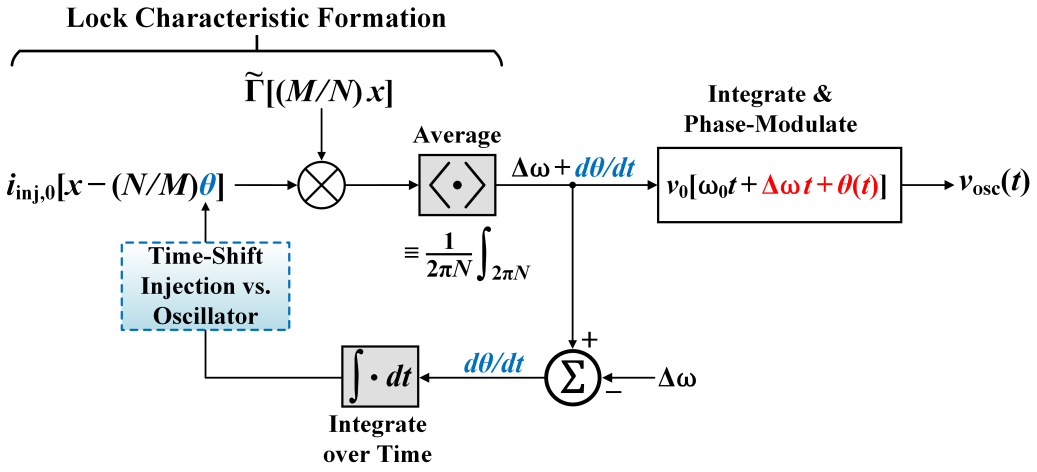

(a) How a periodic injection at the fractional $(N/M)^{\text{th}}$ harmonic with respect to the oscillator affects the oscillator's phase.

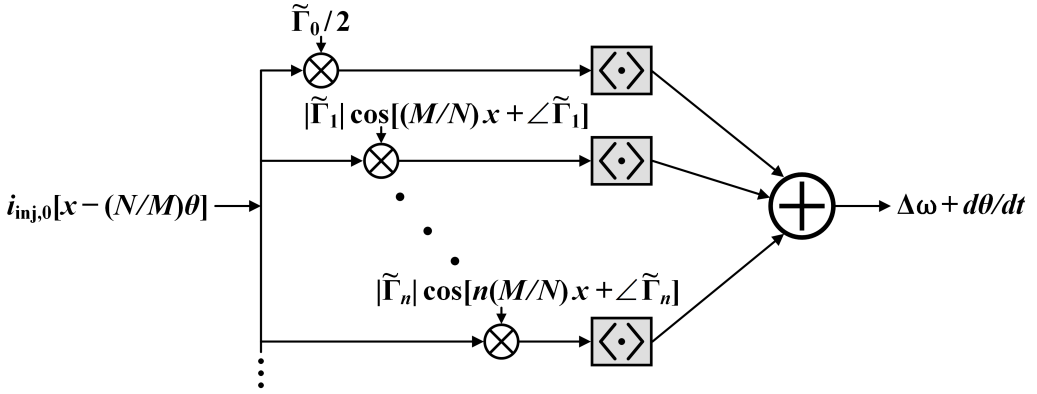

(b) Decomposition of the ISF into its Fourier series components.

Figure 6.14: Generalization of Figures 4.3 and 4.4 to allow for M:N sub-/super-harmonic injection locking and pulling.

lock characteristic—albeit with different solutions for θ in general. This usually occurs for rather large injections, as it requires the lock characteristics of different harmonics to overlap for a range of injection frequencies.

The foregoing analysis might also seem to suggest that an oscillator is capable of locking to practically *any* injection frequency, since any positive real number can be approximated by a ratio of coprime integers—a rational number—to an arbitrary degree of accuracy (i.e., by "increasing the number of decimal places"). This is because the rational numbers are *dense* in the set of real numbers [103]. However, one should note that M and N increase with the accuracy of the approximation, and it is difficult in practice to generate very high-order harmonics of appreciable amplitude.

6.7 Example: Multi-Phase Injections into a Ring Oscillator

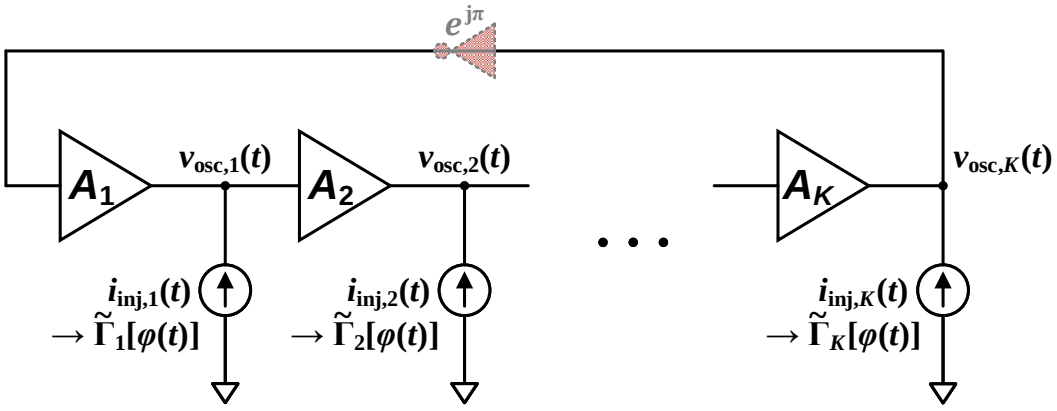

Figure 6.15: A ring oscillator with an injection applied to every stage. Differential ring oscillators consisting of an even number of stages have an additional inversion in the feedback path.

Consider a K-stage ring oscillator with injection current $i_{\text{inj},i}(t)$ applied at the i^{th} stage for $i = 1, \ldots, K$, as shown in Figure 6.15. Assume that the only differences between the K injection currents are their phases—they all have the same frequency, shape, and size. In other words, there exists a 2π-periodic injection waveform $i_{\text{inj},0}(x)$ such that for all $i \in \{1, \ldots, K\}$, we can write

$$i_{\text{inj},i}(t) = i_{\text{inj},0}(\omega_{\text{inj}} t + \alpha_i), \tag{6.13}$$

where α_i represents the phase of the i^{th} injection. The objective of this section is to figure out how to set the injection phases to optimize the lock range.

By symmetry, the only differences between the K oscillation voltages are also their phases. So, there also exists a 2π-periodic oscillation waveform $v_0(x)$ such that

$$v_{\text{osc},i}(t) = v_0\left[\varphi(t) + \phi_i\right], \tag{6.14}$$

where $\varphi(t) \equiv \omega_0 t + \phi(t)$ is a "global" total phase for the entire oscillator which admits some disturbance $\phi(t)$ in excess of free-running ($\omega_0 t$) due to the injections [see Eq. (1.3)], and the (constant) ϕ_i's capture the phase distribution between the ring's different stages. Similarly, the K impulse sensitivity functions must also be related via

$$\tilde{\Gamma}_i(x) = \tilde{\Gamma}(x + \phi_i) \tag{6.15}$$

for some $\tilde{\Gamma}(x)$, a "global" ISF for all of the injection sites.

Again, we define the oscillator's phase θ with respect to the injection by the relation $\varphi(t) = (\omega_{\text{inj}}/N)t + \theta(t)$, where we assumed the injection to be at the N^{th} superharmonic. Due to the linearity of our model, we know that θ satisfies the differential equation:

$$\frac{d\theta}{dt} = \omega_0 - \frac{\omega_{\text{inj}}}{N} + \sum_{i=1}^{K} \frac{1}{NT_{\text{inj}}} \int_{NT_{\text{inj}}} \tilde{\Gamma}_i\Big(\frac{\omega_{\text{inj}}}{N}t + \theta\Big)\, i_{\text{inj},i}(t)\, dt. \tag{6.16}$$

Assuming the oscillator is locked and simplifying the right-hand-side, we arrive at the following lock characteristic:

$$\Delta\omega \equiv \frac{\omega_{\text{inj}}}{N} - \omega_0 = \sum_{i=1}^{K} \left\langle \tilde{\Gamma}\left(\frac{x}{N} + \theta + \phi_i\right) i_{\text{inj},0}(x + \alpha_i) \right\rangle_{2\pi N}. \tag{6.17}$$

Extremizing this with respect to θ then yields the lock range. Without loss of generality, consider just the upper lock range, which we shall denote as ω_L. Assume θ^* maximizes the lock characteristic, meaning that $\omega_L = \Omega(\theta^*)$, whereas θ_i^* is the value of θ that maximizes only the i^{th} term in the above sum. Noting that the maximum of a sum is bounded by the sum of the individual maxima, we have that

$$\begin{aligned} \omega_L &= \sum_{i=1}^{K} \left\langle \tilde{\Gamma}\left(\frac{x}{N} + \theta^* + \phi_i\right) i_{\text{inj},0}(x + \alpha_i) \right\rangle_{2\pi N} \\ &\leq \sum_{i=1}^{K} \left\langle \tilde{\Gamma}\left(\frac{x}{N} + \theta_i^* + \phi_i\right) i_{\text{inj},0}(x + \alpha_i) \right\rangle_{2\pi N}, \end{aligned} \tag{6.18}$$

where equality is attained only if all the θ_i^*'s are the same. This, of course, is achievable: we simply need to distribute the phases of the injection currents, α_i, in accordance with the phases of the oscillation voltages and ISFs, ϕ_i. More precisely, we obtain the largest lock range under this injection topology by setting $\alpha_i = N\phi_i$ (up to a constant shift which can be absorbed into θ). This renders all the terms in the sum equal to one another, as the functions being averaged become shifted versions of each other. Therefore, both the lock characteristic and the lock range are enhanced by a factor of K compared to having a single injection:

$$\Delta\omega = K \times \left\langle \tilde{\Gamma}\left(\frac{x}{N} + \theta\right) i_{\text{inj},0}(x) \right\rangle_{2\pi N}. \tag{6.19}$$

Note that if only P out of the K stages are injected into, simply replace K with P.

In a ring oscillator where the amplifiers A_i are all inverting, the phase difference between successive stages is[3]

$$\Delta\phi \equiv \phi_{i+1} - \phi_i = \pi - \frac{\pi}{N}. \tag{6.20}$$

[3]We are implicitly (yet reasonably) assuming that the *relative* phases of the *free-running* oscillation voltages at different stages remain preserved under injection.

Thus, the phase difference between successive injections should therefore be N times this:

$$\boxed{\Delta\alpha_i \equiv \alpha_{i+1} - \alpha_i = N \times \left(\pi - \frac{\pi}{N}\right).} \tag{6.21}$$

This result was implemented by Mirzaei *et al.* in [10], [60]. We will also use this scheme in Chapter 9 for the design of our injection-locked prescaler.

Simulation Results

To demonstrate the validity of the above result, we took the 7-stage asymmetric ring oscillator of Figure 6.4 and applied a sinusoidal injection current to every single stage. We distributed the phases in accordance with Eq. (6.21), and we show that altering the phase distribution by changing N enables the oscillator to divide by different integer ratios. We then compared the simulated lock characteristic against a theoretically calculated one, which was obtained by simply multiplying the ISF-based lock characteristic for a single injection by 7. The results for the first five harmonics are shown in Figure 6.16. We used an injection amplitude of $I_{\text{inj}} = 0.1\text{mA}$ throughout, except for the $N = 3$ case (Figure 6.16c) where we used $I_{\text{inj}} = 0.05$ mA due to bizarre nonlinear behavior which appeared at stronger injection strengths. Compare these results against those shown in Figure 6.5.

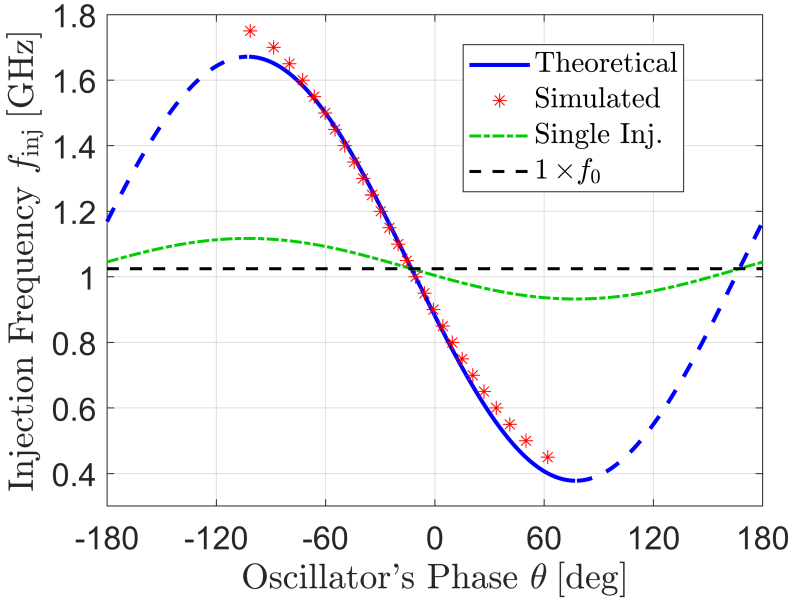

(a) $N = 1$ (fundamental harmonic)

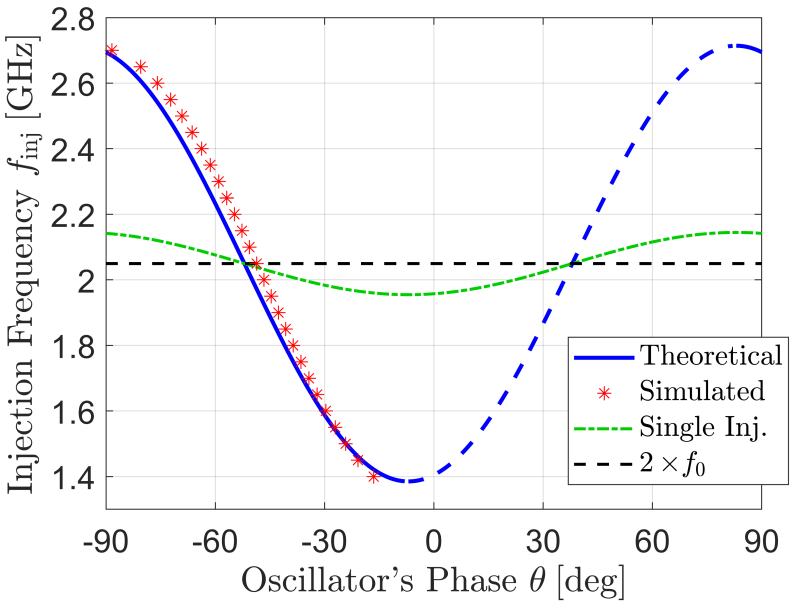

(b) Divide by $N = 2$

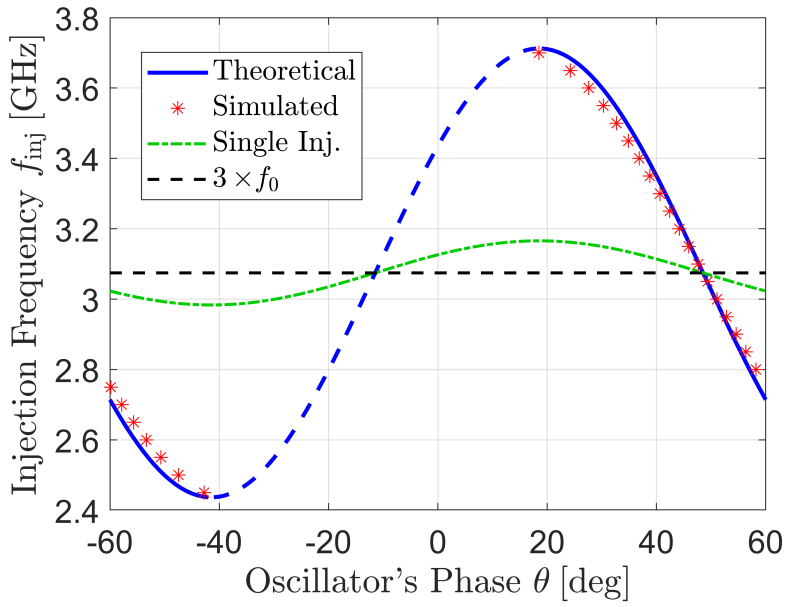

(c) Divide by $N = 3$

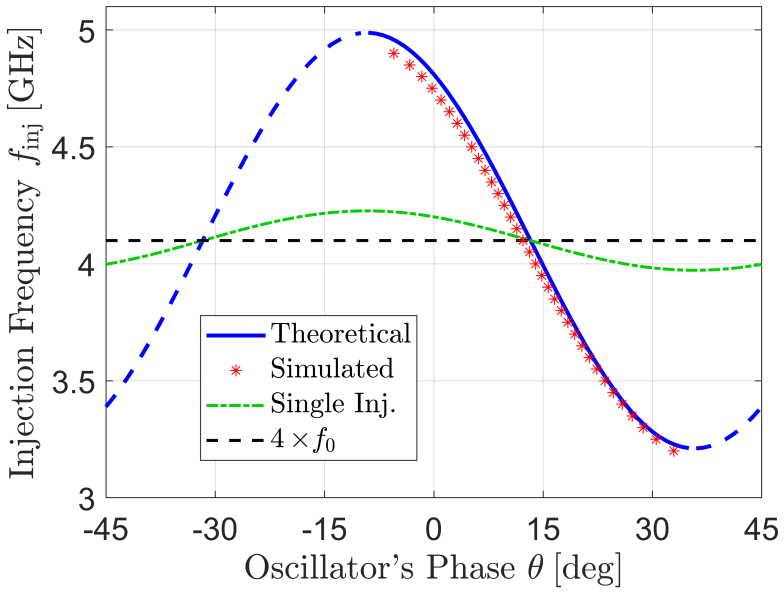

(d) Divide by $N = 4$

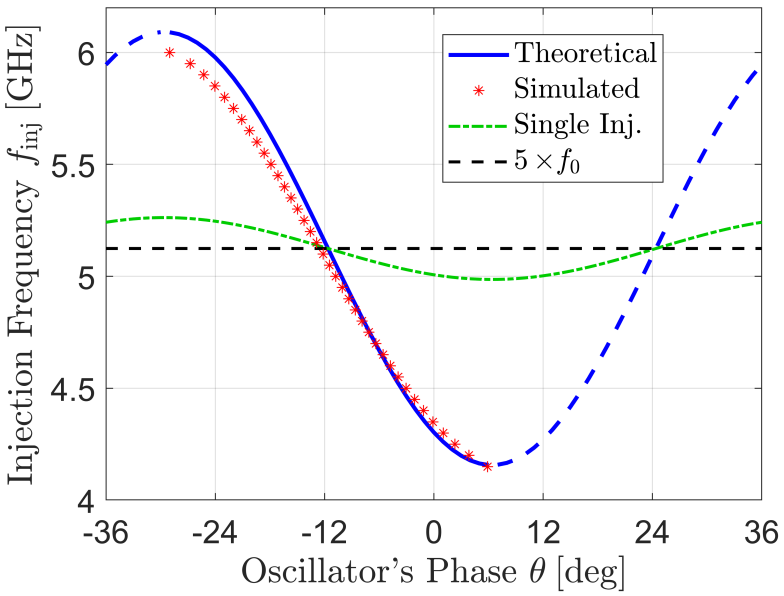

(e) Divide by $N = 5$

Figure 6.16: Multi-phase injection lock characteristic of the 7-stage single-ended asymmetric ring oscillator for a sinusoidal injection at the first 5 harmonics.

6.8 General Definition of the Phase Difference θ

In this section, we attack the problem of using the oscillation voltage $v_{\text{osc}}(t)$ and the injection current $i_{\text{inj}}(t)$ to calculate the phase difference θ between a locked oscillator and its injection. Note that θ is unambiguously given once the oscillation waveform $v_0(x)$ and the injection waveform $i_{\text{inj},0}(x)$ are defined, since

$$\begin{aligned} v_{\text{osc}}(t) &= v_0\left(\frac{M}{N}\omega_{\text{inj}}t + \theta\right) \\ i_{\text{inj}}(t) &\equiv i_{\text{inj},0}(\omega_{\text{inj}}t). \end{aligned} \tag{6.22}$$

However, the idea of determining the phase difference between two non-sinusoidal periodic functions with possibly different frequencies may seem confusing or even ill-posed at first glance. Therefore, we address the technical details of this process below.

First, let us expand the oscillation waveform, $v_0(x)$, using Fourier series:

$$v_0(x) = \frac{V_{\text{osc},0}}{2} + \sum_{n=1}^{\infty} \left|V_{\text{osc},n}\right| \cos(nx + \angle V_{\text{osc},n}), \tag{6.23}$$

where

$$V_{\text{osc},n} = \frac{1}{\pi}\int_{2\pi} v_0(x)e^{-jnx}\,dx. \tag{6.24}$$

Therefore, the fundamental components of the oscillation voltage and the injection current are given by

$$\begin{aligned} v_{\text{osc}}(t) &= \left|V_{\text{osc},1}\right| \cos\left(\frac{M}{N}\omega_{\text{inj}}t + \theta + \angle V_{\text{osc},1}\right) + \cdots \\ i_{\text{inj}}(t) &= \left|I_{\text{inj},1}\right| \cos(\omega_{\text{inj}}t + \angle I_{\text{inj},1}) + \cdots, \end{aligned} \tag{6.25}$$

where the other harmonics (including DC) are suppressed in this representation.

The objective of this analysis is to compute θ from $v_{\text{osc}}(t)$ and $i_{\text{inj}}(t)$. Before we do so, however, let us set up some basic conventions.

Technical Details and Assumptions:

1. Both the oscillation waveform, $v_0(x)$, and the injection waveform, $i_{\text{inj},0}(x)$, have nonzero fundamental components, meaning $V_{\text{osc},1} \neq 0$ and $I_{\text{inj},1} \neq 0$. Note that the absence of this condition does not pose any difficulty from a mathematical standpoint—but, this assumption is reasonable to make in practice for our purposes, and it simplifies the exposition of our solution.

2. The oscillation waveform, $v_0(x)$, and the injection waveform, $i_{\text{inj},0}(x)$, are defined such that their fundamental components are aligned in the following sense:

$$N\angle V_{\text{osc},1} \equiv M\angle I_{\text{inj},1}. \tag{6.26}$$

   Although this condition may seem arbitrary, it is actually necessary to avoid confusion. For the simplest case of a sinusoidal injection and a sinusoidal oscillation voltage at the same frequency, we want θ to be a reflection of the "actual" phase difference between the two waveforms. For example, if we defined $v_0(x) = V_{\text{osc}}\cos(x)$ and $i_{\text{inj},0}(x) = I_{\text{inj}|}\sin(x)$, then $\theta = 0$ corresponds to the injection and the oscillation being in quadrature, which makes no sense.

Suppose we observe the oscillation voltage and the injection current with respect to some time reference t'. The first step is to calculate their fundamental components:

$$\begin{aligned} v_{\text{osc}}(t') &= \left|V_{\text{osc},1}\right|\cos\left(\frac{M}{N}\omega_{\text{inj}}t' + \phi_{\text{osc}}\right) + \cdots \\ i_{\text{inj}}(t') &= \left|I_{\text{inj},1}\right|\cos(\omega_{\text{inj}}t' + \phi_{\text{inj}}) + \cdots . \end{aligned} \tag{6.27}$$

To translate these signals back to our reference t, define

$$\omega_{\text{inj}}t' + \phi_{\text{inj}} \equiv \omega_{\text{inj}}t + \angle I_{\text{inj},1}. \tag{6.28}$$

Substituting back into Eq. (6.27) yields

$$\begin{aligned} v_{\text{osc}}(t) &= \left|V_{\text{osc},1}\right|\cos\left(\frac{M}{N}\omega_{\text{inj}}t + \frac{M}{N}\angle I_{\text{inj},1} - \frac{M}{N}\phi_{\text{inj}} + \phi_{\text{osc}}\right) + \cdots \\ i_{\text{inj}}(t) &= \left|I_{\text{inj},1}\right|\cos(\omega_{\text{inj}}t + \angle I_{\text{inj},1}) + \cdots . \end{aligned} \tag{6.29}$$

Comparison with Eq. (6.25) reveals that

$$\frac{M}{N}\angle I_{\text{inj},1} - \frac{M}{N}\phi_{\text{inj}} + \phi_{\text{osc}} = \theta + \angle V_{\text{osc},1}. \tag{6.30}$$

Since $N\angle V_{\text{osc},1} \equiv M\angle I_{\text{inj},1}$, we get

$$\boxed{\theta = \phi_{\text{osc}} - \frac{M}{N}\phi_{\text{inj}}.} \tag{6.31}$$

In other words, ***θ is obtained by comparing the phases of the fundamental components of the oscillation voltage and the injection current, where the phase of the injection is scaled by M/N.*** This scaling factor can be understood intuitively

by noting that the same time delay at the N^{th} harmonic corresponds to N times the phase shift.

One may wonder how our phase convention affects the representation of the lock characteristic as shown in Eq. (6.12), for example. Note that the definition of the ISF, $\tilde{\Gamma}(x)$, must be consistent, or synchronized, with the oscillation waveform $v_0(x)$. Specifically, this means that $\tilde{\Gamma}(0)$ must correspond to the phase shift incurred when the oscillator, as *represented* by $v_0(x)$, experiences an injection at $x = 0$. In light of the fact that $N\angle V_{\text{osc},1} \equiv M\angle I_{\text{inj},1}$, observe how the phase of the n^{th} harmonic of the lock characteristic can be written as

$$\begin{aligned} \alpha_n &\coloneqq nN\theta + \angle\tilde{\Gamma}_{nN} - \angle I_{\text{inj},nM} \\ &= nN\theta + \left(\angle\tilde{\Gamma}_{nN} - nN\angle V_{\text{osc},1}\right) - \left(\angle I_{\text{inj},nM} - nM\angle I_{\text{inj},1}\right). \end{aligned} \tag{6.32}$$

In other words, by relating the oscillation and injection waveforms through Eq. (6.26), the phases $\angle\tilde{\Gamma}_{nN}$ and $\angle I_{\text{inj},nM}$ are effectively referenced to the fundamental phases of the oscillation and injection waveforms, respectively.

Finally, notice how the lock characteristic is periodic with a period of $2\pi/N$. This is because shifting the oscillation voltage by $1/N^{\text{th}}$ of a cycle does not change the relative timing between the oscillation and the injection. For example, if the injection frequency is twice the oscillation frequency, an oscillation voltage which is shifted by half of a cycle appears the same from the perspective of the injection.

Examples

Let us illustrate these concepts with a few quick examples. Figure 6.17 depicts one period of the oscillation voltage and the corresponding injection current for a 1 mA sinusoidal injection at the 2^{nd} harmonic into the tail of a CMOS differential LC oscillator. The lock characteristic for this scenario was shown in Figure 6.2a. Three specific examples are shown: the lower edge of the lock range, the upper edge of the lock range, and an injection at $2f_0$.

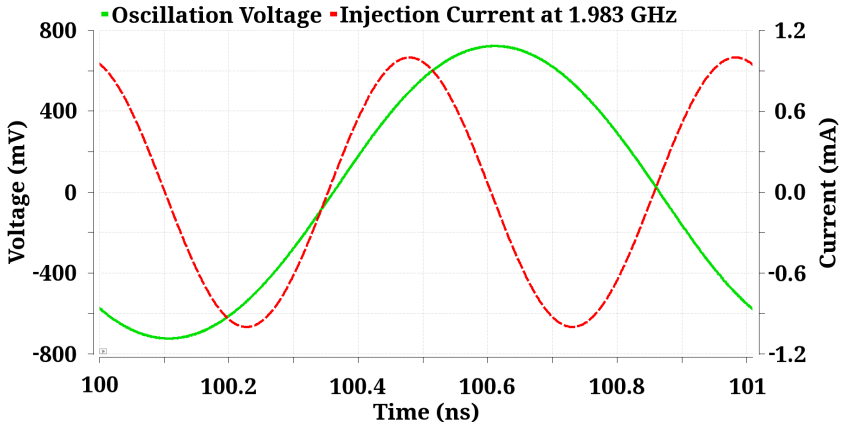

(a) $\phi_{\text{inj}} = 18°$ and $\phi_{\text{osc}} = -39°$, which yields $\theta = -48°$.

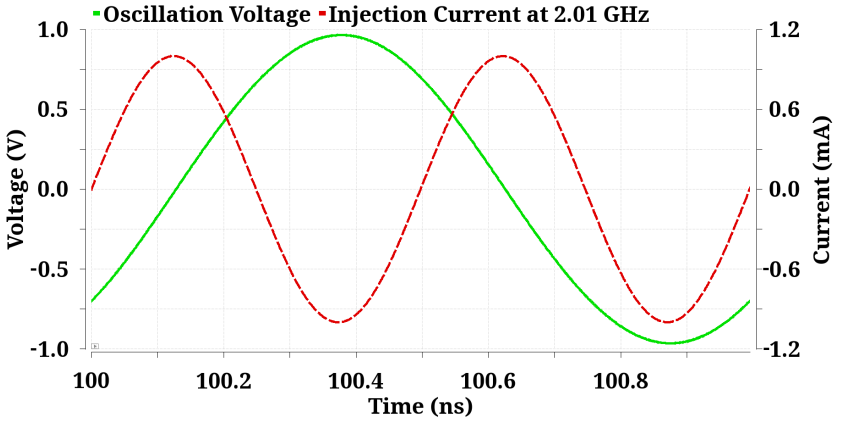

(b) $\phi_{\text{inj}} = -90°$ and $\phi_{\text{osc}} = -135°$, which yields $\theta = -90° = 90°$.

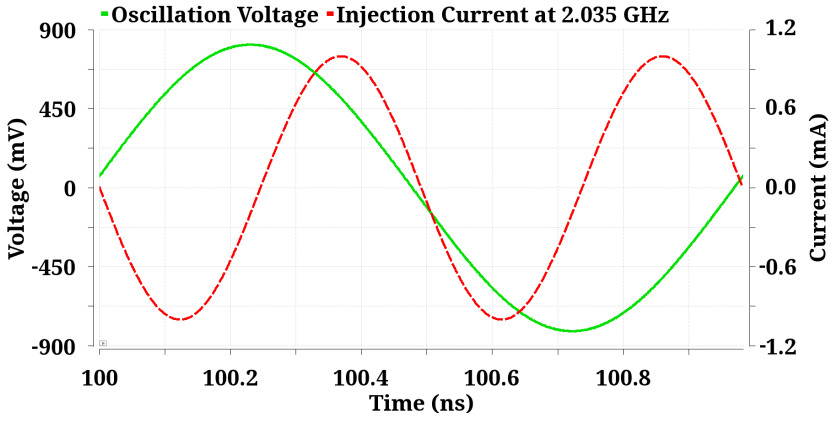

(c) $\phi_{\text{inj}} = 90°$ and $\phi_{\text{osc}} = -85°$, which yields $\theta = -130° = 50°$.

Figure 6.17: Example calculations of θ for a 2^{nd} harmonic sinusoidal injection into the tail of a differential LC oscillator. The phases ϕ_{inj} and ϕ_{osc} are computed assuming the time reference t' starts at the beginning of the depicted window.

For a more analytical example, consider the following injection current consisting of triangular pulses:[4]

$$i_{\text{inj}}(t) = 2I_{\text{inj}} \sum_{n=-\infty}^{\infty} \left[\text{tri}(8f_{\text{ref}}t - 1 - 4n) - \text{tri}(8f_{\text{ref}}t - 3 - 4n)\right], \tag{6.33}$$

and square-wave oscillation voltage:[5]

$$v_{\text{osc}}(t) = V_{\text{max}} \sum_{n=-\infty}^{\infty} \text{rect}\left(6f_{\text{ref}}t + \frac{1}{10} - 2n\right), \tag{6.34}$$

where I_{inj} is the injection current amplitude, V_{max} is the maximum voltage swing, and f_{ref} is some reference frequency. A plot of these two signals is shown in Figure 6.18 for $V_{\text{max}} = 1.2$ V, $I_{\text{inj}} = 2$ mA, and $f_{\text{ref}} = 1$ GHz. As we can see, the fundamental frequencies of the injection current and the oscillation voltage are $2f_{\text{ref}}$ and $3f_{\text{ref}}$, respectively, which means that $M = 3$ and $N = 2$.

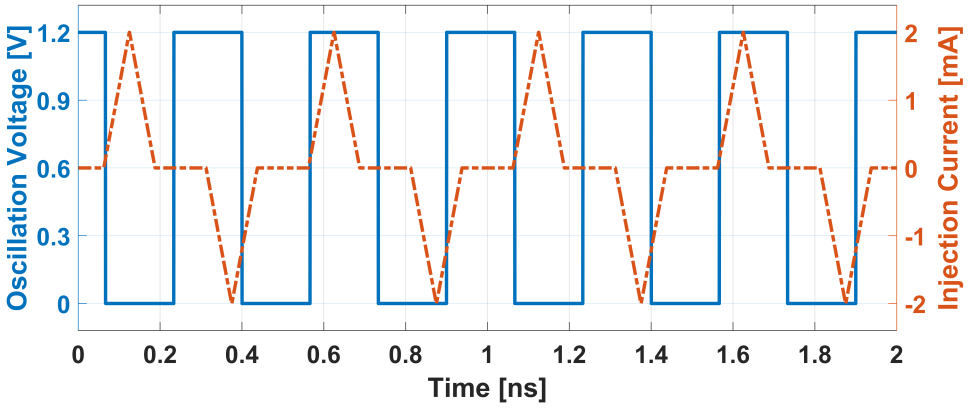

Figure 6.18: A plot of the example oscillation voltage from Eq. (6.34) and injection current from Eq. (6.33).

[4]We use the standard definition of the triangle function:

$$\text{tri}(x) := \begin{cases} 1 - |x|, & |x| \le 1 \\ 0, & \text{otherwise.} \end{cases}$$

[5]We use the standard definition of the rectangle function:

$$\text{rect}(x) := \begin{cases} 1, & |x| \le \frac{1}{2} \\ 0, & \text{otherwise.} \end{cases}$$

The fundamental components are easily shown to be

$$\begin{aligned} v_{\text{osc}}(t) &= \frac{2}{\pi} V_{\text{max}} \cos\left(6\pi f_{\text{ref}} t + \frac{\pi}{10}\right) \\ i_{\text{inj}}(t) &= \frac{8(2-\sqrt{2})}{\pi^2} I_{\text{inj}} \sin(4\pi f_{\text{ref}} t), \end{aligned} \tag{6.35}$$

from which we deduce that $\phi_{\text{osc}} = \pi/10$ and $\phi_{\text{inj}} = -\pi/2$. Therefore, we calculate

$$\theta = \phi_{\text{osc}} - \frac{M}{N}\phi_{\text{inj}} = \frac{17\pi}{20} = 153^\circ. \tag{6.36}$$

On a final note, observe how the two waveforms look identical with respect to one another, thereby leaving θ invariant, when $v_{\text{osc}}(t)$ is shifted by half of a cycle or when $i_{\text{inj}}(t)$ is shifted by a third of a cycle. Furthermore, notice how removing either the upward or the downward triangular pulses from $i_{\text{inj}}(t)$ also does not change θ, as this preserves the phase of the fundamental (while halving its amplitude).

Chapter 7

TRANSIENT BEHAVIOR: STABILITY, PULLING, AND NOISE

7.1 Introduction

Our analyses thus far have really only focused on the steady-state, locked behavior of the oscillator—namely when $d\theta/dt = 0$. In this chapter, we show how the *transient* behavior of the differential equations Eqs. (4.20) and (4.26) can be used to predict a wide range of interesting properties: stable vs. unstable modes, the dynamics of injection pulling both inside and outside of the lock range, and phase noise in both free-running and injection-locked oscillators.

7.2 Range of Stable Oscillation Phases

Recall that the lock characteristic $\Omega(\theta)$, which is the steady-state relationship between the frequency deviation $\Delta\omega \coloneqq (M/N)\,\omega_{\text{inj}} - \omega_0$ and the oscillator's phase θ under lock, is periodic in θ with a period of $2\pi/N$. Consequently, for each frequency deviation $\Delta\omega$ within the lock range, there are multiple solutions for θ to the equation $\Omega(\theta) = \Delta\omega$, which implies the existence of more than one *mode* that the oscillator can lock to. For example, the lock characteristic for a sinusoidal injection at the fundamental harmonic, given in Eq. (4.31) to be $\Delta\omega = (1/2)I_{\text{inj}}\left|\tilde{\Gamma}_1\right|\cos\left(\theta + \angle\tilde{\Gamma}_1\right)$, features two modes. In this section, we will employ a perturbation analysis of our pulling equation Eq. (4.20) to show that not all of these modes are mathematically stable, and consequently, only stable modes will be observed in practice.

We will make extensive usage of the lock characteristic, which was defined in Chapter 4 as the relationship between the frequency deviation $\Delta\omega$ and the oscillation phase θ under lock. We will work in the more general setting of an injection at the fractional M^{th}:N^{th} sub-/super-harmonic, as this does not complicate the analysis in any way. The lock characteristic can be expressed in several different ways, which we reproduce below:

$$\begin{aligned}\Omega(\theta) &\coloneqq \frac{1}{NT_{\text{inj}}}\int_{NT_{\text{inj}}} \tilde{\Gamma}\left(\frac{M}{N}\omega_{\text{inj}}t + \theta\right) i_{\text{inj}}(t)\,dt \\ &= \left\langle \tilde{\Gamma}\left(\frac{M}{N}x + \theta\right) i_{\text{inj},0}(x)\right\rangle_{2\pi N} \\ &= \frac{1}{2}\left[\frac{I_{\text{inj},0}\tilde{\Gamma}_0}{2} + \sum_{n=1}^{\infty}\left|I_{\text{inj},nM}\tilde{\Gamma}_{nN}\right|\cos\left(nN\theta + \angle\tilde{\Gamma}_{nN} - \angle I_{\text{inj},nM}\right)\right].\end{aligned} \tag{7.1}$$

Notice that we can use $\Omega(\theta)$ to write the pulling equation in the following way:

$$\frac{d\theta}{dt} = -\Delta\omega + \Omega(\theta). \tag{7.2}$$

We now carry out a perturbation analysis. Assume the injection is capable of locking the oscillator (i.e., is within the lock range), and that $\theta(t) = \theta_0 + \hat{\theta}(t)$, where θ_0 is the steady-state injection-locked phase and $\hat{\theta} \ll 1$ is some small disturbance. Then, utilizing a first-order Taylor series approximation yields the following differential equation for $\hat{\theta}(t)$:

$$\frac{d\hat{\theta}}{dt} = \Omega'(\theta_0) \cdot \hat{\theta}. \tag{7.3}$$

For θ_0 to be a stable oscillation phase under lock, $\hat{\theta}$ must decay to 0 as time progresses. That is,

$$\theta_0 \text{ is a stable mode} \qquad \Longleftrightarrow \qquad \Omega'(\theta_0) < 0. \tag{7.4}$$

In other words, θ_0 is stable if and only if the lock characteristic has a negative slope at θ_0. But, recall that the lock characteristic gives the relationship between the frequency deviation $\Delta\omega$ and the oscillator's phase. Therefore, we conclude that

$$\boxed{\theta_0 \text{ is a stable mode} \qquad \Longleftrightarrow \qquad \left.\frac{\partial \Delta\omega}{\partial \theta}\right|_{\theta=\theta_0} < 0.} \tag{7.5}$$

This explains why all of the simulated lock characteristics depicted thus far only feature data where the injection frequency f_{inj} *decreases* with the oscillator's phase θ. In the next few sections, we will see how the value of the slope itself contains important information about the oscillator as well.

7.3 Graphical Interpretation

With an understanding of how the slope of the lock characteristic affects stability, it is useful to think about the dynamics of a periodically perturbed oscillator from another perspective. We start by rearranging the pulling equation. Recall that the oscillator's total phase is equal to $\varphi(t) = \omega_{\text{inj}}t + \theta(t)$. Therefore, Eq. (7.2) can be written as

$$\Omega(\theta) = \frac{d\varphi}{dt} - \omega_0. \tag{7.6}$$

But the derivative of $\varphi(t)$ is the oscillator's *instantaneous* oscillation frequency ω_{osc}. Thus,

$$\boxed{\Omega(\theta) = \omega_{\text{osc}} - \omega_0.} \tag{7.7}$$

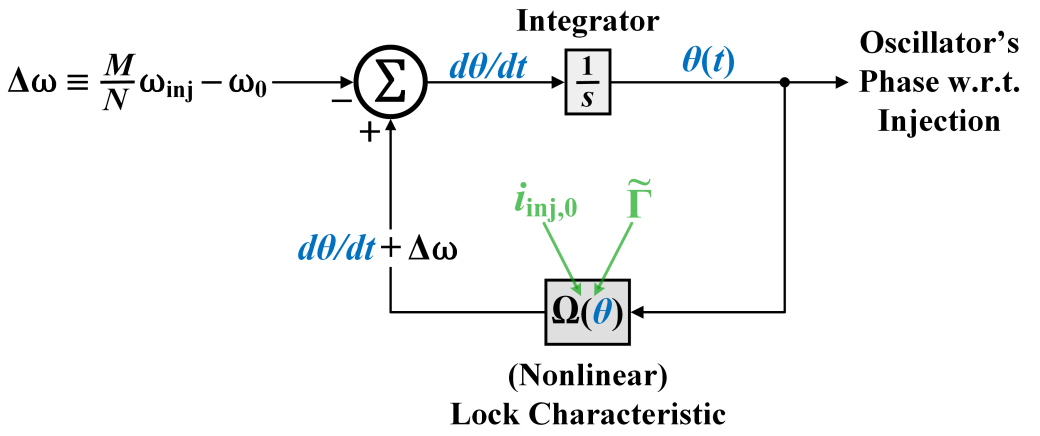

Figure 7.1: A feedback block diagram representation of fundamental pulling equation. The ISF and the injection waveform govern the behavior of the lock characteristic $\Omega(\theta)$.

In other words, the lock characteristic does not only represent the relationship between the oscillator's phase θ and the locked frequency difference $\Delta\omega$ between the injection and the oscillator—it is equal to the amount by which the oscillator's *instantaneous* frequency differs from the free-running frequency for a particular phase shift θ between the oscillator and the injection. If this difference is equal to $\Delta\omega$, then the oscillator is locked. Otherwise, any deviation between $\Omega(\theta)$ and $\Delta\omega$ causes θ to change with time, which in turn *feeds back* into the lock characteristic and alters $\Omega(\theta)$. We emphasize this feedback process by redrawing the block diagram of Figure 6.14a in the form of Figure 7.1. The averaging of the product $i_{\text{inj},0}[x-(N/M)\theta]\cdot\tilde{\Gamma}[(M/N)x]$ has been abstracted away into a single feedback block: the lock characteristic $\Omega(\theta)$, which is nonlinear with respect to θ. The frequency difference $\Delta\omega$ is portrayed as an *input* that the system is trying to match.

Let us see how the graph of the lock characteristic affects this process. A plot of a hypothetical lock characteristic is shown in Figure 7.2. Based on the pulling equation, we see that θ moves to the right or to the left whenever $\Omega(\theta)$ is above or below $\Delta\omega$, respectively. Therefore, for a given frequency deviation $\Delta\omega$ which lies within the lock range, the red arrows drawn in Figure 7.2 indicate the direction in which a perturbation from a solution to the equation $\Omega(\theta) = \Delta\omega$ will move, giving rise to the stable and unstable regions shown. Consequently, the only *stable* solution for the phase associated with the frequency deviation $\Delta\omega$ is θ_0. Observe how this reasoning jibes with our analysis of the lock characteristic's slope from Section 7.2.

We can also consider a frequency deviation $\Delta\omega_{\text{pull}}$ which is outside of the lock

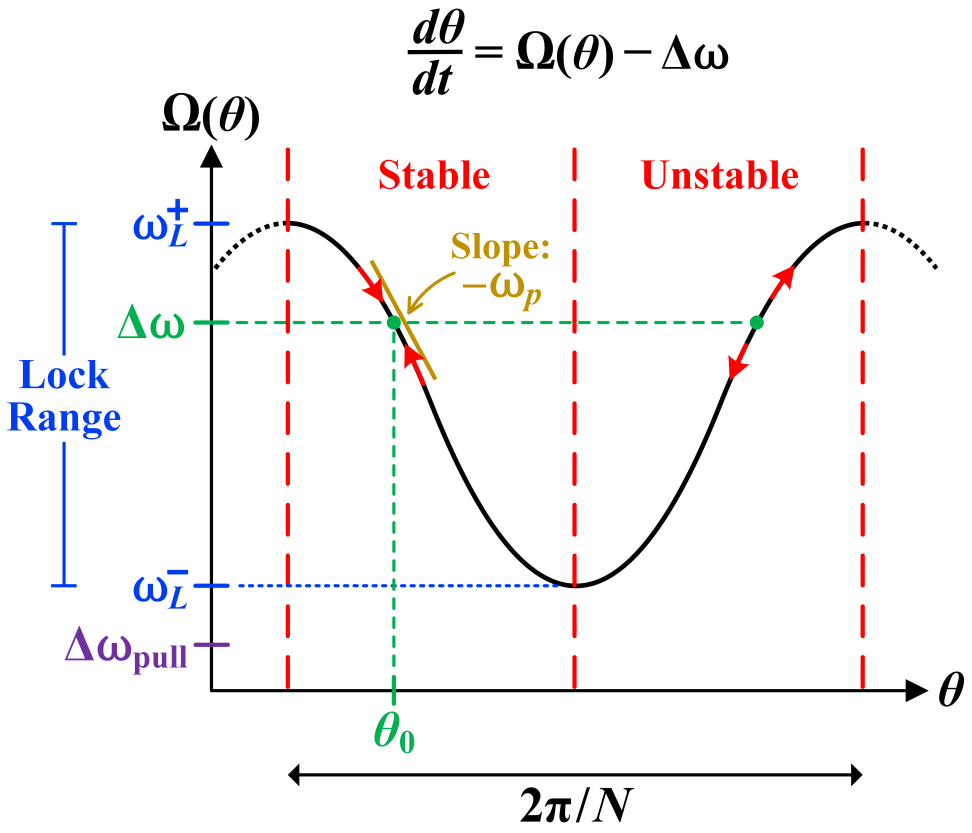

Figure 7.2: A graphical viewpoint of the lock characteristic which shows the lock range and stable vs. unstable regions. Note that the lock characteristic is periodic with a period of $2\pi/N$.

range, causing injection pulling. Now, the lock characteristic $\Omega(\theta)$ is always strictly greater than $\Delta\omega_{\text{pull}}$, and so $d\theta/dt > 0$ for all time, preventing the oscillator from ever locking. The phenomenon of "beating," first depicted in Figure 1.5, occurs as $\Omega(\theta)$ periodically moves toward and away from $\Delta\omega$. When $\Omega(\theta)$ ventures close to the lower edge of the lock range and $\Omega(\theta) - \Delta\omega_{\text{pull}}$ is small, θ will change more slowly, giving rise to the flatter portion of the curve in Figure 1.6b. Eventually, however, θ will have moved sufficiently to the right that $\Omega(\theta) - \Delta\omega_{\text{pull}}$ begins to grow, thereby increasing $d\theta/dt$ until the oscillator slips by an entire period relative to the injection. (In fact, if the upper and lower lock ranges have opposite signs ($\omega_L^- < 0 < \omega_L^+$) as is usually the case, then $|d\theta/dt| > |\Delta\omega|$ whenever $\Omega(\theta)$ is on the opposite side of zero from $\Delta\omega$, which means that the injection actually causes the oscillator's phase θ to change more rapidly during slippage than if the oscillator were free-running!) The repetition of this process creates the "beats" observed in a pulled oscillator.

7.4 The Pull-In Process

The pull-in process is a term used to describe the behavior of an oscillator within the lock range of the injection when its phase $\theta(t)$ has not yet reached its steady-state value θ_0. Solving the differential equation Eq. (7.3) for the disturbance $\hat{\theta}$ reveals that for small perturbations, the pull-in process follows an exponential decay dynamic:

$$\hat{\theta}(t) \propto e^{-t/\tau_p} \tag{7.8}$$

where the pull-in time constant τ_p is given by

$$\tau_p = -\frac{1}{\Omega'(\theta_0)}. \tag{7.9}$$

Furthermore, this means that the pull-in time constant is related to the slope of the lock characteristic through

$$\boxed{\frac{1}{\tau_p} \equiv \omega_p = -\left.\frac{\partial \Delta\omega}{\partial \theta}\right|_{\theta=\theta_0},} \tag{7.10}$$

where we defined the *pull-in frequency* $\omega_p \coloneqq 1/\tau_p$ as the reciprocal of the pull-in time constant. An example of ω_p is depicted graphically in Figure 7.2.

Finally, using the definition of $\Omega(\theta)$, we can use Eq. (7.1) to express ω_p in terms of the ISF in the following ways:

$$\begin{aligned}
\omega_p &= -\frac{1}{NT_{\text{inj}}} \int_{NT_{\text{inj}}} \tilde{\Gamma}'\left(\frac{M}{N}\omega_{\text{inj}} t + \theta_0\right) i_{\text{inj}}(t)\, dt \\
&= -\left\langle \tilde{\Gamma}'\left(\frac{M}{N}x + \theta_0\right) i_{\text{inj},0}(x) \right\rangle_{2\pi N} \\
&= \frac{1}{2}\sum_{n=1}^{\infty} nN \left|I_{\text{inj},nM}\tilde{\Gamma}_{nN}\right| \sin\left(nN\theta_0 + \angle\tilde{\Gamma}_{nN} - \angle I_{\text{inj},nM}\right).
\end{aligned} \tag{7.11}$$

A block diagram showing how the ISF's Fourier series coefficients can be used to calculate ω_p is given in Figure 7.3.

Sinusoidal Injection: In the case of a sinusoidal injection (at the N^{th} superharmonic), the only nonzero term in its Fourier series is the fundamental component or the first harmonic, whose amplitude and phase we shall denote as $I_{\text{inj}} \equiv |I_{\text{inj},1}|$ and $\angle I_{\text{inj}}$ respectively. Thus, the pull-in frequency becomes

$$\omega_p = \frac{1}{2} N I_{\text{inj}} \left|\tilde{\Gamma}_N\right| \sin\left(N\theta_0 + \angle\tilde{\Gamma}_N - \angle I_{\text{inj}}\right). \tag{7.12}$$

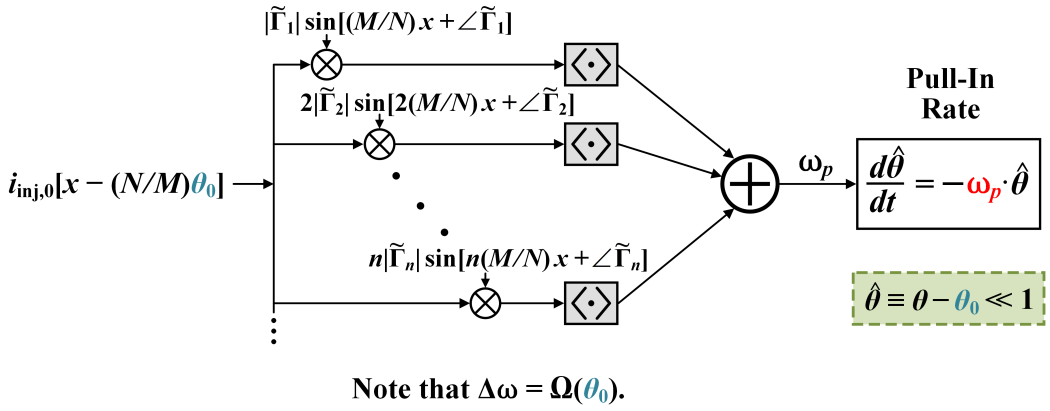

Figure 7.3: A block diagram showing how the injection waveform and the ISF interact to form the pull-in frequency.

But based on the lock characteristic of Eq. (7.1), we also know that the frequency deviation under lock between the injection and the free-running oscillator is given by

$$\Delta\omega \equiv \frac{\omega_{\text{inj}}}{N} - \omega_0 = \frac{1}{2} I_{\text{inj}} \left|\tilde{\Gamma}_N\right| \cos\left(N\theta_0 + \angle\tilde{\Gamma}_N - \angle I_{\text{inj}}\right). \tag{7.13}$$

Additionally, extremizing this lock characteristic yields the sinusoidal lock range:

$$\omega_L = \frac{1}{2} I_{\text{inj}} \left|\tilde{\Gamma}_N\right|. \tag{7.14}$$

Therefore, these three equations reveal that the pull-in frequency, the frequency deviation, and the lock range are related through a Pythagorean relationship:

$$\boxed{\omega_p = \pm N\sqrt{{\omega_L}^2 - \Delta\omega^2},} \tag{7.15}$$

where $\omega_p > 0$ if and only if θ_0 is a stable solution.

Simulation Results: Figure 7.4 depicts the Spectre simulated pull-in process for a 1 GHz 17-stage ring oscillator injection locked to a 1 GHz sinusoidal injection current for two different injection strengths. The phase deviation is introduced into the locked oscillator by injecting a small impulse of charge onto one of the nodes of the ring. This simulation was repeated for 10 different injection times which were equally distributed throughout a cycle. For each simulation, the deviation of the oscillator's phase from its steady-state value θ_0 was normalized to its initial value after the injection[1], and the result was plotted as a function of the number of elapsed

[1]We waited for 10% of a period (i.e., 0.1 ns) to allow orbital deviations to decay so the phase could be unambiguously determined through comparing threshold crossings.

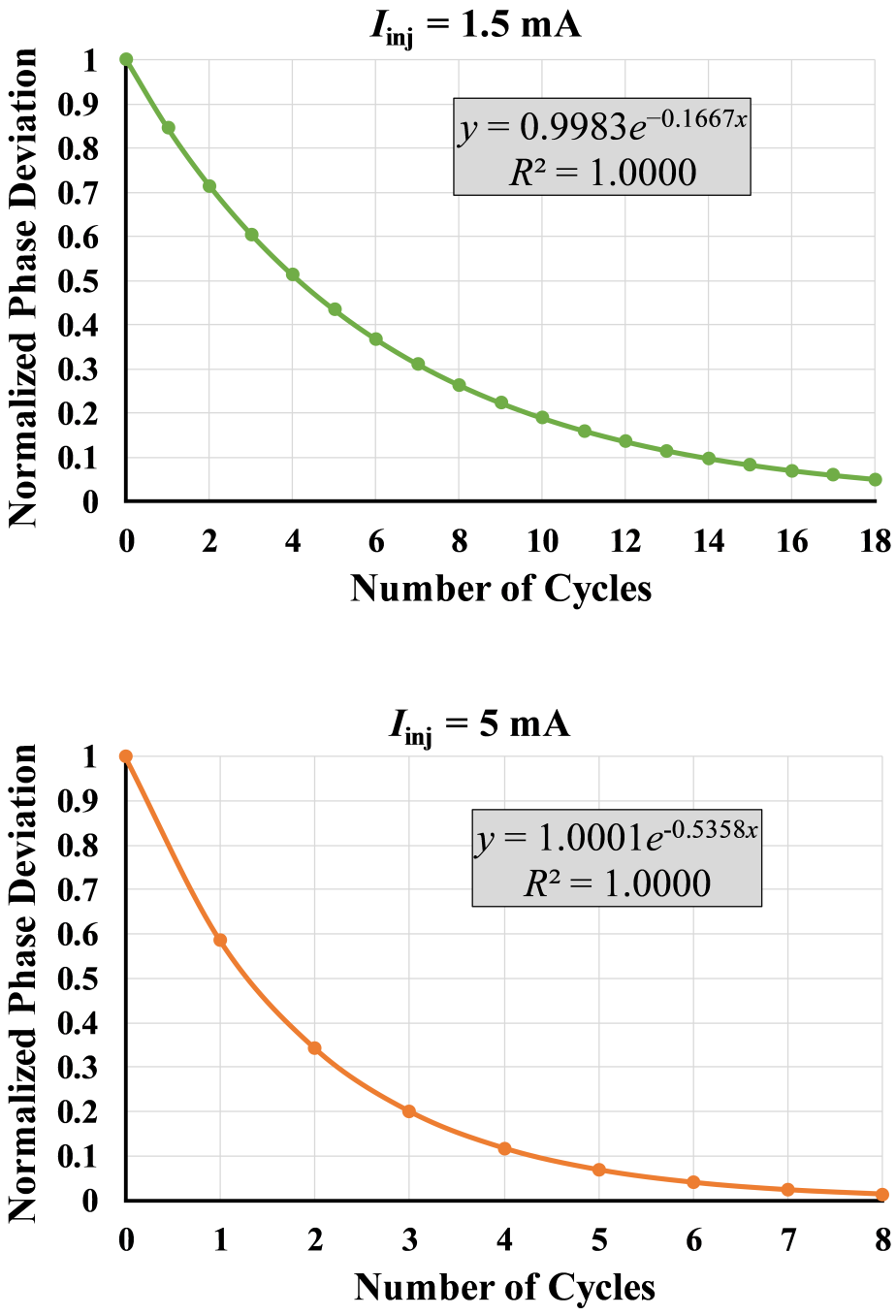

Figure 7.4: Simulated pull-in process of a sinusoidally injection-locked 17-stage ring oscillator for two different injection amplitudes.

cycles. An exponential decay dynamic is evident. At this point, let us define the pull-in "cycle constant" γ as the number of cycles needed for the phase perturbation to decay by a factor of $1/e$. Therefore,

$$\gamma = \frac{\tau_p}{T_{\text{inj}}}. \tag{7.16}$$

The simulated value of γ is easily found from the displayed trendline equation, which was averaged over all 10 simulations. Across simulations, the data points were all within 5% of each other, which led to a less than 1% total variation in γ. This supports our model's implication that the rate at which an oscillator gets pulled toward lock depends only on the current discrepancy between the oscillator's phase and its steady-state solution, $\hat{\theta} \equiv \theta - \theta_0$, and not on how the discrepancy was initially introduced.

Next, we will calculate the value of γ predicted by our model. The magnitude of the ISF's fundamental component is $|\tilde{\Gamma}_1| = 2.24 \times 10^{11}$ rad/C. Since $\Delta\omega = 0$, we know that $\theta_0 + \angle\tilde{\Gamma}_1 - \angle I_{\text{inj}} = \pi/2$. Therefore, the pull-in frequency simplifies to $\omega_p = I_{\text{inj}} \left|\tilde{\Gamma}_1\right| /2$. The results of this analysis are summarized in the table below. As we can see, simulation and theory match quite closely, even for larger injections.

Injection Amplitude	Theoretical γ	Simulated γ
$I_{\text{inj}} = 1.5$ mA	$\dfrac{2f_{\text{inj}}}{I_{\text{inj}}\left\|\tilde{\Gamma}_1\right\|} = 5.95$	$\dfrac{1}{0.1667} = 6$
$I_{\text{inj}} = 5$ mA	$\dfrac{2f_{\text{inj}}}{I_{\text{inj}}\left\|\tilde{\Gamma}_1\right\|} = 1.79$	$\dfrac{1}{0.5358} = 1.87$

Let us look at an example with a more complicated lock characteristic. Figure 7.5 shows the Spectre simulated pull-in process for a 1 GHz CMOS differential LC oscillator injection locked to a 1 GHz 0.5 mA sinusoidal injection current. Instead of differentiating the pulling equation involving the APF Eq. (5.17) directly, we numerically calculated the slope of the lock characteristic. However, because the oscillator is current-limited, its behavior should also be reasonably well-captured by Mirzaei's Generalized Adler's equation, the simplified version of the pulling equation for ideal LC oscillators derived in Section 5.7. To that end, we can differentiate the lock characteristic from Eq. (5.46) to obtain the following pull-in time constant [21]:

$$\tau_p = \frac{2Q}{\omega_0} \frac{\left(I_{\text{osc}} + I_{\text{inj}} \cos\theta_0\right)^2}{I_{\text{inj}}(I_{\text{inj}} + I_{\text{osc}} \cos\theta_0)}. \tag{7.17}$$

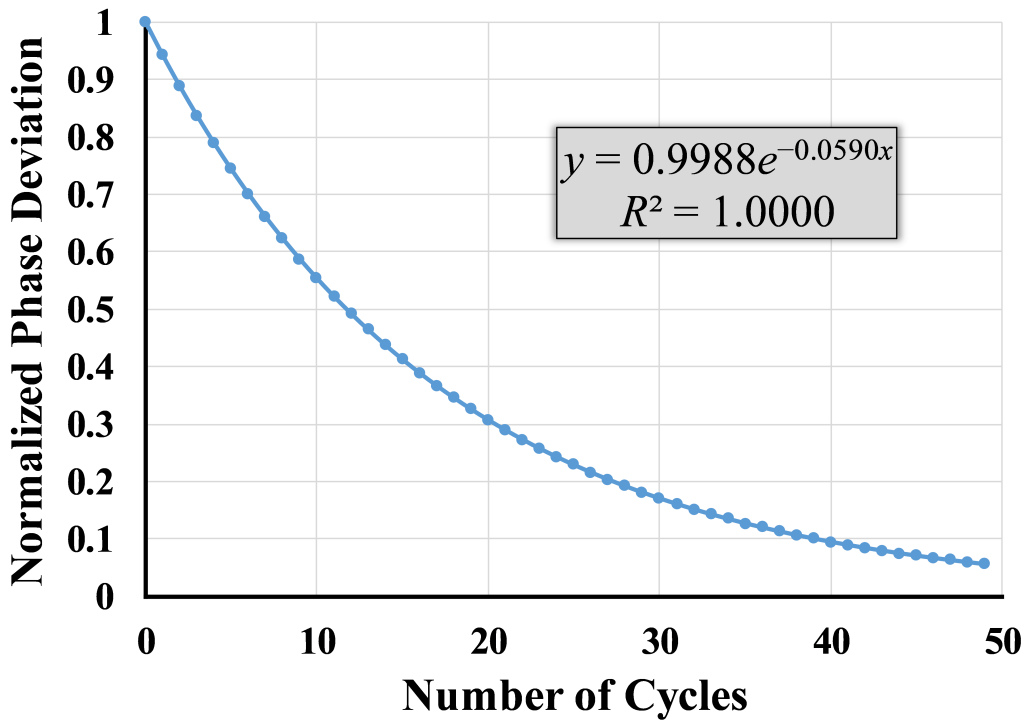

Figure 7.5: Simulated pull-in process of a sinusoidally injection-locked CMOS differential LC oscillator.

A comparison of these two approaches to the simulated pull-in cycle constant is given in the table below. Note that this oscillator features an oscillator current of $I_{\text{osc}} = (4/\pi)$ mA and a quality factor of $Q = 15$, whereas the solution for the oscillator's phase is $\theta_0 = 0$. Once again, simulation and theory match very closely.

Theor. γ from $\Omega'(\theta_0)$	Theor. γ from Eq. (7.17)	Simulated γ
17.4	16.9	$\dfrac{1}{0.059} = 16.9$

The Large-Perturbation Pull-In Process for a Sinusoidal Injection

It turns out that for the case of a sinusoidal injection, we can actually solve the pulling equation exactly—without assuming that $\theta(t)$ only exhibits small perturbations from its steady-state locked value θ_0. Note that this analysis will parallel the treatment by Adler [47] and Kurokawa [52], which was for the specific case of an LC oscillator injected at the fundamental harmonic.

Suppose a sinusoidal injection at the N^{th} superharmonic, represented by the phasor $I_{\text{inj}}e^{j\angle I_{\text{inj}}}$, pulls the oscillator toward lock. Then, the pulling equation Eq. (6.2) can

be written as

$$\begin{aligned}\frac{d\theta}{dt} &= \omega_0 - \frac{\omega_{\text{inj}}}{N} + \frac{1}{2} I_{\text{inj}} \left|\tilde{\Gamma}_N\right| \cos(N\theta + \angle\tilde{\Gamma}_N - \angle I_{\text{inj}}) \\ &= -\Delta\omega + \omega_L \cos N\tilde{\theta},\end{aligned} \tag{7.18}$$

where we have used the definition of $\Delta\omega$, substituted in the lock range ω_L for a sinusoidal injection at the N^{th} superharmonic, and defined a new phase variable $\tilde{\theta}$ out of notational convenience via

$$N\tilde{\theta} \equiv N\theta + \angle\tilde{\Gamma}_N - \angle I_{\text{inj}}, \tag{7.19}$$

which simply differs from θ by a constant offset. Note that for this analysis, we assume that the oscillator is *within* the lock range of the injection; that is, $|\Delta\omega| < \omega_L$. Separating variables, we get

$$\frac{d\tilde{\theta}}{-\Delta\omega + \omega_L \cos N\tilde{\theta}} = dt. \tag{7.20}$$

Since $|\Delta\omega| < \omega_L$, we can apply the integral Eq. (C.3) from Appendix C.1:

$$\frac{2}{\sqrt{{\omega_L}^2 - \Delta\omega^2}} \tanh^{-1}\left[\frac{\omega_L + \Delta\omega}{\sqrt{{\omega_L}^2 - \Delta\omega^2}} \tan\left(\frac{N\tilde{\theta}}{2}\right)\right] = Nt + C, \tag{7.21}$$

where C is an integration constant. But we know that $\sqrt{{\omega_L}^2 - \Delta\omega^2} = \omega_p/N$, assuming the steady-state solution is stable. Thus,

$$\tan\left(\frac{N\tilde{\theta}}{2}\right) = \frac{1}{N}\frac{\omega_p}{\omega_L + \Delta\omega} \tanh\left(\frac{\omega_p t + \phi_0}{2}\right), \tag{7.22}$$

where the constant ϕ_0 is set by initial conditions.

Observe the important fact that $\theta(t)$ always tends toward the *stable* solution (as expected). This can be seen by noting that since $\lim_{x\to\infty} \tanh(x) = 1$, the steady-state solution $\tilde{\theta}_0$ for $\tilde{\theta}$ satisfies

$$\tan\left(\frac{N\tilde{\theta}_0}{2}\right) = \frac{1}{N}\frac{\omega_p}{\omega_L + \Delta\omega}. \tag{7.23}$$

Using the half-angle formula for the tangent function and recalling that the lock characteristic is $\Delta\omega = \omega_L \cos N\tilde{\theta}_0$, we can rearrange this equation to get

$$\sin(N\tilde{\theta}_0) = \frac{1}{N}\frac{\omega_p}{\omega_L}. \tag{7.24}$$

This is consistent with Eq. (7.12). Since we replaced $\sqrt{{\omega_L}^2 - \Delta\omega^2}$ with ω_p/N earlier, this shows that $\omega_L \sin(N\tilde{\theta}_0) > 0$, which indicates that the steady-state solution $\tilde{\theta}_0$ for $\tilde{\theta}$ is indeed stable.

Finally, let us rewrite the solution for $\tilde{\theta}(t)$ in terms of its steady-state value $\tilde{\theta}_0$:

$$\boxed{\tan\left(\frac{N\tilde{\theta}}{2}\right) = \tan\left(\frac{N\tilde{\theta}_0}{2}\right)\tanh\left(\frac{\omega_p t + \phi_0}{2}\right).} \tag{7.25}$$

By using the approximation $\tanh x \approx 1 - 2e^{-2x}$ for $x \gg 1$, one can verify that this solution reduces to the small-perturbation pull-in dynamic derived above in Eq. (7.8) as time progresses.

7.5 The Spectrum of an Injection-Pulled Oscillator

Our derivation above begs the question of what would happen if $|\Delta\omega| > \omega_L$ when Eq. (7.20) is integrated; that is, what if the oscillator is *outside* the lock range of the injection. Before carrying out this calculation, however, let us think about what we qualitatively expect the behavior of an injection-*pulled* oscillator to be. Because the oscillator is unable to lock to the injection and hence θ never reaches a steady-state *constant* value, the periodicity of the oscillator's output is corrupted, resulting in a frequency spectrum which exhibits a rich collection of tones, or sidebands. This behavior has been treated analytically by a number of authors [38], [86], [104], but only for the case of an LC oscillator being pulled near (the fundamental of) its free-running frequency.

In general, Eq. (4.20) can be solved numerically to observe the time evolution of the oscillator's phase θ. Of course, this information alone may not reveal all of the properties of the spectrum of $v_{\text{osc}}(t)$, since amplitude modulation (i.e., orbital deviations) is also present in general. Still, $\theta(t)$ readily captures the way in which a pulled oscillator "beats" at a low frequency, which is typically considered to be the salient feature of injection pulling. In this section, we analytically describe the scenario where an oscillator is injection pulled by a sinusoidal injection at the N^{th} superharmonic. In doing so, we also derive a simple expression which quantifies the aforementioned beat frequency.

Again, we start with the superharmonic pulling equation Eq. (6.2) from Section 6.1 and echo the first few steps of Section 7.4 to arrive at the separated differential equation for the phase $\tilde{\theta} \equiv \theta + (\angle\tilde{\Gamma}_N - \angle I_{\text{inj}})/N$ given in Eq. (7.20):

$$\frac{d\tilde{\theta}}{-\Delta\omega + \omega_L \cos N\tilde{\theta}} = dt.$$

This time, however, $|\Delta\omega| > \omega_L$, and so we apply the integral Eq. (C.1) from Appendix C.1:

$$\frac{2}{\sqrt{\Delta\omega^2 - {\omega_L}^2}} \tan^{-1}\left[-\frac{\omega_L + \Delta\omega}{\sqrt{\Delta\omega^2 - {\omega_L}^2}} \tan\left(\frac{N\tilde{\theta}}{2}\right)\right] = Nt + C, \tag{7.26}$$

At this point, we define the *beat frequency* ω_b as

$$\boxed{\omega_b \coloneqq N\sqrt{\Delta\omega^2 - {\omega_L}^2}.} \tag{7.27}$$

Rearranging, we have that

$$\boxed{\tan\left(\frac{N\tilde{\theta}}{2}\right) = -\frac{1}{N}\frac{\omega_b}{\omega_L + \Delta\omega} \tan\left(\frac{\omega_b t + \phi_0}{2}\right),} \tag{7.28}$$

where ϕ_0 is again set by initial conditions. The tangent function has a period of π, and so $\theta(t)$ is periodic with the beat frequency ω_b (hence its name). Thus, elementary phase modulation theory tells us that the distance between adjacent sidebands is ω_b.

Examples

Figure 7.6 shows two examples of the magnitude spectrum of an injection-pulled 17-stage ring oscillator, obtained via an FFT of a Spectre transient simulation over several hundred injection periods. For both examples, the spectrum is also calculated numerically by solving the pulling equation Eq. (4.20) over several thousand injection periods. Because the pulling equation only conveys phase information, we normalized the spectrum by the amplitude of the strongest tone, leaving us with a unit-less y-axis. The match is reasonable—note that any deviations between the actual and ISF-predicted lock characteristics will contribute directly to discrepancies between the simulated and numerically calculated spectra.

Because the injection is sinusoidal, we should also be able to analytically predict the *distance* between adjacent sidebands via $\omega_b = \sqrt{\Delta\omega^2 - {\omega_L}^2}$. To focus on the predictive power of this formula, we will use the *simulated* upper and lower lock ranges for ω_L instead of the theoretical lock range predicted by the ISF-based lock characteristic. For the first example of Figure 7.6a where $f_{\text{inj}} = 1.04$ GHz, the simulated upper lock range is $f_L^+ = 23.8$ MHz and the frequency deviation is $\Delta f = 38.8$ MHz. For the second example of Figure 7.6b where $f_{\text{inj}} = 0.95$ GHz, the simulated lower lock range is $f_L^- = -30.6$ MHz and the frequency deviation is $\Delta f = -51.3$ MHz. The comparison between simulation and theory is summarized in the table below:

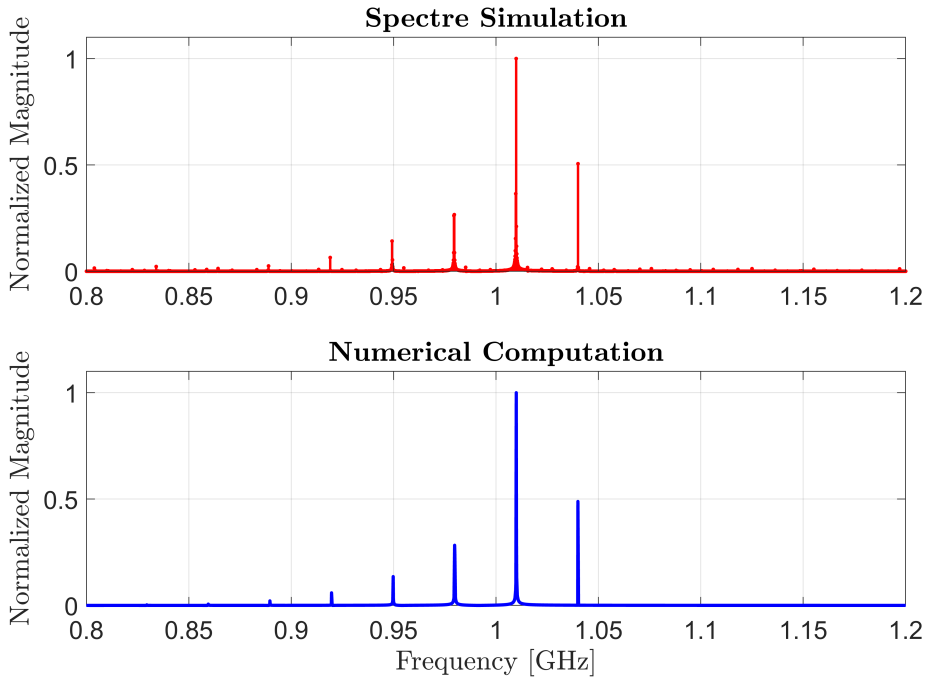

(a) $f_{\text{inj}} = 1.04$ GHz

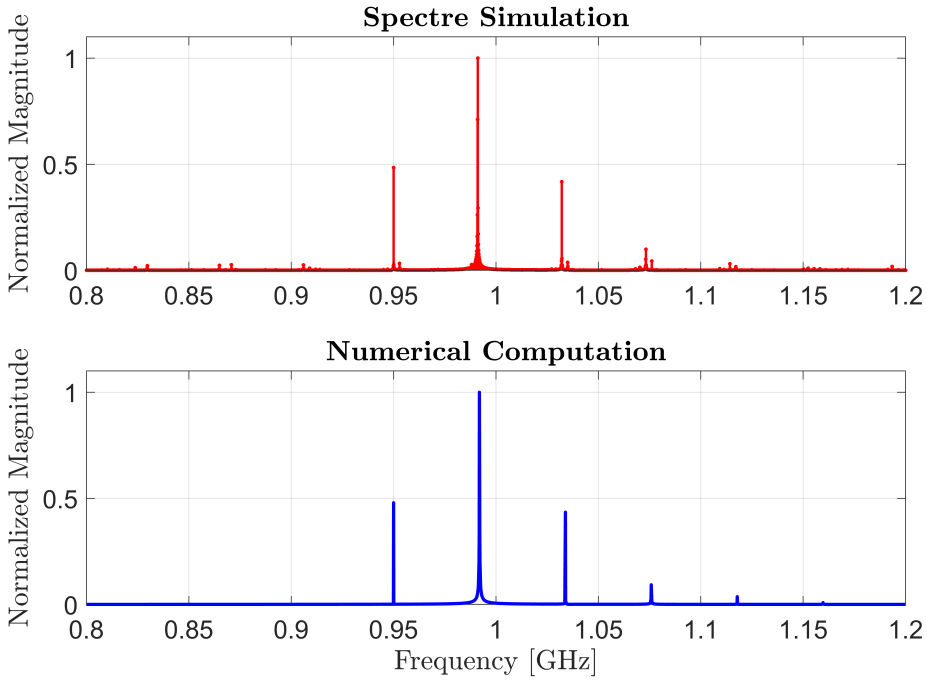

(b) $f_{\text{inj}} = 0.95$ GHz

Figure 7.6: Two examples of the magnitude spectrum of an injection-pulled 17-stage ring oscillator. The free-running frequency is $f_0 = 1.0013$ GHz and the injection is sinusoidal with an amplitude of $I_{\text{inj}} = 1.5$ mA.

Injection Frequency	Theoretical f_b	Simulated f_b
$f_{\text{inj}} = 1.04$ GHz	$\sqrt{\Delta f^2 - {f_L}^2} = 30.6$ MHz	30.4 MHz
$f_{\text{inj}} = 0.95$ GHz	$\sqrt{\Delta f^2 - {f_L}^2} = 41.2$ MHz	40.9 MHz

Let us consider an example where the oscillator is at the cusp of being injection locked. Figure 7.7 shows the spectrum of the 17-stage ring oscillator being injection pulled at $f_{\text{inj}} = 0.97$ GHz, which is barely below the lower edge of the lock range at $f_0 + f_L^- = 0.9707$ GHz. In this situation, the dominant tone is no longer one sideband away from the injection as we saw in Figure 7.6 but is instead at the injection frequency [104]. Again, notice the agreement between the numerically calculated and the Spectre simulated results. Also, the predicted distance between sidebands is $\sqrt{\Delta f^2 - {f_L}^2} = 6.6$ MHz, which matches the simulated value of $f_b = 6.8$ MHz.

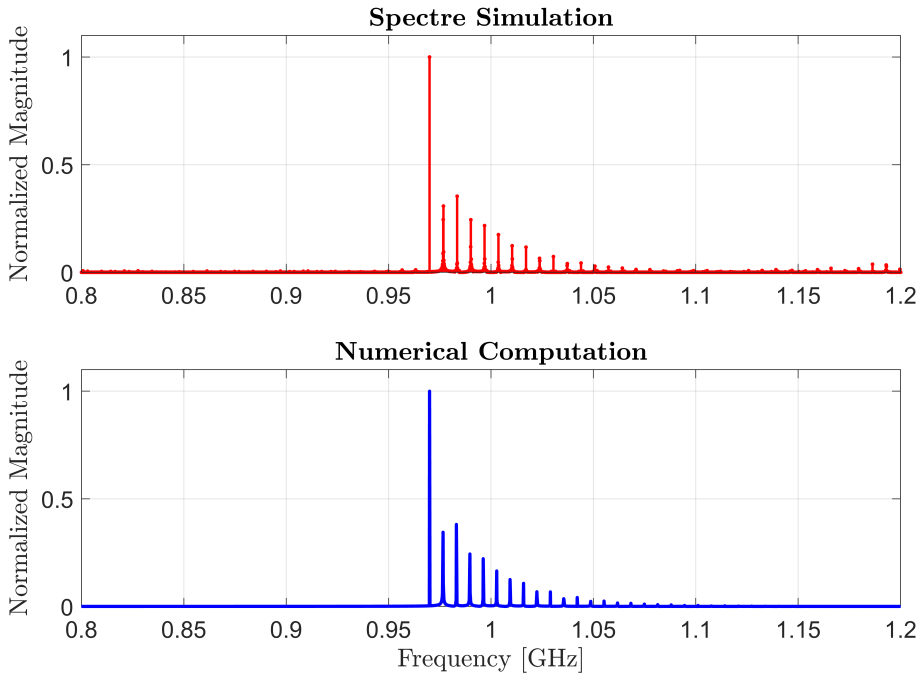

Figure 7.7: Magnitude spectrum of a 1.0013 GHz 17-stage ring oscillator pulled by a 1.5 mA sinusoidal injection at 0.97 GHz.

Our final example examines the opposite scenario where the injection is very far away from the edge of the lock range. Figure 7.8 shows the spectrum of a 1 GHz Colpitts oscillator perturbed by a 7.5 mA sinusoidal injection at 0.7 GHz. The lower lock range at this injection amplitude is $f_L^- = -135$ MHz, indicating that the

minimum injection frequency that can lock the oscillator is 0.865 GHz. Because this is an LC oscillator, we need to account for amplitude modulation by the injection. This was done by solving the pulling equation of Eq. (5.17), which includes the APF augmentation, *and* by assuming the following form for the oscillation voltage:

$$v_{\text{osc}}(t) \propto [1 + \xi(t)] \cdot \cos[\omega_{\text{inj}} t + \theta(t)],$$

where the amplitude deviation term ξ was also updated at every time step due to its dependence on θ [see Eq. (5.14)]. As we can see from Figure 7.8, incorporating the APF into the analysis is critical here. Furthermore, an ISF-only model would allow us to use the formula $f_b = \sqrt{\Delta f^2 - {f_L}^2}$, which erroneously predicts a beat frequency of 268 MHz. Finally, note that as the injection becomes weaker or moves further away, the magnitude of the sideband on the opposite side of the main tone from the injection (i.e., at 1.3 GHz in our example) will approach the magnitude of the tone at the injection [87], [88], [105].

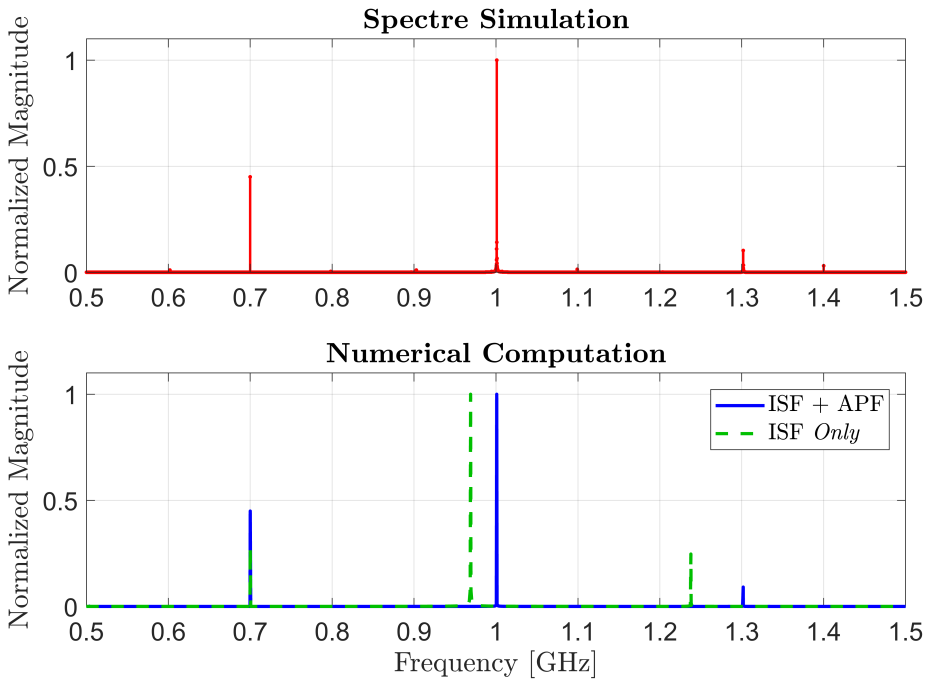

Figure 7.8: Magnitude spectrum of a 1 GHz Colpitts oscillator pulled by a 7.5 mA sinusoidal injection at 0.7 GHz.

7.6 The Phase Noise of a Free-Running Oscillator

There is a deep mathematical connection between the concepts of phase noise and injection pulling. At its core, the relationship between these two phenomena stems

from the fact that phase noise can be interpreted as the result of being pulled by small, random noise currents. Indeed, the impulse sensitivity function (ISF) was first used by Hajimiri and Lee [87], [88] to characterize phase noise within an oscillator. As fully autonomous systems, oscillators do not possess an absolute time reference, which explains why perturbations to their phase both manifest immediately and remain permanently. Mathematically, this is expressed by the unit-step function which appears in the time-varying impulse response of the phase, as we saw in Eq. (4.5) and Figure 4.1. Therefore, one can surmise that the oscillator's phase response can be viewed as a time-varying *integrator* of external disturbances. Consequently, it becomes possible for a deterministic, periodic input to effect a fixed average phase shift per period, thereby changing the oscillation frequency. On the other hand, a *random* perturbation would cause the phase to become increasingly less predictable over time. Physically, this property of oscillators bears significant implications—it allows oscillators to exhibit entrainment and synchronization phenomena, and it fundamentally underlies the mechanism by which clock jitter grows unbounded with time [106].

In this section, we illuminate this connection by using our phase pulling equation to calculate the phase noise spectrum of an arbitrary (free-running) oscillator subject to white noise, which was originally derived by Hajimiri and Lee [87], [88]. Before we do so, however, we will first show the much simpler case of how Adler's equation [47] leads to Leeson's phase noise expression for an ideal LC oscillator [107], an exercise first carried out by Mirzaei [104].

The Phase Noise of an Ideal LC Oscillator: From Adler to Leeson

We start with Adler's equation:

$$\frac{d\theta}{dt} = \omega_0 - \omega_{\text{inj}} - \frac{\omega_0}{2Q}\frac{I_{\text{inj}}}{I_{\text{osc}}}\sin\theta. \tag{7.29}$$

Let $i_{\text{inj}}(t) = i_n \cos[(\omega_0 + \Delta\omega)t]$ be a small, sinusoidal noise current at an offset frequency $\Delta\omega$ from free-running.[2] Thus, $I_{\text{inj}} = i_n \ll I_{\text{osc}}$ and $\omega_{\text{inj}} = \omega_0 + \Delta\omega$. To characterize phase noise, we write the total phase as $\varphi \equiv \omega_{\text{inj}}t + \theta = \omega_0 t + \hat{\phi}$, where $\hat{\phi}$ is the perturbation from the free-running phase $\omega_0 t$ induced by the current. That is, $\hat{\phi}$ is the *phase noise*. Substituting into Adler's equation, we get

$$\frac{d\hat{\phi}}{dt} = -\frac{\omega_0}{2Q}\frac{i_n}{I_{\text{osc}}}\sin\left(-\Delta\omega t + \hat{\phi}\right). \tag{7.30}$$

[2]Noise "near" other harmonics is irrelevant because Adler's equation implicitly assumes that the ISF is perfectly sinusoidal and hence has no components at DC or higher-order harmonics.

Because $\hat{\phi}$ represents noise, we assume it is *small* in the sense that $\left|\hat{\phi}'\right| \ll |\Delta\omega|$. Applying this approximation and solving the differential equation, we obtain

$$\hat{\phi} = -\frac{\omega_0}{2Q\Delta\omega}\frac{i_n}{I_{\text{osc}}}\cos(\Delta\omega t). \tag{7.31}$$

On average, $\langle\hat{\phi}\rangle = 0$, but the *mean-square variation* of the phase is

$$\left\langle\hat{\phi}^2\right\rangle = \frac{1}{2}\left(\frac{\omega_0}{2Q\Delta\omega}\right)^2\frac{{i_n}^2}{{I_{\text{osc}}}^2}. \tag{7.32}$$

For an LC oscillator featuring a loss resistance R, the power spectral density of the noise current can be written as

$$\frac{\overline{i_n^2}}{\Delta f} = \frac{4FkT}{R} \tag{7.33}$$

where F is an empirical noise-fitting factor, left unspecified by Leeson, but later separately clarified by Hajimiri [87], Rael [108], and Hegazi [109], [110], among others.

Note that noise current on the other side of the free-running frequency (i.e., $\omega_{\text{inj}} = \omega_0 - \Delta\omega$) contributes the same amount of variance in the phase. So, the (single-sideband) power spectral density of the phase is

$$S_\phi(\Delta\omega) = 2\times\frac{\mathbb{E}\left[\left\langle\hat{\phi}^2\right\rangle\right]}{\Delta f} = 2\times\frac{1}{2}\left(\frac{\omega_0}{2Q\Delta\omega}\right)^2\frac{1}{{I_{\text{osc}}}^2}\times\frac{\overline{i_n^2}}{\Delta f}. \tag{7.34}$$

Thus, the single-sideband phase noise at an offset $\Delta\omega$ is given by

$$\mathcal{L}\{\Delta\omega\} = S_\phi(\Delta\omega) = \left(\frac{\omega_0}{2Q\Delta\omega}\right)^2\frac{4FkT}{{I_{\text{osc}}}^2R} = \frac{2FkT}{P}\left(\frac{\omega_0}{2Q\Delta\omega}\right)^2, \tag{7.35}$$

where P is the average power dissipated by the oscillator. This is the result from Leeson [107] in the $1/f^2$ region.[3]

The Phase Noise of a General Oscillator

This time, we will use the model for the phase of an oscillator under injection developed in Chapter 4. However, because we are interested in noise, let us hold off on averaging the differential equation and start with Eq. (4.16) instead:

$$\frac{d\theta}{dt} = \omega_0 - \omega_{\text{inj}} + \tilde{\Gamma}\left(\omega_{\text{inj}}t + \theta\right)i_{\text{inj}}(t). \tag{7.36}$$

[3]The relationship $\mathcal{L}\{\Delta\omega\} = S_\phi(\Delta\omega)$ does not hold for very close-in offsets $\Delta\omega$, in which case one must defer to the full derivation of the Lorentzian spectrum.

Now, let $i_{\text{inj}}(t) = i_n \cos[(n\omega_0 + \Delta\omega)t]$ be a small, sinusoidal noise current at an offset $\Delta\omega$ from the n^{th} harmonic of the free-running frequency, where $n = 0, 1, 2, \ldots$ is a nonnegative integer. Thus, the injection frequency is $\omega_{\text{inj}} = n\omega_0 + \Delta\omega$. Again, we write the total phase as $\varphi = \omega_{\text{inj}}t + \theta = \omega_0 t + \hat{\phi}$, where $\hat{\phi}$ is the *phase noise*. Substituting, we get

$$\frac{d\hat{\phi}}{dt} = \tilde{\Gamma}\left(\omega_0 t + \hat{\phi}\right) \cdot i_n \cos[(n\omega_0 + \Delta\omega)t]\,. \tag{7.37}$$

Notice that $\Delta\omega$ is arbitrary, and so the right-hand-side is no longer periodic. To resolve non-periodic scenarios, we must resort to an indefinite average [96]:

$$\frac{d\hat{\phi}}{dt} = \lim_{T\to\infty} \frac{1}{T} \int_T \tilde{\Gamma}\left(\omega_0 t + \hat{\phi}\right) \cdot i_n \cos[(n\omega_0 + \Delta\omega)t]\, dt. \tag{7.38}$$

Again, the solution to the averaged equation can be shown to be $\delta(\varepsilon)$-close to the original equation on a time scale of $1/\varepsilon$, where $\delta(\varepsilon)$ is a suitable order function [96].

At this point, it becomes convenient to expand the ISF in terms of its Fourier series. Referring to Eqs. (4.24) and (4.25), we get

$$\frac{d\hat{\phi}}{dt} = i_n \lim_{T\to\infty} \frac{1}{T} \int_T \left[\frac{\tilde{\Gamma}_0}{2} + \sum_{k=1}^{\infty} \left|\tilde{\Gamma}_k\right| \cos\left(k\omega_0 t + k\hat{\phi} + \angle\tilde{\Gamma}_k\right) \right] \cos[(n\omega_0 + \Delta\omega)t]\, dt.$$

Recall from above that $n\omega_0 = \omega_{\text{inj}} - \Delta\omega$. Therefore, the most significant term that emerges from this averaging integral is the "DC component" from the frequency difference term at $k = n$:

$$\frac{d\hat{\phi}}{dt} \approx \frac{i_n \left|\tilde{\Gamma}_n\right|}{2} \cos\left(\Delta\omega t - n\hat{\phi} - \angle\tilde{\Gamma}_n\right). \tag{7.39}$$

Assuming the phase noise is small in the sense that $\left|n\hat{\phi}'\right| \ll |\Delta\omega|$ and solving the differential equation, we get

$$\hat{\phi} = \frac{i_n \left|\tilde{\Gamma}_n\right|}{2\Delta\omega} \sin\left(\Delta\omega t - \angle\tilde{\Gamma}_n\right), \tag{7.40}$$

which has a *mean-square variation* of

$$\left\langle \hat{\phi}^2 \right\rangle = \frac{1}{2} \left(\frac{i_n \left|\tilde{\Gamma}_n\right|}{2\Delta\omega} \right)^2. \tag{7.41}$$

Assuming the noise is white and therefore has a flat spectrum, we now account for all the other (uncorrelated) noise components of equal amplitude at the same *absolute*

offset $\pm\Delta\omega$ from different harmonics $n\omega_0$ of the free-running frequency. Note that for $n = 0$, we only have $\omega_{\text{inj}} = \Delta\omega$ since the frequency must be positive. This yields

$$\left\langle \hat{\phi}^2 \right\rangle_{\text{Total}} = \left(\frac{i_n}{2\Delta\omega}\right)^2 \left(\frac{1}{2}\left|\tilde{\Gamma}_0\right|^2 + \sum_{n=1}^{\infty}\left|\tilde{\Gamma}_n\right|^2\right) = 2\left(\frac{i_n\tilde{\Gamma}_{\text{rms}}}{2\Delta\omega}\right)^2, \tag{7.42}$$

where $\tilde{\Gamma}_{\text{rms}}$ is the root-mean-square of the ISF. Note that Parseval's identity was used:

$$2\tilde{\Gamma}_{\text{rms}}^2 \equiv \frac{1}{\pi}\int_{2\pi}\tilde{\Gamma}^2(x)\,dx = \frac{1}{2}\left|\tilde{\Gamma}_0\right|^2 + \sum_{n=1}^{\infty}\left|\tilde{\Gamma}_n\right|^2. \tag{7.43}$$

Thus, the single-sideband phase noise at an offset $\Delta\omega$ is given by

$$\mathcal{L}\{\Delta\omega\} = S_\phi(\Delta\omega) = \frac{\mathbb{E}\left[\left\langle \hat{\phi}^2 \right\rangle_{\text{Total}}\right]}{\Delta f} = \frac{\tilde{\Gamma}_{\text{rms}}^2}{2\cdot\Delta\omega^2}\cdot\frac{\overline{i_n^2}}{\Delta f}, \tag{7.44}$$

which is the result from Hajimiri [87], [88] in the $1/f^2$ region. Again, for very close-in offsets, $\mathcal{L}\{\Delta\omega\} = S_\phi(\Delta\omega)$ is no longer valid and one must defer to the full derivation of the Lorentzian spectrum.

7.7 The Phase Noise of an Injection-Locked Oscillator

Due to the dynamics of the locking phenomena, injection-locked oscillators display qualitatively different phase noise behavior than free-running oscillators. In this section, we use the perturbation analysis carried out in Section 7.2 to express the phase noise of an injection-locked oscillator in terms of the phase noise profiles of the underlying free-running oscillator and of the injection signal. The key piece of insight that governs this analysis is that it *takes time* for the oscillator to track the phase of the injection signal. To form a more general analysis, we will work in the setting of an M:N sub-/super-harmonic injection-locked oscillator.

Free-Running Noise

Let us analyze the effect of the free-running phase noise first, which we shall denote as $\mathcal{L}_0\{\Delta\omega\}$. We know from Section 7.2 that an injection-locked oscillator recovers from small deviations from the locked phase via a first-order exponential decay dynamic. Thus, we can model the time-varying impulse response of the oscillator's phase (relative to lock) to a noise source with associated ISF $\hat{\tilde{\Gamma}}(\cdot)$ as

$$h_{\hat{\theta}}(t,\tau) = \hat{\tilde{\Gamma}}[\varphi(\tau)]\,e^{-\omega_p(t-\tau)}u(t-\tau), \tag{7.45}$$

where ω_p, the pull-in frequency introduced in Section 7.4, is the negative of the slope of the lock characteristic.

In the free-running case, there is no phase restoration process and the perturbation persists indefinitely, meaning that $h_\phi(t,\tau) = \hat{\hat{\Gamma}}[\varphi(\tau)]\,u(t-\tau)$ as given in Eq. (4.5). (The concept of a "perturbation" is context dependent—whereas the phase perturbation in the free-running case is ϕ, it becomes $\hat{\theta}$ in the injection-locked scenario.) Of course, this response is what gives rise to the free-running phase noise $\mathcal{L}_0\{\Delta\omega\}$. Hence, we can now see that ***the process of injection locking passes the oscillator's free-running phase perturbations through an additional linear, time-invariant system*** whose unit step response is [79]

$$s_0(t) = e^{-\omega_p t}u(t). \tag{7.46}$$

This can be proven by calculating the the response of the system formed from cascading $h_\phi(t,\tau)$ with $h_0(t) \equiv s_0'(t)$ to an impulse $x(t) = \delta(t-\tau_0)$ at some time τ_0. The response to the first system is $h_\phi(t,\tau_0)$, and so the cascaded response is given by

$$\begin{aligned} y(t) &= h_\phi(t,\tau_0) * h_0(t) \\ &= \int_{-\infty}^{\infty} h_0(\tau)h_\phi(t-\tau,\tau_0)\,d\tau \\ &= \hat{\hat{\Gamma}}[\varphi(\tau_0)] \int_{-\infty}^{\infty} s_0'(\tau)u(t-\tau-\tau_0)\,d\tau \\ &= \hat{\hat{\Gamma}}[\varphi(\tau_0)]\,s_0(t-\tau_0) \\ &= h_{\hat{\theta}}(t,\tau). \end{aligned} \tag{7.47}$$

Next, the transfer function associated with the impulse response $h_0(t)$ is

$$H_0(s) = \frac{s}{s+\omega_p}, \tag{7.48}$$

which is a first-order high-pass filter with its pole at $s = -\omega_p$.

On a more subtle note, notice that the "*noiseless*" argument of the ISF—the oscillator's total phase—becomes $\varphi(t) = \omega_{\text{inj}}t + \theta_0$ for the injection-locked case as opposed to $\varphi(t) = \omega_0 t$ in the free-running case. Consequently, the injection locking process also *shifts* the free-running phase noise profile such that the offset $\Delta\omega$ is referred to the injection frequency ω_{inj} instead of the free-running frequency ω_0.

Injection Noise

Next, let us analyze how the oscillator reacts to phase noise in the injection $\mathcal{L}_{\text{inj}}\{\Delta\omega\}$. Suppose the injection phase suddenly changes by some amount $\Delta\varphi_{\text{inj}}$. We know that the oscillator will "track" this change, approaching a new steady-state value through a first-order exponential decay dynamic with time constant $\tau_p \equiv 1/\omega_p$. Because

the same time shift at the N^{th}-harmonic corresponds to N times the phase shift, the steady-state change in the oscillator's phase should be $\Delta\theta_0 = (M/N)\Delta\varphi_{\text{inj}}$. More rigorously, we can see this by noting that preservation of the oscillation frequency as dictated by the lock characteristic requires

$$\Delta\omega = \left\langle \tilde{\Gamma}\left(\frac{M}{N}x + \theta_0 + \Delta\theta_0\right) i_{\text{inj},0}(x + \Delta\varphi_{\text{inj}}) \right\rangle_{2\pi N} = \left\langle \tilde{\Gamma}\left(\frac{M}{N}x + \theta_0\right) i_{\text{inj},0}(x) \right\rangle_{2\pi N}.$$

As we can see, for this equation to be satisfied, we need

$$\Delta\theta_0 = \frac{M}{N}\Delta\varphi_{\text{inj}}. \tag{7.49}$$

Notice that what we have effectively reasoned through is the *step response* of the oscillator's phase with respect to small changes in the injection phase [79]:

$$s_{\text{inj}}(t) = \frac{M}{N}\left(1 - e^{-\omega_p t}\right) u(t). \tag{7.50}$$

This corresponds to the following transfer function:

$$H_{\text{inj}}(s) = s \times \frac{M}{N} \times \left(\frac{1}{s} - \frac{1}{s + \omega_p}\right) = \frac{M}{N} \cdot \frac{\omega_p}{s + \omega_p}, \tag{7.51}$$

which is a first-order *low-pass* filter with its pole at $s = -\omega_p$.

Total Noise

Now, assuming that the oscillator and the injection have uncorrelated sources of noise, we can use the Wiener-Khinchin Theorem and basic properties of LTI systems to derive the power spectral density of the locked oscillator's phase [111], which serves as a good estimate of the phase noise in the $1/f^2$ region:[4]

$$\mathcal{L}\{\Delta\omega\} = |H_0(j\Delta\omega)|^2 \, \mathcal{L}_0\{\Delta\omega\} + \left|H_{\text{inj}}(j\Delta\omega)\right|^2 \mathcal{L}_{\text{inj}}\{\Delta\omega\}. \tag{7.52}$$

Utilizing the transfer functions we derived, we get [79]

$$\implies \boxed{\mathcal{L}\{\Delta\omega\} = \frac{\Delta\omega^2}{\Delta\omega^2 + {\omega_p}^2}\mathcal{L}_0\{\Delta\omega\} + \left(\frac{M}{N}\right)^2 \frac{{\omega_p}^2}{\Delta\omega^2 + {\omega_p}^2}\mathcal{L}_{\text{inj}}\{\Delta\omega\}.} \tag{7.53}$$

[4]Note that $\Delta\omega$ here represents the frequency offset from the carrier (ω_{inj} in this case) at which the oscillator's noise level is being evaluated. In this section, $\Delta\omega$ is *not* the frequency deviation $\omega_{\text{inj}} - \omega_0$ we have previously defined.

As a simple example, consider an ideal LC oscillator locked to a sinusoidal injection ($M = N = 1$). Eqs. (7.12) and (7.14) reveal that $\omega_p = \omega_L \sin\big(\theta_0 + \angle\tilde{\Gamma}_1 - \angle I_{\text{inj}}\big)$. Adopting the usual convention that v_0 and $i_{\text{inj},0}$ have the same phase reference and referring to Table 5.5, we have that $\angle\tilde{\Gamma}_1 - \angle I_{\text{inj}} = \pi/2$. Therefore, the pull-in frequency reduces to $\omega_p = \omega_L \cos\theta_0$; substituting this into Eq. (7.53) yields the same result for phase noise from [81].

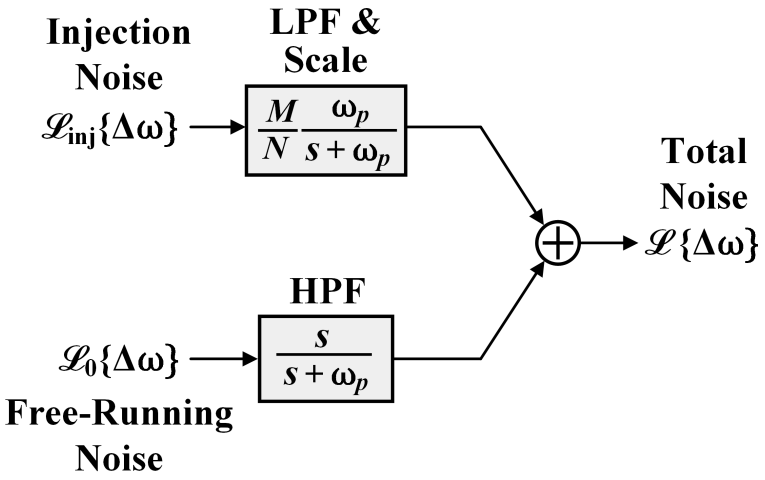

Figure 7.9: Evolution of an injection-locked oscillator's phase noise from the injection noise and the free-running noise. The injection noise is low-pass filtered, whereas the free-running noise is high-pass filtered.

The results of this analysis are summarized in Figure 7.9. Effectively, the oscillator is only capable of tracking the injection phase over time scales slower than the pull-in process. Consequently, *low-frequency* phase noise originating from the free-running oscillator is filtered out by the locking dynamic, whereas *high-frequency* noise in the injection is transparent to the oscillator and therefore does not appear in the oscillation voltage either. For this reason, the phase dynamics of an injection-locked oscillator are similar to that of a first-order phase-locked loop (PLL), where the injection signal takes the place of the PLL's input reference and ω_p is the loop bandwidth of the PLL.[5]

[5]One main difference is that in a PLL, the input frequency can be M times lower than the output frequency (e.g., high-frequency clock generation from a clean low-frequency crystal reference) without the presence of the M^{th}-harmonic in the reference signal, as the loop's implementation inherently accounts for the frequency multiplication that needs to take place.

Chapter 8

DESIGN INSIGHTS – OPTIMIZATION OF THE LOCK RANGE

8.1 Introduction

In this chapter, we put the theory we have developed to use, aiding in the design and practical implementation of electronic systems that rely on injection locking. The endeavor which holds the most potential in this context is that of utilizing the lock characteristic to expand the range of frequencies over which the oscillator will lock. We will first explore how the injection can be modulated to achieve this, and then look at how the oscillator itself can be changed to widen the lock range.

8.2 Constraining the Injection Power

Since the lock range increases with the injection strength, we must constrain the size of the injection current in a meaningful way to form a well-defined optimization problem. Although this may be straightforward to do for relatively simple waveforms like sine or square waves, it becomes difficult to ascertain the injection "amplitude" when a complicated assortment of harmonics is present. A more universal measure of the injection size which accounts for power in all harmonics is the *root-mean-square* (RMS) of the injection current:

$$I_{\text{rms}} \equiv \sqrt{\left\langle i_{\text{inj}}^2 \right\rangle} \coloneqq \sqrt{\frac{1}{T_{\text{inj}}} \int_{T_{\text{inj}}} i_{\text{inj}}(t)^2 \, dt} = \sqrt{\frac{1}{2\pi} \int_{2\pi} i_{\text{inj},0}(x)^2 \, dx}. \tag{8.1}$$

At first glance, the RMS injection current might also seem to represent the average power injected into the oscillator, but this assumes a fixed load, which is rarely the case in practice for the input impedances of actual oscillators. However, from a different and much more practical perspective, I_{rms} actually serves as a good measure of the average power consumption of the injection circuitry itself.

To understand why, consider the differential transistor pair in Figure 8.1 which commutates a static tail bias current I_{bias}. In the most efficient scenario, the differential injected current i_{inj} strictly alternates between $\pm I_{\text{bias}}$. This injection current has an RMS amplitude of $I_{\text{rms}} = I_{\text{bias}}$, which is proportional to the static power consumption of the injection circuit: $I_{\text{bias}} V_{DD}$. In reality, however, the circuit cannot transition between $\pm I_{\text{bias}}$ instantaneously, resulting in time periods where the circuit

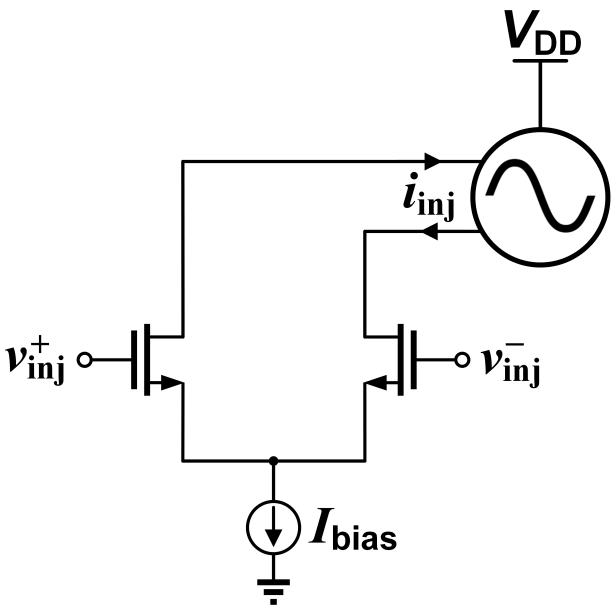

Figure 8.1: Simplified schematic showing an example of how the injection circuitry's static bias current I_{bias}, which dictates the power consumption, is converted to the injected current i_{inj}.

is injecting less current. Thus, the average power consumption of the injection circuitry is usually *at least* $I_{\text{rms}}V_{\text{DD}}$.

In summary, the root-mean-square injection current is a meaningful metric to consider because of its physical significance from a design standpoint—the minimum average power drawn by the injection circuitry scales with I_{rms}—and because it serves as an unambiguous definition of the injection amplitude regardless of the shape of the injection waveform. With this in mind, we are now in a position to think about how we can broaden the lock range by shaping the injection current for a fixed "injection power," or more precisely, RMS amplitude I_{rms}.

8.3 Maximizing the Lock Range

We are interested in optimizing the lock range for a given injection power by changing the injection waveform $i_{\text{inj},0}$:

$$\begin{aligned} \left(\omega_L^{\pm}\right)^* \coloneqq \max_{i_{\text{inj},0}}/\min \quad & \omega_L^{\pm} \\ \text{s.t.} \quad & \left\langle i_{\text{inj}}^2 \right\rangle = I_{\text{RMS}}^2, \end{aligned} \tag{8.2}$$

where I_{RMS} is a fixed *constant* which represents our constraint on the RMS injection current I_{rms} (with lowercase subscripts). But, recall that the lock range itself is given

by the largest achievable steady-state frequency deviation (i.e., $\omega_L^{\pm} \coloneqq \max/\min \Delta\omega$ for $d\theta/dt = 0$) for a given injection waveform, which is akin to extremizing the lock characteristic with respect to the oscillator's phase θ:

$$\omega_L^{\pm} = \max_{\theta}/\min_{\theta} \left\langle \tilde{\Gamma}(x + \theta)\, i_{\text{inj},0}(x) \right\rangle_{2\pi} . \tag{8.3}$$

Although this technically completes the description of the optimization problem we are trying to solve, there are two important observations we can make at this point which greatly simplify the problem's statement.

1. Shifting the relative phase θ between the oscillator and the injection can be interpreted as a way in which the injection waveform can be modulated without changing the injection power. After all, the optimization of the lock range should always seek out the value of θ that achieves the maximal frequency shift for a given injection waveform, and so the optimal solution is impervious to the specification of θ in the problem's formulation. In other words, we can "bypass" the optimization problem in Eq. (8.3) altogether, since the degree of freedom embodied in θ has already been absorbed into the setup of Eq. (8.2) and is therefore redundant.

2. While the upper and lower lock ranges $\omega_L^{\pm}$ for a given injection waveform $i_{\text{inj},0}$ could in general be quite different, the upper and lower *optimal* lock ranges $(\omega_L^{\pm})^*$ for a given injection power I_{RMS} are always equal and opposite. To see this, notice that reversing the direction of the injection current requires an equal but opposite injection frequency difference $\Delta\omega$ to achieve the same oscillation phase θ, thereby interchanging the upper and lower lock ranges (in magnitude). Consequently, the injection waveforms which optimize the upper and lower lock ranges must be the negative of one another. As a result, the problem of separately optimizing the upper and lower lock ranges can be reduced to a single *absolute* lock range optimization problem.

With these two ideas in mind, we can rewrite our lock range optimization problem as:

$$\omega_L^* = \max_{\langle i_{\text{inj}}^2 \rangle = I_{\text{RMS}}^2} \left| \left\langle \tilde{\Gamma}(x)\, i_{\text{inj},0}(x) \right\rangle_{2\pi} \right| . \tag{8.4}$$

Based on our first observation above, this formulation has the added benefit that its solution automatically tells us what what relative phase θ achieves the lock range for the optimal injection waveform.

Now, we proceed to solve this optimization problem. Observe that the average of the product of the ISF and the injection waveform, $\left\langle \tilde{\Gamma}(x)\, i_{\text{inj},0}(x) \right\rangle$, is actually a (real) *inner product* of $\tilde{\Gamma}(x)$ and $i_{\text{inj},0}(x)$ on the space of 2π-periodic functions square-integrable over a single period.[1] That is, for any two 2π-periodic functions $f(x)$ and $g(x)$ square-integrable over a single period, the following constitutes an inner product over $\mathbb{R}$:

$$\langle f, g \rangle \coloneqq \langle f(x)g(x) \rangle_{2\pi} \equiv \frac{1}{2\pi} \int_{2\pi} f(x)g(x)\, dx. \tag{8.5}$$

Furthermore, the norm induced by this inner product is the root-mean-square amplitude of the function:

$$\|f\| \equiv \sqrt{\left\langle f^2(x) \right\rangle_{2\pi}} \equiv \sqrt{\frac{1}{2\pi} \int_{2\pi} f(x)^2\, dx} \equiv f_{\text{rms}}. \tag{8.6}$$

Therefore, the constraint on the injection power is equivalent to fixing the *norm* of the injection current $i_{\text{inj},0}$, and our optimization problem can be rewritten as

$$\omega_L^* = \max_{\|i_{\text{inj},0}\| = I_{\text{RMS}}} \left| \left\langle \tilde{\Gamma}, i_{\text{inj},0} \right\rangle \right|. \tag{8.7}$$

This optimization problem is readily solved by applying the Cauchy-Schwarz Inequality [112]. Specifically, optimality is obtained when the vectors are collinear, and so the optimal injection current $i_{\text{inj},0}^*$ satisfies:

$$\boxed{i_{\text{inj},0}^*(x) \propto \tilde{\Gamma}(x).} \tag{8.8}$$

Of course, the constant of proportionality is dictated by the constraint on the injection power. Specifically,

$$i_{\text{inj},0}^*(x) = \pm \frac{I_{\text{rms}}}{\tilde{\Gamma}_{\text{rms}}} \tilde{\Gamma}(x), \tag{8.9}$$

where the positive solution optimizes the upper lock range $(\omega_L^+)^*$ and the negative solution optimizes the lower lock range $(\omega_L^-)^*$. Finally, the optimal lock range is therefore equal to the product of their norms:

$$\omega_L^* = \left| \left\langle \tilde{\Gamma}, i_{\text{inj},0}^* \right\rangle \right| = \|i_{\text{inj},0}\| \cdot \|\tilde{\Gamma}\| = I_{\text{rms}} \tilde{\Gamma}_{\text{rms}}. \tag{8.10}$$

Effectively, the lock range is maximized when the injection current waveform is *proportional to* the ISF. This idea is illustrated conceptually in the cartoon of

[1] In fact, it is equal to the standard L^2 inner product over any 2π-long interval, normalized by a factor of 2π.

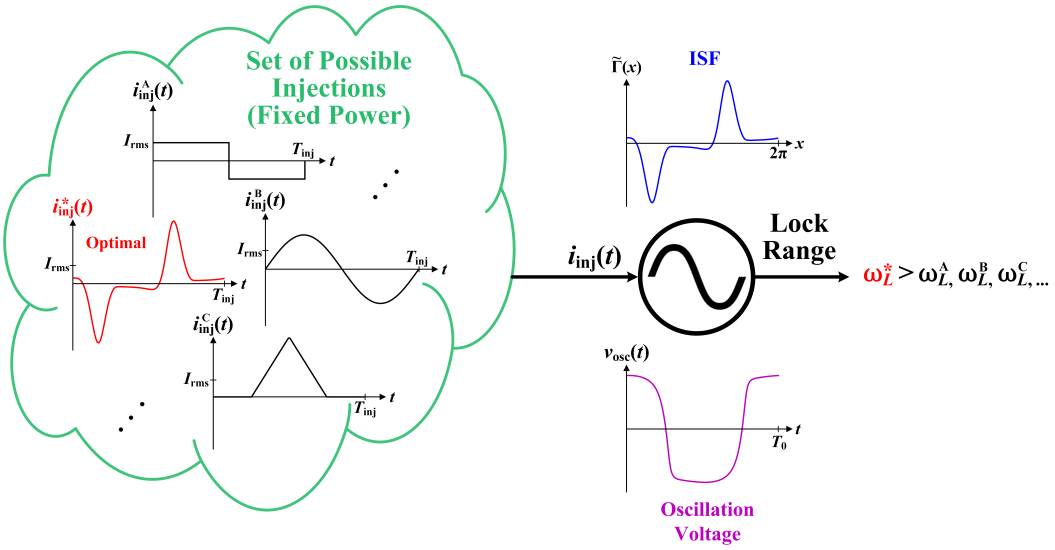

Figure 8.2: For a fixed injection power I_{rms}, the injection waveform that optimizes the lock range is one whose shape matches that of the ISF.

Figure 8.2. After all, the ISF is a measure of the *sensitivity* of the oscillator's phase to external disturbances as a function of when the disturbance is applied. Therefore, an injection waveform which looks like the ISF is more active at points along the oscillation cycle that are more sensitive to the injection. We can also extend this intuition to a more physical level. For a given injection node, the oscillator's phase is more impressionable—and the ISF is larger—when the voltage at that node is changing more rapidly.[2] It makes sense that displacing charge at the injection node during these times will advance or retard the oscillation more effectively. We will explore this idea in more detail in the following example.

Considerations for Rapidly Switching Oscillators

Oscillators which feature rapid switching behavior, such as long ring oscillators and the differential astable multivibrator, have ISFs which contain short, tall pulses. Physically, this corresponds to the marked increase in the phase's sensitivity to perturbations when the oscillator is switching. Consequently, the lock range for such oscillators can be widened significantly by taking advantage of this fact and more "efficiently" injecting the same amount of power. We present three examples below. Notice how the deviation of the shape of the lock characteristic compared to a sinusoidal injection is accurately captured by our model.

[2]To the first order, this is embodied by the numerator of Eq. (4.6), the formula for the ISF assuming orthogonal state variables.

Our first example is applying a rectangular pulse injection to the 17-stage ring oscillator of Figure 4.12. This injection waveform is shown alongside the ISF in Figure 8.3. Note that the vertical axis for $i_{\text{inj},0}$ has "arbitrary units," as we will specify the injection amplitude for each example. Specifically, we will use the same root-mean-square amplitudes of the sinusoidal injections from Figure 4.13.

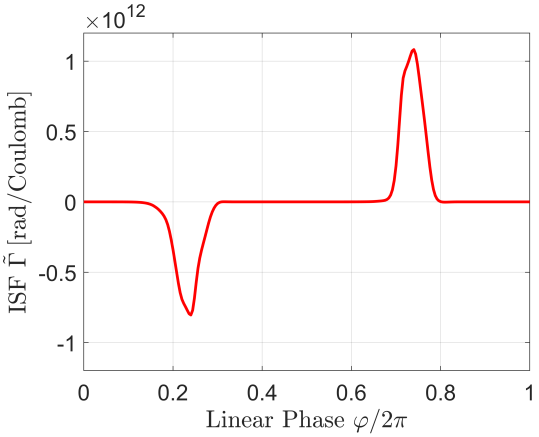

(a) Impulse sensitivity function.

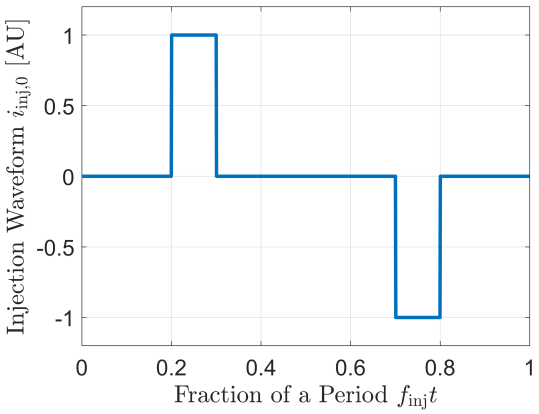

(b) Injection waveform.

Figure 8.3: Using a rectangular pulse injection to match the ISF of a 17-stage ring.

The lock characteristics for several different injection strengths are shown in Figure 8.4. Theoretical lock characteristics for a sinusoidal injection and for the optimal injection which exactly matches the shape of the ISF[3] (of the same RMS amplitude) are also shown for comparison. Observe the deviation between theory and simulation for the lower edge of the lock range at higher injection strengths, which also appeared in the sinusoidal lock characteristics of Figure 4.13.

[3]This optimizes the *upper* lock range. The lower lock range is optimized by matching the *negative* of the ISF. This distinction is not terribly significant here, as the ISF is fairly symmetric.

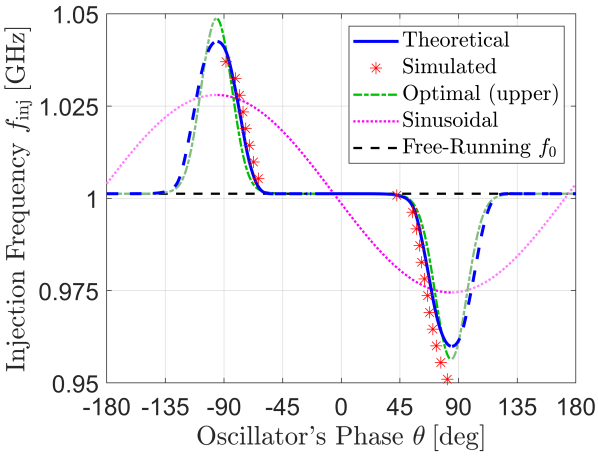

(a) $I_{\text{rms}} = 1.5/\sqrt{2}$ mA

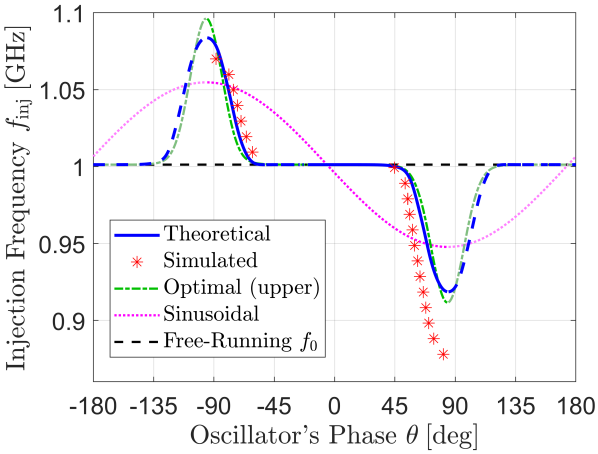

(b) $I_{\text{rms}} = 3/\sqrt{2}$ mA

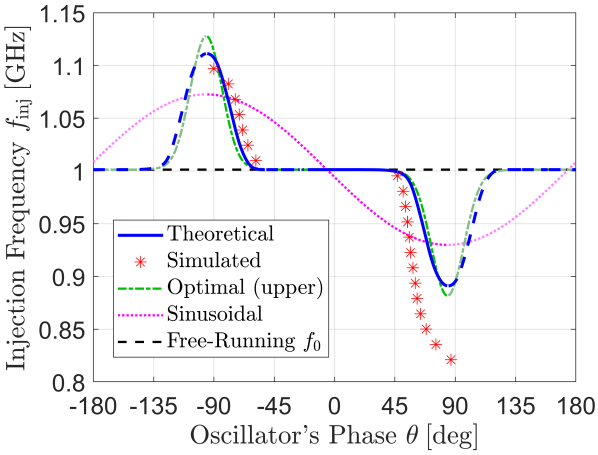

(c) $I_{\text{rms}} = 4/\sqrt{2}$ mA

Figure 8.4: Lock characteristic of the 17-stage ring oscillator for rectangular pulse injections of varying power.

Although using a rectangular pulse enhances the lock range by over 50% (in theory) compared to a sinusoidal injection, there is still room for improvement, as is apparent from the optimal lock characteristic shown in Figure 8.4. To mimic the ISF even more closely, we use pulses shaped like "half sine waves," as shown in Figure 8.5.

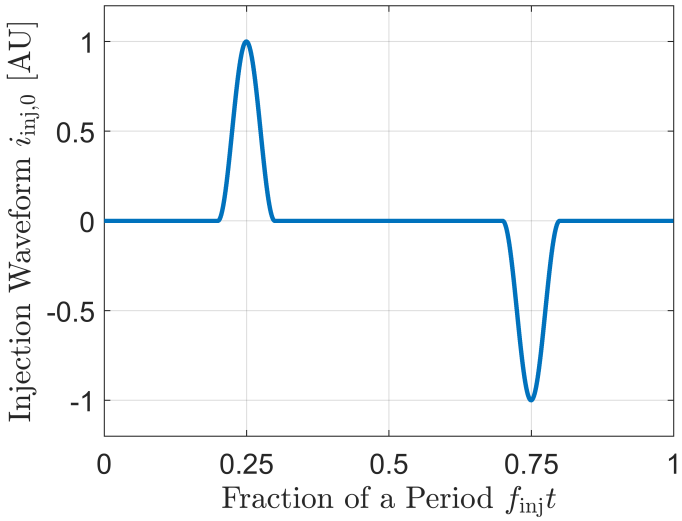

Figure 8.5: Using a sinusoidally shaped pulse injection to more closely match the ISF of a 17-stage ring oscillator.

The lock characteristics for several different injection strengths are shown in Figure 8.6. Note that the optimal lock range is nearly *double* the sinusoidal lock range. Also, even though the lock characteristic for these sinusoidally shaped pulses now matches the optimal one much more closely in theory, observe how injecting rectangular pulses results in a wider *simulated* lower lock for injections strong enough to invoke nonlinear behavior.

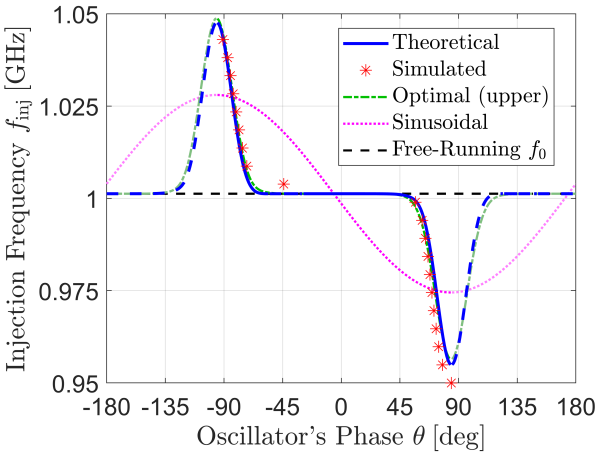

(a) $I_{\text{rms}} = 1.5/\sqrt{2}$ mA

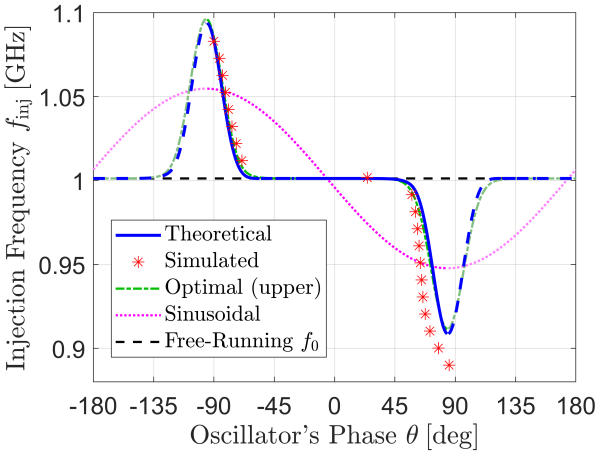

(b) $I_{\text{rms}} = 3/\sqrt{2}$ mA

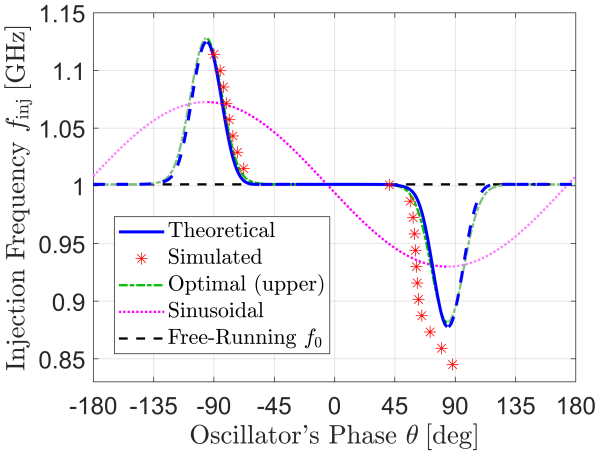

(c) $I_{\text{rms}} = 4/\sqrt{2}$ mA

Figure 8.6: Lock characteristic of the 17-stage ring oscillator for sinusoidally shaped pulse injections of varying power.

To gain a deeper understanding of how this injection shape enhances the lock range, Figure 8.7 shows the injection current and the oscillation voltage (which is observed at the injection node) at the lower and upper edges of the lock range for $I_{\text{rms}} = 1.5/\sqrt{2}$ mA. Observe how the pulses target the *transitions* of the oscillation voltage—specifically, the pulses *aid* the transitions at the upper edge (upward pulses at rising transitions and vice versa), while they *hinder* the transitions at the lower edge (upward pulses at falling transitions and vice versa). In fact, due to the opposing nature of the injection pulses at the lower edge of the lock range, one can see how the rising and falling transitions are both less steep, and therefore longer, than the transitions at the upper edge. Lastly, note that this transition-targeting behavior must occur at the *edges* of the lock range, as injecting current into a supply- or ground-saturated node has little effect on the oscillator's phase.

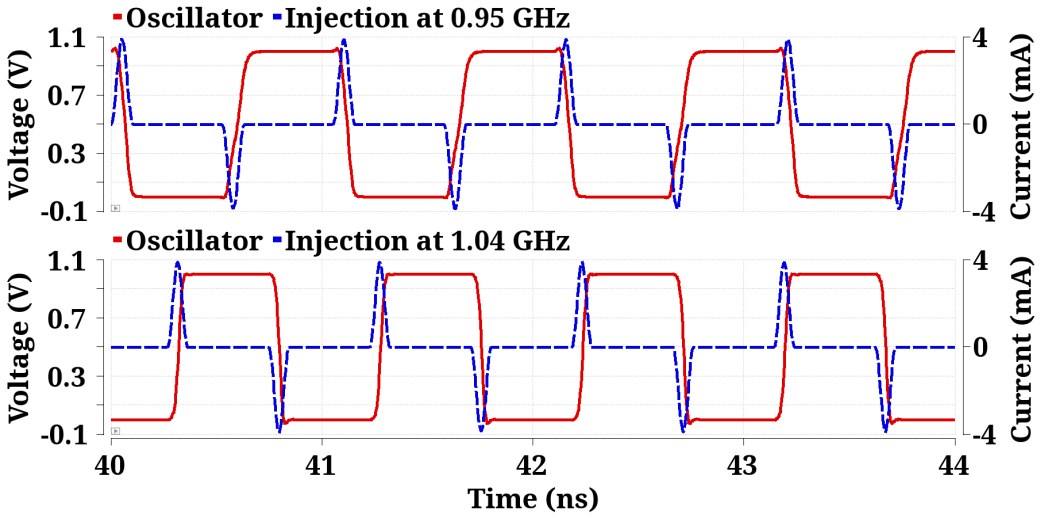

Figure 8.7: A depiction of how an optimized injection current targets the transitions of rapidly switching oscillators at the lower and upper edges of the lock range ($f_{\text{inj}} = 0.95$ GHz and $f_{\text{inj}} = 1.04$ GHz, respectively).

As another example of a rapidly switching oscillator, we will look at injecting triangular pulses into the differential NMOS astable multivibrator of Figure 4.17. Note that the optimal lock range is only around 36% wider than the sinusoidal one. The results are shown in Figure 8.8.

To summarize, the primary takeaway from the examples presented here is that the lock range for rapidly switching oscillators is generally enhanced by injecting short, tall pulses of current.

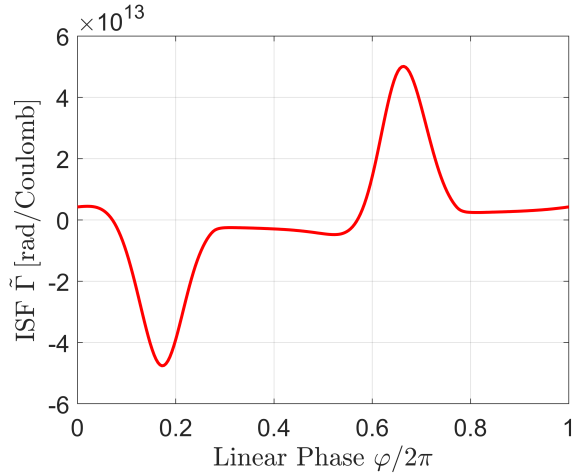

(a) Impulse sensitivity function.

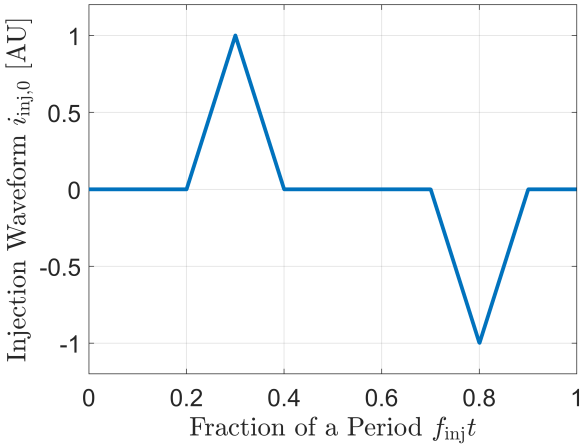

(b) Injection waveform.

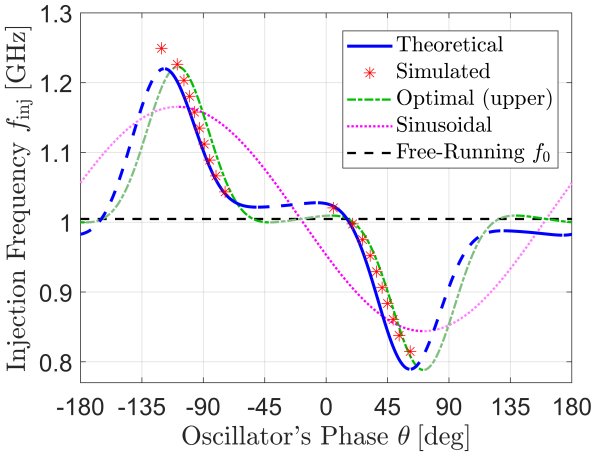

(c) $I_{\text{rms}} = 0.1/\sqrt{2}$ mA

Figure 8.8: Lock characteristic of the astable multivibrator for a triangular pulse injection.

Other Examples

Not all oscillators benefit significantly from altering the injection shape. For example, the lock range of the ideal Bose oscillator would only increase by roughly 10% after optimizing the injection waveform. Furthermore, this optimal injection would be difficult to generate in practice, due to the exponentially-rising and discontinuous nature of the ISF. Instead, we will consider the square wave injection shown in Figure 8.9.

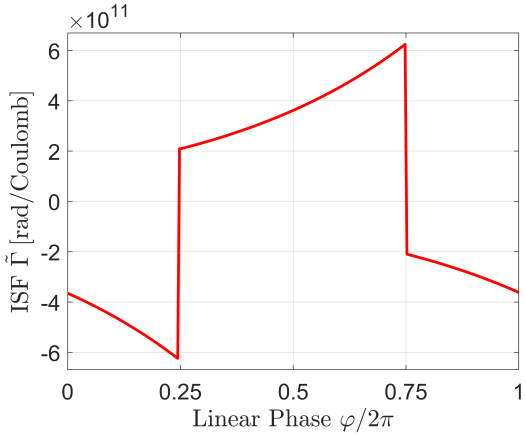

(a) Impulse sensitivity function.

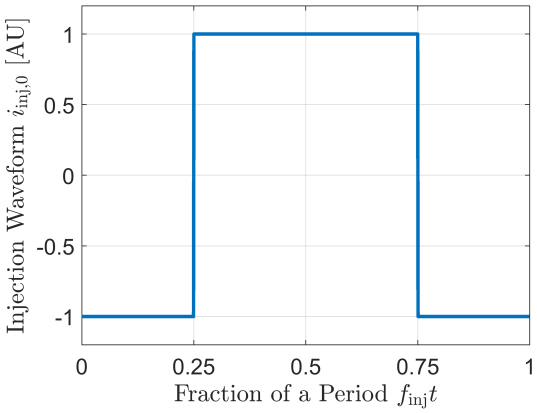

(b) Injection waveform.

Figure 8.9: Injecting a square wave into an ideal Bose oscillator.

The lock characteristics for several different injection strengths are shown in Figure 8.10. While little difference between the lock ranges exists, notice how our theoretical framework accurately captures the subtle changes in the shape of the lock characteristic. Also, observe the lack of smoothness (discontinuous derivative) at the points dividing the stable and unstable portions of the lock characteristic. This occurs because *both* the ISF and the injection are not smooth themselves.

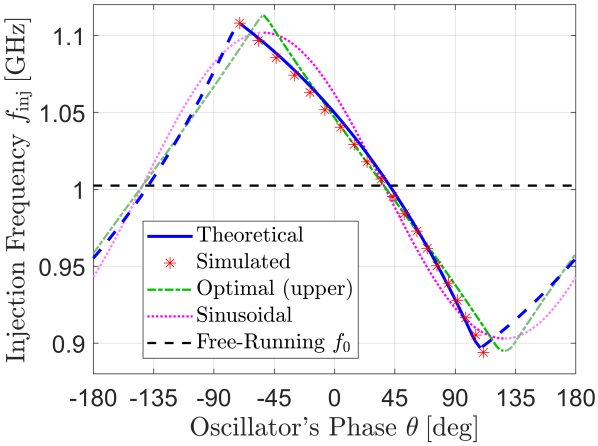

(a) $I_{\text{rms}} = 2.5/\sqrt{2}$ mA

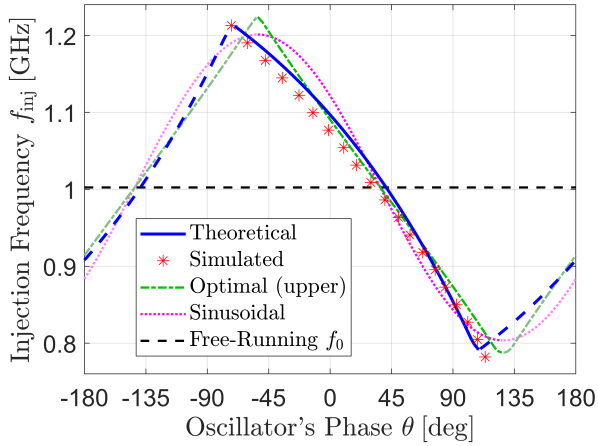

(b) $I_{\text{rms}} = 5/\sqrt{2}$ mA

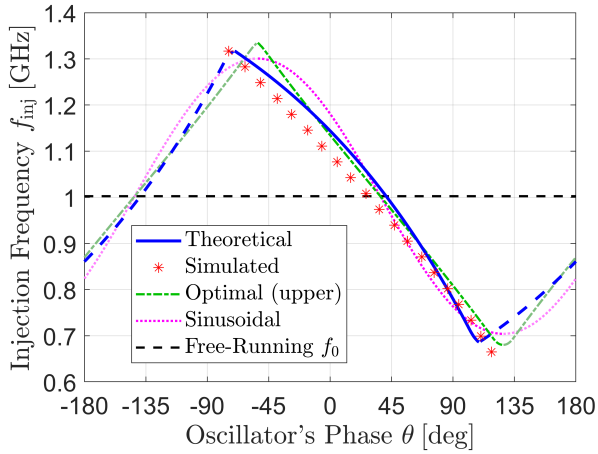

(c) $I_{\text{rms}} = 7.5/\sqrt{2}$ mA

Figure 8.10: Lock characteristic of the ideal Bose oscillator for square wave injections of varying power.

8.4 Optimization of Injection-Locked Frequency Dividers

While the preceding section dealt with optimizing the *fundamental* lock range of an oscillator, injection-locked oscillators which lock to higher-order harmonics are arguably more important due to their prevalence in RF frequency synthesizer applications. However, the case of optimizing the lock range of injection-locked frequency dividers (ILFDs) is not merely a straightforward extension of optimizing the fundamental lock range. We cannot simply set the injection current to be proportional to the ISF, as the injection waveform must "iterate through" N periods over a single period of the ISF. More precisely, our new optimization problem can be posed as

$$\begin{aligned} \omega_L^* = \max_{\langle i_{\text{inj}}^2 \rangle = I_{\text{RMS}}^2} & \left| \left\langle \tilde{\Gamma}\left(\frac{x}{N}\right) i_{\text{inj},0}(x) \right\rangle_{2\pi N} \right| \\ \text{s.t.} \quad & i_{\text{inj},0}(x) = i_{\text{inj},0}(x + 2\pi) \ \forall x. \end{aligned} \tag{8.11}$$

Although this additional constraint may seem difficult to manage at first glance, we can recast this optimization problem in the frequency domain via Fourier series:

$$\omega_L^* = \max_{\langle i_{\text{inj}}^2 \rangle = I_{\text{RMS}}^2} \frac{1}{2} \left[\frac{I_{\text{inj},0} \tilde{\Gamma}_0}{2} + \sum_{n=1}^{\infty} \left| I_{\text{inj},n} \tilde{\Gamma}_{nN} \right| \cos\left(\angle \tilde{\Gamma}_{nN} - \angle I_{\text{inj},n} \right) \right]. \tag{8.12}$$

We can further rewrite this expression using complex vector notation:

$$\omega_L^* = \frac{1}{2} \max_{\langle i_{\text{inj}}^2 \rangle = I_{\text{RMS}}^2} \left| \text{Re} \left\{ \begin{bmatrix} \frac{I_{\text{inj},0}}{\sqrt{2}} \\ I_{\text{inj},1} \\ I_{\text{inj},2} \\ \vdots \end{bmatrix}^H \begin{bmatrix} \frac{\tilde{\Gamma}_0}{\sqrt{2}} \\ \tilde{\Gamma}_N \\ \tilde{\Gamma}_{2N} \\ \vdots \end{bmatrix} \right\} \right|, \tag{8.13}$$

where $\mathbf{u}^H$ denotes the conjugate transpose or Hermitian of $\mathbf{u}$. The quantity being optimized can again be shown to be the absolute value of a *real inner product*. That is, we have the following proposition [112].

Claim 8.4.1. *For any pair of square-summable complex sequences $\mathbf{u} = \{u_n\}$ and $\mathbf{v} = \{v_n\}$, the following is an inner product over the field of real numbers $\mathbb{R}$:*

$$\langle \mathbf{u}, \mathbf{v} \rangle \coloneqq \text{Re}\{\mathbf{u}^H \mathbf{v}\} \equiv \text{Re}\left\{ \sum_n \overline{u_n} v_n \right\}, \tag{8.14}$$

with the same induced norm as the usual Euclidean complex inner product $\mathbf{u}^H \mathbf{v}$. (See Appendix C.2 for a proof of this.)

By Parseval's relation, our constraint on the root-mean-square injection current $\langle i_{\text{inj}}^2 \rangle$ is equivalent to specifying the *norm* of the injection current *vector* in Eq. (8.13). Therefore, the Cauchy-Schwarz inequality [112] is directly applicable once again, and optimality is similarly obtained when the two vectors are collinear:

$$\implies \begin{bmatrix} \frac{I_{\text{inj},0}^*}{\sqrt{2}} \\ I_{\text{inj},1}^* \\ I_{\text{inj},2}^* \\ \vdots \end{bmatrix} \propto \begin{bmatrix} \frac{\tilde{\Gamma}_0}{\sqrt{2}} \\ \tilde{\Gamma}_N \\ \tilde{\Gamma}_{2N} \\ \vdots \end{bmatrix}. \tag{8.15}$$

Carefully note at this point that even though the vectors themselves might feature complex elements (as they are Fourier series coefficients), the inner product is a *real* inner product. Therefore, the constant of proportionality must be real[4], which leads to the following set of expressions for the optimal injection current:

$$\boxed{I_{\text{inj},n}^* = \pm \frac{I_{\text{rms}}}{\sqrt{\frac{\tilde{\Gamma}_0^2}{2} + \sum_{n=1}^{\infty} \left|\tilde{\Gamma}_{nN}\right|^2}} \tilde{\Gamma}_{nN},} \tag{8.16}$$

where $n = 0, 1, \ldots$. With this optimizer, the optimal lock range is:

$$\omega_L^* = I_{\text{rms}} \sqrt{\frac{\tilde{\Gamma}_0^2}{2} + \sum_{n=1}^{\infty} \left|\tilde{\Gamma}_{nN}\right|^2}. \tag{8.17}$$

Thus, the shape of the optimal injection current can thus be constructed by setting its Fourier series coefficients equal to the N^{th}-multiple Fourier series coefficients of the ISF. In some sense, the remaining spectral components of the ISF are "irrelevant" because the corresponding components of the injection current are zero by definition of the divide-by-N nature of the problem.

Example: Locking Long Ring Oscillators to 2nd Harmonic Pulses

The preceding results are best illustrated on oscillators where the ISF contains significant power at harmonics which are multiples of N. Consider locking the 17-stage ring oscillator of Figure 4.12 to an injection at the second harmonic. Figure 8.11 shows the upper and lower optimal injection currents calculated from

[4]This is because the Cauchy-Schwarz inequality relies on the the property of *linearity in the first argument*, $\langle \alpha \mathbf{u}, \mathbf{v} \rangle = \alpha \langle \mathbf{u}, \mathbf{v} \rangle$ where α is a scalar, which is not satisfied if the inner product is real and α is complex with nonzero imaginary part. In other words, $\text{Re}\{\mathbf{u}^H \mathbf{v}\}$ is not an inner product over the field of complex numbers $\mathbb{C}$.

Eq. (8.16) over a single oscillation period, or two injection periods. Because this shape may be difficult to generate in practice, we injected a rectangular pulse instead with a pulse width equal to 20% of the injection period. Note that unlike the rectangular pulse of Figure 8.3, these waveforms only contain upward *or* downward pulses, not both. For comparison, the results from injecting a sinusoidal current with the same RMS amplitude were also simulated. To avoid the nonlinearities that result when a DC current is injected into the oscillator, as was demonstrated in Section 4.5, we zeroed the DC component of the injection current ($I_{\text{inj},0} = 0$), with the remaining components re-normalized to the original RMS amplitude.

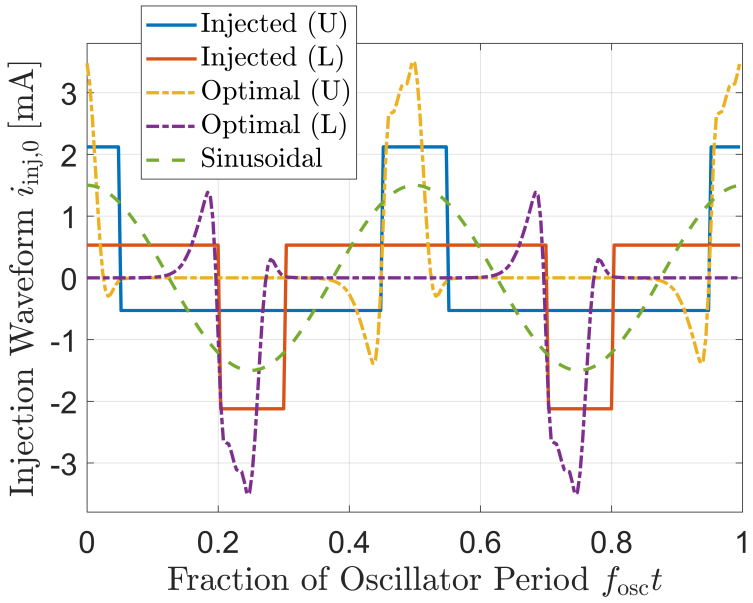

Figure 8.11: Optimizing the injection waveform for using a 17-stage inverter-chain ring oscillator as a divide-by-2 ILFD. Injections for optimizing the upper and lower lock ranges are signified with '(U)' and '(L)', respectively. The RMS injection amplitude is $I_{\text{rms}} = 1.5/\sqrt{2}$ mA.

The resultant lock characteristic is shown in Figure 8.12. Although deviations between prediction and simulation due to nonlinear behavior are apparent, using this theoretical framework still lead to the discovery of the downward rectangular pulse injection, whose simulated lock range is more than double the sinusoidal lock range.

Notice how the lock range is extremely narrow—the sinusoidal lock range is only 16 MHz, while the lock range for a sinusoidal injection of the same amplitude at the *third* harmonic is 148 MHz (see Figure 6.3), for example. This is because the ISF of the 17-stage ring oscillator does not contain strong even harmonics due to

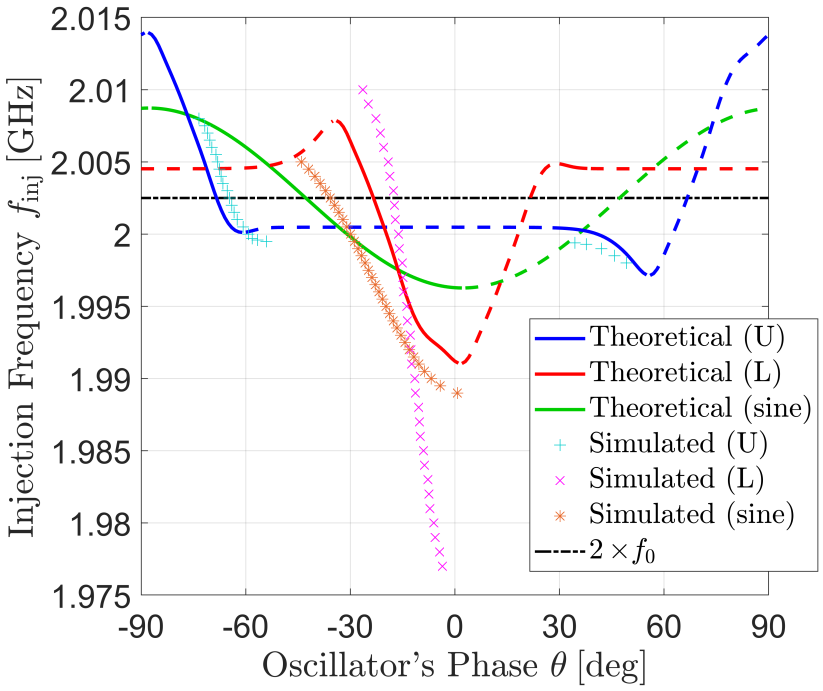

Figure 8.12: Lock characteristic for a 17-stage ring oscillator with a division ratio of $N = 2$ using the injection waveforms shown in Figure 8.11.

the symmetry between the rising and falling edges of the oscillation waveform. Essentially, the technique presented in this section is capitalizing on the *slight* asymmetry between the rising and falling edges, which becomes more pronounced in the ISF as the number of stages increases. Therefore, in addition to shaping the injection, it is perhaps fruitful to think about how the *oscillator* can be topologically altered in order to optimize the lock range. This concept will be explored next.

8.5 Shaping the ISF

Although we saw in the previous sections how we can "shape" the injection $i_{\text{inj}}(t)$ to optimize the lock range, this can be quite difficult to do in practice from a circuit design perspective. Thus far, we have taken the injection for granted as if it came from an ideal current source—in reality, the injection current is usually generated by one or more transistors whose gate voltage is being driven by the desired injection signal. But transistors have a finite large-signal output impedance—a particularly troublesome issue if the voltage at the injection terminal varies significantly. In fact, this is frequently the case, since most injections are applied across the oscillator's "output" terminals, which feature oscillation voltages whose swing is comparable to the supply voltage. In other words, in addition to the desired dependence of

the injection current on V_{GS}, the large voltage swing at the drain can also influence the injection current rather drastically [113], [114]. Thus, the time-domain characteristics of the injection current are heavily affected by the oscillation voltage $v_{\text{osc}}(t)$ itself, resulting in a complicated dynamic that can be difficult to control. Consequently, designing the injection circuitry to have a sufficiently high output impedance often presents a significant challenge in the implementation of systems that rely on injection locking.

One way to address this issue is to directly increase the output impedance through the use of a *series* "injection resistor." In doing so, we intentionally shift our design efforts to generating an injection *voltage* instead of an injection current. This is because the Norton equivalent of this circuit is a current source in parallel with the injection resistor [115], as shown in Figure 8.13. Reliable voltage waveforms can be much easier to generate and maintain through the design of a proper buffer. (Buffers are also necessary for isolation purposes if the desired injection signal is the output voltage of another oscillator.) Note that the buffer is anything that converts the original source of the injection to a voltage—if we are interested in locking to an optical signal, for example, we could use a photodiode combined with a transimpedance amplifier [116].

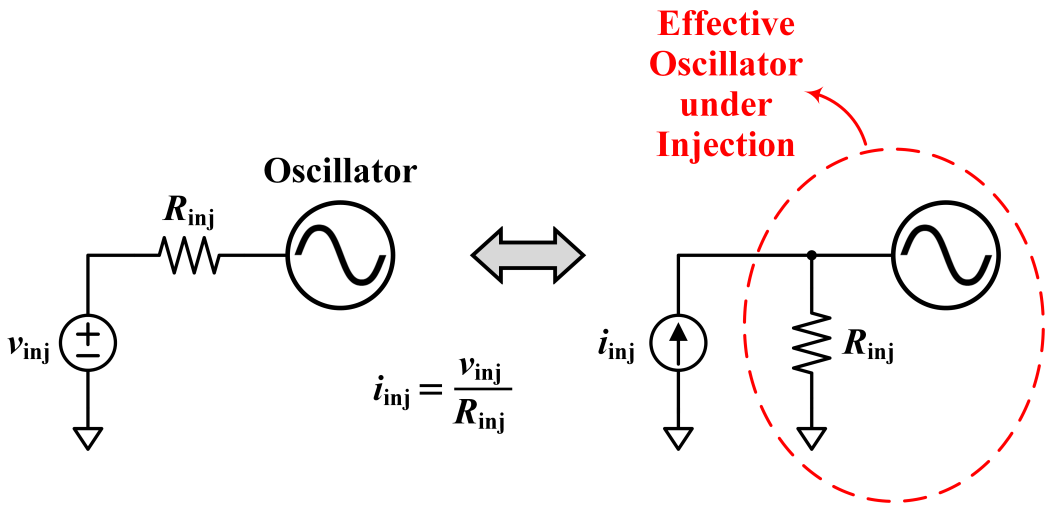

Figure 8.13: Actual implementation of the injection circuitry (left) and its Norton equivalent (right). The voltage source v_{inj} can come from an off-chip signal generator or from the output of an amplifier, for example.

This technique entails several design considerations. First, the buffer's output impedance must be small compared to the injection resistor. Put another way, the output devices of the buffer must be large enough to supply the desired amount of

injection current. Second, the effect of the injection resistor should be accounted for in the design of the oscillator, as indicated in Figure 8.13. These two constraints imply a fundamental trade-off with the injection strength: a larger injection resistor will load the oscillator and the buffer less, but it will also decrease the injection current amplitude for a given output swing from the buffer. In particular, the maximum peak-to-peak injection current for a given supply V_{DD} is $I_{\mathrm{inj}} = V_{\mathrm{DD}}/R_{\mathrm{inj}}$.

Even with this technique at our disposal, it can still be challenging to create specific shapes in the injection voltage at high frequencies, since these shapes require higher-order harmonics which are attenuated or distorted by the parasitics in the active devices. Note that passive linear filters are incapable of shaping a signal *without* changing the signal power, as this process requires energy to be moved around *between* harmonics. However, it is often difficult to justify the extra power that is needed by an active circuit to shape the injection voltage, as this power might have been better spent increasing the amplitude of a sinusoidal or otherwise sub-optimally shaped injection current.

Therefore, it may be much more convenient—or even necessary—in many scenarios to shape the *ISF* instead of the injection in order to widen the lock range. This is done by altering the design of the oscillator. One such example was alluded to at the end of the last section—introducing asymmetry between the rising and falling edges of of a ring oscillator to enable frequency division by even ratios. We will explore this technique below.

Half-Wave Symmetry in the ISF

Most oscillators feature symmetry between the "rise" and "fall" of their oscillation waveform, either due to the circuit's differential nature or the physical similarity between how the node capacitances charge and discharge. Consequently, many ISFs exhibit what is known as half-wave symmetry:

$$\tilde{\Gamma}(x) = -\tilde{\Gamma}(x + \pi). \tag{8.18}$$

In other words, each half period is the negative of the previous half period. A hypothetical example of an ISF which exhibits half-wave symmetry is shown in Figure 8.14. Periodic functions which satisfy this property contain no even harmonics [115]; that is, $\tilde{\Gamma}_n = 0$ for all $n = 0, 2, 4, \ldots$. This is easy to see through direct

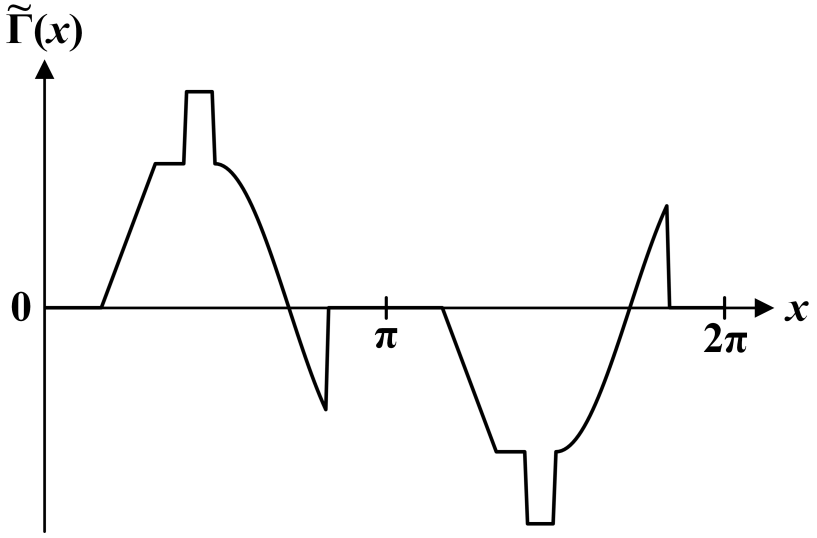

Figure 8.14: Hypothetical ISF which contains no even harmonics due to its half-wave symmetry. The "rising edge" happens when $0 < x < \pi$ and the "falling edge" happens when $\pi < x < 2\pi$.

calculation:

$$\begin{aligned}
\tilde{\Gamma}_n &= \frac{1}{\pi}\int_{-\pi}^{\pi} \tilde{\Gamma}(x)e^{-jnx}\,dx \\
&= \frac{1}{\pi}\int_{-\pi}^{0} \tilde{\Gamma}(x)e^{-jnx}\,dx + \frac{1}{\pi}\int_{0}^{\pi} \tilde{\Gamma}(x)e^{-jnx}\,dx \\
&= -\frac{1}{\pi}\int_{-\pi}^{0} \tilde{\Gamma}(x+\pi)e^{-jnx}\,dx + \frac{1}{\pi}\int_{0}^{\pi} \tilde{\Gamma}(x)e^{-jnx}\,dx \\
&= -\frac{1}{\pi}\int_{0}^{\pi} \tilde{\Gamma}(u)e^{-jnu}e^{jn\pi}\,du + \frac{1}{\pi}\int_{0}^{\pi} \tilde{\Gamma}(x)e^{-jnx}\,dx \\
&= [1-(-1)^n]\,\frac{1}{\pi}\int_{0}^{\pi} \tilde{\Gamma}(x)e^{-jnx}\,dx,
\end{aligned} \tag{8.19}$$

which vanishes for n even. This makes most oscillators incapable of dividing by an even ratio when the injection is applied across the terminals at which the oscillation voltage is observed. Instead, even-ratio division is usually achieved by injecting into the *tail* node of a differential LC oscillator [4], [5], [8], [11] or a differential ring oscillator [6], [10], [60], [63], since the tail voltage iterates through two cycles per oscillation period, giving the ISF at that node rich even-harmonic behavior. However, these two oscillators are costly in terms of area and power, respectively. Single-ended inverter-chain ring oscillators, which are small and power-efficient, present a unique opportunity here because their rising and falling edges can be independently designed and need not be perfectly symmetric. As

shown in Figure 8.15, this is achieved by controlling the widths of the P-channel and N-channel transistors.

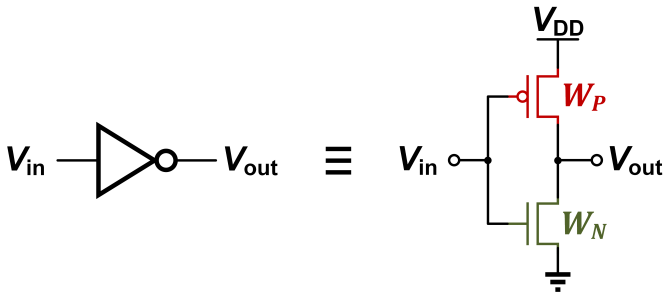

Figure 8.15: Intentionally introducing asymmetry into the rising and falling edges of the inverters in a ring oscillator by modifying the device sizes, W_P and W_N.

For a brief analytical example, consider the triangular approximation to the ISF of a ring oscillator proposed by Hajimiri *et al.* [90], shown in Figure 8.16. The parameters $\hat{t}_R$ and $\hat{t}_F$ are the rise and fall times of the oscillation waveform, normalized to the oscillation period and multiplied by 2π.[5] The magnitudes of the Fourier series coefficient of this particular ISF can be calculated to be:

$$\left|\tilde{\Gamma}_n\right| = \begin{cases} \dfrac{2}{\pi N^2 q_{\max}} \left|\cos\left(N\hat{t}_R\right) - \cos\left(N\hat{t}_F\right)\right|, & n = 0, 2, 4, \ldots \\ \dfrac{2}{\pi N^2 q_{\max}} \left[2 - \cos\left(N\hat{t}_R\right) - \cos\left(N\hat{t}_F\right)\right], & n = 1, 3, 5, \ldots \end{cases} \tag{8.20}$$

We see that all the even harmonics are equal to zero if $\hat{t}_R = \hat{t}_F$. Within reason, these expressions can be used to optimize for a particular harmonic of the ISF.

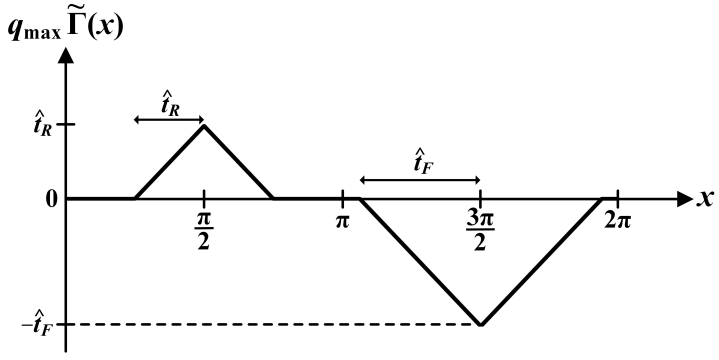

Figure 8.16: Triangular approximation of the ISF of a ring oscillator with asymmetric rising and falling edges [90]. Note that $q_{\max}$ is the maximum charge swing at the injection node.

[5] They are also equal to $1/f'_{\text{rise}}$ and $1/f'_{\text{fall}}$ from Appendix B of [90].

Design Example: Single-Ended Ring Oscillators with Asymmetric Inverters

For a more design-oriented example, we will implement another 1 GHz 17-stage single-ended ring oscillator using asymmetric inverters whose rising transition is shorter and steeper than the falling transition ($W_P \gg W_N$). The 2nd harmonic locking properties of this oscillator will then be compared against the oscillator from the previous section, which featured fairly symmetric inverters. Figure 8.17 shows the rising and falling edges of the symmetric inverter, while Figure 8.18 shows them for the asymmetric inverter.

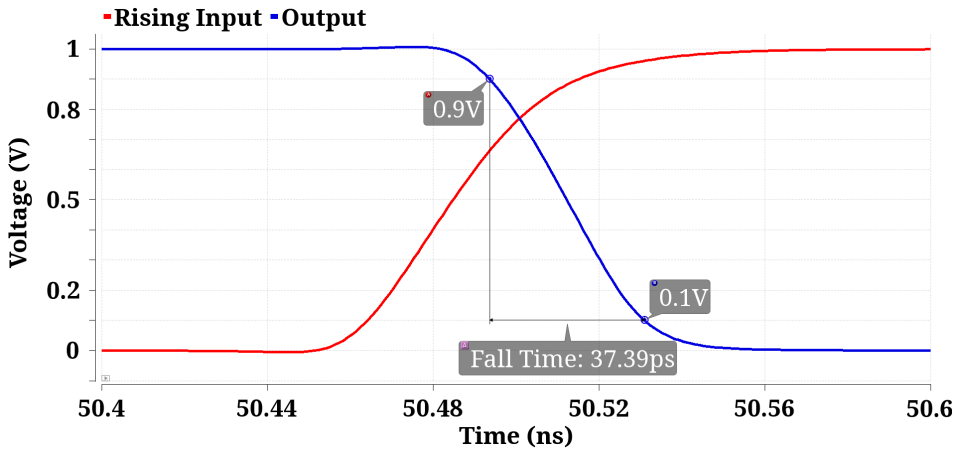

(a) Fall time of the inverter's output from 90% to 10% of the maximum swing V_{DD} in response to a rising input from the previous stage.

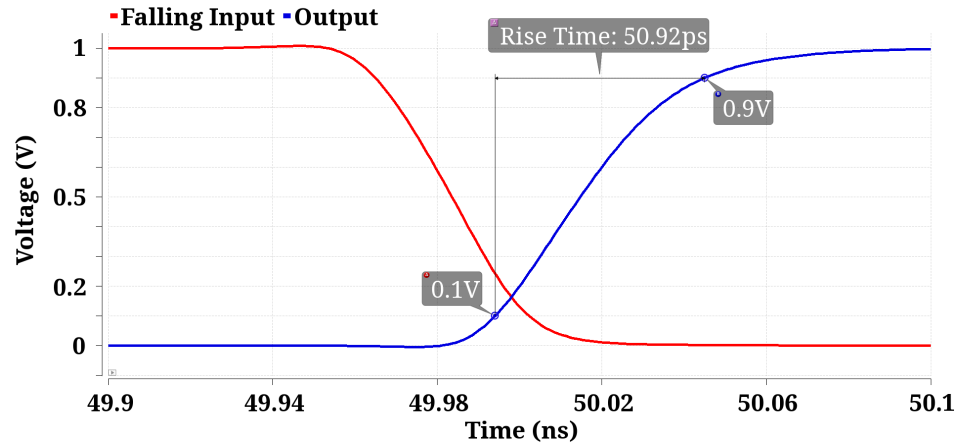

(b) Rise time of the inverter's output from 10% to 90% of the maximum swing V_{DD} in response to a falling input from the previous stage.

Figure 8.17: Rising and falling edges of an inverter inside a fairly symmetric 17-stage single-ended inverter-chain ring oscillator.

Note that the depicted signals are steady-state oscillation waveforms—the input voltage to the inverter is the output from the preceding inverter. Although rise and

fall times are usually simulated by placing an idealized ramp or sequence of steps at the input [117] since the actual waveforms are not known a priori, we are not interested in illustrating the design process of the inverter here. We only want to show how the actual switching behavior during oscillation is affected.

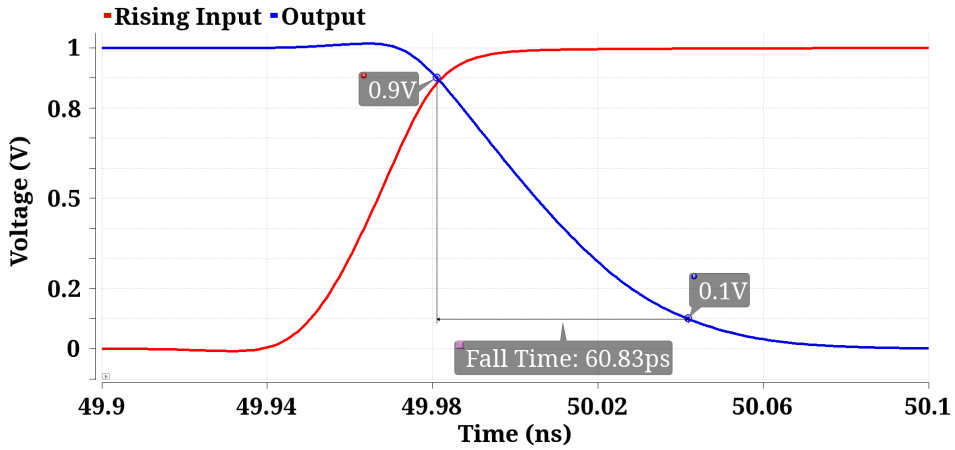

(a) Fall time of the inverter's output from 90% to 10% of the maximum swing V_{DD} in response to a rising input from the previous stage.

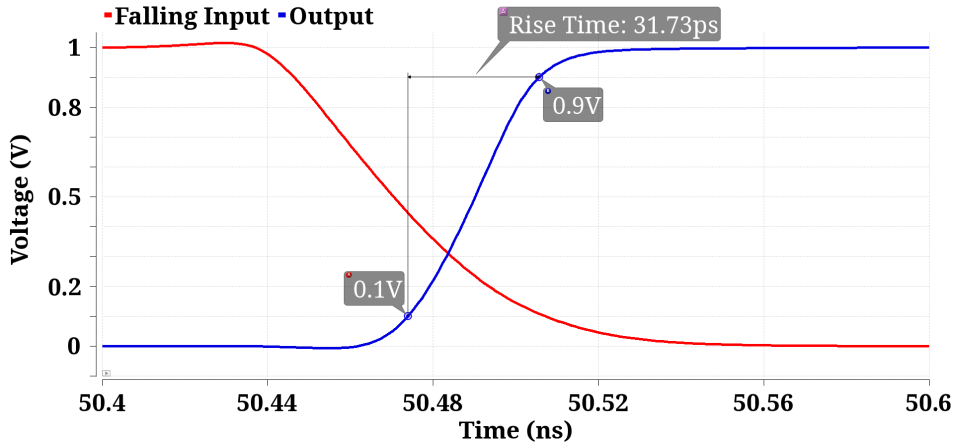

(b) Rise time of the inverter's output from 10% to 90% of the maximum swing V_{DD} in response to a falling input from the previous stage.

Figure 8.18: Rising and falling edges of an inverter inside an asymmetric 17-stage single-ended inverter-chain ring oscillator with stronger PFETs.

Also, keep in mind that the rise and fall times are different from the propagation delays used to calculate the oscillation frequency [90] (although they are related), which is defined as the delay between when the input and the output reach the inverter's toggle point.[6] The sum of the rising and falling propagation delays,

[6]The toggle point is the input voltage that results in the same output voltage—namely the intersection between the large-signal input-output characteristic and the line $V_{out} = V_{in}$.

multiplied by the number of stages, then yields the oscillation period. Although the asymmetry also affects the rising and falling propagation delays, what is relevant for our purposes is not the propagation delay but the whole switching period, as the oscillator's phase remains sensitive to injections during this entire time. Figure 8.19 depicts the asymmetry's effect on the oscillation waveform and the ISF.

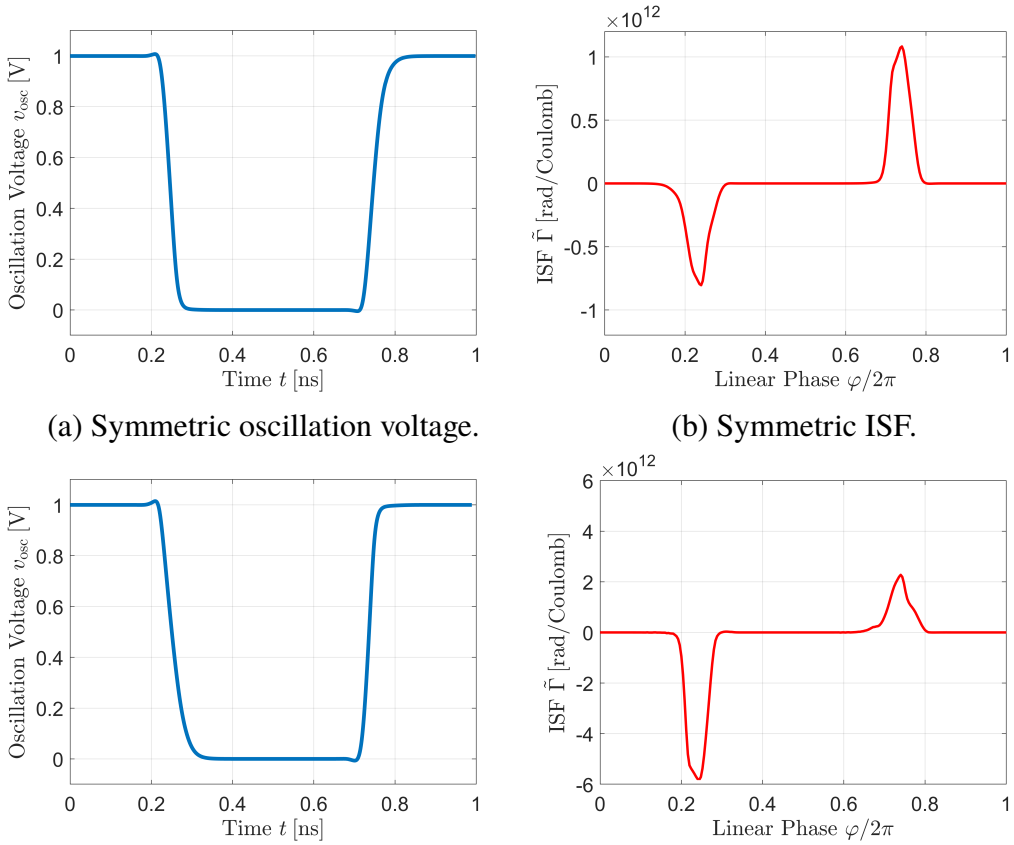

(a) Symmetric oscillation voltage.

(b) Symmetric ISF.

(c) Asymmetric oscillation voltage.

(d) Asymmetric ISF.

Figure 8.19: Comparison of symmetric and PFET-dominant asymmetric 17-stage ring oscillators.

For the asymmetric ring oscillator, we can also optimize the shape of the injection for dividing by 2 as we did for the relatively symmetric version in the previous section. The results of this optimization for an RMS amplitude of $0.5/\sqrt{2}$ mA are shown in Figure 8.20. Notice how the optimized injection waveforms for the upper and lower lock ranges are in the opposite direction compared to Figure 8.11 because now the dominant lobe of the ISF points downward, in the negative direction. Although the inverters in the original ring oscillator optimized in Figure 4.12 are fairly symmetrical, they still exhibit a slight asymmetry—with the NFETs being stronger than the PFETs.

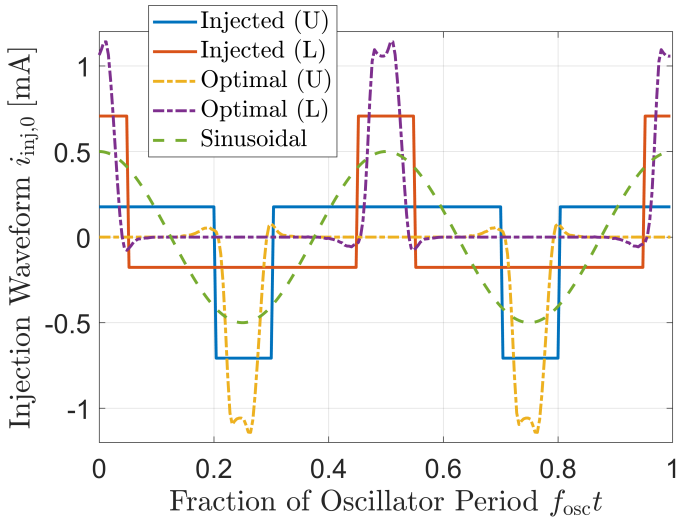

(a) Injections for optimizing the upper and lower lock ranges are signified with '(U)' and '(L)', respectively. The RMS injection amplitude is $I_{\text{rms}} = 0.5/\sqrt{2}$ mA.

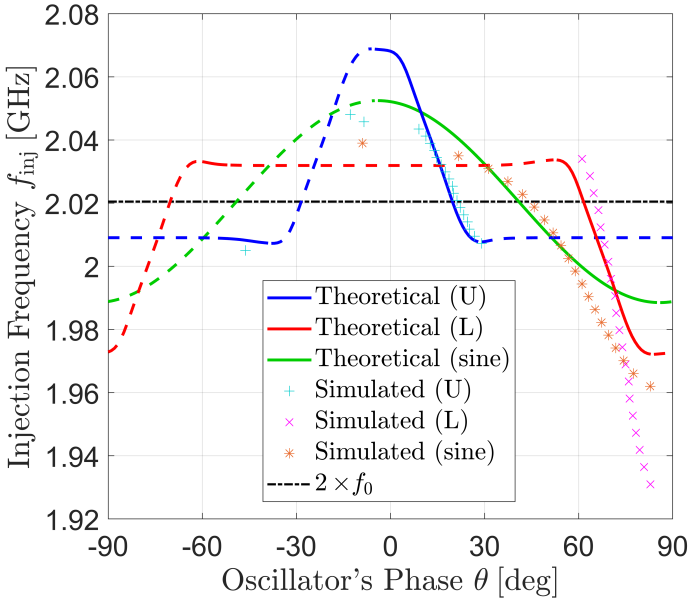

(b) Lock characteristics with a division ratio of $N = 2$ using the injection waveforms shown in Figure 8.20a.

Figure 8.20: Optimizing the injection waveform for using the PFET-dominant asymmetric 17-stage inverter-chain ring oscillator as a divide-by-2 ILFD.

Therefore, we surmise that reversing the asymmetry also reverses the the polarity of the injection current needed to optimize the lock range in a particular direction (i.e., upper or lower). Consequently, in contrast to the symmetric ring oscillator, the total lock range is enhanced by using the *upward* rectangular pulse injection instead.

Comparison with Figure 8.12 reveals that all three lock ranges are more than tripled for the asymmetric ring oscillator, despite using an injection amplitude that is three times smaller. However, this comparison is not entirely fair, as the asymmetric ring oscillator features a somewhat lower maximum charge swing due to the smaller amount of capacitance loading each stage, which leads to a larger overall ISF [87]. We will discuss this in more detail shortly.

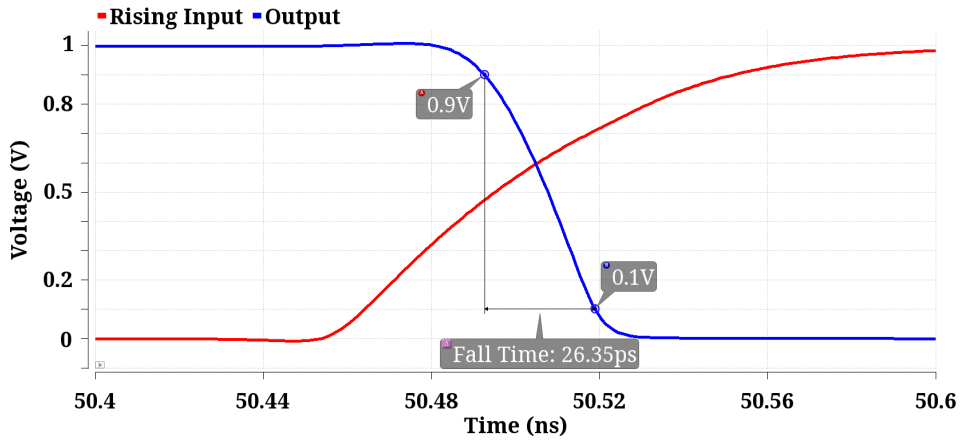

(a) Fall time of the inverter's output from 90% to 10% of the maximum swing V_{DD} in response to a rising input from the previous stage.

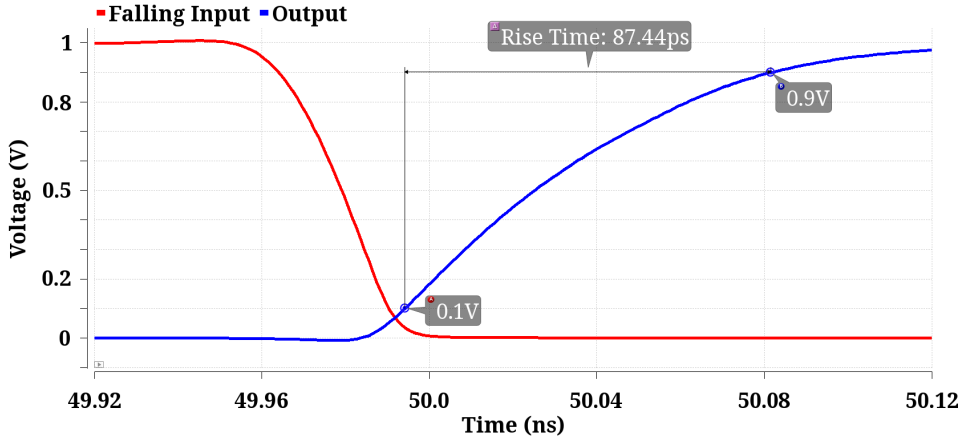

(b) Rise time of the inverter's output from 10% to 90% of the maximum swing V_{DD} in response to a falling input from the previous stage.

Figure 8.21: Rising and falling edges of an inverter inside an asymmetric 17-stage single-ended inverter-chain ring oscillator with stronger NFETs.

From a design standpoint, asymmetry is more efficiently introduced by making the NFETs stronger than the PFETs. This is because the electron mobility μ_n is already two to three times larger than the hole mobility μ_p [118]. Therefore, we repeated the above exercise for an asymmetric 17-stage inverter-chain ring oscillator where

we set $W_N \gg W_P$ instead, and we demonstrate how the 2$^{\text{nd}}$ harmonic lock range is enhanced even further (essentially for the same area and power consumption). Figure 8.21 shows the rising and falling edges of the inverters in this oscillator, and Figure 8.22 contrasts the oscillation waveform and ISF against that of our original, fairly symmetric 17-stage ring oscillator.

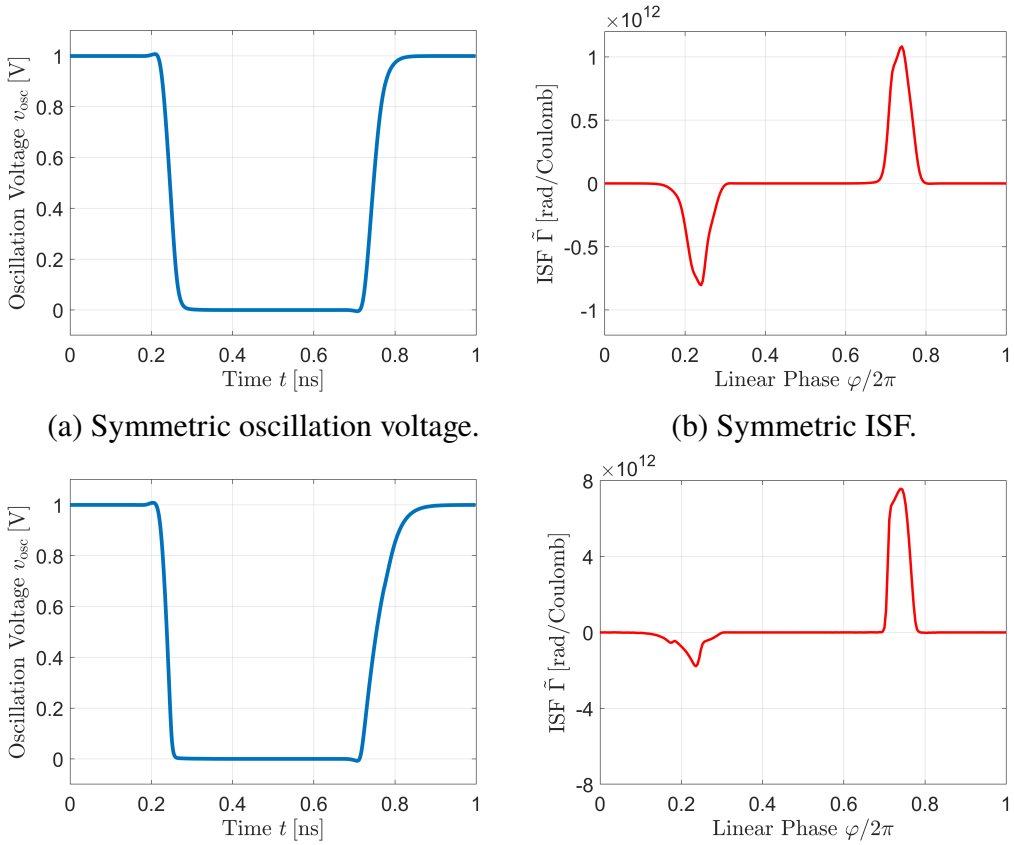

(a) Symmetric oscillation voltage.

(b) Symmetric ISF.

(c) Asymmetric oscillation voltage.

(d) Asymmetric ISF.

Figure 8.22: Comparison of symmetric and NFET-dominant asymmetric 17-stage ring oscillators.

Optimizing the shape of the injection waveform for division-by-2 is again performed on this oscillator, with the results shown in Figure 8.23. Because of the even lower charge swing compared to the PFET-dominant oscillator, the RMS amplitude of the injection current was further decreased to $0.4/\sqrt{2}$ mA. Notice how the waveform for optimizing the upper lock range consists of upward oriented pulses (and vice versa), unlike the optimal waveforms for the PFET-dominant oscillator, but similar to the those for the "symmetric" oscillator which contained inverters with slightly stronger NFETs. Once again, we utilized 20% duty-cycle rectangular pulses (with an average value of zero) to emulate the optimal injection waveforms.

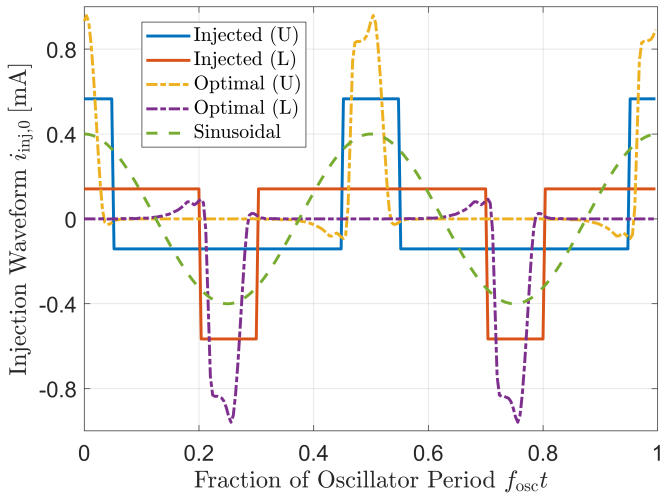

(a) Injections for optimizing the upper and lower lock ranges are signified with '(U)' and '(L)', respectively. The RMS injection amplitude is $I_{\text{rms}} = 0.4/\sqrt{2}$ mA.

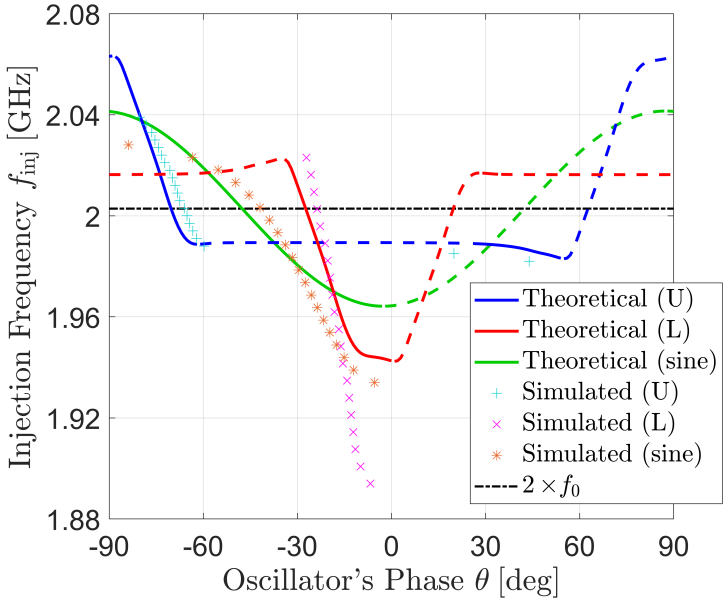

(b) Lock characteristics with a division ratio of $N = 2$ using the injection waveforms shown in Figure 8.23a.

Figure 8.23: Optimizing the injection waveform for using the NFET-dominant asymmetric 17-stage inverter-chain ring oscillator as a divide-by-2 ILFD.

Table 8.1 summarizes the differences between these three ring oscillators. The parameters W_P and W_N are the widths of the PMOS and NMOS devices in the inverter, and t_R and t_F are the rise and fall times of the inverter. Note that all lock ranges (LRs) are simulated, not predicted.

To tune all of the oscillators to free-run at roughly the same frequency, we used smaller transistors *overall* and a smaller load capacitance per stage (40 fF instead of 200 fF) to construct the asymmetric ring oscillator, which lead to a smaller $q_{\max}$ and hence a larger ISF. Therefore, to form a more unbiased comparison, we need to account for the "overall size" of the ISF, which is embodied in its RMS amplitude $\tilde{\Gamma}_{\text{rms}}$. In particular, the 2nd harmonic magnitudes of the ISFs should first be normalized by $\sqrt{2}\tilde{\Gamma}_{\text{rms}}$. (This ratio cannot exceed unity due to Parseval's identity.) Observe how the oscillator's 2nd harmonic injection locking properties are starkly influenced by making the inverters asymmetrical.

Table 8.1: Comparison Between Symmetric and Asymmetric Ring Oscillators

	(Fairly) Symmetric	PFET-Dom. Asymmetric	NFET-Dom. Asymmetric
Device Sizing: $\frac{W_P\ [\mu\text{m}]}{W_N\ [\mu\text{m}]}$	$\frac{17.76}{12.96} \approx 1.37$	$\frac{12}{1.44} \approx 8.33$	$\frac{2.1}{12} = 0.175$
Rise/Fall Asymmetry: $\frac{t_F\ [\text{ps}]}{t_R\ [\text{ps}]}$	$\frac{37.93}{50.92} \approx 0.74$	$\frac{60.83}{31.73} \approx 1.92$	$\frac{26.35}{87.44} \approx 0.30$
Free-Running Oscillation Frequency f_0	1.001 GHz	1.010 GHz	1.001 GHz
ISF RMS Amplitude $\tilde{\Gamma}_{\text{rms}}$ [rad/pC]	0.282	1.33	1.64
ISF 2nd Harm. $\frac{\lvert\tilde{\Gamma}_2\rvert}{\sqrt{2}\tilde{\Gamma}_{\text{rms}}}$	0.0655	0.213	0.262
2nd Harmonic Compliance η_2	0.30%	1.04%	1.30%
2nd Harmonic 1.5 mA Sinusoidal LR $2f_L$	16 MHz	560 MHz	710 MHz
RMS Injection Amplitude for Optimization I_{rms}	$1.5/\sqrt{2}$ mA	$0.5/\sqrt{2}$ mA	$0.4/\sqrt{2}$ mA
2nd Harmonic Sinusoidal LR $2f_L$ at I_{rms}	16 MHz	77 MHz	94 MHz
2nd Harmonic Upper Optimal LR $2f_L$ at I_{rms}	10 MHz	43 MHz	57 MHz
2nd Harmonic Lower Optimal LR $2f_L$ at I_{rms}	33 MHz	103 MHz	129 MHz

Chapter 9

A LOW-POWER DUAL-MODULI PRESCALER FOR FRACTIONAL-*N* FREQUENCY SYNTHESIS APPLICATIONS

9.1 Motivation

Modern frequency synthesizers see an ever increasing demand for higher operation frequency and lower power consumption [119]–[123]. Implementations based on phase-locked loops (PLLs) typically generate the output frequency from a stable, low-frequency reference such as a crystal. Therefore, in the loop's feedback path, the output frequency of the voltage-controlled oscillator (VCO) needs to be divided down to the input frequency provided by the reference. While the overall division ratio would need to be in the hundreds or thousands for output frequencies in the gigahertz and terahertz ranges, it is the "first few" divisions—the initial reduction of f_{out} to f_{out}/P where $P = 2$, 3, or 4, for example—that experience the sharpest trade-off between speed and power and therefore prove the most challenging to realize.

To enable the synthesis of multiple output frequencies from the same reference, another design consideration for the frequency divider is the ability to be configurable between different division ratios. The minimum spacing between possible output frequencies is the synthesizer's reference frequency, f_{ref}, as the output frequency must be an integer multiple of f_{ref}. However, by dynamically toggling or continuously dithering between division ratios, a fractional relationship between the output and reference frequencies can be achieved, leading to a finer frequency tuning resolution. This approach is known as fractional-*N* frequency synthesis [124]. Over the years, a variety of techniques for countering the non-idealities associated with dithering (e.g., spurs, quantization noise) have been developed, such as Δ-Σ modulation [125].

Digital and current-mode logic (CML) dividers [126]–[128] can operate over a wide range of frequencies and division ratios but consume unacceptably high amounts of power as the frequency of operation increases [7]. This is because the capacitances of the active devices in these implementations must fully charge and discharge every cycle [5]. Consequently, frequency dividers based on injection-locked oscillators (i.e., ILFDs) are usually used to "pre-scale" the output down to frequencies that

can be feasibly handled by programmable digital dividers. However, ILFDs have conventionally been associated with a number of drawbacks:

1. They suffer from a limited lock range, and methods to enhance the lock range are not well understood.

2. LC dividers, which are used to divide-by-2 or divide-by-4 [5], [8], [11], require a large amount of area for the on-chip inductor, adding additional cost to the system.

3. They traditionally have only a single division ratio, as an oscillator's operation frequency and lock characteristic are topology and parameter dependent.

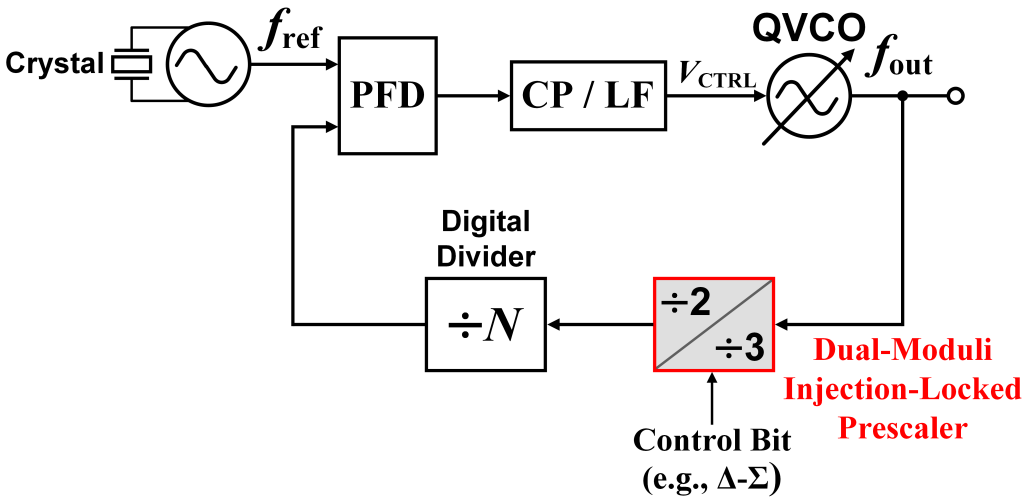

Figure 9.1: A fractional-N PLL which synthesizes output frequencies in the range $2N f_{ref} \leq f_{out} \leq 3N f_{ref}$ from a crystal reference. A general implementation based on a phase-frequency detector (PFD), charge pump (CP), and loop filter (LF) in the forward path is assumed.

In this chapter, we will present the design of an injection-locked prescaler which addresses all three of these issues. Our design, which is based on a reconfigurable ring oscillator, is capable of dividing by both 2 and 3 from 8.4 GHz to 11.5 GHz, consumes less than 2.5 mW of power off of a 1 V supply, and occupies only 30×15 μm^2 of area in a 65-nm bulk CMOS process. A system diagram of a fractional-N frequency synthesizer which places this work in context is shown in Figure 9.1.

9.2 Theory

The core of our design is a single-ended inverter-chain ring oscillator, switchable between five and seven stages. The 5-stage configuration is designed for divide-by-2 operation, whereas the 7-stage configuration is designed for divide-by-3 operation. Asymmetric inverters were used to enable efficient division by an even ratio, as discussed in Section 8.5. We assumed the frequency synthesizer's VCO produced quadrature outputs, which gives us access to four injection signals with quadrature phases: IP ($\phi_{\text{inj}} = 0$), IN ($\phi_{\text{inj}} = \pi$), QP ($\phi_{\text{inj}} = \pi/2$), and QN ($\phi_{\text{inj}} = 3\pi/2$). To decide which stages of the ring oscillator to inject into, we followed the scheme discussed in Section 6.7. Specifically, the phase of the injection into stage k (relative to stage 0) needs to be

$$\phi_{\text{inj}}(k) = kN\left(\pi - \frac{\pi}{K}\right), \tag{9.1}$$

for $k = 0, 1, \ldots, K-1$, where K is the total number of stages and N is the division ratio. Tables 9.1 and 9.2 show the phases that should be injected into each stage of the 5-stage and 7-stage ring oscillators, respectively.

Table 9.1: Quadrature Injection Scheme: 5 Stages for Division-By-2

Stage	Ideal Phase to be Injected	Closest QVCO Injection
0	0 (reference)	IP
1	$8\pi/5 = 1.6\pi$	QN
2	$6\pi/5 = 1.2\pi$	IN
3	$4\pi/5 = 0.8\pi$	IN
4	$2\pi/5 = 0.4\pi$	QP

Table 9.2: Quadrature Injection Scheme: 7 Stages for Division-By-3

Stage	Ideal Phase to be Injected	Closest QVCO Injection
0	0 (reference)	IP
1	$4\pi/7 \approx 0.57\pi$	QP
2	$8\pi/7 \approx 1.14\pi$	IN
3	$12\pi/7 \approx 1.71\pi$	
4	$2\pi/7 \approx 0.29\pi$	
5	$6\pi/7 \approx 0.86\pi$	
6	$10\pi/7 \approx 1.43\pi$	QN

In general, by following Eq. (9.1), this design scheme is applicable for any number of stages and for an arbitrary division ratio. However, utilizing a smaller number of stages increases the operating frequency that we can obtain from a ring oscillator

for a particular design process, and lower division ratios feature wider lock ranges since most of the energy in an ISF is contained in its first few harmonics.

9.3 Design

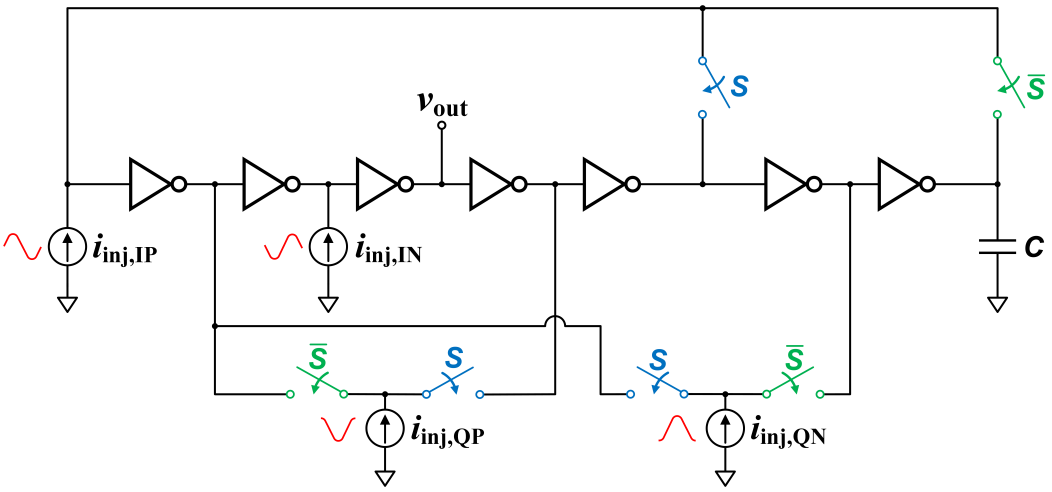

Figure 9.2: Schematic of the designed injection-locked prescaler.

The schematic of the prescaler is shown in Figure 9.2. The inverters were made asymmetric by setting

$$\frac{W_N}{W_P} = \frac{4.5\ \mu\text{m}}{3\ \mu\text{m}} = 1.5, \tag{9.2}$$

where W_N and W_P are the widths of the NMOS and PMOS devices, respectively. To ensure maximum overlap between the divide-by-2 and divide-by-3 lock ranges of the 5-stage and 7-stage ring oscillators, the "last" stage of the 7-stage ring oscillator was loaded with a 20 fF MIM capacitor. A signal bit, S, controls the switches.

The injection currents, shown as ideal current sources, were implemented using the technique discussed at the beginning of Section 8.5 and shown in Figure 8.13. Specifically, the buffered outputs of the quadrature VCO were used to drive series "injection resistors." A short chain of inverters served as each buffer, and each injection resistor was a 780 Ω un-silicided poly-resistor. The layouts of the prescaler and the QVCO[1] are shown in Figure 9.3.

[1]The QVCO was designed by Dr. Behrooz Abiri.

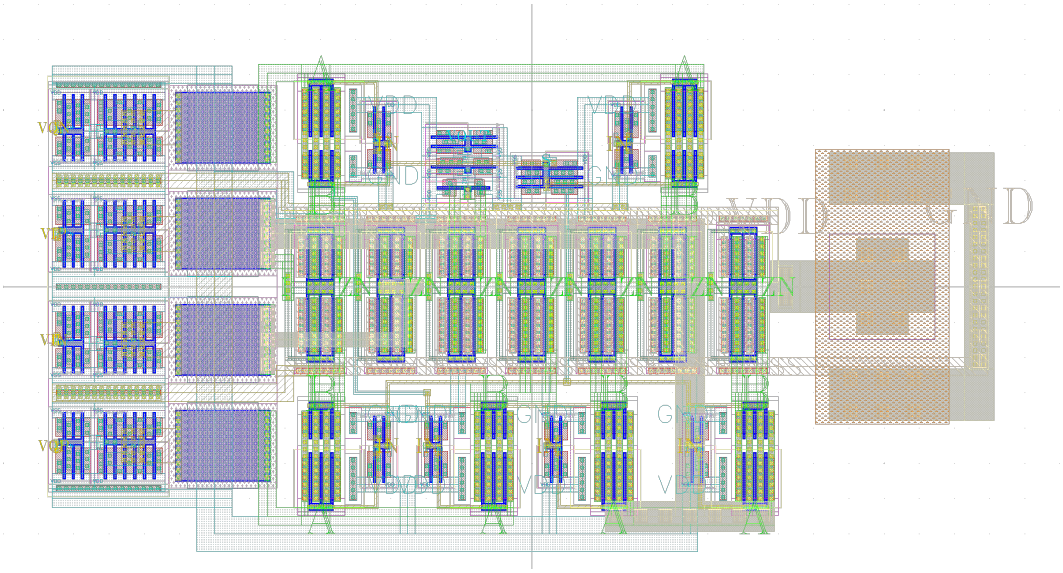

(a) Injection-locked prescaler, measuring 30×15 μm^2.

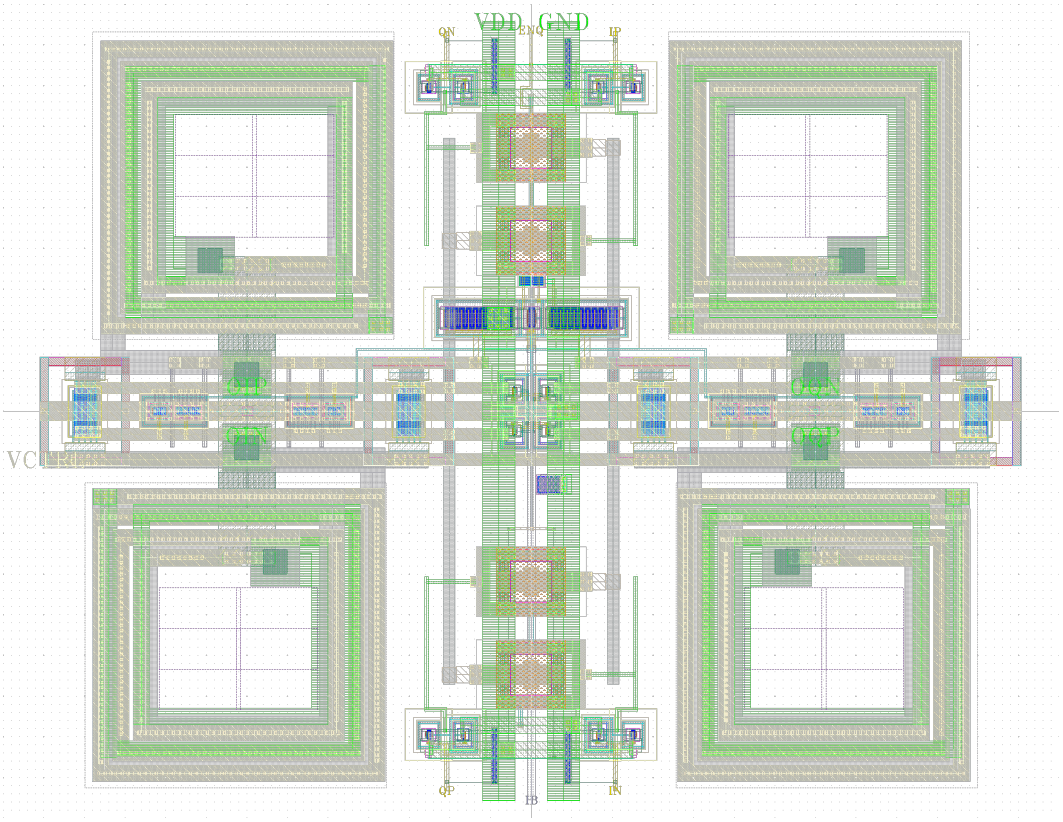

(b) Quadrature voltage-controlled CMOS LC oscillator, measuring 120×95 μm^2 (courtesy of Dr. B. Abiri).

Figure 9.3: Layouts of the ring oscillator prescaler and the quadrature LC VCO which was fabricated alongside it.

9.4 Extracted Simulation Results

The sensitivity of the ring oscillator to parasitic resistances and capacitances, particularly at multi-GHz frequencies, necessitated an iterative schematic-layout design process. The free-running oscillation frequencies of the 5-stage and 7-stage ring oscillators after extraction are given in the table below.

5 Stages (÷2)	7 Stages (÷3)
f_0 = 4.124 GHz	f_0 = 2.948 GHz

Figure 9.4 depicts the lock range of the prescaler by plotting the ratio of the injection frequency from the VCO to the output frequency of the divider as a function of the injection frequency. As we can see, there is a range of injection frequencies for which this ratio is constant, equal to the desired division ratio for a given configuration, indicating lock. The effective lock range of the prescaler is the intersection of the lock ranges for the divide-by-2 and divide-by-3 configurations. This simulation was performed by replacing the QVCO with ideal voltage sources so the injection frequency could be swept beyond the QVCO's tuning range. The lock range was also simulated with the quadrature injections QP and QN disabled (grounded), showing how the quadrature injections nearly double the lock range.

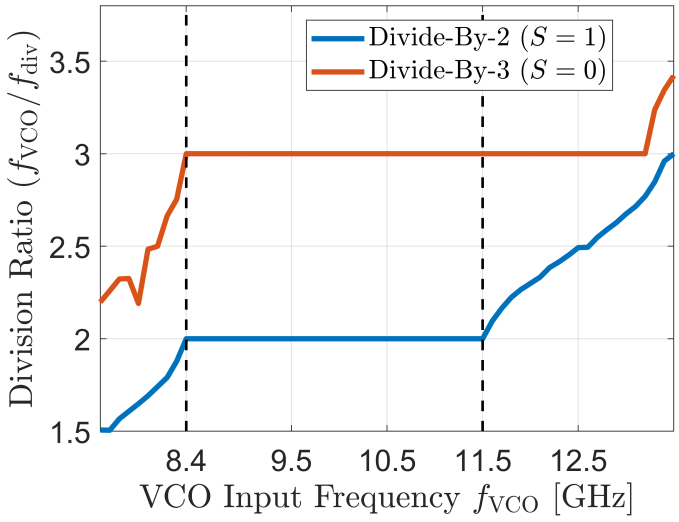

(a) With all four quadrature injections, the effective lock range is 3.1 GHz.

The QVCO is tunable from 9 GHz to 11 GHz, which is encompassed by the effective lock range of the prescaler. Figure 9.5 plots the output voltage of the prescaler alongside one of the injection voltages from the QVCO for both division ratios and at multiple injection frequencies.

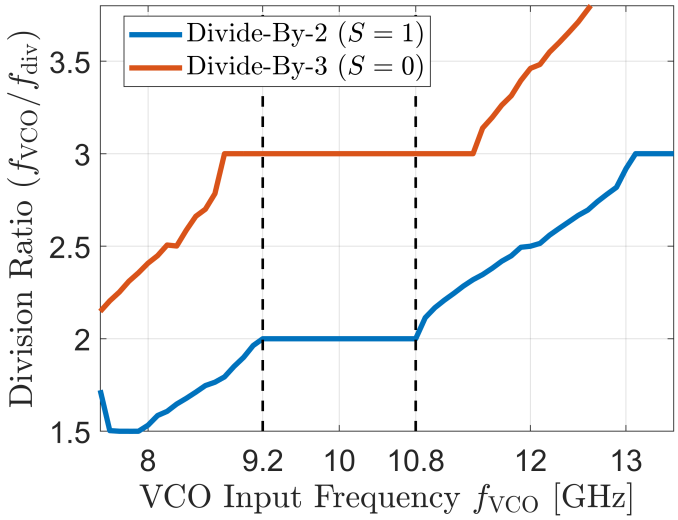

(b) With only differential injections (IP and IN), the effective lock range is 1.6 GHz.

Figure 9.4: Extracted simulation of the divide-by-2 and divide-by-3 lock ranges of the designed prescaler.

The prescaler alone consumes less than 2.5 mW over the entire effective lock range for both division ratio configurations. Table 9.3 compares the simulated performance of this design against the measured results of state-of-the-art frequency dividers.

Table 9.3: Prescaler Performance Comparison

Reference	Process / Area [μm^2]	Type	Division Ratios	Frequency [GHz]	Power [mW]
This Work	65-nm / 30×15	Ring	2, 3	8.4 – 11.5	2.5
JSSC 2007 [63]	0.18-μm / 60×50	Ring	2	13 – 25	24
TMTT 2009 [11]	90-nm / 130×290	LC	2	51 – 74	3
TMTT 2012 [12]	90-nm / 800×700	LC	3	91.4 – 93.5	1.5
ESSCIRC 2014 [127]	65-nm / 25×50	Digital	64, 80, 96, 100, 112, 120, 140	~0 – 17	2
TVLSI 2015 [128]	0.18-μm / 40×80	Digital	16, 17	0.002 – 5.8	2.6

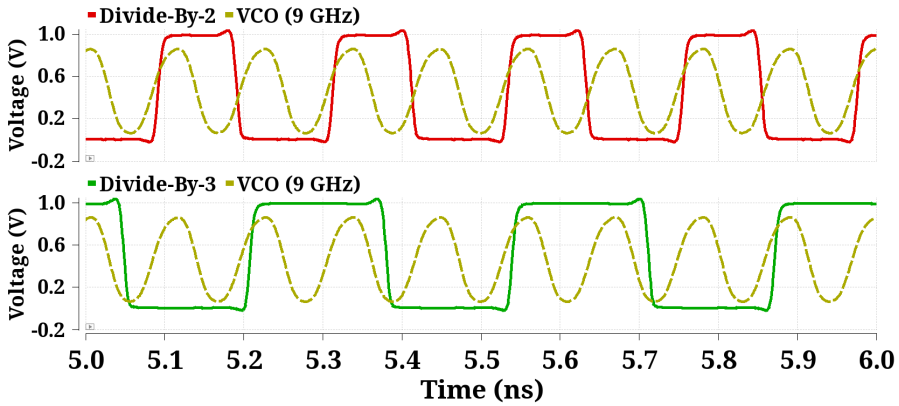

(a) f_{VCO} = 9 GHz

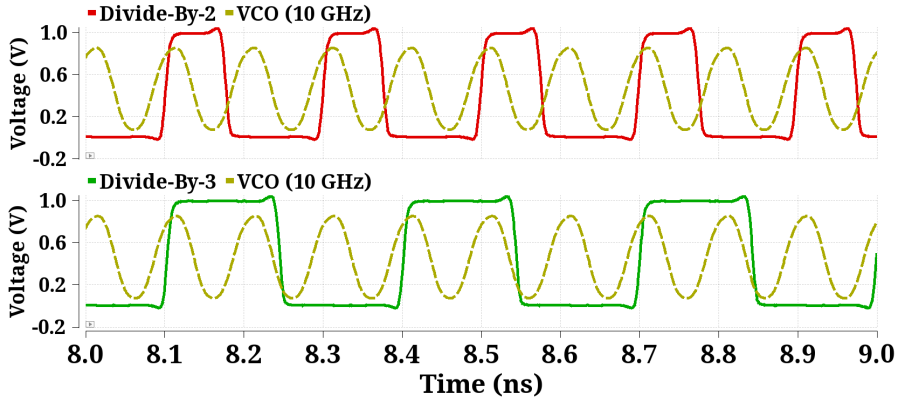

(b) f_{VCO} = 10 GHz

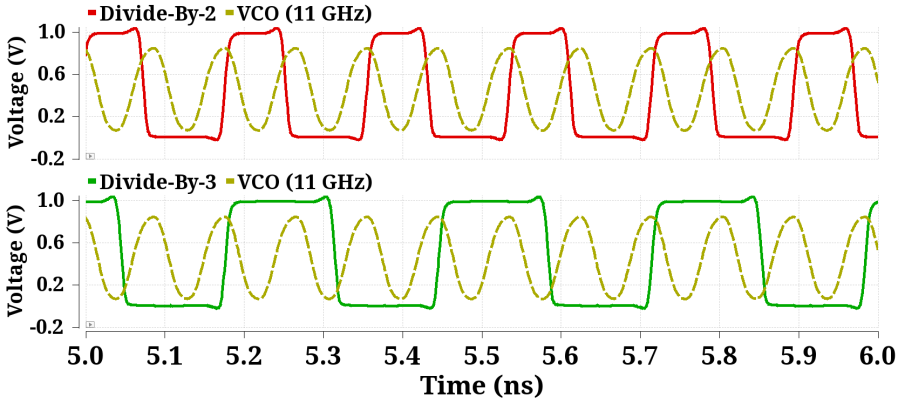

(c) f_{VCO} = 11 GHz

Figure 9.5: Extracted simulation of one of the injection voltages from the QVCO and the locked oscillation voltage of the designed prescaler.

Chapter 10

A PHASOR-BASED ANALYSIS OF SINUSOIDAL INJECTION LOCKING IN LC AND RING OSCILLATORS

[1] B. Hong and A. Hajimiri, "A phasor-based analysis of sinusoidal injection locking in LC and ring oscillators," *IEEE Transactions on Circuits and Systems I: Regular Papers*, vol. 66, no. 1, pp. 355–368, Jan. 2019. DOI: 10.1109/TCSI.2018.2860045,

In this chapter, we present an alternative perspective into the locking behavior of LC and ring oscillators. By decomposing a sinusoidal injection current into in-phase and quadrature-phase components, exact expressions for the amplitude and phase of an injection-locked LC oscillator which hold for any injection strength and frequency are derived and confirmed by simulation. The analysis, which can be naturally extended to an arbitrary LC resonator topology, leads to a rigorous understanding of the fundamental physics underlying the locking phenomenon. Furthermore, an investigation of the different necessary and sufficient conditions for injection locking to occur is carried out, leading to a more precise notion of the lock range. The ring oscillator is also analyzed in an analogous fashion, resulting in simple yet accurate closed-form expressions for the fractional lock range in the small-injection and long-ring regimes; the expressions are validated by simulations of single-ended inverter-based ring oscillators in 65-nm CMOS. The mathematics behind how the injection modifies the phase delay contributed by each stage in the ring is discussed. A corollary that generalizes the small-injection lock range to any feedback-based oscillator topology is established. Conceptual and analytical connections to the existing literature are reviewed.

10.1 Introduction

As we mentioned in Chapter 2, the behavior of LC oscillators under a sinusoidal injection of current has been studied extensively over the years by many, including Adler [47], Razavi [38], and Mirzaei [21]. Still, the analyses thus far fail to completely address some important scenarios or make simplifying assumptions which can yield inaccurate results. For example, the large-signal lock range derived in [38], [49] is infinite when the injection current exceeds the oscillator current, which

can be verified via simulation to be untrue. All of these analyses also do not fully consider the important question of how the oscillator's core nonlinearity reacts to phase modulation in the oscillation voltage, which is of critical concern since the phase of the oscillation voltage is exactly what gets modulated under injection. This chapter derives a comprehensive, large-signal model of injection-locked LC oscillators based on a physical analysis of the currents flowing through the circuit in sinusoidal steady state.

The material is organized as follows. Section 10.2 sets up the problem, introduces notation, and defines a new parameter known as the *reactive tangent*; while Section 10.3 briefly reviews the geometry of injection. Section 10.4 carries out a physically-based analysis of the LC oscillator under injection by calculating the various currents flowing within the oscillator, which leads to a derivation of distinct necessary and sufficient conditions for injection locking to occur. Section 10.5 addresses some important general issues governing the behavior of LC oscillators. Section 10.6 adapts the analytical tools developed for the LC oscillator to calculate the lock range of the ring oscillator. Section 10.7 establishes a general corollary relating the small-injection lock range to the oscillator's open-loop transfer function.

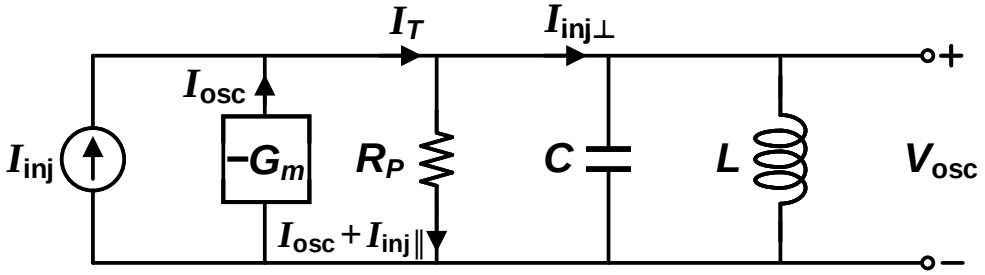

Figure 10.1: Conceptual circuit model of an injection-locked LC oscillator. All depicted signals are sinusoidal steady-state phasors at ω_{inj}, the injection frequency.

10.2 Preliminaries

Problem Setup and Circuit Model

Our problem setup is depicted in Figure 10.1. The oscillator is behaviorally modeled as an ideal LC tank in parallel[1] with a loss resistance R_P, compensated for by an active transconductor presenting a negative conductance: the $-G_m$-cell. The

[1] The scenario where the inductor Q is very low and its series loss is no longer accurately modeled as a parallel resistance is considered in detail elsewhere [3]; however, a natural modification to our framework also easily subsumes the analysis of this situation (Section 10.4).

transconductor's instantaneous current, $i_{G_m}(t)$, is a memoryless, time-invariant, and nonlinear function, $f(\cdot)$, of the instantaneous voltage $v_{\text{osc}}(t)$ across it. We adopt the usual assumption [21], [89] that the impedance of the LC tank filters out all but the fundamental component of the transconductor current $i_{G_m}(t)$ near the tank's resonant frequency $\omega_0 = 1/\sqrt{LC}$, resulting in a sinusoidal oscillation voltage $v_{\text{osc}}(t)$ with amplitude V_{osc} and frequency ω_{osc}. We will refer to the fundamental component of $i_{G_m}(t)$ as the *oscillator current* $i_{\text{osc}}(t)$; its phasor $\overrightarrow{I}_{\text{osc}}$ is labeled in the circuit model of Figure 10.1. This set of abstractions allows us to work exclusively with phasors in sinusoidal steady state.

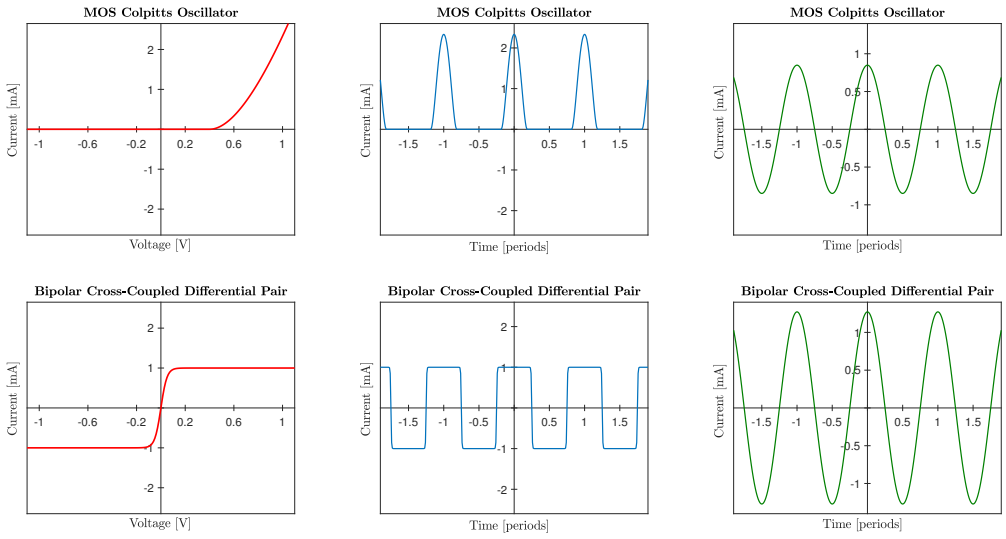

(a) $I = f(V)$ (b) $i_{G_m}(t)$ (c) $i_{\text{osc}}(t)$

Figure 10.2: Example depictions of a nonlinear, time-invariant, memoryless transconductor's response to a cosine oscillation voltage $v_{\text{osc}}(t) = V_0 \cos(\omega_{\text{osc}} t)$ with an amplitude of $V_0 = 1$ V. The (a) transconductor's $I = f(V)$ characteristic, (b) resultant transconductor current $i_{G_m}(t)$, and (c) its fundamental component or oscillator current $i_{\text{osc}}(t)$ are shown for a MOS Colpitts oscillator (top) and a cross-coupled bipolar differential pair (bottom). Note how $i_{\text{osc}}(t)$ is perfectly in phase with $v_{\text{osc}}(t)$ in both cases.

Since the $-G_m$-cell is memoryless and time-invariant, the oscillator current $\overrightarrow{I}_{\text{osc}}$ and the oscillation voltage $\overrightarrow{V}_{\text{osc}}$ are either perfectly in phase or in antiphase.[2] However, considering the fact that the transconductor is *active*—it generates power—the former must be true. Figure 10.2 shows the transconductor and oscillator currents for two different oscillator transconductor examples. The amplitude of the oscillator

[2]This is easily proven by comparing the Fourier series expansions of $v_{\text{osc}}(t)$ and $i_{G_m}(t)$.

current I_{osc} can thus be computed as

$$I_{\text{osc}} = \frac{2}{T}\int_T f[V_{\text{osc}}\cos(\omega_{\text{osc}}t)]\cdot\cos(\omega_{\text{osc}}t)\,dt. \tag{10.1}$$

As an example, if the transconductor is a hard-limited current commutator $f(x) = \text{sign}(x)\cdot I_{\text{bias}}$, then $I_{\text{osc}} = (4/\pi)I_{\text{bias}}$. This serves as a reasonable model of a cross-coupled differential pair wherein $I_{\text{bias}} = I_{\text{tail}}/2$ (or for complementary pairs $I_{\text{bias}} = I_{\text{tail}}$) [88], [89], [129]. We assume throughout that I_{osc} is a (known) constant and does not depend on V_{osc}, as is usually the case for well-designed (current-biased) oscillators that have sufficient loop gain to fully saturate the transconductor (i.e., $G_m := f'(0) > 1/R_P$, although this constraint must be tightened for "softer" nonlinearities that saturate more smoothly). Finally, observe that because the oscillator current $\vec{I}_{\text{osc}}$ is in phase with the oscillation voltage $\vec{V}_{\text{osc}}$, it can only flow into the parallel loss resistance R_P.

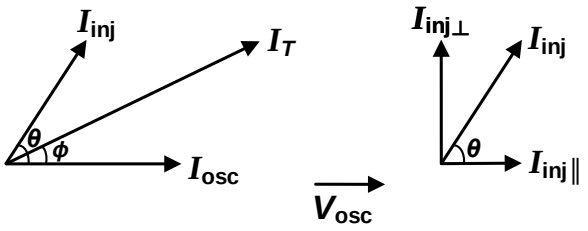

Figure 10.3: Phasor diagram depicting the injection current, the oscillator current, the tank current, the injection current's orthogonal decomposition, and the phase of the oscillation voltage.

In the absence of injection ($I_{\text{inj}} = 0$), the oscillation frequency is[3] $\omega_{\text{osc}} = \omega_0$ and the oscillation amplitude is $V_{\text{osc}} = I_{\text{osc}}R_P$ [88], [89], [129]. Now, suppose the oscillator is perturbed by some periodic injection current $i_{\text{inj}}(t)$ at a frequency ω_{inj} near ω_0. We once again assume that the bandpass nature of the LC tank leaves us with only the voltage due to the injection current's fundamental component at ω_{inj}, whose phasor we shall denote by $\vec{I}_{\text{inj}}$. A key observation—key to the rest of this analysis—is that in order for the circuit to oscillate at the injection frequency, or be *injection locked*, the injection current must supply net reactive current to the LC tank. This is because if $\omega_{\text{inj}} \neq \omega_0$, the LC tank no longer appears as an open circuit at ω_{inj} as it does at resonance and therefore must draw current. Based on our reasoning

[3] In actuality, higher-order harmonics in $i_{G_m}(t)$ slightly disrupt the tank's harmonic balance and *decrease* the free-running oscillation frequency away from resonance [108], [130]. Also see [131] for a transient analysis of the impact that an oscillator's nonlinearity has on its oscillation frequency.

above, this current, which is ±90° out of phase with $\overrightarrow{V}_{\text{osc}}$, cannot be provided by the transconductor. Instead, this *reactive* current must be supplied in its entirety by the injection—we thus label it as $\overrightarrow{I}_{\text{inj}\perp}$. The remaining component of the injection current, which we denote as $\overrightarrow{I}_{\text{inj}\parallel}$, is therefore co-linear (i.e., either in-phase or 180° out-of-phase) with $\overrightarrow{V}_{\text{osc}}$ and $\overrightarrow{I}_{\text{osc}}$.

Therefore, we have the following phasor decomposition of the injection current:

$$\overrightarrow{I}_{\text{inj}} = \overrightarrow{I}_{\text{inj}\parallel} + \overrightarrow{I}_{\text{inj}\perp}, \tag{10.2}$$

which by the Pythagorean theorem implies

$$I_{\text{inj}}{}^2 = I_{\text{inj}\parallel}{}^2 + I_{\text{inj}\perp}{}^2. \tag{10.3}$$

Finally, by KCL, it is obvious that the total current $\overrightarrow{I}_T$ flowing into the lossy resonator (LC tank + parallel resistance R_P) comes from the oscillator and injection currents:

$$\overrightarrow{I}_T = \overrightarrow{I}_{\text{osc}} + \overrightarrow{I}_{\text{inj}}. \tag{10.4}$$

These decompositions are depicted physically in Figure 10.1 and geometrically in Figure 10.3.

Geometric Conventions

Let us precisely define the various angles in Figure 10.3. We see that $\phi \coloneqq \angle \overrightarrow{V}_{\text{osc}} - \angle \overrightarrow{I}_T$ is the phase difference between the oscillation voltage and the tank current, which is equal to the phase of the resonator's impedance. For resonators featuring a positive net conductance, ϕ is bounded between ±90°.

Also, $\theta \coloneqq \angle \overrightarrow{V}_{\text{osc}} - \angle \overrightarrow{I}_{\text{inj}}$ is the phase difference between the oscillation voltage and the injection current. We will adopt the convention that the angular domain is $\theta \in [-\pi, \pi)$. Much of the literature on injection locking and pulling focuses on the dynamics of θ, the most notable result being Adler's original equation [47]. Note that ϕ and θ are both positive (negative) if the voltage *leads* (*lags*) the currents, which occurs if $\Delta\omega < 0$ ($\Delta\omega > 0$) and we inject below (above) resonance.

The Reactive Tangent $\chi(\omega_{\text{inj}})$

Here, we will introduce a new parameter, which we call the *reactive tangent* $\chi(\omega_{\text{inj}})$, defined as the tangent of the phase of the resonator's impedance at the injection frequency:

$$\boxed{\chi(\omega_{\text{inj}}) \coloneqq \tan\phi.} \tag{10.5}$$

The reactive tangent is a measure of "how reactive" the resonator is at the injection frequency. If $\omega_{\text{inj}} = \omega_0$, the tank is purely resistive and not reactive at all, and so $\chi(\omega_0) = 0$. On the other hand, frequencies below resonance result in $\chi(\omega_{\text{inj}}) > 0$ and a resonator that appears partially inductive. Finally, if $\omega_{\text{inj}} > \omega_0$, then the reactive tangent is negative and the resonator appears partially capacitive.

For the parallel RLC resonator under consideration,

$$\begin{aligned}\chi(\omega_{\text{inj}}) &= \frac{R_P}{X_{LC}(\omega_{\text{inj}})} \\ &= \frac{R_P}{\omega_{\text{inj}} L}\left(1 - \frac{{\omega_{\text{inj}}}^2}{{\omega_0}^2}\right) \\ &= Q\left(\frac{\omega_0}{\omega_{\text{inj}}} - \frac{\omega_{\text{inj}}}{\omega_0}\right)\end{aligned} \tag{10.6}$$

where X_{LC} is the reactance of the *ideal* parallel LC tank (without R_P) and $Q = R_P/\omega_0 L$ is the resonator's quality factor. If the injection and free-running frequencies are close to one another (i.e., $|\Delta\omega| \ll \omega_0$, where $\Delta\omega \coloneqq \omega_{\text{inj}} - \omega_0$) as most papers assume, we can approximate

$$\chi(\omega_{\text{inj}}) \approx -2Q\left(\frac{\Delta\omega}{\omega_0}\right). \tag{10.7}$$

Figure 10.4 compares this approximation against Eq. (10.6).

Although the reactive tangent is not a fundamentally novel parameter, its significance stems from the following facts:

1. Its magnitude is the ratio of the net reactive current to the net resistive current flowing into the lossy resonator. It will therefore serve as a convenient quantity to deal with in the subsequent analysis.

2. The lock range on $\chi(\omega_{\text{inj}})$ is symmetric (about 0), whereas the lock range on $\Delta\omega$ is not.

3. The reactive tangent is applicable to other types of tank topologies, and so our analysis will not be constrained to the parallel RLC resonator (e.g., see the discussion on low-Q inductors in Section 10.4).

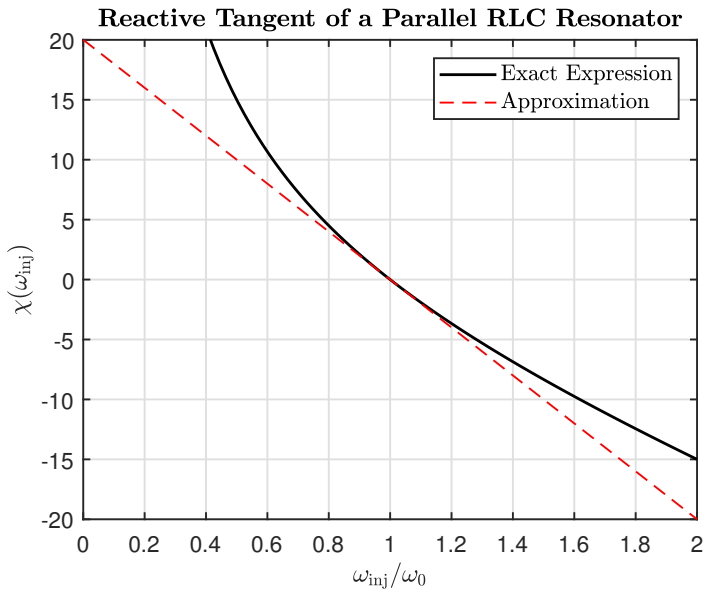

Figure 10.4: A plot of $\chi(\omega_{\text{inj}})$ against $\omega_{\text{inj}}/\omega_0$ for a parallel RLC resonator with a quality factor of $Q = 10$. Observe that $\chi(\omega_{\text{inj}})$ decreases monotonically from $+\infty$ to $-\infty$ as ω_{inj} increases from DC to $+\infty$.

10.3 Review of Injection Geometry

Here, we will briefly review the geometric argument the existing literature [38], [49] has used to derive the lock range for large injections. However, we will also illustrate how such an analysis may not fully lend itself to a solid understanding of the physics governing the phenomenon of injection locking, particularly at the edge of the lock range. Consider Figure 10.3. The lock range is defined as the range of allowable injection frequencies ω_{inj} over all possible injection phases θ for a given resonator, injection current I_{inj}, and oscillator current I_{osc}. Since ϕ is the phase of the resonator's impedance at ω_{inj}, the quantity $\sin\phi$ decreases monotonically from $+1$ to -1 as ω_{inj} varies from 0 to ∞. Therefore, optimizing for the injection frequency is akin to extremizing $\sin\phi$, which yields the following solution for the optimum injection phase θ^* [38]:

$$\cos\theta^* = \begin{cases} -\dfrac{I_{\text{inj}}}{I_{\text{osc}}}, & I_{\text{inj}} \leq I_{\text{osc}} \\ -\dfrac{I_{\text{osc}}}{I_{\text{inj}}}, & I_{\text{inj}} \geq I_{\text{osc}}. \end{cases} \tag{10.8}$$

This implies

$$|\sin\phi| \leq \begin{cases} \dfrac{I_{\text{inj}}}{I_{\text{osc}}}, & I_{\text{inj}} \leq I_{\text{osc}} \\ 1\ , & I_{\text{inj}} \geq I_{\text{osc}}. \end{cases} \tag{10.9}$$

Since $\chi(\omega_{\text{inj}}) = \tan\phi$, the lock range on $\chi(\omega_{\text{inj}})$ is

$$\left|\chi(\omega_{\text{inj}})\right| \leq \begin{cases} \dfrac{1}{\sqrt{\dfrac{{I_{\text{osc}}}^2}{{I_{\text{inj}}}^2} - 1}}, & I_{\text{inj}} < I_{\text{osc}} \\ +\infty\ , & I_{\text{inj}} \geq I_{\text{osc}}. \end{cases} \tag{10.10}$$

Shown in Figure 10.5, there is a geometric picture which illuminates this situation quite clearly [21]. The oscillator current phasor $\overrightarrow{I}_{\text{osc}}$ is always oriented horizontally, as its phase is equal to that of the oscillation voltage and is therefore taken as the reference. The injection phase θ (the angle that $\overrightarrow{I}_{\text{inj}}$ makes with $\overrightarrow{I}_{\text{osc}}$) is allowed to vary over $[-\pi, \pi)$, creating a circle of radius I_{inj} centered at the endpoint of $\overrightarrow{I}_{\text{osc}}$. Therefore, each point on the circle represents a possible solution for $\overrightarrow{I}_T = \overrightarrow{I}_{\text{osc}} + \overrightarrow{I}_{\text{inj}}$. The phase ϕ of the lossy resonator's impedance is equal to the angle between $\overrightarrow{I}_T$ and $\overrightarrow{I}_{\text{osc}}$. For $R_P > 0$, $\phi \in [-\pi/2, \pi/2]$. The lock range is dictated by the attainable values for ϕ. Optimal solutions, corresponding to the edge of the lock range where $\phi = \phi_{\max}$, are indicated by an asterisk: " * ".

The $I_{\text{inj}} < I_{\text{osc}}$ case is well-documented [38], [49]. But, this result does bring up the intriguing notion of an *infinite* lock range when $I_{\text{inj}} \geq I_{\text{osc}}$. Although *mathematically* accurate within the presented geometric framework, we will demonstrate in Section 10.4 that this conclusion for the lock range when the injection current exceeds the oscillator current is *physically* incorrect.

10.4 A Physically-Based Analysis

We start by using the parameter $\chi(\omega_{\text{inj}})$ to quantify a very specific relationship between the currents within the oscillator, alluded to at the end of Section 10.2. For notational simplicity, we will sometimes write $\chi(\omega_{\text{inj}})$ as χ with the understanding that this parameter is always to be evaluated at ω_{inj}. Given the parallel nature of the resonator, the oscillation amplitude can be written as the net resistive current multiplied by R_P or as the net reactive current multiplied by X_{LC}. In light of Eq. (10.6), we can therefore write

$$V_{\text{osc}} = \left(I_{\text{osc}} + I_{\text{inj}\parallel}\right) R_P = I_{\text{inj}\perp} \frac{R_P}{\chi(\omega_{\text{inj}})}. \tag{10.11}$$

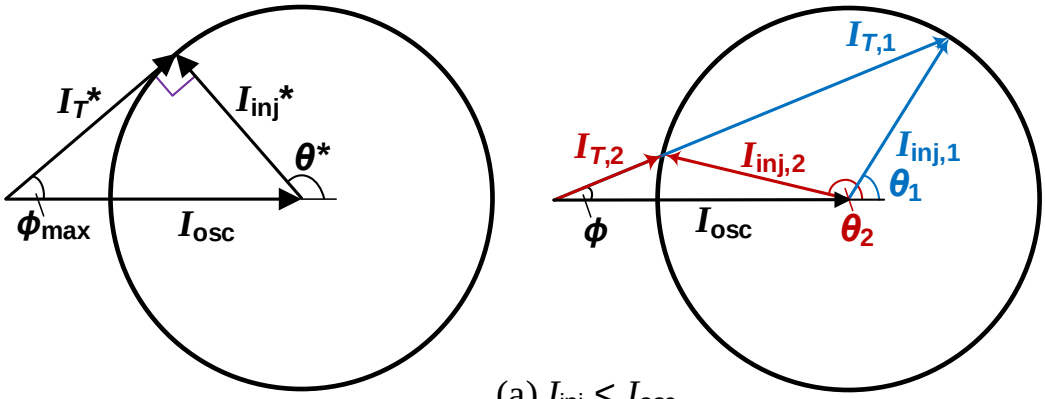

(a) $I_{inj} < I_{osc}$

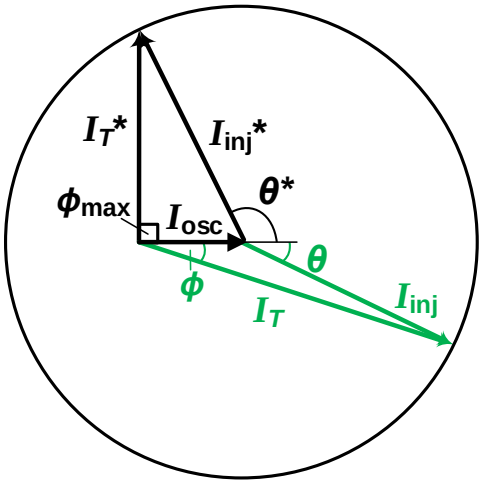

(b) $I_{inj} \geq I_{osc}$

Figure 10.5: Geometric depiction of the lock range (a) Left: The (lower) edge of the lock range, showing that $|\phi_{max}| < \pi/2$ if $I_{inj} < I_{osc}$. Right: For each ϕ where $|\phi| < |\phi_{max}|$ (i.e., for each injection frequency strictly inside the lock range), two possible solutions exist. Solution 1 (blue) is stable whereas Solution 2 (red) is unstable. (b) If $I_{inj} \geq I_{osc}$, then the edge of the lock range corresponds to $\phi_{max} = \pm\pi/2$. Also, only one mode exists.

Here, we leave open the possibility that $I_{inj\parallel} < 0$. That is, the non-reactive component of the injection could be 180° *out-of-phase* with the oscillation voltage and *oppose* the oscillator current (see Figure 10.5). Note that we are also adopting the convention that $I_{inj\perp}$ shares the same sign as θ and ϕ. Using Eq. (10.3) then yields

$$I_{osc} + I_{inj\parallel} = \frac{\sqrt{{I_{inj}}^2 - {I_{inj\parallel}}^2}}{|\chi(\omega_{inj})|}. \tag{10.12}$$

Solving for $I_{\text{inj}\|}$, we get

$$I_{\text{inj}\|} = \frac{\pm\sqrt{\left(1+\chi^2\right) {I_{\text{inj}}}^2 - \chi^2 {I_{\text{osc}}}^2} - \chi^2 I_{\text{osc}}}{1+\chi^2} \tag{10.13}$$

which indicates two possible solutions or modes [21], as depicted in Figure 10.5(a).

For the solutions to be real, the discriminant needs to be nonnegative, which is always the case if $I_{\text{inj}} \geq I_{\text{osc}}$. Assume not. Then we need

$$\left|\chi(\omega_{\text{inj}})\right| \leq \frac{1}{\sqrt{\dfrac{{I_{\text{osc}}}^2}{{I_{\text{inj}}}^2} - 1}}, \tag{10.14}$$

which is equivalent to Eq. (10.10), re-derived *physically* instead of *geometrically*. Thus, the "lock range" derived in Section 10.3 is precisely the condition that needs to be satisfied in order for the oscillator to have a sinusoidal steady-state solution at the injection frequency ω_{inj}. In other words, Eq. (10.10) is a *necessary condition* for injection locking to occur.

We will now consider the two solutions of Eq. (10.13) separately. In [21], Mirzaei *et al.* derive a differential equation for perturbations in the phase to show that only the solution with the higher oscillation amplitude is mathematically stable. However, the subtle issue of stability extends beyond the notion of being able to recover from disturbances in the phase. Notice from both Figure 10.5 and Eq. (10.13) that solutions exist where $I_{\text{inj}\|} < 0$ and the injection's non-reactive component is 180° out of phase with the oscillation voltage. This implies that although the oscillator current is supplying power to the resonator, the injection current is dissipating power. Consequently, in the presence of perturbations (due to noise for example), while the transconductor will always strive to restore the oscillation amplitude to its equilibrium value, the injection current will "fight" the transconductor's efforts. As the circuit ventures closer to the edge of Eq. (10.14), these two opposing forces become comparable since $I_{\text{inj}\|}$ approaches $-I_{\text{osc}}$. Therefore, at some point, it will become energetically favorable for the oscillator to lose lock altogether and become *injection pulled*. We suspect that a simple first-order equation for modeling the oscillation amplitude like Eq. (10.36) (also see [21]) is unable to capture this dynamic.

The Stable Solution: The stable solution is

$$I_{\text{inj}\|,1} = \frac{\sqrt{\left(1+\chi^2\right) {I_{\text{inj}}}^2 - \left(\chi I_{\text{osc}}\right)^2} - \chi^2 I_{\text{osc}}}{1+\chi^2}. \tag{10.15}$$

It is not hard to see that $I_{\text{inj}\|,1} \geq 0$ if and only if $I_{\text{inj}} \geq \left|\chi(\omega_{\text{inj}})\right| I_{\text{osc}}$. This result is highly intuitive. If the non-reactive portion of the injection current is in-phase with the oscillation voltage and therefore adds to the oscillator current, then the oscillation amplitude is at least $I_{\text{osc}} R_P$ (the free-running amplitude). Therefore, the injection must be able to supply at least $|X_{\text{LC}}|\, I_{\text{osc}} R_P$ of reactive current, which leads to $I_{\text{inj}} \geq \left|\chi(\omega_{\text{inj}})\right| I_{\text{osc}}$. In light of our discussion regarding energetic stability, we can therefore see that

$$|\chi_{\text{tank}}| \leq \frac{I_{\text{inj}}}{I_{\text{osc}}} \tag{10.16}$$

is a *sufficient condition* for injection locking to occur, since there will always exist an *energetically* stable sinusoidal steady-state solution at ω_{inj} provided that Eq. (10.16) holds.

The Unstable Solution: The unstable solution, shown in red in Figure 10.5(a), is

$$I_{\text{inj}\|,2} = \frac{-\sqrt{\left(1+\chi^2\right) {I_{\text{inj}}}^2 - (\chi I_{\text{osc}})^2} - \chi^2 I_{\text{osc}}}{1+\chi^2}. \tag{10.17}$$

This solution is valid only if $I_{\text{osc}} + I_{\text{inj}\|,2} \geq 0$, as indicated by the original equation Eq. (10.12). Thus, this mode comes into existence if and only if $I_{\text{inj}} \leq I_{\text{osc}}$. Note that the two solutions coincide at the edge of the lock range.

Summary

Let us recapitulate our results. First, recall that the lock range was formally computed in terms of the reactive tangent $\chi(\omega_{\text{inj}})$, defined in Eq. (10.5). For a parallel RLC resonator,

$$\chi(\omega_{\text{inj}}) = Q\left(\frac{\omega_0}{\omega_{\text{inj}}} - \frac{\omega_{\text{inj}}}{\omega_0}\right).$$

Next, the lock range was deconstructed into necessary and sufficient conditions which are distinct.

Sufficient Condition: If the following condition holds:

$$\boxed{\left|\chi(\omega_{\text{inj}})\right| \leq \frac{I_{\text{inj}}}{I_{\text{osc}}},} \tag{10.18}$$

then the oscillator will injection lock (in steady state).

Necessary Condition: In order for the oscillator to injection lock, the following condition must hold:

$$\boxed{\left|\chi(\omega_{\text{inj}})\right| \leq \begin{cases} \dfrac{1}{\sqrt{\dfrac{{I_{\text{osc}}}^2}{{I_{\text{inj}}}^2} - 1}}, & I_{\text{inj}} < I_{\text{osc}} \\ +\infty \quad , & I_{\text{inj}} \geq I_{\text{osc}}. \end{cases}} \tag{10.19}$$

Notice that the sufficient condition subsumes the necessary one. Unfortunately, given the current framework, we were not able to develop a necessary *and* sufficient condition for injection locking. Fortunately, for I_{inj} reasonably smaller than I_{osc} (e.g., $I_{\text{inj}}/I_{\text{osc}} \lessapprox 1/2$), which covers many practical scenarios, it can be verified empirically that the necessary condition is a sufficient one as well. We suspect that satisfying Eq. (10.19) allows an oscillator to lock onto the injection initially in its *transient* response, but an oscillator which does not satisfy Eq. (10.18) may have trouble maintaining lock in *steady state* and will be prone to being pulled eventually.

Note that if the frequency deviation is small $|\Delta\omega| \ll \omega_0$ and the injection is weak $I_{\text{inj}} \ll I_{\text{osc}}$, then both Eqs. (10.18) and (10.19) simplify to the lock range originally given by Adler [47]:

$$|\Delta\omega| \leq \omega_L = \frac{\omega_0}{2Q} \cdot \frac{I_{\text{inj}}}{I_{\text{osc}}}. \tag{10.20}$$

Assuming the oscillator is injection-locked, the non-reactive component of the injection current is given by

$$I_{\text{inj}\|} = \frac{\sqrt{\left(1+\chi^2\right){I_{\text{inj}}}^2 - \left(\chi I_{\text{osc}}\right)^2} - \chi^2 I_{\text{osc}}}{1+\chi^2}.$$

The oscillation amplitude is given by

$$\boxed{V_{\text{osc}} = \left(I_{\text{osc}} + I_{\text{inj}\|}\right) R_P.}$$

Accounting for the correct sign, the oscillator's phase relative to the injection is given by

$$\boxed{\theta = -\operatorname{sign}(\Delta\omega) \cdot \cos^{-1}\left(\frac{I_{\text{inj}\|}}{I_{\text{inj}}}\right).}$$

Note that the oscillator's phase $|\theta|$ increases monotonically from 0 as $\left|\chi(\omega_{\text{inj}})\right|$ increases from 0, and it reaches 90° when $I_{\text{inj}} = \left|\chi(\omega_{\text{inj}})\right| I_{\text{osc}}$.

A Driven Parallel RLC Resonator

We would like to demonstrate how this framework reduces when the transconductor turns off ($I_{\text{osc}} = 0$) and the system is not an oscillator—just a damped LC resonator. Notice that based on Eq. (10.18), the "lock range" becomes infinite. Then

$$I_{\text{inj}\parallel} = \frac{I_{\text{inj}}}{\sqrt{1 + \chi(\omega_{\text{inj}})^2}}. \tag{10.21}$$

It is not hard to see that this yields an oscillation amplitude of $V_{\text{osc}} = \left|Z_{\text{res}}(j\omega_{\text{inj}})\right| I_{\text{inj}}$ and an oscillation phase of $\theta = \tan^{-1}\chi(\omega_{\text{inj}}) = \angle Z_{\text{res}}(j\omega_{\text{inj}})$, where Z_{res} is the impedance of the RLC resonator. These results are in accordance with LTI system theory: a sinusoidal input results in a sinusoidal output at the same frequency (infinite lock range), whose amplitude and phase are shaped by the magnitude and phase of the system's transfer function at the input frequency.

Low-Q Inductors

Tanks featuring inductors with very low quality factors cannot be accurately modeled by a parallel loss resistance [3]. Still, the concept of decomposing the net current which flows into the resonator into in-phase and quadrature-phase components is still valid, and so the analysis above can be modified very simply to account for this scenario. In particular, we need to compute the reactive tangent based on its fundamental definition Eq. (10.5) $\chi(\omega_{\text{inj}}) \coloneqq \tan\phi$; physically, it still represents the ratio of the net reactive to resistive current drawn by the entire resonator, and so Eq. (10.12) still holds.

We now consider a capacitor C in parallel with an inductor L that features a series loss resistance R_s. The quality factor is now defined as $Q = \omega_0 L/R_s$, where ω_0 is the resonant frequency—the frequency at which the resonator's admittance is purely real. Assuming $L/R_s > R_s C$, it is not hard to show that

$$\omega_0 = \sqrt{\frac{1}{LC} - \left(\frac{R_s}{L}\right)^2} = \frac{1}{\sqrt{LC\left(1 + \frac{1}{Q^2}\right)}}, \tag{10.22}$$

and[4]

$$\chi(\omega_{\text{inj}}) = \frac{Q}{1 + \frac{1}{Q^2}} \frac{\omega_{\text{inj}}}{\omega_0}\left(1 - \frac{{\omega_{\text{inj}}}^2}{{\omega_0}^2}\right). \tag{10.23}$$

[4]Equation (2) in [3] is incorrect. The term $\left(1 - 1/Q^2\right)^{1.5}$ should be $\left(1 + 1/Q^2\right)^{-1}$. Their expression makes no sense when $Q < 1$.

To compute the oscillation amplitude, replace R_P with the inverse of the resonator's conductance $G(\omega_{\text{inj}})$, given by

$$\frac{1}{G(\omega_{\text{inj}})} = \frac{\omega_0 L}{Q}\left[1 + \left(\frac{Q\omega_{\text{inj}}}{\omega_0}\right)^2\right]. \tag{10.24}$$

Simulation Results

To demonstrate the validity of the phase and amplitude expressions we derived above, we used SpectreRF to simulate the behavioral model of Figure 10.1 under lock. The transconductor was implemented using a Verilog-A cell coded with the usual hard-limited current commutator functionality $f(x) = \text{sign}(x) \cdot I_{\text{bias}}$ and so $I_{\text{osc}} = (4/\pi)I_{\text{bias}}$. The resonator featured a parallel resistance of $R_P = 300\ \Omega$, an inductance of $L = 5\ \mu$H, and a capacitance of $C = 5.066$ nF, resulting in a resonant frequency of approximately $f_0 = 1$ MHz.

The first set of simulations, depicted in Figure 10.6a, sweeps the injection current while the bias current is held at $I_{\text{bias}} = 1$ mA. The injection frequency is $f_{\text{inj}} = 1.1$ MHz, resulting in $\chi(\omega_{\text{inj}}) \cong -1.823$. Note that it is important that we use Eq. (10.6) and not its approximation Eq. (10.7) to compute the reactive tangent, as the approximation gives $\chi(1.1\text{ MHz}) \approx -1.910$.

The second set of simulations, depicted in Figure 10.6b, sweeps the bias current while the injection current is held at $I_{\text{inj}} = 2.5$ mA. The injection frequency is $f_{\text{inj}} = 0.98$ MHz. The plots are given as a function of the oscillator current. A smooth plot for the theoretical predictions could not be generated here, since the strength of the oscillator current slightly lowers the oscillation frequency due to the higher-order harmonics contained in its square waveform [108], [130]. We therefore simulated the free-running oscillation frequency f_0 and computed the reactive tangent at each simulation point. On average, $\chi(0.98\text{ MHz}) \sim 0.4759$.

To demonstrate how drastically large injections can change the behavior of the oscillator, we also plotted the steady-state solution to Adler's equation [47] for the oscillation phase:

$$\theta = -\sin^{-1}\left(2Q\frac{\Delta\omega}{\omega_0}\frac{I_{\text{inj}}}{I_{\text{osc}}}\right). \tag{10.25}$$

Note that Adler's solution does not allow $|\theta|$ to exceed 90°.

There is excellent agreement between the presented model and the example simulations. The error increases near the edge of the lock range, which is in accordance with our discussion in Section 10.4 that our sinusoidal steady-state framework is

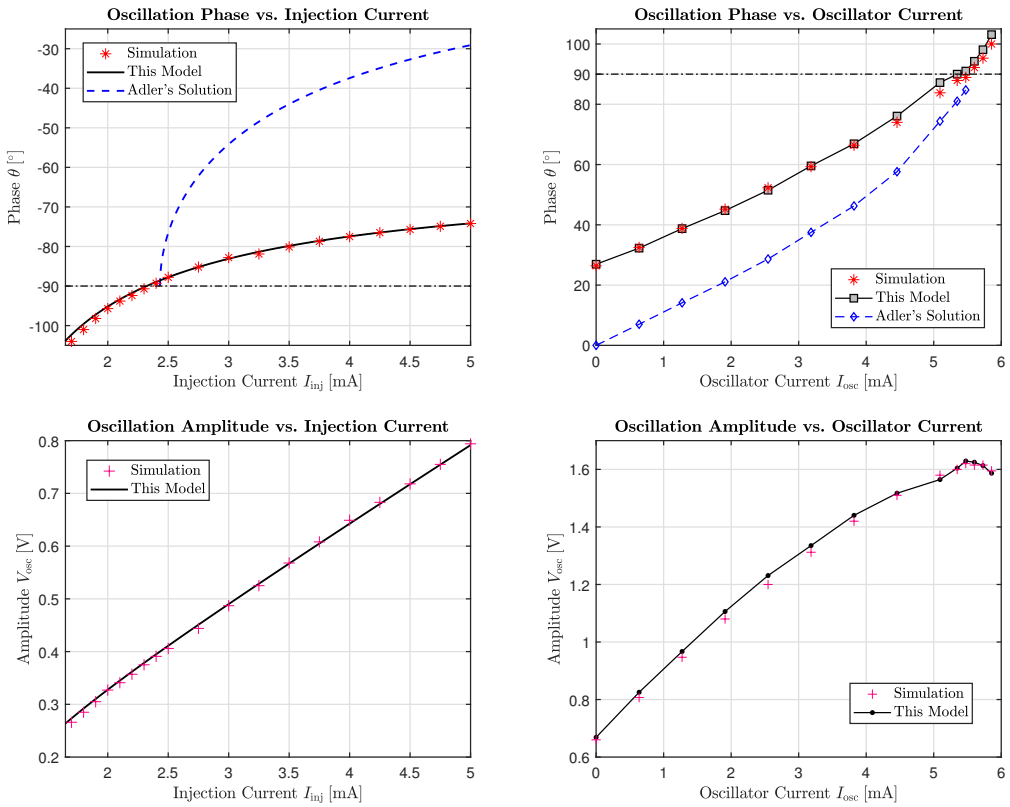

(a) $f_{inj} = 1.1$ MHz and $I_{osc} = (4/\pi)$ mA (b) $f_{inj} = 0.98$ MHz and $I_{inj} = 2.5$ mA

Figure 10.6: Theoretical and simulated oscillation phase relative to the injection θ (top) and amplitude V_{osc} (bottom) of an injection-locked LC oscillator plotted (a) against the injection current I_{inj} and (b) against the oscillator current I_{osc}. For the graphs depicting θ, Adler's solution for the phase is also plotted for comparison.

incapable of predicting when and how the energetics and dynamics of injection pulling become apparent.

10.5 General Considerations for LC Oscillators under Sinusoidal Injection

In this section, we will use the same circuit model of Figure 10.1, but without the assumption of sinusoidal steady state.

The Transconductor's Effect on Phase Modulation

An important but often overlooked issue is how the transconductor reacts to phase modulation (PM) in the oscillation voltage. We stated in Section 10.2 that if $v_{osc}(t)$ is *purely* sinusoidal at a single tone (constant phase), then the fundamental component of the transconductor current $i_{G_m}(t) = f[v_{osc}(t)]$ has the same phase as $v_{osc}(t)$. But, what if the oscillation voltage has a time-varying phase $\theta(t)$? Intuitively, we

would expect a memoryless, time-invariant system to be incapable of changing the time- or phase- dynamics of its input. However, the situation is complicated by the higher-order harmonics that are introduced by the nonlinearity.

We will assume the usual setting of an oscillator under injection: that the carrier frequency is $\omega_{\text{osc}} = \omega_{\text{inj}}$ and so any PM $\theta(t)$ is referred to $\omega_{\text{inj}}t$. Thus, we write the oscillation voltage as $v_{\text{osc}}(t) = V_{\text{osc}} \cos\big[\omega_{\text{inj}}t + \theta(t)\big]$, where $\theta(t)$ is an arbitrary signal. Define the PM-free $v_0(t) \coloneqq V_{\text{osc}} \cos(\omega_{\text{inj}}t)$ and its corresponding output $i_0(t) \coloneqq f[v_0(t)]$. Starting from $i_{G_m}(t) \coloneqq f[v_{\text{osc}}(t)]$, we can therefore write

$$\begin{aligned} i_{G_m}(t) &= f\left(V_{\text{osc}} \cos[\omega_{\text{inj}}t + \theta(t)]\right) \\ &= f\left[v_0\left(t + \frac{\theta(t)}{\omega_{\text{inj}}}\right)\right] \\ &= i_0\left(t + \frac{\theta(t)}{\omega_{\text{inj}}}\right), \end{aligned} \tag{10.26}$$

where the last step follows from the fact that for any $t_0 \in \mathbb{R}$, $f\,[x(t_0)]$ depends only on the *value* that $x(t)$ takes on at $t = t_0$ and not explicitly on t_0 itself (time-invariant) or on what $x(t)$ is when $t \neq t_0$ (memoryless). Next, notice that $i_0(t) \equiv f\left[V_{\text{osc}} \cos\left(\omega_{\text{inj}}t\right)\right]$ is an even, periodic function with period ω_{inj} and therefore admits the following Fourier series representation:

$$i_0(t) = \sum_{n=0}^{\infty} F_n \cos(n\omega_{\text{inj}}t), \tag{10.27}$$

where the F_n are the Fourier series coefficients of the transconductor current in response to $v_0(t)$. Consequently, we can similarly expand the transconductor current due to $v_{\text{osc}}(t)$ as

$$i_{G_m}(t) = \sum_{n=0}^{\infty} F_n \cos\big(n[\omega_{\text{inj}}t + \theta(t)]\big)\,. \tag{10.28}$$

This result confirms the intuition that the transconductor preserves the input voltage's phase modulation in its first harmonic term $F_1 \cos[\omega_{\text{inj}}t + \theta(t)]$. More importantly, however, this analysis elicits the core issue at hand: PM accompanying higher-order harmonics ($n > 1$) could interfere or overlap with that of the fundamental ($n = 1$), as shown in Figure 10.7.

Although describing the spectra of the various harmonics $\cos\big(n[\omega_{\text{inj}}t + \theta(t)]\big)$ is in general quite difficult for arbitrary $\theta(t)$,[5] we can use Carson's bandwidth rule [132],

[5]For example, a single-tone PM $\theta(t) \propto \sin(\omega_m t)$ results in a spectrum with infinitely many side-tones about ω_{inj}, separated by ω_m, whose strengths are modulated by Bessel functions of the first kind.

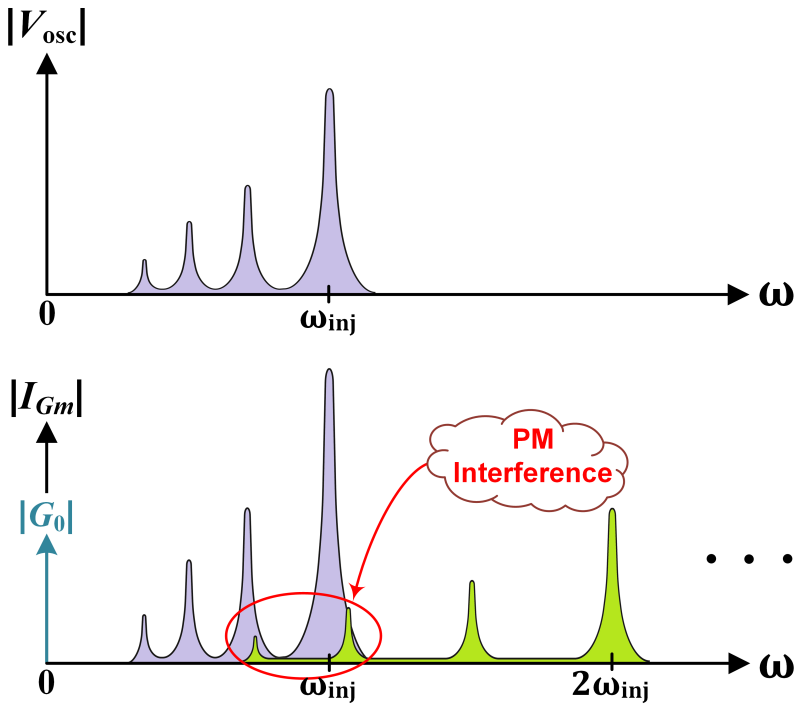

Figure 10.7: Conceptual depiction of how nonlinearities in the transconductor can cause PM accompanying higher-order harmonics to "spill over" into PM of the fundamental. The graphs represent the magnitude spectra of $v_{\text{osc}}(t)$ (top) and $i_{G_m}(t)$ (bottom). Notice that the sideband-to-carrier ratios of the fundamental harmonic's PM are preserved by the transconductor.

for example, to approximate the bandwidths (up to a 2% error in the energy) of the individual phase-modulated components of $i_{G_m}(t)$. Some simple algebra then leads to the following condition for keeping the input voltage's PM intact, and therefore recoverable, at the output of the transconductor:

$$\boxed{4\theta'_{\text{max}} + 2\sigma_\theta < \omega_{\text{inj}},} \tag{10.29}$$

where $\theta'_{\text{max}} = \max_{t\in\mathbb{R}} |\theta'(t)|$ is the maximum absolute time-derivative of $\theta(t)$ and σ_θ is the one-sided bandwidth of or maximum frequency present within $\theta(t)$. As a mathematical note, Bernstein's inequality [133] allows us to bound the derivative of a bounded, band-limited signal via $\theta'_{\text{max}} \leq \sigma_\theta \theta_{\text{max}}$. Therefore, another sufficient condition in place of Eq. (10.29) would be $2\sigma_\theta\,(2\theta_{\text{max}} + 1) < \omega_{\text{inj}}$.

It is noteworthy that by using a Taylor series to linearize the time-dependent transconductance $f'(v_{\text{osc}}(t))$ about the phase modulation, and then using a Fourier series to expand the result, Samori *et al.* [110], [134], [135] prove that small, *single-tone*

PM about the fundamental is preserved. Our argument above, using Eq. (10.28), shows that *arbitrary* PM about the fundamental is always preserved, a much more general conclusion. However, they failed to consider the important issue of whether or not PM from higher-order harmonics might interfere with the PM about the fundamental. Our analysis above addresses this crucial point.

General Equations for the Amplitude and Phase

Referring to the circuit of Figure 10.1, KCL yields

$$\frac{v_{\text{osc}}(t)}{L} + C\frac{d^2 v_{\text{osc}}(t)}{dt^2} + \frac{1}{R_P}\frac{dv_{\text{osc}}(t)}{dt} = \frac{d}{dt}\left[i_{G_m}(t) + i_{\text{inj}}(t)\right]. \tag{10.30}$$

We utilize a complex exponential representation for the injection current $i_{\text{inj}}(t) = I_{\text{inj}}e^{j\omega_{\text{inj}}t}$, and we assume the following ansatz for the oscillation voltage $v_{\text{osc}}(t) = V_{\text{osc}}(t)e^{j\cdot\theta_{\text{osc}}(t)}$, which allows for amplitude modulation in the envelope $V_{\text{osc}}(t)$. Denote $\theta(t) \coloneqq \theta_{\text{osc}}(t) - \omega_{\text{inj}}t$ as the phase difference between the oscillator and the injection. Assuming the conditions discussed in the previous subsection are met, and accounting for the filtering action of the resonator, we approximate the oscillator current as $i_{\text{osc}}(t) \approx I_{\text{osc}}(t)e^{j\cdot\theta_{\text{osc}}(t)}$, which has the same phase as the oscillation voltage.

Substituting these expressions into Eq. (10.30) and separating out the real and imaginary parts (i.e., sine and cosine components), we get the following two coupled differential equations:

$$\begin{aligned}\frac{Q}{\omega_0\omega_{\text{inj}}}\frac{d^2V_{\text{osc}}}{dt^2} + \frac{1}{\omega_{\text{inj}}}\frac{dV_{\text{osc}}}{dt} + \left[\chi(\omega_{\text{inj}}) - 2\frac{Q}{\omega_0}\frac{d\theta}{dt} - \frac{Q}{\omega_0\omega_{\text{inj}}}\left(\frac{d\theta}{dt}\right)^2\right]V_{\text{osc}} \\ = \left(\frac{1}{\omega_{\text{inj}}}\frac{dI_{\text{osc}}}{dt} + I_{\text{inj}}\sin\theta\right)R_P\end{aligned} \tag{10.31}$$

$$\frac{Q}{\omega_0\omega_{\text{inj}}}V_{\text{osc}}\frac{d^2\theta}{dt^2} + \left(2\frac{Q}{\omega_0}\frac{dV_{\text{osc}}}{dt} + V_{\text{osc}} - I_{\text{osc}}R_P\right)\left(1 + \frac{1}{\omega_{\text{inj}}}\frac{d\theta}{dt}\right) = I_{\text{inj}}R_P\cos\theta. \tag{10.32}$$

In the subsequent sections, we will use these general equations to subsume various existing models.

Reduction to the Locked Model of Section 10.4

In an injection-locked oscillator in steady state, all quantities V_{osc}, I_{osc}, and θ are constant in time. Therefore, taking $d/dt \to 0$, Eqs. (10.31) and (10.32) reduce to

$$\chi(\omega_{\text{inj}})V_{\text{osc}} = I_{\text{inj}}R_P\sin\theta \tag{10.33}$$

and

$$V_{\text{osc}} = \left(I_{\text{osc}} + I_{\text{inj}} \cos\theta\right) R_P \tag{10.34}$$

respectively. Recalling from Figure 10.3 that $I_{\text{inj}\parallel} = I_{\text{inj}} \cos\theta$ and $I_{\text{inj}\perp} = I_{\text{inj}} \sin\theta$, we can simplify these to

$$V_{\text{osc}} = \left(I_{\text{osc}} + I_{\text{inj}\parallel}\right) R_P = I_{\text{inj}\perp} \frac{R_P}{\chi(\omega_{\text{inj}})}, \tag{10.35}$$

which matches Eq. (10.11), the entire analytical basis for our physically-based model of an injection-locked LC oscillator.

Reduction to "Generalized Adler's Equation" [21]

Here, we show how Eqs. (10.31) and (10.32) can be reduced to Mirzaei's Generalized Adler's equation [21]. First, we derive a differential equation that captures the dynamics of the oscillation amplitude. Assuming the phase is sufficiently slowly varying such that $|\theta'(t)| \ll \omega_0$ and $|\theta''(t)| \ll {\omega_0}^2/Q$, it is easily seen that Eq. (10.32) simplifies to

$$2R_P C \frac{dV_{\text{osc}}}{dt} + V_{\text{osc}} = \left(I_{\text{osc}} + I_{\text{inj}} \cos\theta\right) R_P \tag{10.36}$$

which matches equation (7) in [21].[6]

Now, we want to obtain a first-order differential equation for the dynamics of the oscillation phase. Further assume that 1) the envelope of the oscillation voltage V_{osc} is roughly constant in time and so Eq. (10.36) becomes $V_{\text{osc}} \approx \left(I_{\text{osc}} + I_{\text{inj}} \cos\theta\right) R_P$, 2) the transconductor is a hard-limited commutator which results in a constant oscillator current $I_{\text{osc}} = 4I/\pi$, and 3) the injection frequency is close to resonance $|\Delta\omega| \ll \omega_0$ and so $\chi(\omega_{\text{inj}}) \approx -2Q\,(\Delta\omega/\omega_0)$. Then Eq. (10.31) can be simplified as

$$\frac{d\theta}{dt} = \omega_0 - \omega_{\text{inj}} - \frac{\omega_0}{2Q} \frac{I_{\text{inj}} \sin\theta}{\dfrac{4I}{\pi} + I_{\text{inj}} \cos\theta}, \tag{10.37}$$

which matches equation (8) from [21], setting aside notational differences for the phase (replace $\theta_{\text{inj}} - \theta$ in [21] with $-\theta$).

Further assuming $I_{\text{inj}} \ll I_{\text{osc}}$ in Eq. (10.37) yields Adler's original equation [47]:

$$\frac{d\theta}{dt} = \omega_0 - \omega_{\text{inj}} - \frac{\omega_0}{2Q} \frac{I_{\text{inj}}}{I_{\text{osc}}} \sin\theta. \tag{10.38}$$

[6] Equation (7) in [21] is missing the factor of 2 in front of the dV_{osc}/dt term. (It is well-known that $2R_P C = 2Q/\omega_0$ is the relaxation time constant of a parallel RLC resonator.)

10.6 The Lock Range of the Ring Oscillator

The analysis carried out for LC oscillators under sinusoidal injection can also be adapted for ring oscillators, provided an appropriate behavioral model is utilized. Again, the physical insight that governs this analysis is that the injection must supply enough "out-of-phase" current, and therefore, induce a large enough phase shift, to cause the circuit to successfully operate away from its free-running oscillation frequency. By finding the maximum phase shift which can be provided for a given injection strength, we can compute the maximum deviation away from free-running at which the circuit can operate, which yields the lock range.

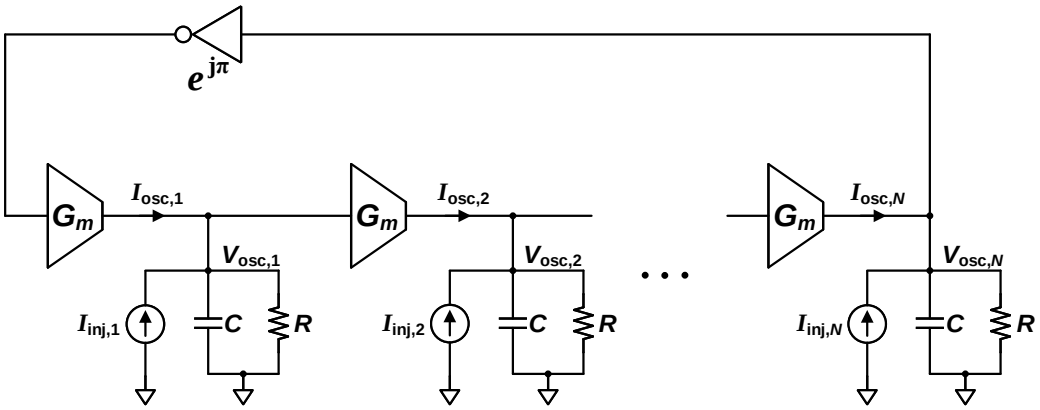

Figure 10.8: Conceptual circuit model of a ring oscillator under injection. Each G_m-cell is a nonlinear system which produces a sinusoidal output current whose phase is the same as the input voltage and whose amplitude I_{osc} is independent of the input amplitude. An ideal inverter in the loop provides a π phase shift along the return path. All depicted signals are assumed to be sinusoidal steady-state phasors at ω_{inj}, the injection frequency.

Behavioral Model

We start with the sinusoidal steady-state behavioral model of a ring oscillator shown in Figure 10.8 [10], [63], which consists of N first-order delay stages and an ideal inverter connected sequentially in a closed loop, where $N > 2$. Note that the number of stages could be either odd or even. Successive stages are interconnected via a nonlinear transconductor (the G_m-cell), which supplies energy to the oscillator by converting the previous stage's output voltage into a current. In general, the transconductor current will contain higher-order harmonics due to its nonlinear behavior. But, within the context of our behavioral model, we assume that these higher-order harmonics are suppressed by the RC-load's low-pass nature, leaving us with a clean fundamental harmonic in steady state with a (fixed) amplitude I_{osc}

which is set through biasing.[7] While this "quasi-linear" assumption makes the analysis tractable by facilitating the use of phasors, it is also this model's greatest limitation [62].

First, we compute the free-running oscillation frequency. The impedance of each stage's load is

$$Z(j\omega) = \frac{R}{1 + j\omega RC}. \tag{10.39}$$

For oscillation to sustain, the phase shift around the loop must be 2π. Since all the stages are identical, each stage must therefore contribute a phase delay of π/N. So, the free-running oscillation frequency satisfies

$$\angle Z(j\omega_0) = -\frac{\pi}{N} \tag{10.40}$$

which implies

$$\boxed{\omega_0 = \frac{1}{RC}\tan\left(\frac{\pi}{N}\right).} \tag{10.41}$$

At this point, we can already gauge the implications of relying on a quasi-linear, sinusoidal steady-state assumption by comparing Eq. (10.41) against simulation. Figure 10.9 shows the simulated free-running oscillation frequency for single-ended inverter-chain ring oscillators designed in a 65-nm bulk CMOS process as the number of (identical) stages varied from $N = 3$ to $N = 17$. As we can see, the oscillation frequency scales as $f_0 \propto 1/N$ instead of $f_0 \propto \tan(\pi/N)$, confirming the conventional wisdom that in the large-signal regime, it is the time delay per stage—as opposed to the phase delay per stage—that is invariant.

Next, the free-running oscillation amplitude is given by

$$V_{\text{osc}} = I_{\text{osc}}\,|Z(j\omega_0)| = I_{\text{osc}}R\cos\left(\frac{\pi}{N}\right). \tag{10.42}$$

In practice, matching an actual ring oscillator with the depicted behavioral model may not be so obvious. Most notably, how does one compute I_{osc}? The most accurate way is to simulate the *fundamental component* of the current flowing onto the capacitor of a particular stage, call it I_C, and note that

$$\frac{I_C}{\omega_0 C} = V_{\text{osc}} = I_{\text{osc}}R\cos\left(\frac{\pi}{N}\right). \tag{10.43}$$

Thus,

$$I_{\text{osc}} = \frac{I_C}{\sin\left(\frac{\pi}{N}\right)}. \tag{10.44}$$

Finally, we define the injection strength $r \coloneqq I_{\text{inj}}/I_{\text{osc}}$.

[7] This assumption loses its validity as the number of stages increases.

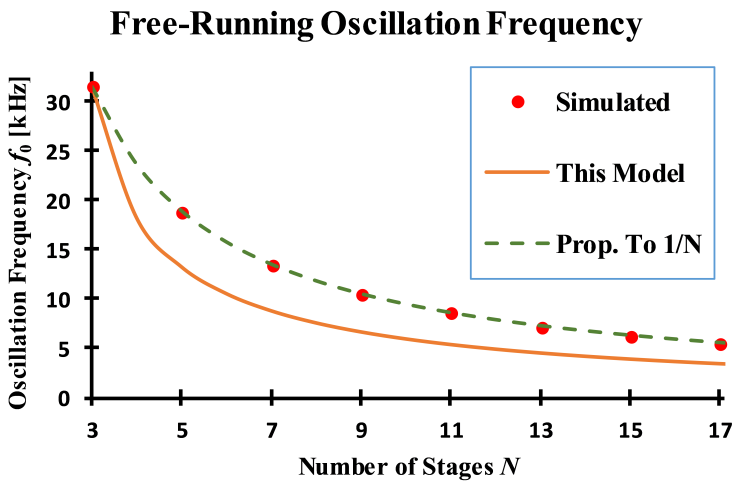

Figure 10.9: Free-running oscillation frequency f_0 of the simulated ring oscillator vs. number of stages N.

Injection into a Single Tap

Here, we assume the traditional setting of injection at a single tap—say tap 1 without loss of generality. To compute the lock range, we will assume that this injection current $\vec{I}_{\text{inj},1}$ exhibits a phase difference of θ with respect to the oscillator current it adds to ($\vec{I}_{\text{osc},1}$). Note that the exact definition of θ is irrelevant—all that is required is that the injection current exhibit some phase shift with respect to any one of the other signals in the circuit; we then treat that phase shift as the decision variable to be optimized over. Specifically,

$$\vec{I}_{\text{inj},n} = I_{\text{inj}} e^{j\theta} \cdot \delta_{n1} \tag{10.45}$$

where δ_{ij} is the Kronecker delta.

Again, for oscillation to occur, the total phase delay along all of the stages must be π. Thus, it can be shown that

$$N \angle Z(j\omega_{\text{inj}}) + \angle(1 + re^{j\theta}) = -\pi. \tag{10.46}$$

Solving for the injection frequency, we get

$$\omega_{\text{inj}} = \frac{1}{RC} \tan \frac{\left[\pi + \angle(1 + re^{j\theta})\right] \bmod 2\pi}{N}. \tag{10.47}$$

We leave it as an exercise to the reader to show that for $r > 1$, the range of $\angle(1 + re^{j\theta})$ is the entire interval $[0, 2\pi)$, and so the range of ω_{inj} becomes $[0, \infty)$.

From a physical standpoint, at infinitely high frequencies, each stage contributes a delay of $-\pi/2$ since the capacitor shorts out the resistor. On the other hand, at DC, the capacitor opens and so none of the stages contribute any delay. Of course, this seemingly infinite lock range, although mathematically correct, is not physically meaningful. Much like the results of the analysis for the LC oscillator (see Section 10.4), in scenarios where a solution mathematically exists at DC or as $\omega_{\text{inj}} \to \infty$, the oscillator will lose lock at some point because the solution is no longer energetically favorable to being pulled.

Assume $I_{\text{inj}} \leq I_{\text{osc}}$. The upper and lower optimizers for θ can be computed to be $\theta_{\text{max/min}} = \pm\cos^{-1}(-r)$ [compare with Eq. (10.8)], which leads to the following optimum values for the injection frequency:

$$\boxed{\omega_{\text{max/min}} = \begin{cases} \dfrac{1}{RC}\tan\left(\dfrac{\pi \pm \sin^{-1} r}{N}\right), & r \leq 1 \\ +\infty/0 \quad , & r > 1. \end{cases}} \tag{10.48}$$

Because the value of R may not be apparent for a particular topology, it is easier to work with the *fractional* lock range $\omega_L^{\pm}/\omega_0$, which is defined as

$$\frac{\omega_L^{\pm}}{\omega_0} := \frac{\omega_{\text{max/min}} - \omega_0}{\omega_0}. \tag{10.49}$$

Let us briefly elucidate some limiting characteristics of the fractional lock range. As the number of stages grows, the fractional lock range approaches

$$\boxed{\lim_{N\to\infty} \frac{\omega_L^{\pm}}{\omega_0} = \pm\frac{1}{\pi}\sin^{-1}\left(\frac{I_{\text{inj}}}{I_{\text{osc}}}\right),} \tag{10.50}$$

whereas for small injections ($r \ll 1$), the small-angle approximation gives

$$\boxed{\left.\frac{\omega_L^{\pm}}{\omega_0}\right|_{I_{\text{inj}} \ll I_{\text{osc}}} \approx \pm\frac{2}{N\sin\left(\dfrac{2\pi}{N}\right)}\frac{I_{\text{inj}}}{I_{\text{osc}}},} \tag{10.51}$$

which matches equation (9) in [63], equation (2) in [62], and equation (29) in [2].

Multiple Distributed-Phase Injections into All N Taps

Here, we analyze the scheme proposed by Mirzaei in [10] to increase the lock range of ring oscillators by injecting current into every single stage, with injections between successive stages separated by a phase of π/N. Although the fact that

this scheme significantly increases the lock range was mentioned and demonstrated experimentally in [10], a simple and intuitive analysis which yields qualitative insight was not provided. Note that injecting N times as much current into a single stage has diminishing returns since it will eventually saturate that stage. Mathematically, the injection phasors are

$$\overrightarrow{I}_{\text{inj},n} = I_{\text{inj}} e^{-j\theta} e^{j(n-1)\pi/N}, \tag{10.52}$$

where the phase is referred to the oscillator current of the first stage. Now, the total phase shift along all the delay stages can be shown to be

$$N\angle Z(j\omega_{\text{inj}}) + N\angle(1 + re^{j\theta}) = -\pi. \tag{10.53}$$

Solving for the injection frequency,

$$\omega_{\text{inj}} = \frac{1}{RC} \tan\left[\angle(1 + re^{j\theta}) + \frac{\pi}{N}\right]. \tag{10.54}$$

Again, we leave it as an exercise to the reader to explore the circumstances under which an infinite lock range would mathematically prevail. Note that due to the symmetric injection topology, each stage must contribute a net phase delay of π/N. Assuming the lock range does not extend to positive infinity or DC, we can again optimize the injection frequency, which again yields $\theta_{\text{max/min}} = \pm\cos^{-1}(-r)$. This gives an upper lock range of

$$\boxed{\omega_{\text{max}} = \begin{cases} \dfrac{1}{RC}\tan\left(\dfrac{\pi}{N} + \sin^{-1} r\right), & r < \cos\left(\dfrac{\pi}{N}\right) \\ +\infty \quad , & \text{otherwise} \end{cases}} \tag{10.55}$$

and a lower lock range of

$$\boxed{\omega_{\text{min}} = \begin{cases} \dfrac{1}{RC}\tan\left(\dfrac{\pi}{N} - \sin^{-1} r\right), & r < \sin\left(\dfrac{\pi}{N}\right) \\ 0 \quad , & \text{otherwise.} \end{cases}} \tag{10.56}$$

For small injections, the small-angle approximation gives a fractional lock range of

$$\boxed{\left.\frac{\omega_L^{\pm}}{\omega_0}\right|_{I_{\text{inj}} \ll I_{\text{osc}}} \approx \pm \frac{2}{\sin\left(\dfrac{2\pi}{N}\right)} \frac{I_{\text{inj}}}{I_{\text{osc}}},} \tag{10.57}$$

which shows that for $I_{\text{inj}} \ll I_{\text{osc}}$, this scheme increases the lock range by a factor of N. Furthermore, it is easy to show that if only a fraction of the N injections were

turned on, say M out of N (with $M \leq N$), and the same phase progression dictated by Eq. (10.52) is maintained, then the lock range would increase by a factor of M instead. By symmetry, this result is independent of which M stages we choose.

On the other hand, for long rings, while $\omega_{\text{min}} = 0$ becomes achievable for sufficiently large N, the upper fractional lock range scales linearly with the number of stages as

$$\boxed{\left.\frac{\omega_L^+}{\omega_0}\right|_{N\to\infty} \longrightarrow \frac{N}{\pi\sqrt{\frac{{I_{\text{osc}}}^2}{{I_{\text{inj}}}^2} - 1}}.} \tag{10.58}$$

Simulation Results

To assess the validity and utility of these results, we ran transient simulations via SpectreRF on single-ended inverter-based ring oscillators with N identical stages designed in a 65-nm bulk CMOS process. Shown in Figure 10.10, we compared the simulated lock ranges against Eqs. (10.48), (10.55), and (10.56). Each tap was loaded with a 1 nF capacitor so as to dominate over the device capacitances within the inverters. This allowed us to compute I_{osc} from the current of this load cap using Eq. (10.44). Interestingly, the oscillator current was found to be roughly 0.12 mA, independent of the number of stages. As we can see from Figure 10.9, the free-running oscillation frequency ranged from $f_0 = 32$ kHz for $N = 3$ to $f_0 = 5.5$ kHz for $N = 17$.

The accuracy of our model degrades most prominently as the injection strength increases (for a fixed N), and as the number of stages decreases (for a fixed r). The reason for this is that Eqs. (10.48), (10.55), and (10.56) diverge to $+\infty/0$ under certain scenarios. Although mathematically valid within the confines of our behavioral model, such lock ranges are not physically realistic (in the same way that Eq. (10.19) is meaningless for $I_{\text{inj}} > I_{\text{osc}}$). Our model's deviation from the simulated results also increases slightly for longer rings, since higher-order harmonics in the waveforms become more apparent.

Our results—while lacking the veracity of the transcendental, exponential-decay-based results of equations (6) and (7) in [10]—are succinct and straightforward, making them amenable to lending design insight, at least to the first order. Furthermore, our expressions for the fractional lock range are independent of the load resistance R, a parameter that appears in the abstract behavioral model which is difficult to estimate in reality. Furthermore, it should be noted that a plethora of other ring oscillator injection locking models and lock range analyses can be found in the

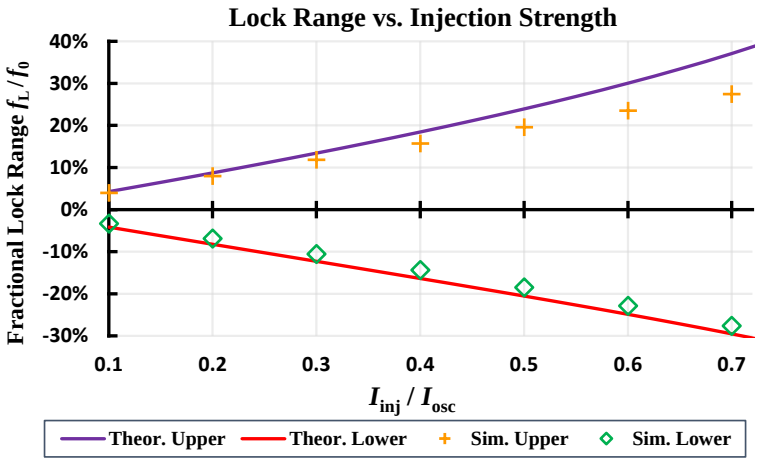

(a) Single Injection, Fixed Number of Stages $N = 5$

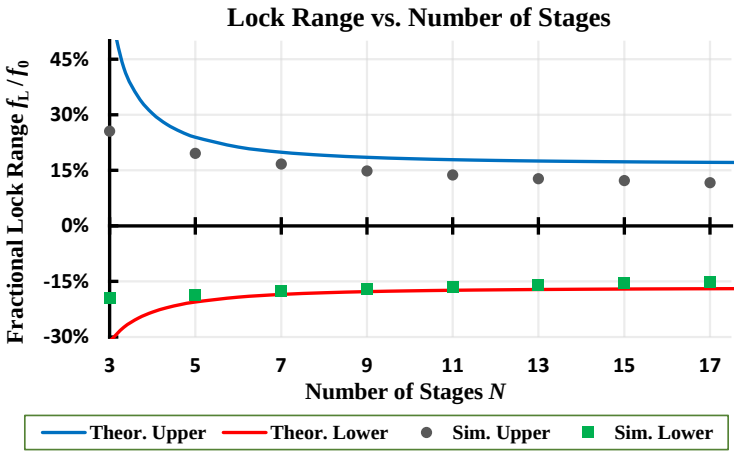

(b) Single Injection, Fixed Injection Strength $r = 0.5$

literature [2], [62]–[65], most of which are considerably more complicated than the presented analysis and some of which are more accurate in one scenario or another. However, none of them depict simulation results over a wide range of the number of stages and of the injection strength. As such, it is difficult to see the general trends that their results and expressions have, nor is it practical to evaluate under what scenarios their models break down. Our analysis leads to good predictions in two asymptotic regimes: the small-injection ($I_{inj} \ll I_{osc}$) regime, given by Eqs. (10.51) and (10.57); and the long ring case ($N \gg 1$), given by Eqs. (10.50) and (10.58).

10.7 The Small-Injection Lock Range: A Corollary

Here, we illuminate a mathematical connection between the small-injection lock ranges of LC oscillators Eq. (10.20) and ring oscillators Eq. (10.51). Let us assume that an arbitrary feedback-based oscillator has a small-signal (i.e., linearized) open-

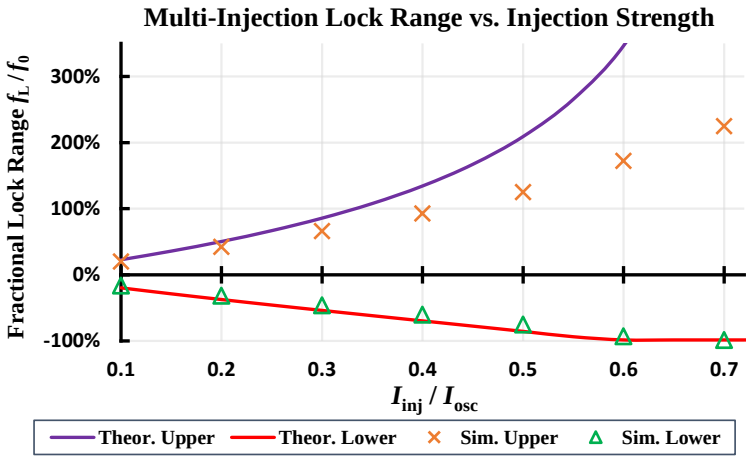

(c) Multiple Distributed-Phase Injections, Fixed Number of Stages $N = 5$

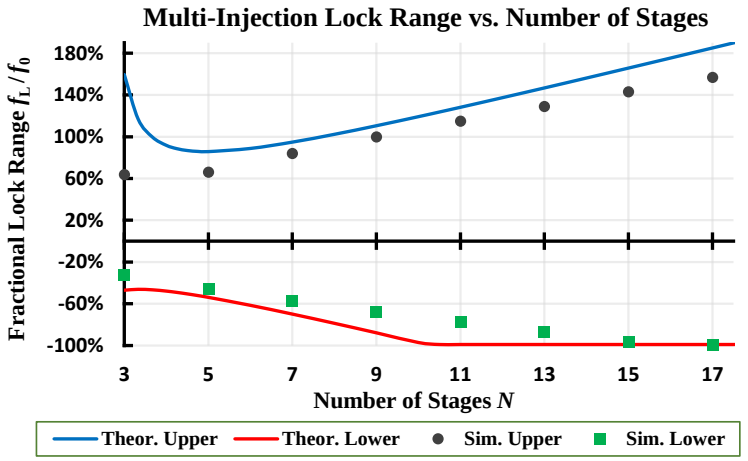

(d) Multiple Distributed-Phase Injections, Fixed Injection Strength $r = 0.3$

Figure 10.10: Theoretical versus simulated fractional lock ranges f_L / f_0 for various scenarios. A fractional lock range of -100% indicates that the oscillator locks for arbitrarily low frequencies ("down to DC").

loop transfer function $H(s)$, as shown in Figure 10.11. It holds true that $\angle H(j\omega_0) = 0$, where ω_0 is the free-running oscillation frequency. In order for the oscillator to lock to ω_{inj}, the phase that the transfer function bears at the injection frequency, $\angle H(j\omega_{\text{inj}})$, must be offset by the phase shift introduced by the injection current $\phi = \angle(\overrightarrow{I}_{\text{inj}} + \overrightarrow{I}_{\text{osc}})$ [2], [62].

Using a first-order Taylor series approximation,

$$\angle H(j\omega_{\text{inj}}) \approx \Delta\omega \cdot \left.\frac{\partial \angle H(j\omega)}{\partial \omega}\right|_{\omega=\omega_0}. \tag{10.59}$$

Next, from injection geometry, in the small-injection limit, the maximum phase shift

that the injection can produce occurs when the injection and oscillator currents are mutually orthogonal (see the phasor triangle in Figure 10.11). Using the small-angle approximation, we get[8]

$$\tan\phi_{\max} \approx \phi_{\max} = \frac{I_{\text{inj}}}{I_{\text{osc}}}. \tag{10.60}$$

Since the maximum allowable frequency deviation occurs when $\left|\angle H(j\omega_{\text{inj}})\right| = \phi_{\max}$, the small-injection ($I_{\text{inj}} \ll I_{\text{osc}}$), one-sided lock range is given by

$$\boxed{\omega_L = \frac{1}{\left|\dfrac{\partial \angle H(j\omega)}{\partial\omega}\right|_{\omega=\omega_0}} \cdot \frac{I_{\text{inj}}}{I_{\text{osc}}}.} \tag{10.61}$$

This expression is applicable to any feedback-based oscillator subject to a sinusoidal current injection which is added to an internal oscillator current that is produced by the oscillator's core energy-restoring nonlinearity.

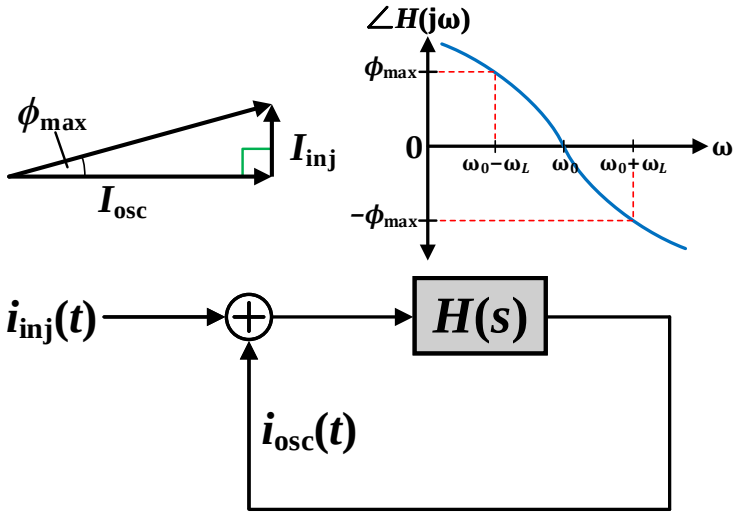

Figure 10.11: Simplified and linearized mathematical model of a feedback-based oscillator under injection.

Example: LC Oscillator of Figure 10.1

It is easy to show that

$$H(s) = \frac{G_m}{\dfrac{1}{R_P} + sC + \dfrac{1}{sL}} = \frac{G_m R_P}{\dfrac{Q}{\omega_0}s + 1 + \dfrac{Q\omega_0}{s}} \tag{10.62}$$

[8]This can also be justified rigorously by linearizing Eq. (10.9) about $I_{\text{inj}} = 0$.

$$\Longrightarrow \left.\frac{\partial \angle H(j\omega)}{\partial \omega}\right|_{\omega=\omega_0} = -\frac{2Q}{\omega_0}, \tag{10.63}$$

which is consistent with Eq. (10.20).

Example: N-Stage Ring Oscillator of Figure 10.8

For this oscillator, the open-loop transfer function is

$$H(s) = -\left(\frac{G_m R}{1+sRC}\right)^N = \frac{(G_m R)^N}{\left[1+\frac{s}{\omega_0}\tan\left(\frac{\pi}{N}\right)\right]^N}, \tag{10.64}$$

and so

$$\left.\frac{\partial \angle H(j\omega)}{\partial \omega}\right|_{\omega=\omega_0} = -\frac{N}{2\omega_0}\sin\left(\frac{2\pi}{N}\right), \tag{10.65}$$

in accordance with Eq. (10.51). It is noteworthy that [2] shows similar derivations for these two specific examples.

10.8 Conclusion

This chapter presented a sinusoidal steady-state analysis of LC and ring oscillators under injection. Exact equations that describe an LC oscillator's amplitude and phase which make no assumptions about the injection strength or frequency were derived and verified by simulation. The extension of the analysis to other types of resonator topologies, such as those with low-Q inductors, was shown. The conditions under which the transconductor "preserves" a time-varying phase in the oscillation voltage—an often overlooked issue in the analysis of oscillators—was illuminated. Next, the response of the ring oscillator to both a single sinusoidal current injection and multiple distributed-phase injections was examined. Simulation results revealed that our analysis possesses good predictive power for small injections and long rings in the form of clean, crisp, closed-form expressions for the fractional lock range that yield significantly more physical intuition than many existing models. Finally, a general corollary was proven that relates the rate of change of the phase of an oscillator's open-loop gain near resonance to its small-injection lock range, underlining the mathematical connection between our apparently disparate analyses of LC and ring oscillators.

At its core, our analysis starts by assuming the circuit is operating at sinusoidal steady state (i.e., the oscillator is already locked), and then solving for the range of frequencies for which a solution to the circuit exists. That a solution does not exist for

all frequencies (as would be the case for a linear circuit) is due to the transconductor elements within the behavioral model, which capture the essential nonlinear aspect of the oscillator's operation. Although powerful, this technique suffers from the main drawback that the existence of a sinusoidal steady-state solution does not guarantee that the solution is energetically stable, and hence does not imply that the oscillator will actually follow that solution. Nevertheless, the physical insight gleaned from applying this methodology to both LC and ring oscillators yields valuable design intuition while also contributing to a fundamental understanding of the injection locking phenomenon.

Chapter 11

CONCLUSION

A general, time-synchronous theory of injection locking and pulling in electrical oscillators was presented, applicable to oscillators of any topology and periodic disturbances of arbitrary shape. The analysis was engendered from a thought experiment—the entrainment of an LC oscillator to an impulse train. This motivated us to develop the model using the concept of the Impulse Sensitivity Function (ISF), which represents the periodically time-varying impulse response of the oscillator's phase to external perturbations. A single first-order differential equation is shown to capture the phase behavior of a periodically disturbed oscillator and accurately predict a wide array of properties. The steady-state solution gave rise to the lock characteristic, defined as the phase difference between the locked oscillator and the injection signal, which allowed us to calculate the lock range. A transient analysis of the equation elucidated the dynamics behind the pull-in process, mode stability, the spectrum of an injection-pulled oscillator, as well as phase noise in both free-running and injection-locked oscillators. The analysis was also extended to cover injections at superharmonic and subharmonic frequencies, along with their general combination whereby the injection and oscillation frequencies are related through any rational number. The developed theory was supported by simulation and measurement results on a diverse collection of LC, ring, and relaxation oscillators.

For the commonly used LC oscillator, an observation concerning the inverse dependence of the ISF on the oscillation amplitude led to a nonlinear generalization of the framework, enabling it to handle large injections as well. The resultant model elucidates hitherto unknown properties of injection-locked LC oscillators, such as asymmetry in the lock range and the benefits of using only an NMOS cross-coupled pair as opposed to complementary pairs. In the specific case of an ideal LC oscillator, the amplitude-dependent pulling equation reduced down to other known models such as Adler's equation and Mirzaei's Generalized Adler's equation.

The framework also shed design insight into how the lock range could be optimized. Specifically, we used the Cauchy-Schwarz inequality to show that the optimal injection waveform for a fixed injection power was one whose shape matched the ISF. This methodology was generalized to frequency dividers by only considering the

relevant spectral components of the ISF. We also investigated how the oscillator's design could be modified to enhance its lock range for certain applications. This led to the realization of a low-power dual-moduli prescaler for frequency synthesis applications which featured a wide range of operating frequencies and a small chip area, making it competitive with the state-of-the-art.

11.1 Future Directions

There are a number of unsolved questions which are of potential interest in light of the results presented in this thesis. On the theoretical front, a challenging but fruitful endeavor would be to investigate the nonlinearity of the lock characteristic with respect to large injections for non-LC oscillators. This may require a number of state-space limit cycle modeling techniques as well as general observations to be made about the behavior of a specific class of oscillators (i.e., ring or relaxation). Another theoretical avenue would be to look into the error associated with the averaging technique that resulted in the autonomous differential equation which formed the basis of our model. Of particular importance would be to figure out under what conditions this error becomes practically significant. Finally, being able to model the stability of the amplitude dynamics in LC oscillators would be very worthwhile, as this would allow us to determine which oscillation amplitudes are too small to sustain lock. In doing so, we would no longer need to, for large injection amplitudes, restrict the range of phases over which the lock characteristic is considered, as this was done in a somewhat ad hoc manner in Chapter 5.

Future research directions also exist on the applied side. For example, optimizing the lock range under different or additional constraints, besides the maximum root-mean-square injection current, would be useful to the design community. Applications where the lock range should be minimized or shifted as opposed to widened could also be investigated. Additionally, a much more systematic method of making the inverters in a ring oscillator asymmetric to enable division by even ratios could be developed. Also, consider the technique of applying distributed-phase injections into multiple stages of a single-ended ring oscillator to be used as a frequency divider. Notice that if the division ratio N and the number of stages K are equal, then according to Eq. (9.1), the injection phase for all of the stages becomes the same: $\phi_{\text{inj}}(k) = kN(\pi - \pi/N) = k(N-1)\pi = 0$, where we used the fact that the number of stages N is odd. This would obviate the need for multi-phase injections and for switching the injection sites for different division ratios, which significantly eases implementation and potentially leads to enhanced performance.

Chapter 12

OTHER WORKS

12.1 Upper and Lower Bounds on a System's Bandwidth Based on its Zero-Value Time Constants

[1] B. Hong and A. Hajimiri, "Upper and lower bounds on a system's bandwidth based on its zero-value time constants," *Electronics Letters*, vol. 52, no. 16, pp. 1383–1385, Aug. 2016. DOI: 10.1049/el.2016.1724,

Introduction

The estimate of a low-pass circuit's 3-dB bandwidth via the method of zero-value time constants is well-known [136]–[138]. This procedure entails computing the time constant of each reactive element in a circuit based on the resistance it sees when all other reactive elements are zero-valued (capacitors opened, inductors shorted). The inverse of the sum of these zero-value time constants, or ZVTs, is then taken to be an estimate of the circuit's 3-dB high-cutoff frequency. For a linear time-invariant n^{th}-order system with m zeros and n poles ($m < n$) whose transfer function can be written as[1]

$$H(s) = \frac{a_0 + a_1 s + a_2 s^2 + \cdots + a_m s^m}{1 + b_1 s + b_2 s^2 + \cdots + b_n s^n}, \tag{12.1}$$

it can be shown [136]–[138] that the sum of the ZVTs is equal to b_1. For now, we will consider systems with no zeros ($a_1 = a_2 = \cdots = a_m = 0$), which serve as a good model for circuits where the zeros occur at very high frequencies beyond the passband and are hence unimportant. We thus rewrite the transfer function as

$$H(s) = \frac{H_0}{1 + b_1 s + b_2 s^2 + \cdots + b_n s^n}, \tag{12.2}$$

where $|H_0| = |a_0|$ is the DC gain of the system. We then argue that as the frequency increases from DC, the first term in the denominator that becomes significant is $b_1 s$, and so near the -3-dB point the system can be approximated as

$$H(s) \approx \frac{H_0}{1 + b_1 s} \tag{12.3}$$

from which the ZVT bandwidth estimate of $\omega_c \approx 1/b_1$ follows [136], [138].

[1] If $b_0 = 0$ as in the case of the impedance of a capacitor, one can consider the reciprocal of the transfer function instead.

In this short treatise, we prove that for a system whose poles are all real, this ZVT estimate of the bandwidth is always a lower bound on the system's actual bandwidth ω_c. We also prove a nontrivial upper bound on ω_c that depends only on the sum of the ZVTs b_1 and the system's order n.

Statement of the Theorem

Consider a linear time-invariant n^{th}-order low-pass system with no zeros and no complex poles whose transfer function is

$$H(s) = \frac{H_0}{1 + b_1 s + b_2 s^2 + \cdots + b_n s^n}. \tag{12.4}$$

The system's 3-dB bandwidth, or high-cutoff frequency, is defined as the (lowest) angular frequency ω_c that satisfies

$$|H(j\omega_c)| \equiv \frac{|H_0|}{\sqrt{2}}. \tag{12.5}$$

If $n = 1$, then trivially $\omega_c = 1/b_1$. For $n > 1$, the following lower and upper bounds on ω_c hold:

$$\boxed{\frac{1}{b_1} < \omega_c \leq \frac{n}{b_1}\sqrt{2^{1/n} - 1}.} \tag{12.6}$$

Furthermore, these inequalities are tight, or achievable, in the sense that there exists systems whose bandwidths are arbitrarily close to the lower bound or are given by the upper bound. ■

A couple comments are in order:

1. The lower bound also holds for systems with *complex poles* whose quality factors are no larger than $Q \leq \sqrt{2}$. (The upper bound does not.) We will prove this separately in a later section.

2. The lower bound is physically intuitive. Loosely speaking, the ZVT estimate $1/b_1$ considers the worst case scenario where the system's reactive elements "energize" one after the other, as the time constants are added together. In general, however, the system's energy-storage elements may energize in parallel, leading to a "faster" response than that dictated by b_1.

Proof of the Lower Bound

Assume $n > 1$. Since all the poles are real, by the fundamental theorem of algebra, the denominator of Eq. (12.4) can be factored as

$$H(s) = H_0 \prod_{i=1}^{n} \frac{1}{1 + \tau_i s} \tag{12.7}$$

where $\tau_i \in \mathbb{R}_{++}$ for $i = 1, \ldots, n$ are the time constants associated with the system's n poles[2]. To simplify the notation, we define the following variables for $i = 1, \ldots, n$:

$$x_i \coloneqq \omega\tau_i \tag{12.8}$$

where the frequency ω will be specified based on context. Lastly, based on the easily seen fact that $b_1 = \sum_{i=1}^{n} \tau_i$, we can also write $\omega b_1 = \sum_{i=1}^{n} x_i$.

To make the proof more analytically tractable, we reformulate the problem statement in an equivalent way. By definition of the bandwidth, the lower bound $\omega_c > 1/b_1$ is equivalent to:

$$|H(j\omega)| > \frac{|H_0|}{\sqrt{2}} \tag{12.9}$$

for all $\omega \leq 1/b_1$. That is, the system's magnitude is always above -3-dB (relative to the DC gain) for frequencies up to $1/b_1$, the ZVT estimate of the high-cutoff frequency.[3]

We can then express the problem statement as follows: for $x_i > 0 \; \forall i$, show that

$$\prod_{i=1}^{n} \left(1 + {x_i}^2\right) < 2 \tag{12.10}$$

$$\text{subject to } \sum_{i=1}^{n} x_i \leq 1. \tag{12.11}$$

Now we proceed with the proof proper. First, we establish the following claim: given constants a and b such that $0 < a, b < 1$, it holds true that

$$\begin{aligned}(1 + a^2)(1 + b^2) &= 1 + a^2 + b^2 + (ab)^2 \\ &= (1 - ab)^2 + (a + b)^2 \\ &< 1 + (a + b)^2\end{aligned} \tag{12.12}$$

where equality is approached by taking $a \to 0$ or $b \to 0$ (or both). We need to repeat this argument for a total of $n - 1$ times, where the k^{th} step features $a = \sum_{i=1}^{k} x_i$ and $b = x_{k+1}$. For each step, it is apparent that $0 < a, b < 1$, since $x_i > 0 \; \forall i$ combined

[2]Note that the τ_i's are only equal to the system's ZVTs if the poles are *decoupled* [138] from one another. In general, each τ_i could depend on multiple energy storage elements. Indeed, there may even be fewer poles than there are reactive elements in the circuit! It is only true that the ZVTs and the τ_i's have the same *total sum*, namely b_1.

[3]We can invoke the fact that $|H(j\omega)|$ decreases monotonically with frequency ω to simplify the reformulation of the lower bound to $|H(j/b_1)| > |H_0|/\sqrt{2}$, but we choose not to do so here because monotonicity no longer holds in the presence of complex poles, which we deal with in a later section.

with the constraint Eq. (12.11) implies that $\sum_{i \in S} x_i < 1 \; \forall S \subset \{1, \ldots, n\}$. Thus, we arrive at

$$\begin{aligned} \prod_{i=1}^{n} \left(1 + {x_i}^2\right) &< \left[1 + (x_1 + x_2)^2\right] \prod_{i=3}^{n} \left(1 + {x_i}^2\right) \\ &< \quad \cdots \\ &< 1 + \left(\sum_{i=1}^{n} x_i\right)^2 \\ &\leq 2 \end{aligned} \tag{12.13}$$

where the final inequality follows from the constraint $\sum_{i=1}^{n} x_i \leq 1$. By letting one of the x_i's approach unity (which takes the remaining x_i's to zero), we can also see that this inequality is tight. This establishes the lower bound. □

Notice what is happening here *physically*. We are "merging" the system's poles together one at a time (by adding their time constants together), and with each step, the bandwidth of the system worsens until we end up with a 1^{st}-order system whose bandwidth is exactly equal to the ZVT estimate $1/b_1$. The proof also shows how this lower bound is achievable: as one of the system's poles becomes increasingly dominant (where to dominate means to have a larger time constant), the system's bandwidth will approach the lower bound dictated by Eq. (12.6).

Proof of the Upper Bound

The proof of the upper bound is somewhat similar in spirit, but we take a slightly different approach. Consider the following system:

$$H_{\max}(s) \coloneqq \frac{H_0}{(1 + \bar{\tau} s)^n}, \tag{12.14}$$

where

$$\bar{\tau} \coloneqq \frac{1}{n} \sum_{i=1}^{n} \tau_i = \frac{b_1}{n} \tag{12.15}$$

is the arithmetic mean of all the time constants. Notice that this system has the same b_1 coefficient as Eq. (12.4). We claim that of all n^{th}-order systems (with no zeros or complex poles) that share the same b_1 coefficient, $H_{\max}(s)$ has the *best*, or maximum, bandwidth. In other words, for a given sum of the ZVTs, the best bandwidth is achieved by stacking all of the poles on top of each other. Appealing to the fact that $|H_{\max}(j\omega)|$ is monotonically decreasing with ω, we can establish this claim by proving that the magnitude of $H_{\max}$ at the cutoff frequency ω_c of Eq. (12.4)

is always no less than −3-dB (relative to the DC gain):

$$|H_{\max}(j\omega_c)| \geq |H(j\omega_c)| \equiv \frac{|H_0|}{\sqrt{2}}. \tag{12.16}$$

Letting $\omega = \omega_c$ in Eq. (12.8), this is equivalent to the following: given $x_i > 0 \; \forall i$, show that

$$\left(1 + \bar{x}^2\right)^n \leq 2 \tag{12.17}$$

$$\text{subject to } \prod_{i=1}^{n} \left(1 + {x_i}^2\right) = 2, \tag{12.18}$$

where $\bar{x} \coloneqq \omega_c \bar{\tau} \equiv \sum_{i=1}^{n} x_i/n$ is the arithmetic mean of the x_i's.

The general idea of the proof is to "move" the τ_i's to $\bar{\tau}$ one by one, whilst *improving* the bandwidth of the system with each move. To that end, we will actually prove, subject to the constraint Eq. (12.18), the equivalent inequality

$$\prod_{i=1}^{n} \left(1 + {x_i}^2\right) \geq \left(1 + \bar{x}^2\right)^n. \tag{12.19}$$

We now proceed with the proof proper. If $x_i = \bar{x} \; \forall i$, the upper bound is trivially attained, so assume otherwise. Then $\exists x_p > \bar{x}, x_q < \bar{x}$. Denote $\Delta_p \coloneqq x_p - \bar{x} > 0$. We will now establish the following inequality:

$$(1 + {x_p}^2)(1 + {x_q}^2) > (1 + \bar{x}^2)\left[1 + (x_q + \Delta_p)^2\right]. \tag{12.20}$$

To see this, define the function

$$f(\zeta) \coloneqq \left[1 + (x_p - \zeta)^2\right]\left[1 + (x_q + \zeta)^2\right]. \tag{12.21}$$

We want to show that $f(0) > f(\Delta_p)$. One can compute that

$$f(0) - f(\Delta_p) = \Delta_p(\bar{x} - x_q)\left\{\Delta_p(\bar{x} - x_q) + 2\left[1 - \bar{x}(x_q + \Delta_p)\right]\right\}.$$

By construction, $x_q < \bar{x}$. Hence, to establish the strict positivity of $f(0) - f(\Delta_p)$, we can just check that $1 - \bar{x}(x_q + \Delta_p) > 0$. Since the x_i's are positive, by the constraint (12.18), we know that $x_i < 1 \; \forall i$. Then we can see that $0 < \bar{x} < x_p < 1$ and $0 < x_q + \Delta_p < \bar{x} + \Delta_p = x_p < 1$. Thus, $0 < \bar{x}(x_q + \Delta_p) < 1$, which shows that $f(0) > f(\Delta_p)$. This proves Eq. (12.20).

By renaming $x_p \leftarrow \bar{x}$ and $x_q \leftarrow x_q + \Delta_p$, we have effectively moved x_p to the mean $\bar{x}$ while moving x_q (which was on the other side of $\bar{x}$) by the same but opposite amount

in order to maintain the average $\bar{x}$. This procedure, as we just showed, decreases $\prod_{i=1}^{n}\left(1+{x_i}^2\right)$. We now repeat the above algorithm until all of the x_i's are equal to[4] $\bar{x}$, which yields the right-hand-side of Eq. (12.19), proves Eq. (12.17) and thus also Eq. (12.16), and finally establishes our claim.

Now that we have shown that $H_{\max}(s)$ is indeed the n^{th}-order system (with no zeros or complex poles) with the best bandwidth for the given b_1 coefficient, all that is left for us to do is to compute this optimal bandwidth. It is a simple exercise to show that the bandwidth of $H_{\max}(s)$, which we shall denote by $\omega_{\max}$, is given by

$$\omega_{\max} = \frac{n}{b_1}\sqrt{2^{1/n}-1}. \tag{12.22}$$

This proves the upper bound and also establishes its tightness. □

There is a simple mathematical intuition that we can glean from the upper bound. Since the lower bound is approached when one of the poles is dominant—in the extreme case all non-dominant poles are infinitely far away and we are left with the 1^{st}-order system $H_0/(1+b_1 s)$ whose bandwidth is exactly $1/b_1$—it makes sense that the upper bound is attained when *none* of the poles dominates, in which case all the poles are identical.

Impact of Complex Poles

Here, we show that the lower bound $\omega_c > 1/b_1$ of Eq. (12.6) still holds when the system has complex poles whose quality factors do not exceed $Q \leq \sqrt{2}$. Consider the canonical form of the denominator polynomial that describes a pair of complex conjugate poles:

$$D(s) = 1 + \frac{s}{Q\omega_0} + \left(\frac{s}{\omega_0}\right)^2 \tag{12.23}$$

where $Q > 1/2$. The time constant associated with this complex pole is the coefficient of the s term $\tau = 1/(Q\omega_0)$, and so we proceed to denote, just like before, $y \coloneqq \omega\tau = \omega/(Q\omega_0)$. Then it holds true that

$$|D(j\omega)|^2 = \left[1-(Qy)^2\right]^2 + y^2 < 1 + y^2 \tag{12.24}$$

if $0 < y < 1$ and $Q \leq \sqrt{2}$. Now, to account for m pairs of complex conjugate poles in the original system, the left-hand-side of Eq. (12.10) is multiplied by the additional term $\prod_{j=1}^{m}\left(\left[1-(Q_j y_j)^2\right]^2 + {y_j}^2\right)$ and the constraint Eq. (12.11) is modified to

[4] Obviously, when there are only two x_i's left that are not equal to $\bar{x}$, they will be equidistant from but on opposite sides of $\bar{x}$, so this procedure "centers" both of them to $\bar{x}$.

$\sum_{i=1}^{n} x_i + \sum_{j=1}^{m} y_j \leq 1$. Noting that $0 < y_j < 1 \, \forall j$ due to the modified constraint and applying the above reasoning of Eq. (12.24) to first deal with the complex poles, we can subsequently proceed with the proof of the lower bound as usual.

It is left as a tedious algebra exercise to show that the upper bound does not hold when the system has complex poles. That is, for any pair of complex conjugate poles, there exists a system with those poles whose bandwidth exceeds the upper bound of Eq. (12.6). To elaborate on this point a little bit further, define

$$Q_0 \coloneqq \frac{1}{2}\sqrt{\frac{7}{2\sqrt{2}-1}} \approx 0.97832.$$

Then, if $Q < Q_0$, the 2^{nd}-order system constructed from the complex poles themselves suffices. On the other hand, when $Q \geq Q_0$ (which implies resonant peaking since $Q_0 > 1/\sqrt{2}$), we need to add a dominant real pole to the system in such a way that $H_{\max}(s)$ decays to -3-dB at a frequency where $H(s)$ is still "riding" the resonant peak. This demands that the time constant of this added pole be large enough such that it dominates b_1 sufficiently, but small enough such that its frequency is still close to the resonance frequency of the complex poles.

Impact of Zeros

The effect that zeros have on the bandwidth is discussed in [138]. Assuming that the zeros are at sufficiently high frequencies, we can approximate the numerator of the transfer function Eq. (12.1) as $H_0(1 + as)$ where $a = a_1/a_0$. Then, since as is still quite small (compared to unity) around the frequencies of interest, we can write $(1 + as) \approx 1/(1 - as)$, which further allows us to crudely approximate Eq. (12.1) as, and therefore replace Eq. (12.4) with

$$H(s) \approx \frac{H_0}{1 + (b_1 - a)s + (b_2 - ab_1)s^2 + \cdots + (b_n - ab_{n-1})s^n - ab_n s^{n+1}}. \quad (12.25)$$

We can then replace the ZVTs with the *modified* ZVTs described in [138], whose sum is equal to $b_1 - a$. The bounds stated in Eq. (12.6) can then be "improved," in some sense, by using $b_1 - a$ in place of b_1. Of course, given the nature of the many approximations being made here, the rigor of these bounds (as established here) no longer holds.

Conclusion

In this chapter, we proved that the (strict) lower bound on the bandwidth of a low-pass system with no zeros, order exceeding unity, and whose complex poles

feature quality factors satisfying $Q \leq \sqrt{2}$ is given by its well-known zero-value time constant estimate

$$\omega_c > \frac{1}{b_1}, \tag{12.26}$$

and this bound can be approached by making one of the system's (real) poles increasingly dominant. We also proved that the upper bound on the bandwidth of an n^{th}-order low-pass system with no zeros and no complex poles is given by

$$\omega_c \leq \frac{n}{b_1}\sqrt{2^{1/n} - 1}, \tag{12.27}$$

and this bound is attained when all the poles are at the same location. Both bounds are equally important from a conceptual standpoint, as the lower bound should not be "favored" over the upper bound, except perhaps for the reason that the system performs at least as well as the lower bound—i.e., the lower bound serves as a conservative estimate. However, in a system where all the poles are around the same ballpark of frequencies, the upper bound may actually serve as a better estimate of the bandwidth.

In passing, we would also like to note that analogous bounds hold for the low-cutoff frequency of a high-pass filter based on its infinite-value time constants (IVTs). Specifically, for the low-cutoff $\omega_{c,l}$ of an n^{th}-order (where $n > 1$) high-pass system with no non-DC zeros and no complex poles, we have

$$\frac{1}{n\sqrt{2^{1/n} - 1}} \leq \frac{\omega_{c,l}}{\sum_k 1/\tau_k^{\infty}} < 1 \tag{12.28}$$

where the τ_k^{∞}'s are the system's IVTs[5], and again, the upper bound also holds in the presence of complex poles with $Q \leq \sqrt{2}$.

[5] As a mathematical note, observe that

$$\sum_k \frac{1}{\tau_k^{\infty}} = \sum_{i=1}^{n} -p_i = \sum_{i=1}^{n} \frac{1}{\tau_i} = \frac{b_{n-1}}{b_n}$$

where $p_i, i = 1, \ldots, n$ are the system's poles.

12.2 Holistic Design of Multi-Phase Switched-Capacitor DC-DC Converters with a Large Number of Conversion Ratios

Sharp tuning resolution and low ripple in the output voltage are essential to power converters for achieving optimal power efficiency in the systems they regulate. Here, we present a switched-capacitor DC-DC converter based on a cascaded architecture of triple-mode reconfigurable blocks, where the number of non-redundant conversion ratios that can be generated by cascading N stages scales as 6^N. Each block consists of 15 parallel sections being switched at equally distributed phases. To the best of the authors' knowledge, this architecture achieves the finest output resolution with the lowest number of cascaded stages to date. The 3-stage cascaded system presented here realizes 115 non-redundant conversion ratios, a peak efficiency of 82%, and a large power density of 1.08 $\mathrm{mW/mm^2}$. The circuit was implemented in a 65-nm bulk CMOS process and occupies 1.31 $\mathrm{mm^2}$ of die area.

Introduction

Modern low-power systems-on-chip (SoCs) operating in the subthreshold regime typically feature multiple systems in different power domains. Consequently, the power efficiency of such systems depends critically on the performance of the power management DC-DC converters regulating each system's supply voltage. Such a converter should lend itself to complete integration, feature high power efficiency, and be capable of providing a large power density. Switched-capacitor (SC) DC-DC converters have been studied extensively due to the superior energy density and quality factor of on-chip capacitors relative to inductors [139]–[147]. While highly efficient SC DC-DC converters have been implemented in various forms, they usually only provide a handful of different conversion ratios [139]–[143]. Regardless, the supply must be regulated to a voltage which is *at least* as high as what the system nominally requires. However, since the circuit must still draw the same amount of current, any supply voltage in excess of what the circuit needs at any point in time is effectively wasted [139]. Therefore, having both a fine output voltage tuning resolution and a smooth, low-ripple output voltage waveform is crucial.

Since a basic SC topology exhibits optimal efficiency at a conversion ratio of $1/2$, systems utilizing blocks of $1/2$-ratio converters have been realized in successive approximation architectures [142] or cascaded recursive SC structures [144]–[146] to provide multiple ratios with finer resolutions. However, cascading blocks together

Joint work with R. Fatemi and P. P. Khial. B. Hong participated in the design of the chip, helped debug its performance, and performed a theoretical analysis of the proposed scheme.

reduces overall efficiency, since each stage contributes additional loss. In fact, for the same tuning resolution, cascading a large number of efficient stages could be significantly less power-efficient than utilizing fewer lossier stages with multiple conversion ratios. Hence, to optimize performance, the design of the SC blocks and the overall system architecture must be considered holistically.

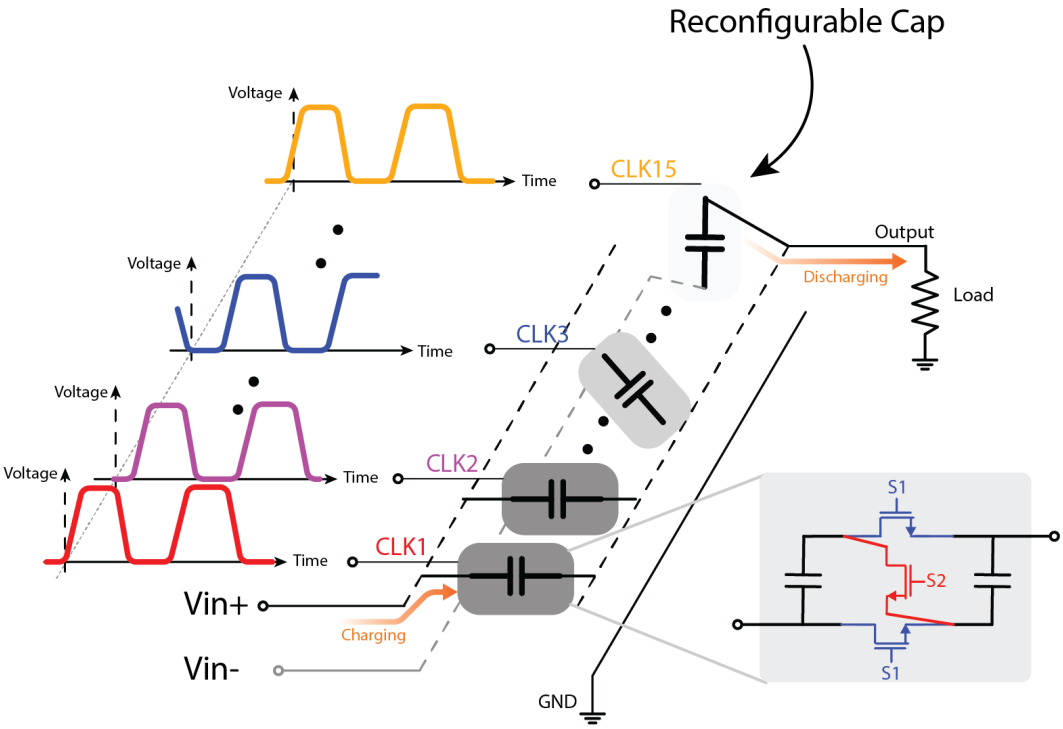

Figure 12.1: High-level schematic of the multi-phase switching scheme of a single conversion block.

Another degree of freedom to achieve voltage regulation is through tuning of the switching frequency, which can change the steady-state output voltage. While deviating from the frequency which optimally trades off the switching loss and the charge-sharing loss of each block might seem inefficient at first glance, the alternatives of adding extra cascaded stages to realize a finer tuning resolution or delivering excess voltage to the load also lower the overall efficiency of the system [139].

Design

We present a switched-capacitor DC-DC converter that utilizes fifteen-phase triple-ratio blocks in a cascaded architecture to provide multiple output voltage levels with a fine resolution. Furthermore, frequency tuning is then used to cover the gaps between these discrete voltage steps, which, due to the small size of the gaps, does

not appreciably degrade the efficiency. Each block can provide output ratios of 1/3, 1/2, and 2/3 [145], which can be set using digital control signals. A reconfigurable flying capacitor was designed to switch between a high-voltage mode (where the two capacitors are in series) and a low-voltage mode (where the two capacitors are in parallel). Non-overlapping switching provides efficient transitions between the modes and eliminates crowbar currents through the switch transistors during switching events. The number of input and ground connections is maximized to minimize charge-sharing loss [144].

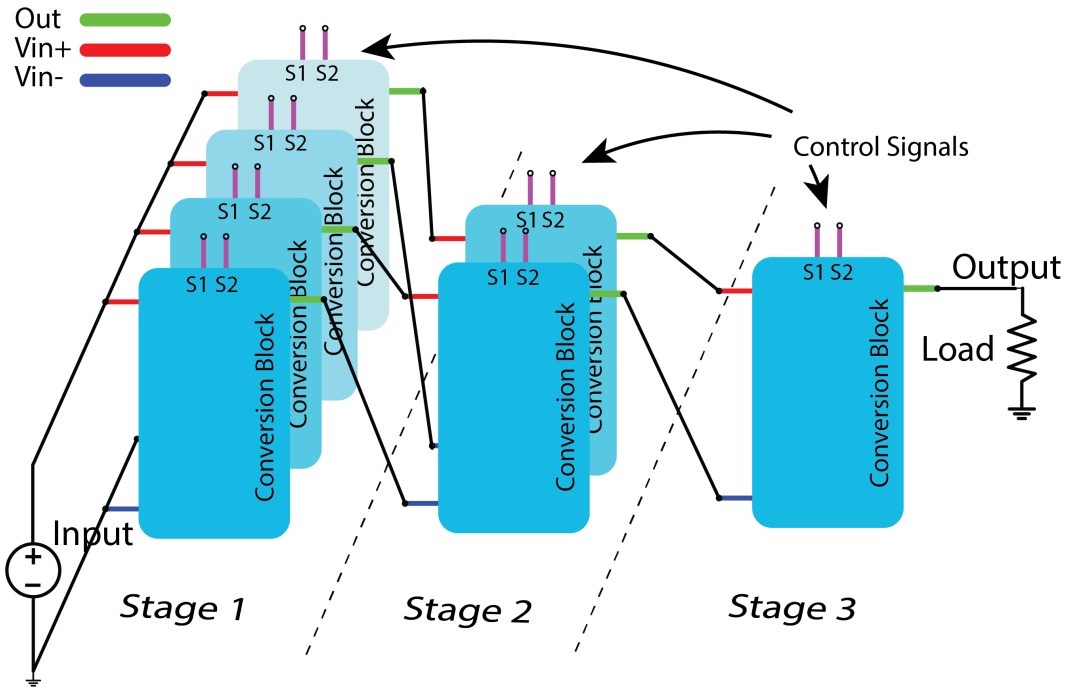

Figure 12.2: Diagram of the cascading topology.

As shown in Figure 12.1, a conversion block consists of 15 parallel stages that operate at different phases, each of which causes one of the flying capacitors to rotate into the charging state or the discharging state. Generated by a ring oscillator, the large number of equally-distributed clock phases reduces the charge-transfer loss between these two modes and suppresses output voltage ripple. The correspondingly smooth output voltage thereby enhances the efficiency of the system [141], since fluctuations in the regulated voltage contribute directly to loss.

While the architecture is scalable, cascading just three stages (shown in Figure 12.2) already gives 115 *unique* conversion ratios, realizable through different settings and which cover a large dynamic range. It is important to note, however, that redundant ratios will not necessarily have the same output voltage in practice due

to the different loss of the system in each setting. Therefore, an even finer tuning resolution is possible than what is combinatorically allowed.

Table 12.1: Number of Unique DC-DC Conversion Ratios

Scheme	Number of Ratios
Ours	$\frac{2 \cdot 6^N - 5 \cdot 3^N + 6 \cdot 2^N}{3}$
Recursive Ternary [145]	$2 \cdot 3^N - 2^N - 1$
Lower Bound from [145]	$\frac{3}{2}\left(3^N - 1\right)$
Binary Successive Approximation [142]	$2^N - 1$

Closed-form expressions for the exact number of non-redundant conversion ratios (not including 0 or 1) as a function of the number of stages N, obtained through proof by induction, are given in Table 12.1 for various cascading schemes. (The lower bound given in [145] for the recursive ternary scheme is also shown for reference.) A numerical simulation counting the number of ratios which confirms these formulas is plotted in Figure 12.3, clearly depicting the advantage of our scheme over others.

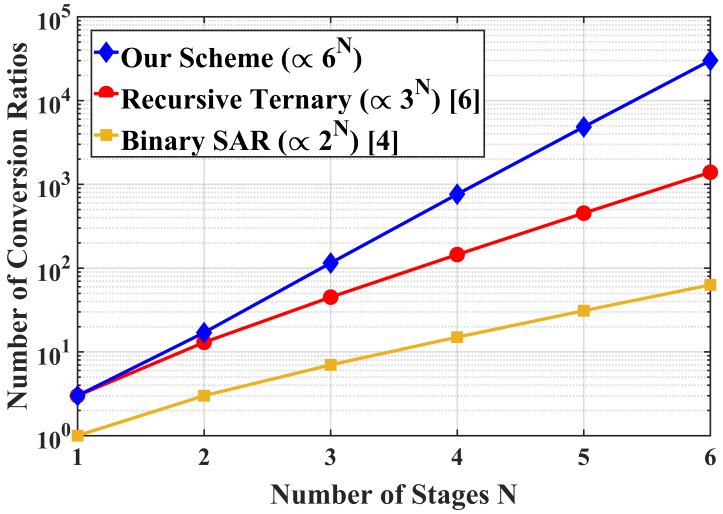

Figure 12.3: Number of conversion ratios (on a log scale) vs. number of cascaded stages for different cascading schemes.

Measurement Results

Figure 12.4 shows the ideal and measured output voltages for a cascade of two stages. A three-stage cascade provides an even finer resolution of output voltages with minimum and maximum step sizes of 4.6 mV and 37 mV, respectively.

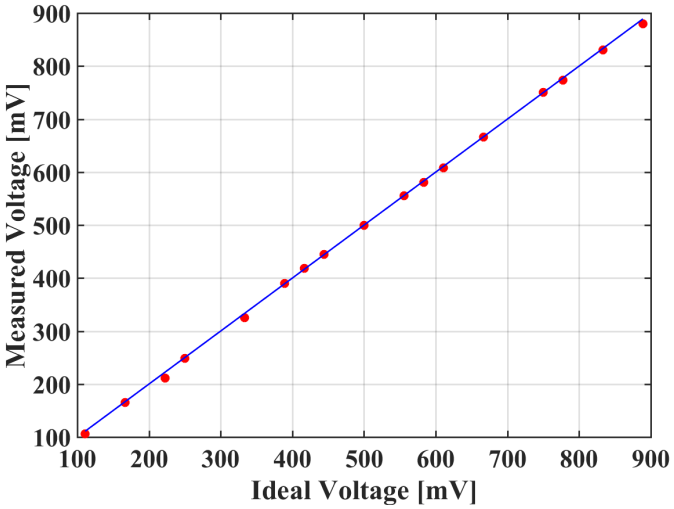

Figure 12.4: Measured output voltage of all 17 ratios for a 2-stage cascade with no load (red dots) plotted against the ideal output voltage (blue line).

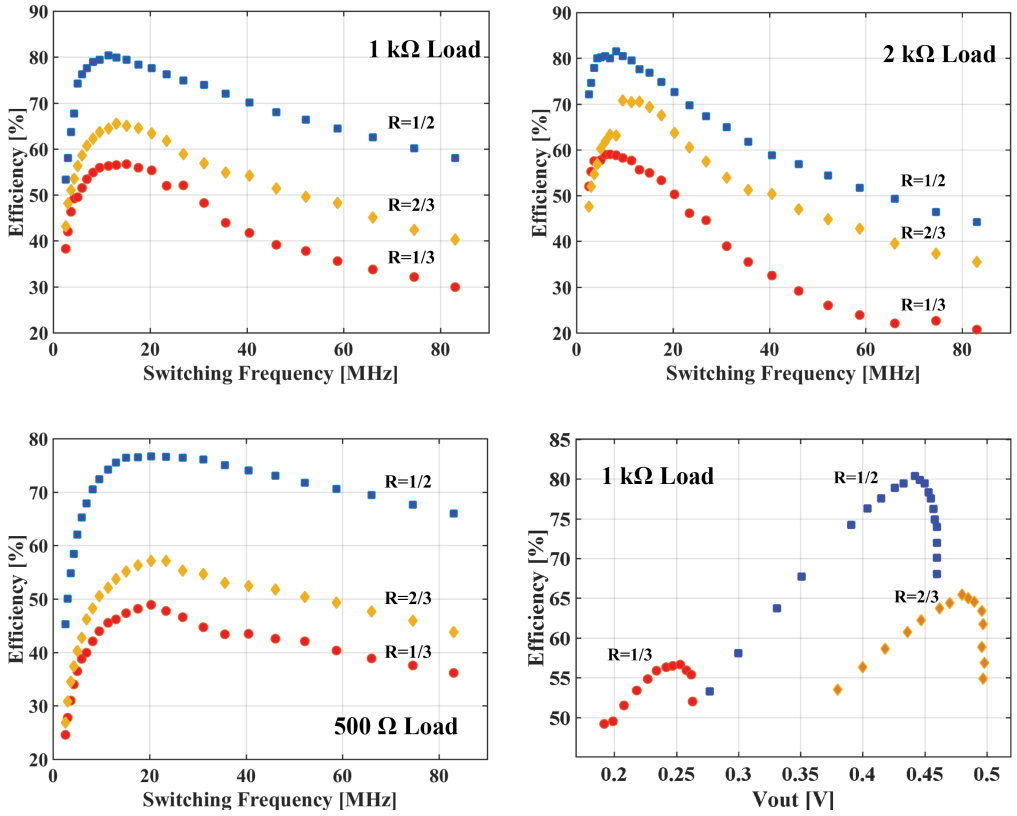

Figure 12.5: Efficiency vs. switching frequency for conversion ratios of 1/3, 1/2, and 2/3 with various loads. (Bottom Right) Efficiency vs. output voltage for the same conversion ratios with a 1 kΩ load.

The efficiency of the system for various settings is shown in Figure 12.5. As we can see, small deviations from the optimum switching frequency do not degrade the efficiency significantly. Therefore, as mentioned above, tuning the switching period can be reliably used as another degree of freedom to adjust the output voltage. Figure 12.6 depicts the peak efficiency of the system as a function of the power density.

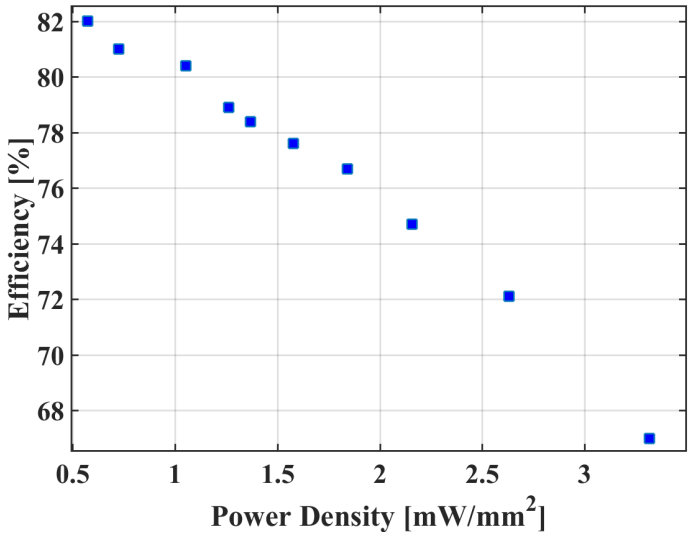

Figure 12.6: Peak efficiency vs. power density.

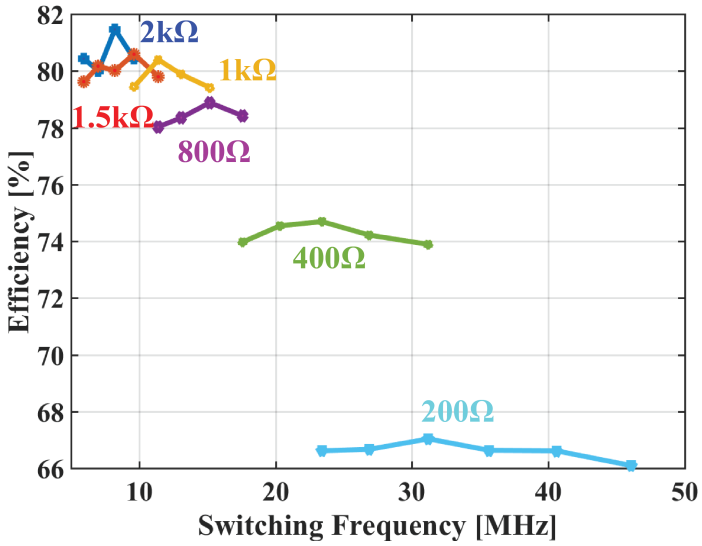

Figure 12.7: Efficiency vs. switching frequency for various loads with a 1/2 conversion ratio.

Finally, Figure 12.7 compares the efficiency vs. switching frequency characteristic of the converter for various different loads. A peak efficiency of 82% is achieved for a load of 2 kΩ. While driving a 1 kΩ load, the converter provides a large power density of 1.08 mW/mm^2 and maintains 80% power efficiency.

Table 12.2: DC-DC Converter Performance Comparison

	JSSC'16 [142]	**ISSCC'14 [144]**	**This Work**
Technology	0.18μm CMOS	0.25μm CMOS	65nm CMOS
Peak Power Efficiency	72%	85%	82%
Number of Stages	7	4	3
Conversion Ratios	117	15	115
Total Capacitance [nF]	2.24	3	1.05
Power Density [mW/mm^2]	0.16 at 3kΩ load	0.86 at 1kΩ load	1.08 at 1kΩ load
Chip Area [mm^2]	4.3	4.645	1.31

Table 12.2 shows a performance comparison with other state-of-the-art DC-DC converters, and a die micrograph of a conversion block is shown in Figure 12.8.

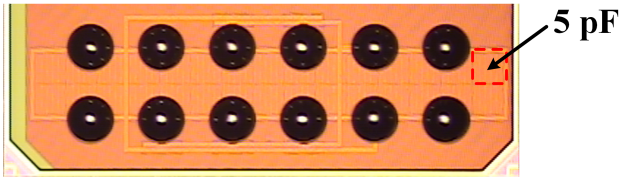

Figure 12.8: Die photo of a conversion block, measuring 1.17mm × 0.16mm.

Conclusion

A high-efficiency switched-capacitor DC-DC converter achieving a large number of conversion ratios was demonstrated in 65-nm bulk CMOS. Measurements show that the circuit is capable of simultaneously providing a large power density while maintaining excellent power efficiency. Combined with the small silicon footprint of the system, this makes it suitable for integration with low-cost, low-power systems.

BIBLIOGRAPHY

[1] J. Lee and M. Liu, "A 20-Gb/s burst-mode clock and data recovery circuit using injection-locking technique," *IEEE Journal of Solid-State Circuits*, vol. 43, no. 3, pp. 619–630, Mar. 2008. DOI: 10.1109/JSSC.2007.916598.

[2] M. Hossain and A. C. Carusone, "CMOS oscillators for clock distribution and injection-locked deskew," *IEEE Journal of Solid-State Circuits*, vol. 44, no. 8, pp. 2138–2153, Aug. 2009. DOI: 10.1109/JSSC.2009.2022917.

[3] S. Shekhar, M. Mansuri, F. O'Mahony, G. Balamurugan, J. E. Jaussi, J. Kennedy, D. J. Allstot, R. Mooney, and B. Casper, "Strong injection locking in low-Q LC oscillators: Modeling and application in a forwarded-clock I/O receiver," *IEEE Transactions on Circuits and Systems I: Regular Papers*, vol. 56, no. 8, pp. 1818–1829, Aug. 2009. DOI: 10.1109/TCSI.2009.2027509.

[4] H. R. Rategh and T. H. Lee, "Superharmonic injection-locked frequency dividers," *IEEE Journal of Solid-State Circuits*, vol. 34, no. 6, pp. 813–821, Jun. 1999. DOI: 10.1109/4.766815.

[5] H. Wu and A. Hajimiri, "A 19GHz 0.5mW 0.35μm CMOS frequency divider with shunt-peaking locking-range enhancement," in *2001 IEEE International Solid-State Circuits Conference (ISSCC) Digest of Technical Papers*, Feb. 2001, pp. 412–413. DOI: 10.1109/ISSCC.2001.912698.

[6] R. J. Betancourt-Zamora, S. Verma, and T. H. Lee, "1-GHz and 2.8-GHz CMOS injection-locked ring oscillator prescalers," in *2001 Symposium on VLSI Circuits Digest of Technical Papers*, Jun. 2001, pp. 47–50. DOI: 10.1109/VLSIC.2001.934191.

[7] M. Acar, D. Leenaerts, and B. Nauta, "A wide-band CMOS injection-locked frequency divider," in *2004 IEEE Radio Frequency Integrated Circuits (RFIC) Symposium Digest of Papers*, Jun. 2004, pp. 211–214. DOI: 10.1109/RFIC.2004.1320574.

[8] M. Tiebout, "A CMOS direct injection-locked oscillator topology as high-frequency low-power frequency divider," *IEEE Journal of Solid-State Circuits*, vol. 39, no. 7, pp. 1170–1174, Jul. 2004. DOI: 10.1109/JSSC.2004.829937.

[9] H. Wu and L. Zhang, "A 16-to-18GHz 0.18μm epi-CMOS divide-by-3 injection-locked frequency divider," in *2006 IEEE International Solid-State Circuits Conference (ISSCC) Digest of Technical Papers*, Feb. 2006, pp. 602–603. DOI: 10.1109/ISSCC.2006.1696312.

[10] A. Mirzaei, M. E. Heidari, R. Bagheri, S. Chehrazi, and A. A. Abidi, "Injection-locked frequency dividers based on ring oscillators with optimum injection for wide lock range," in *2006 Symposium on VLSI Circuits Digest of Technical Papers*, Jun. 2006, pp. 174–175. DOI: 10.1109/VLSIC.2006.1705366.

[11] C.-C. Chen, H.-W. Tsao, and H. Wang, "Design and analysis of CMOS frequency dividers with wide input locking ranges," *IEEE Transactions on Microwave Theory and Techniques*, vol. 57, no. 12, pp. 3060–3069, Dec. 2009. DOI: 10.1109/TMTT.2009.2033239.

[12] Y.-L. Yeh and H.-Y. Chang, "Design and analysis of a W-band divide-by-three injection-locked frequency divider using second harmonic enhancement technique," *IEEE Transactions on Microwave Theory and Techniques*, vol. 60, no. 6, pp. 1617–1625, Jun. 2012. DOI: 10.1109/TMTT.2012.2189244.

[13] A. Imani and H. Hashemi, "Distributed injection-locked frequency dividers," *IEEE Journal of Solid-State Circuits*, vol. 52, no. 8, pp. 2083–2093, Aug. 2017. DOI: 10.1109/JSSC.2017.2701325.

[14] M.-C. Chen and C.-Y. Wu, "Design and analysis of CMOS subharmonic injection-locked frequency triplers," *IEEE Transactions on Microwave Theory and Techniques*, vol. 56, no. 8, pp. 1869–1878, Aug. 2008. DOI: 10.1109/TMTT.2008.926566.

[15] W. L. Chan and J. R. Long, "A 56–65 GHz injection-locked frequency tripler with quadrature outputs in 90-nm CMOS," *IEEE Journal of Solid-State Circuits*, vol. 43, no. 12, pp. 2739–2746, Dec. 2008. DOI: 10.1109/JSSC.2008.2004869.

[16] C.-Y. Wu, M.-C. Chen, and Y.-K. Lo, "A phase-locked loop with injection-locked frequency multiplier in 0.18-μm CMOS for V-band applications," *IEEE Transactions on Microwave Theory and Techniques*, vol. 57, no. 7, pp. 1629–1636, Jul. 2009. DOI: 10.1109/TMTT.2009.2021833.

[17] E. Monaco, M. Pozzoni, F. Svelto, and A. Mazzanti, "Injection-locked CMOS frequency doublers for μ-wave and mm-wave applications," *IEEE Journal of Solid-State Circuits*, vol. 45, no. 8, pp. 1565–1574, Aug. 2010. DOI: 10.1109/JSSC.2010.2049780.

[18] A. Elkholy, M. Talegaonkar, T. Anand, and P. K. Hanumolu, "Design and analysis of low-power high-frequency robust sub-harmonic injection-locked clock multipliers," *IEEE Journal of Solid-State Circuits*, vol. 50, no. 12, pp. 3160–3174, Dec. 2015. DOI: 10.1109/JSSC.2015.2478449.

[19] A. Rofougaran, J. Rael, M. Rofougaran, and A. Abidi, "A 900MHz CMOS LC-oscillator with quadrature outputs," in *1996 IEEE International Solid-State Circuits Conference (ISSCC) Digest of Technical Papers*, Feb. 1996, pp. 392–393. DOI: 10.1109/ISSCC.1996.488731.

[20] P. Kinget, R. Melville, D. Long, and V. Gopinathan, "An injection-locking scheme for precision quadrature generation," *IEEE Journal of Solid-State Circuits*, vol. 37, no. 7, pp. 845–851, Jul. 2002. DOI: 10.1109/JSSC.2002.1015681.

[21] A. Mirzaei, M. E. Heidari, R. Bagheri, S. Chehrazi, and A. A. Abidi, "The quadrature LC oscillator: A complete portrait based on injection locking," *IEEE Journal of Solid-State Circuits*, vol. 42, no. 9, pp. 1916–1932, Sep. 2007. DOI: 10.1109/JSSC.2007.903047.

[22] M. Raj and A. Emami, "A wideband injection-locking scheme and quadrature phase generation in 65-nm CMOS," *IEEE Transactions on Microwave Theory and Techniques*, vol. 62, no. 4, pp. 763–772, Apr. 2014. DOI: 10.1109/TMTT.2014.2310172.

[23] M. Raj, S. Saeedi, and A. Emami, "A wideband injection locked quadrature clock generation and distribution technique for an energy-proportional 16–32 Gb/s optical receiver in 28 nm FDSOI CMOS," *IEEE Journal of Solid-State Circuits*, vol. 51, no. 10, pp. 2446–2462, Oct. 2016. DOI: 10.1109/JSSC.2016.2584643.

[24] L. Romanò, S. Levantino, C. Samori, and A. L. Lacaita, "Multiphase *LC* oscillators," *IEEE Transactions on Circuits and Systems I: Regular Papers*, vol. 53, no. 7, pp. 1579–1588, Jul. 2006. DOI: 10.1109/TCSI.2006.876415.

[25] K. Stephan, "Inter-injection-locked oscillators for power combining and phased arrays," *IEEE Transactions on Microwave Theory and Techniques*, vol. 34, no. 10, pp. 1017–1025, Oct. 1986. DOI: 10.1109/TMTT.1986.1133491.

[26] K. Stephan and W. Morgan, "Analysis of interinjection-locked oscillators for integrated phased arrays," *IEEE Transactions on Antennas and Propagation*, vol. 35, no. 7, pp. 771–781, Jul. 1987. DOI: 10.1109/TAP.1987.1144184.

[27] R. A. York, "Nonlinear analysis of phase relationships in quasi-optical oscillator arrays," *IEEE Transactions on Microwave Theory and Techniques*, vol. 41, no. 10, pp. 1799–1809, Oct. 1993. DOI: 10.1109/22.247926.

[28] R. A. York, P. Liao, and J. J. Lynch, "Oscillator array dynamics with broadband *N*-port coupling networks," *IEEE Transactions on Microwave Theory and Techniques*, vol. 42, no. 11, pp. 2040–2045, Nov. 1994. DOI: 10.1109/22.330116.

[29] R. A. York and T. Itoh, "Injection- and phase-locking techniques for beam control," *IEEE Transactions on Microwave Theory and Techniques*, vol. 46, no. 11, pp. 1920–1929, Nov. 1998. DOI: 10.1109/22.734513.

[30] C. J. Buczek, R. J. Freiberg, and M. L. Skolnick, "Laser injection locking," *Proceedings of the IEEE*, vol. 61, no. 10, pp. 1411–1431, Oct. 1973. DOI: 10.1109/PROC.1973.9294.

[31] R. Lang, "Injection locking properties of a semiconductor laser," *IEEE Journal of Quantum Electronics*, vol. 18, no. 6, pp. 976–983, Jun. 1982. DOI: 10.1109/JQE.1982.1071632.

[32] F. Mogensen, H. Olesen, and G. Jacobsen, "Locking conditions and stability properties for a semiconductor laser with external light injection," *IEEE Journal of Quantum Electronics*, vol. 21, no. 7, pp. 784–793, Jul. 1985. DOI: 10.1109/JQE.1985.1072760.

[33] C.-H. Chang, L. Chrostowski, and C. J. Chang-Hasnain, "Injection locking of VCSELs," *IEEE Journal of Selected Topics in Quantum Electronics*, vol. 9, no. 5, pp. 1386–1393, Sep./Oct. 2003. DOI: 10.1109/JSTQE.2003.819510.

[34] A. Pikovsky, M. Rosenblum, and J. Kurths, *Synchronization: A Universal Concept in Nonlinear Sciences*. Cambridge University Press, 2003.

[35] Y. Kuramoto, *Chemical Oscillations, Waves, and Turbulence*. Dover Publications, 2003.

[36] E. M. Izhikevich, *Dynamical Systems in Neuroscience: The Geometry of Excitability and Bursting*. MIT Press, 2007.

[37] A. T. Winfree, *The Geometry of Biological Time*. Springer, 2001.

[38] B. Razavi, "A study of injection locking and pulling in oscillators," *IEEE Journal of Solid-State Circuits*, vol. 39, no. 9, pp. 1415–1424, Sep. 2004. DOI: 10.1109/JSSC.2004.831608.

[39] A. A. Andronov, A. A. Vitt, and S. E. Khaikin, *Theory of Oscillators*. Dover, 1987.

[40] L. Perko, *Differential Equations and Dynamical Systems*, 3rd ed. Springer, 2001.

[41] T. Djurhuus, V. Krozer, J. Vidkjær, and T. K. Johansen, "Oscillator phase noise: A geometrical approach," *IEEE Transactions on Circuits and Systems I: Regular Papers*, vol. 56, no. 7, pp. 1373–1382, Jul. 2009. DOI: 10.1109/TCSI.2008.2006211.

[42] F. L. Traversa and F. Bonani, "Oscillator noise: A nonlinear perturbative theory including orbital fluctuations and phase-orbital correlation," *IEEE Transactions on Circuits and Systems I: Regular Papers*, vol. 58, no. 10, pp. 2485–2497, Oct. 2011. DOI: 10.1109/TCSI.2011.2123531.

[43] Ö. Suvak and A. Demir, "On phase models for oscillators," *IEEE Transactions on Computer-Aided Design of Integrated Circuits and Systems*, vol. 30, no. 7, pp. 972–985, Jul. 2011. DOI: 10.1109/TCAD.2011.2113630.

[44] J. H. Vincent, "On some experiments in which two neighbouring maintained oscillatory circuits affect a resonating circuit," *Proceedings of the Physical Society of London*, vol. 32, no. 1, pp. 84–91, 1919. DOI: 10.1088/1478-7814/32/1/311.

[45] E. V. Appleton, "The automatic synchronization of triode oscillators," *Proceedings of the Cambridge Philosophical Society*, vol. 21, no. 3, pp. 231–248, 1922.

[46] B. van der Pol, "Forced oscillations in a circuit with non-linear resistance. (reception with reactive triode)," *The London, Edinburgh, and Dublin Philosophical Magazine and Journal of Science*, vol. 3, no. 13, pp. 65–80, Jan. 1927. DOI: 10.1080/14786440108564176.

[47] R. Adler, "A study of locking phenomena in oscillators," *Proceedings of the IRE*, vol. 34, no. 6, pp. 351–357, Jun. 1946. DOI: 10.1109/JRPROC.1946.229930.

[48] R. D. Huntoon and A. Weiss, "Synchronization of oscillators," *Proceedings of the IRE*, vol. 35, no. 12, pp. 1415–1423, Dec. 1947. DOI: 10.1109/JRPROC.1947.226202.

[49] L. J. Paciorek, "Injection locking of oscillators," *Proceedings of the IEEE*, vol. 53, no. 11, pp. 1723–1727, Nov. 1965. DOI: 10.1109/PROC.1965.4345.

[50] H. L. Stover, "Theoretical explanation for the output spectra of unlocked driven oscillators," *Proceedings of the IEEE*, vol. 54, no. 2, pp. 310–311, Feb. 1966. DOI: 10.1109/PROC.1966.4664.

[51] M. Armand, "On the output spectrum of unlocked driven oscillators," *Proceedings of the IEEE*, vol. 57, no. 5, pp. 798–799, May 1969. DOI: 10.1109/PROC.1969.7077.

[52] K. Kurokawa, "Stability of injection-locked oscillators," *Proceedings of the IEEE*, vol. 60, no. 7, pp. 907–908, Jul. 1972. DOI: 10.1109/PROC.1972.8799.

[53] ——, "Injection locking of microwave solid-state oscillators," *Proceedings of the IEEE*, vol. 61, no. 10, pp. 1386–1410, Oct. 1973. DOI: 10.1109/PROC.1973.9293.

[54] G. H. B. Hansson and K. I. Lundström, "Stability criteria for phase-locked oscillators," *IEEE Transactions on Microwave Theory and Techniques*, vol. 20, no. 10, pp. 641–645, Oct. 1972. DOI: 10.1109/TMTT.1972.1127837.

[55] E. F. Calandra and A. M. Sommariva, "Stability analysis of injection-locked oscillators in their fundamental mode of operation," *IEEE Transactions on Microwave Theory and Techniques*, vol. 29, no. 11, pp. 1137–1144, Nov. 1981. DOI: 10.1109/TMTT.1981.1130522.

[56] X. Zhang, X. Zhou, B. Aliener, and A. S. Daryoush, "A study of subharmonic injection locking for local oscillators," *IEEE Microwave and Guided Wave Letters*, vol. 2, no. 3, pp. 97–99, Mar. 1992. DOI: 10.1109/75.124911.

[57] J. Dixon, E. Bradley, and Z. B. Popović, "Nonlinear time-domain analysis of injection-locked microwave MESFET oscillators," *IEEE Transactions on Microwave Theory and Techniques*, vol. 45, no. 7, pp. 1050–1057, Jul. 1997. DOI: 10.1109/22.598440.

[58] C.-C. Huang and T.-H. Chu, "Analysis of MESFET injection-locked oscillators in fundamental mode of operation," *IEEE Transactions on Microwave Theory and Techniques*, vol. 42, no. 10, pp. 1851–1857, Oct. 1994. DOI: 10.1109/22.320764.

[59] A. Mirzaei, M. E. Heidari, and A. A. Abidi, "Analysis of oscillators locked by large injection signals: Generalized Adler's equation and geometrical interpretation," in *Proceedings of the IEEE 2006 Custom Integrated Circuits Conference (CICC)*, Sep. 2006, pp. 737–740. DOI: 10.1109/CICC.2006.320928.

[60] A. Mirzaei, M. E. Heidari, R. Bagheri, and A. A. Abidi, "Multi-phase injection widens lock range of ring-oscillator-based frequency dividers," *IEEE Journal of Solid-State Circuits*, vol. 43, no. 3, pp. 656–671, Mar. 2008. DOI: 10.1109/JSSC.2007.916602.

[61] G. R. Gangasani and P. R. Kinget, "A time-domain model for predicting the injection locking bandwidth of nonharmonic oscillators," *IEEE Transactions on Circuits and Systems II: Express Briefs*, vol. 53, no. 10, pp. 1035–1038, Oct. 2006. DOI: 10.1109/TCSII.2006.882239.

[62] ——, "Time-domain model for injection locking in nonharmonic oscillators," *IEEE Transactions on Circuits and Systems I: Regular Papers*, vol. 55, no. 6, pp. 1648–1658, Jul. 2008. DOI: 10.1109/TCSI.2008.916605.

[63] J.-C. Chien and L.-H. Lu, "Analysis and design of wideband injection-locked ring oscillators with multiple-input injection," *IEEE Journal of Solid-State Circuits*, vol. 42, no. 9, pp. 1906–1915, Sep. 2007. DOI: 10.1109/JSSC.2007.903058.

[64] A. Tofangdarzade and A. Jalali, "An efficient method to analyze lock range in ring oscillators with multiple injections," *IEEE Transactions on Circuits and Systems II: Express Briefs*, vol. 62, no. 11, pp. 1013–1017, Nov. 2015. DOI: 10.1109/TCSII.2015.2456095.

[65] A. R. Hazeri and H. M.-Naimi, "Generalized analytical equations for injected ring oscillator with *RC*-load," *IEEE Transactions on Circuits and Systems I: Regular Papers*, vol. 65, no. 1, pp. 223–234, Jan. 2018. DOI: 10.1109/TCSI.2017.2726100.

[66] X. Lai and J. Roychowdhury, "Capturing oscillator injection locking via nonlinear phase-domain macromodels," *IEEE Transactions on Microwave Theory and Techniques*, vol. 52, no. 9, pp. 2251–2261, Sep. 2004. DOI: 10.1109/TMTT.2004.834579.

[67] ——, "Automated oscillator macromodelling techniques for capturing amplitude variations and injection locking," in *Proceedings of the 2004 IEEE/ACM International Conference on Computer-Aided Design (ICCAD)*, Nov. 2004, pp. 687–694. DOI: 10.1109/ICCAD.2004.1382663.

[68] ——, "Analytical equations for predicting injection locking in LC and ring oscillators," in *Proceedings of the IEEE 2005 Custom Integrated Circuits Conference (CICC)*, Sep. 2005, pp. 461–464. DOI: 10.1109/CICC.2005.1568706.

[69] Y. Wan, X. Lai, and J. Roychowdhury, "Understanding injection locking in negative-resistance LC oscillators intuitively using nonlinear feedback analysis," in *Proceedings of the IEEE 2005 Custom Integrated Circuits Conference (CICC)*, Sep. 2005, pp. 729–732. DOI: 10.1109/CICC.2005.1568771.

[70] T. Mei and J. Roychowdhury, "Rigorous analytical/graphical injection locking analysis of two-port negative resistance oscillators," in *Proceedings of the IEEE 2006 Custom Integrated Circuits Conference (CICC)*, Sep. 2006, pp. 741–744. DOI: 10.1109/CICC.2006.320965.

[71] P. Bhansali and J. Roychowdhury, "Gen-Adler: The Generalized Adler's equation for injection locking analysis in oscillators," in *2009 Asia and South Pacific Design Automation Conference (ASP-DAC)*, Jan. 2009, pp. 522–527. DOI: 10.1109/ASPDAC.2009.4796533.

[72] P. Maffezzoni, "Analysis of oscillator injection locking through phase-domain impulse-response," *IEEE Transactions on Circuits and Systems I: Regular Papers*, vol. 55, no. 5, pp. 1297–1305, Jun. 2008. DOI: 10.1109/TCSI.2008.916692.

[73] P. Maffezzoni and D. D'Amore, "Evaluating pulling effects in oscillators due to small-signal injection," *IEEE Transactions on Computer-Aided Design of Integrated Circuits and Systems*, vol. 28, no. 1, pp. 22–31, Jan. 2009. DOI: 10.1109/TCAD.2008.2009142.

[74] P. Maffezzoni, "Synchronization analysis of two weakly coupled oscillators through a PPV macromodel," *IEEE Transactions on Circuits and Systems I: Regular Papers*, vol. 57, no. 3, pp. 654–663, Mar. 2010. DOI: 10.1109/TCSI.2009.2025000.

[75] P. Maffezzoni, D. D'Amore, S. Daneshgar, and M. P. Kennedy, "Analysis and design of injection-locked frequency dividers by means of a phase-domain macromodel," *IEEE Transactions on Circuits and Systems I: Regular Papers*,

vol. 57, no. 11, pp. 2956–2966, Nov. 2010. DOI: 10.1109/TCSI.2010.2050233.

[76] P. Maffezzoni, "Nonlinear phase-domain macromodeling of injection-locked frequency dividers," *IEEE Transactions on Circuits and Systems I: Regular Papers*, vol. 60, no. 11, pp. 2878–2887, Nov. 2013. DOI: 10.1109/TCSI.2013.2256237.

[77] D. Dunwell and A. C. Carusone, "Modeling oscillator injection locking using the phase domain response," *IEEE Transactions on Circuits and Systems I: Regular Papers*, vol. 60, no. 11, pp. 2823–2833, Nov. 2013. DOI: 10.1109/TCSI.2013.2252654.

[78] P. Maffezzoni and S. Levantino, "Phase noise of pulse injection-locked oscillators," *IEEE Transactions on Circuits and Systems I: Regular Papers*, vol. 61, no. 10, pp. 2912–2919, Oct. 2014. DOI: 10.1109/TCSI.2014.2321200.

[79] S. Verma, H. R. Rategh, and T. H. Lee, "A unified model for injection-locked frequency dividers," *IEEE Journal of Solid-State Circuits*, vol. 38, no. 6, pp. 1015–1027, Jun. 2003. DOI: 10.1109/JSSC.2003.811975.

[80] H.-C. Chang, X. Cao, U. K. Mishra, and R. A. York, "Phase noise in coupled oscillators: Theory and experiment," *IEEE Transactions on Microwave Theory and Techniques*, vol. 45, no. 7, pp. 604–615, May 1997. DOI: 10.1109/22.575575.

[81] H.-C. Chang, X. Cao, M. J. Vaughan, U. K. Mishra, and R. A. York, "Phase noise in externally injection-locked oscillator arrays," *IEEE Transactions on Microwave Theory and Techniques*, vol. 45, no. 11, pp. 2035–2042, Nov. 1997. DOI: 10.1109/22.644229.

[82] H.-A. Tanaka, "Synchronization limit of weakly forced nonlinear oscillators," *Journal of Physics A: Mathematical and Theoretical*, vol. 47, no. 40, Sep. 2014. DOI: 10.1088/1751-8113/47/40/402002.

[83] ——, "Optimal entrainment with smooth, pulse, and square signals in weakly forced nonlinear oscillators," *Physica D: Nonlinear Phenomena*, vol. 288, pp. 1–22, Nov. 2014. DOI: 10.1016/j.physd.2014.07.003.

[84] T. Nagashima, X. Wei, H.-A. Tanaka, and H. Sekiya, "Locking range derivations for injection-locked class-E oscillator applying phase reduction theory," *IEEE Transactions on Circuits and Systems I: Regular Papers*, vol. 61, no. 10, pp. 2904–2911, Oct. 2014. DOI: 10.1109/TCSI.2014.2327276.

[85] H.-A. Tanaka, A. Hasegawa, H. Mizuno, and T. Endo, "Synchronizability of distributed clock oscillators," *IEEE Transactions on Circuits and Systems I: Fundamental Theory and Applications*, vol. 49, no. 9, pp. 1271–1278, Sep. 2002. DOI: 10.1109/TCSI.2002.802361.

[86] A. Mirzaei and H. Darabi, "Mutual pulling between two oscillators," *IEEE Journal of Solid-State Circuits*, vol. 49, no. 2, pp. 360–372, Feb. 2014. DOI: 10.1109/JSSC.2013.2290298.

[87] A. Hajimiri and T. H. Lee, "A general theory of phase noise in electrical oscillators," *IEEE Journal of Solid-State Circuits*, vol. 33, no. 2, pp. 179–194, Feb. 1998. DOI: 10.1109/4.658619.

[88] ——, *The Design of Low Noise Oscillators*. Springer, 1999.

[89] ——, "Design issues in CMOS differential *LC* oscillators," *IEEE Journal of Solid-State Circuits*, vol. 34, no. 5, pp. 717–724, May 1999. DOI: 10.1109/4.760384.

[90] A. Hajimiri, S. Limotyrakis, and T. H. Lee, "Jitter and phase noise in ring oscillators," *IEEE Journal of Solid-State Circuits*, vol. 34, no. 6, pp. 790–804, Jun. 1999. DOI: 10.1109/4.766813.

[91] A. Demir, A. Mehrotra, and J. Roychowdhury, "Phase noise in oscillators: A unifying theory and numerical methods for characterization," *IEEE Transactions on Circuits and Systems I: Fundamental Theory and Applications*, vol. 47, no. 5, pp. 655–674, May 2000. DOI: 10.1109/81.847872.

[92] A. Demir, "Phase noise in oscillators: DAEs and colored noise sources," in *Proceedings of the 1998 IEEE/ACM International Conference on Computer-Aided Design (ICCAD)*, Nov. 1998, pp. 170–177. DOI: 10.1109/ICCAD.1998.144262.

[93] ——, "Phase noise and timing jitter in oscillators with colored-noise sources," *IEEE Transactions on Circuits and Systems I: Fundamental Theory and Applications*, vol. 49, no. 12, pp. 1782–1791, Dec. 2002. DOI: 10.1109/TCSI.2002.805707.

[94] P. Vanassche, G. Gielen, and W. Sansen, "On the difference between two widely publicized methods for analyzing oscillator phase behavior," in *Proceedings of the 2002 IEEE/ACM International Conference on Computer-Aided Design (ICCAD)*, Nov. 2002, pp. 229–233. DOI: 10.1109/ICCAD.2002.1167539.

[95] S. Levantino, P. Maffezzoni, F. Pepe, A. Bonfanti, C. Samori, and A. L. Lacaita, "Efficient calculation of the impulse sensitivity function in oscillators," *IEEE Transactions on Circuits and Systems II: Express Briefs*, vol. 59, no. 10, pp. 628–632, Oct. 2012. DOI: 10.1109/TCSII.2012.2208679.

[96] J. A. Sanders, F. Verhulst, and J. Murdock, *Averaging Methods in Nonlinear Dynamical Systems*, 2nd ed. Springer, 2007.

[97] A. M. Niknejad and R. G. Meyer, "Analysis, design, and optimization of spiral inductors and transformers for Si RF IC's," *IEEE Journal of Solid-State Circuits*, vol. 33, no. 10, pp. 1470–1481, Oct. 1998. DOI: 10.1109/4.720393.

[98] S. S. Mohan, M. Hershenson, S. P. Boyd, and T. H. Lee, "Simple accurate expressions for planar spiral inductances," *IEEE Journal of Solid-State Circuits*, vol. 34, no. 10, pp. 1419–1424, Oct. 1999. DOI: 10.1109/4.792620.

[99] C. P. Yue and S. S. Wong, "Physical modeling of spiral inductors on silicon," *IEEE Transactions on Electron Devices*, vol. 47, no. 3, pp. 560–568, Mar. 2000. DOI: 10.1109/16.824729.

[100] T. H. Lee and A. Hajimiri, "Oscillator phase noise: A tutorial," *IEEE Journal of Solid-State Circuits*, vol. 35, no. 3, pp. 326–336, Mar. 2000. DOI: 10.1109/4.826814.

[101] D. Ham and A. Hajimiri, "Concepts and methods in optimization of integrated *LC* VCOs," *IEEE Journal of Solid-State Circuits*, vol. 36, no. 6, pp. 896–909, Jun. 2001. DOI: 10.1109/4.924852.

[102] Q. Huang, "Phase noise to carrier ratio in LC oscillators," *IEEE Transactions on Circuits and Systems I: Fundamental Theory and Applications*, vol. 47, no. 7, pp. 965–980, Jul. 2000. DOI: 10.1109/81.855452.

[103] W. Rudin, *Principles of Mathematical Analysis*, 3rd ed. McGraw-Hill, 1976.

[104] A. Mirzaei and A. A. Abidi, "The spectrum of a noisy free-running oscillator explained by random frequency pulling," *IEEE Transactions on Circuits and Systems I: Regular Papers*, vol. 57, no. 3, pp. 642–653, Mar. 2010. DOI: 10.1109/TCSI.2009.2024970.

[105] B. Razavi, "A study of phase noise in CMOS oscillators," *IEEE Journal of Solid-State Circuits*, vol. 31, no. 3, pp. 331–343, Mar. 1996. DOI: 10.1109/4.494195.

[106] D. Ham and A. Hajimiri, "Virtual damping and Einstein relation in oscillators," *IEEE Journal of Solid-State Circuits*, vol. 38, no. 3, pp. 407–418, Mar. 2003. DOI: 10.1109/JSSC.2002.808283.

[107] D. B. Leeson, "A simple model of feedback oscillator noise spectrum," *Proceedings of the IEEE*, vol. 54, no. 2, pp. 329–330, Feb. 1966. DOI: 10.1109/PROC.1966.4682.

[108] J. J. Rael and A. A. Abidi, "Physical processes of phase noise in differential LC oscillators," in *Proceedings of the IEEE 2000 Custom Integrated Circuits Conference (CICC)*, May 2000, pp. 569–572. DOI: 10.1109/CICC.2000.852732.

[109] E. Hegazi, H. Sjöland, and A. A. Abidi, "A filtering technique to lower *LC* oscillator phase noise," *IEEE Journal of Solid-State Circuits*, vol. 36, no. 12, pp. 1921–1930, Dec. 2001. DOI: 10.1109/4.972142.

[110] E. Hegazi, J. Rael, and A. A. Abidi, *The Designer's Guide to High Purity Oscillators*. Kluwer Academic, 2005.

[111] A. Leon-Garcia, *Probability, Statistics, and Random Processes for Electrical Engineering*, 3rd ed. Prentice Hall, 2008.

[112] A. W. Naylor and G. R. Sell, *Linear Operator Theory in Engineering and Science*. Springer, 2000.

[113] B. Razavi, *Design of Analog CMOS Integrated Circuits*. McGraw-Hill, 2000.

[114] P. R. Gray, P. J. Hurst, S. H. Lewis, and R. G. Meyer, *Analysis and Design of Analog Integrated Circuits*, 5th ed. Wiley, 2009.

[115] M. E. Van Valkenburg, *Network Analysis*, 3rd ed. Prentice Hall, 1974.

[116] B. Razavi, *Design of Integrated Circuits for Optical Communications*, 1st ed. McGraw-Hill, 2002.

[117] A. A. Abidi, "Phase noise and jitter in CMOS ring oscillators," *IEEE Journal of Solid-State Circuits*, vol. 41, no. 8, pp. 1803–1816, Aug. 2006. DOI: 10.1109/JSSC.2006.876206.

[118] S. M. Sze and K. K. Ng, *Physics of Semiconductor Devices*, 3rd ed. Wiley-Interscience, 2006.

[119] B. Razavi, K. F. Lee, and R. H. Yan, "Design of high-speed, low-power frequency dividers and phase-locked loops in deep submicron CMOS," *IEEE Journal of Solid-State Circuits*, vol. 30, no. 2, pp. 101–109, Feb. 1995. DOI: 10.1109/4.341736.

[120] A. Li, S. Zheng, J. Yin, X. Luo, and H. C. Luong, "A 21–48 GHz subharmonic injection-locked fractional-N frequency synthesizer for multiband point-to-point backhaul communications," *IEEE Journal of Solid-State Circuits*, vol. 49, no. 8, pp. 1785–1799, Aug. 2014. DOI: 10.1109/JSSC.2014.2320952.

[121] M. Ferriss, B. Sadhu, A. Rylyakov, H. Ainspan, and D. Friedman, "A 13.1-to-28GHz fractional-N PLL in 32nm SOI CMOS with a $\Delta\Sigma$ noise-cancellation scheme," in *2015 IEEE International Solid-State Circuits Conference (ISSCC) Digest of Technical Papers*, Feb. 2015, pp. 192–193. DOI: 10.1109/ISSCC.2015.7062991.

[122] A. Hussein, S. Vasadi, M. Soliman, and J. Paramesh, "A 50-to-66GHz 65nm CMOS all-digital fractional-N PLL with 220fs$_{\text{rms}}$ jitter," in *2017 IEEE International Solid-State Circuits Conference (ISSCC) Digest of Technical Papers*, Feb. 2017, pp. 326–327. DOI: 10.1109/ISSCC.2017.7870393.

[123] H. Yoon, J. Kim, S. Park, Y. Lim, Y. Lee, J. Bang, K. Lim, and J. Choi, "A -31dBc integrated-phase-noise 29GHz fractional-N frequency synthesizer supporting multiple frequency bands for backward-compatible 5G using a frequency doubler and injection-locked frequency multipliers," in *2018 IEEE International Solid-State Circuits Conference (ISSCC) Digest of Technical Papers*, Feb. 2018, pp. 366–367. DOI: 10.1109/ISSCC.2018.8310336.

[124] B. Razavi, *RF Microelectronics*, 2nd ed. Prentice Hall, 2011.

[125] T. A. D. Riley, M. A. Copeland, and T. A. Kwasniewski, "Delta-sigma modulation in fractional-*N* frequency synthesis," *IEEE Journal of Solid-State Circuits*, vol. 28, no. 5, pp. 553–559, May 1993. DOI: 10.1109/4.229400.

[126] H. Wang, "A 1.8V 3mW 16.8GHz frequency divider in 0.25μm CMOS," in *2000 IEEE International Solid-State Circuits Conference (ISSCC) Digest of Technical Papers*, Feb. 2000, pp. 196–197. DOI: 10.1109/ISSCC.2000.839746.

[127] M. V. Krishna, A. Jain, N. A. Quadir, P. D. Townsend, and P. Ossieur, "A 1V 2mW 17GHz multi-modulus frequency divider based on TSPC logic using 65nm CMOS," in *Proceedings of the 40th European Solid-State Circuits Conference (ESSCIRC 2014)*, Sep. 2014, pp. 431–434. DOI: 10.1109/ESSCIRC.2014.6942114.

[128] W. Zhu, H. Yang, T. Gao, F. Liu, T. Yin, D. Zhang, and H. Zhang, "A 5.8-GHz wideband TSPC divide-by-16/17 dual modulus prescaler," *IEEE Transactions on Very Large Scale Integration (VLSI) Systems*, vol. 23, no. 1, pp. 194–197, Jan. 2015. DOI: 10.1109/TVLSI.2014.2300871.

[129] H. Wang, A. Hajimiri, and T. H. Lee, "Comments on 'Design issues in CMOS differential *LC* oscillators' [and reply]," *IEEE Journal of Solid-State Circuits*, vol. 35, no. 2, pp. 286–287, Feb. 2000. DOI: 10.1109/4.823455.

[130] J. Groszkowski, "The interdependence of frequency variation and harmonic content, and the problem of constant-frequency oscillators," *Proceedings of the Institute of Radio Engineers*, vol. 21, no. 7, pp. 958–981, Jul. 1933. DOI: 10.1109/JRPROC.1933.227821.

[131] S. M. Fatemi, M. Sharifkhani, and A. Fotowat-Ahmady, "A unified solution for super-regenerative systems with application to correlator-based UWB transceivers," *IEEE Transactions on Circuits and Systems I: Regular Papers*, vol. 62, no. 4, pp. 1033–1041, Apr. 2015. DOI: 10.1109/TCSI.2015.2395592.

[132] J. R. Carson, "Notes on the theory of modulation," *Proceedings of the Institute of Radio Engineers*, vol. 10, no. 1, pp. 57–64, Feb. 1922. DOI: 10.1109/JRPROC.1922.219793.

[133] S. N. Bernstein, *Leçons sur les propriétós extrómales et la meilleure approximation des fonctions analytiques d'une variable róelle*. Paris, France: Gauthier-Villars et Cie, 1926, (Translation: Lectures on extremal properties and the best approximation of analytic functions of a real variable).

[134] C. Samori, A. L. Lacaita, F. Villa, and F. Zappa, "Spectrum folding and phase noise in *LC* tuned oscillators," *IEEE Transactions on Circuits and Systems II: Analog and Digital Signal Processing*, vol. 45, no. 7, pp. 781–790, Jul. 1998. DOI: 10.1109/82.700925.

[135] D. Murphy, J. J. Rael, and A. A. Abidi, "Phase noise in *LC* oscillators: A phasor-based analysis of a general result and of loaded *Q*," *IEEE Transactions on Circuits and Systems I: Regular Papers*, vol. 57, no. 6, pp. 1187–1203, Jun. 2010. DOI: 10.1109/TCSI.2009.2030110.

[136] R. D. Thornton, C. L. Searle, D. O. Pederson, R. B. Adler, and E. J. Angelo Jr., *Multistage Transistor Circuits*. Wiley, 1965.

[137] B. Cochrun and A. Grabel, "A method for the determination of the transfer function of electronic circuits," *IEEE Transactions on Circuit Theory*, vol. 20, no. 1, pp. 16–20, Jan. 1973. DOI: 10.1109/TCT.1973.1083615.

[138] A. Hajimiri, "Generalized time- and transfer-constant circuit analysis," *IEEE Transactions on Circuits and Systems I: Regular Papers*, vol. 57, no. 6, pp. 1105–1121, Jun. 2010. DOI: 10.1109/TCSI.2009.2030092.

[139] H.-P. Le, S. R. Sanders, and E. Alon, "Design techniques for fully integrated switched-capacitor DC-DC converters," *IEEE Journal of Solid-State Circuits*, vol. 46, no. 9, pp. 2120–2131, Sep. 2011. DOI: 10.1109/JSSC.2011.2159054.

[140] W. Jung, D. Sylvester, and D. Blaauw, "A rational-conversion-ratio switched-capacitor DC-DC converter using negative-output feedback," in *2016 IEEE International Solid-State Circuits Conference (ISSCC) Digest of Technical Papers*, Feb. 2016, pp. 218–219. DOI: 10.1109/ISSCC.2016.7417985.

[141] Y. Lu, J. Jiang, W.-H. Ki, C. P. Yue, S.-W. Sin, S.-P. U, and R. P. Martins, "A 123-phase DC-DC converter-ring with fast-DVS for microprocessors," in *2015 IEEE International Solid-State Circuits Conference (ISSCC) Digest of Technical Papers*, Feb. 2015, pp. 364–365. DOI: 10.1109/ISSCC.2015.7063077.

[142] S. Bang, D. Blaauw, and D. Sylvester, "A successive-approximation switched-capacitor DC–DC converter with resolution of $V_{IN}/2^N$ for a wide range of input and output voltages," *IEEE Journal of Solid-State Circuits*, vol. 51, no. 2, pp. 543–556, Feb. 2016. DOI: 10.1109/JSSC.2015.2501985.

[143] T. M. Van Breussegem, M. Wens, E. Geukens, D. Geys, and M. S. J. Steyaert, "Area-driven optimisation of switched-capacitor DC/DC converters," *Electronics Letters*, vol. 44, no. 25, pp. 1488–1490, Dec. 2008. DOI: 10.1049/el:20081687.

[144] L. G. Salem and P. P. Mercier, "An 85%-efficiency fully integrated 15-ratio recursive switched-capacitor DC-DC converter with 0.1-to-2.2V output voltage range," in *2014 IEEE International Solid-State Circuits Conference (ISSCC) Digest of Technical Papers*, Feb. 2014, pp. 88–89. DOI: 10.1109/ISSCC.2014.6757350.

[145] ——, "A 45-ratio recursively sliced series-parallel switched-capacitor DC-DC converter achieving 86% efficiency," in *Proceedings of the IEEE 2014 Custom Integrated Circuits Conference (CICC)*, Sep. 2014, pp. 1–4. DOI: 10.1109/CICC.2014.6946051.

[146] ——, "A recursive switched-capacitor DC-DC converter achieving $2^N - 1$ ratios with high efficiency over a wide output voltage range," *IEEE Journal of Solid-State Circuits*, vol. 49, no. 12, pp. 2773–2787, Dec. 2014. DOI: 10.1109/JSSC.2014.2353791.

[147] Z. Safarian and H. Hashemi, "Capacitance-sharing, dual-output, compact, switched-capacitor DC–DC converter for low-power biomedical implants," *Electronics Letters*, vol. 50, no. 23, pp. 1673–1675, Nov. 2014. DOI: 10.1049/el.2014.1842.

Appendix A

MEASUREMENT SETUP

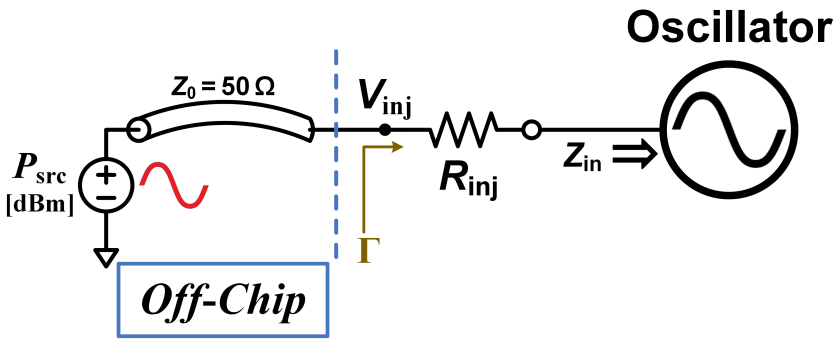

(a) Setup for a single-ended injection.

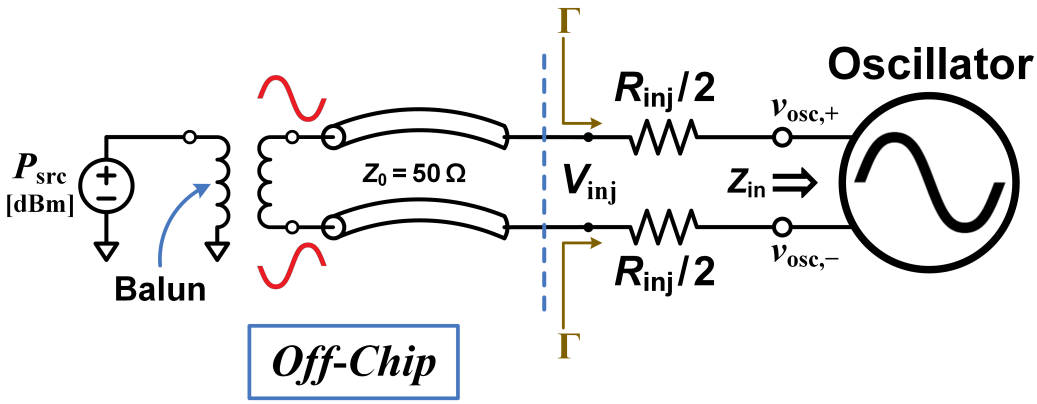

(b) Setup for a differential injection. The balun was implemented with a Krytar Double Arrow 180° Hybrid Coupler.

Figure A.1: Setup for injecting a current into an on-chip oscillator to measure its lock range. The injection signal, P_{src}, came from an off-chip signal source.

To build reliable and precise injection current sources, we resorted to the technique discussed at the beginning of Section 8.5, whereby an injection voltage was used to drive an injection resistor in series with the oscillator. While the injection resistor was integrated on-chip, the sinusoidal injection voltage came from an off-chip signal generator. Figure A.1 shows the details of the setup for the injection circuitry; note that both single-ended and differential injections were needed. An Agilent MXG Analog Signal Generator (N5181B) and a Hewlett Packard Synthesized Sweeper (83650B) were used to produce injections below and above 3 GHz, respectively.

As illustrated in Figure 8.13, the injection resistor was accounted for in the design process and included as part of the oscillator in the simulation of the ISF. The value of the injection resistance, R_{inj}, was chosen based on the range of injection strengths we wished to test, while also ensuring that it was sufficiently large compared to the input impedance looking into the injection port, Z_{in}, so as to not load the oscillator significantly.

The effective injection current is the Norton equivalent current of the depicted injection voltage, V_{inj}, and the series injection resistor, R_{inj}. For both the single-ended and differential cases, the amplitude of the injection current is given by

$$\boxed{I_{\text{inj}} = \frac{V_{\text{inj}}}{R_{\text{inj}}}.} \tag{A.1}$$

We will now calculate V_{inj} from the power output of the signal generator, P_{src}. Note that P_{src} is the power that would be delivered to a matched load, $Z_L = Z_0 = 50\,\Omega$. Therefore, the incident voltage produced by the signal generator is given by

$$\boxed{V^+ = \sqrt{2P_{\text{src}}Z_0},} \tag{A.2}$$

where

$$P_{\text{src}} = 10^{\,P_{\text{src}}\,[\text{dBm}]\,/\,10\,\text{dBm}}\,[\text{mW}]. \tag{A.3}$$

The injection voltage is given by the sum of the incident and the reflected voltages,

$$V_{\text{inj}} = V^+ + V^- = |1 + \Gamma|\,V^+, \tag{A.4}$$

where Γ is the reflection coefficient:

Single-Ended:

$$\Gamma = \frac{R_{\text{inj}} + Z_{\text{in}} - Z_0}{R_{\text{inj}} + Z_{\text{in}} + Z_0}$$

Differential:

$$\Gamma = \frac{R_{\text{inj}} + Z_{\text{in}} - 2Z_0}{R_{\text{inj}} + Z_{\text{in}} + 2Z_0}.$$

Putting everything together, the injection current amplitude is therefore given by

Single-Ended:

$$I_{\text{inj}} = \frac{2V^+}{R_{\text{inj}}\left|1 + \dfrac{Z_0}{R_{\text{inj}} + Z_{\text{in}}}\right|}$$

Differential:

$$I_{\text{inj}} = \frac{2V^+}{R_{\text{inj}}\left|1 + \dfrac{2Z_0}{R_{\text{inj}} + Z_{\text{in}}}\right|}.$$

Because the injection resistors for all of the oscillators are at least several kΩs, the reflection coefficient is very nearly unity: $\Gamma \approx 1$. Thus, for both the single-ended and differential injection scenarios, we can approximate[1]

$$\boxed{I_{\text{inj}} \approx \frac{2V^{+}}{R_{\text{inj}}}.} \tag{A.5}$$

A list of the injection resistance R_{inj} used for each oscillator is provided in Table A.1. Finally, the lock range was measured by observing the spectrum of the oscillation voltage on a Keysight PXA Signal Analyzer (N9030B).

Table A.1: List of Injection Resistors for the Measured Oscillators

Oscillator	Injection Resistor R_{inj}
3-Stage Ring	20 kΩ
17-Stage Ring	4 kΩ
6-Stage Differential Ring	10 kΩ
Bose Oscillator	1 MΩ
Astable Multivibrator	20 kΩ
CMOS Differential LC	8 kΩ
CMOS Differential LC Tail	4 kΩ
NMOS-only Differential LC	8 kΩ
NMOS-only Differential LC Tail	4 kΩ
Colpitts Oscillator	2.5 kΩ

A die micrograph of the fabricated chip containing all of the oscillators and a photo of the PCB used for testing the chip is shown in Figure A.2.

[1] This means that nearly all of the power delivered by the signal generator was reflected. We did not care about matching here, as the fraction of power which was delivered to the oscillator was sufficient to establish the injection current amplitudes that we needed.

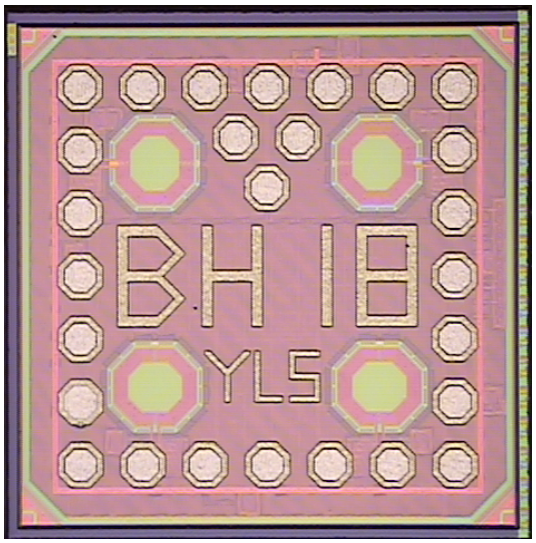

(a) Die photo of the measured oscillators fabricated in TSMC's 65-nm GP bulk-CMOS process, measuring 1×1 mm^2.

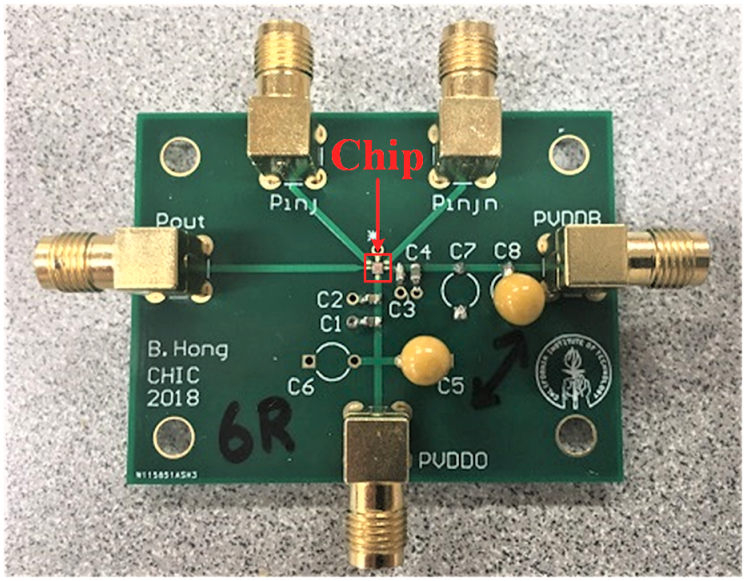

(b) Printed-circuit board (PCB) used to test the chip. Clockwise from the top: 'Pinj' and 'Pinjn' are the differential injection ports, 'PVDDB' and 'PVDDO' are the respective supplies for the output buffer and the oscillator, and 'Pout' is the output (from the buffer). For single-ended injections, 'Pinjn' was left floating.

Figure A.2: The hardware underlying the experimental results in this thesis. Note that the testing of each oscillator required its own chip wirebonded to its own PCB.

Appendix B

THE PROBLEM WITH THE SINGLE-PERIOD INJECTION RESPONSE (SPIR)

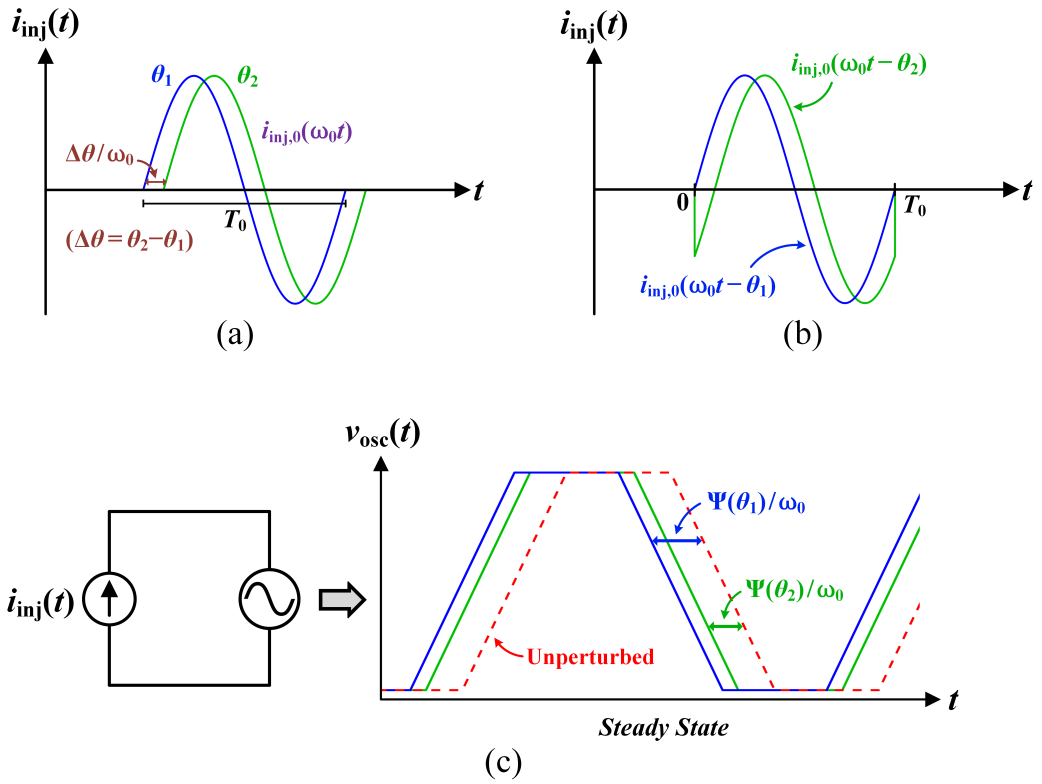

Figure B.1: Conceptual diagram of the Single-Period Injection Response. Two possible ways of varying θ are shown: (a) shifting the oscillator's injection window, and (b) phase-shifting the injection waveform itself. That these two methods result in the same phase shift is demonstrated in Figure B.3. (c) The resultant time shift in the oscillation voltage is then used to calculate the SPIR $\Psi(\theta)$.

Earlier in Section 2.2, we mentioned an injection locking model based on the Single Period Injection Response (SPIR) [77]. The SPIR is formally defined as the phase shift $\Psi(\theta)$ induced by injecting into the oscillator a single period of the injection current $i_{\text{inj},0}(\omega_0 t)$ time-scaled to the free-running period T_0, where θ is the oscillator's *initial* phase relative to the injection. Specifically, the Phase Domain Response (PDR) $P(\cdot)$ defined in [77] is related to the SPIR via $\Psi(x) = -P(x)$. A cartoon that depicts this definition is given in Figure B.1. An actual example

simulation of the SPIR is shown in Figure B.2.

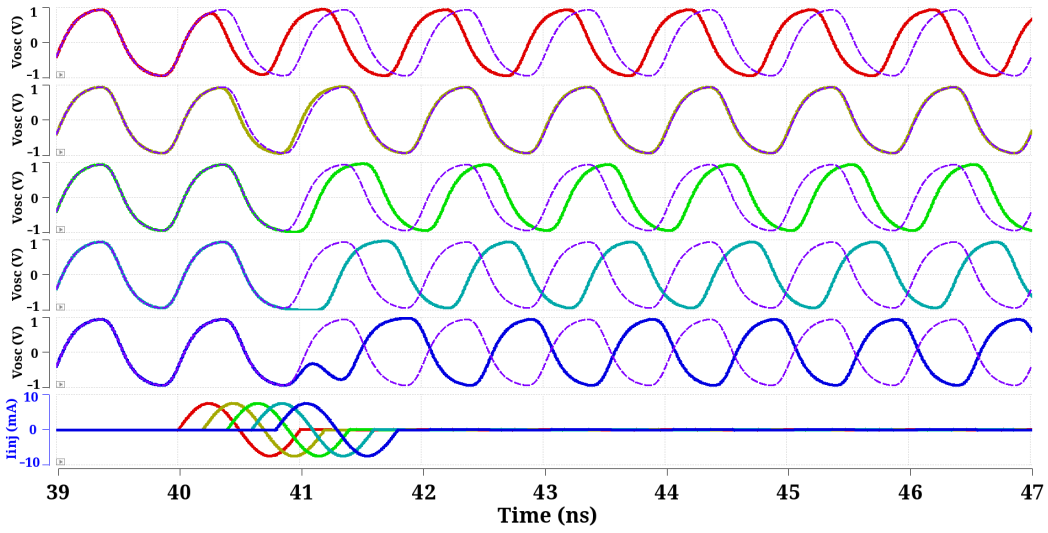

Figure B.2: SPIR simulation on a 6-stage differential ring oscillator for a 7.5 mA sinusoidal injection current. Five different values of θ are shown.

Proponents of the SPIR tout that it is capable of capturing nonlinear aspects of the injection-to-phase relationship as it directly exposes the oscillator to the entire waveform at the desired amplitude instead of calculating the response from a linear, impulse-response based model [77]. However, we claimed in Section 2.2 that this approach was fundamentally flawed, stating that injection locking was a steady-state phenomena while the SPIR is only capable of capturing the oscillator's transient behavior in response to the injection. We demonstrate this analytically here.

Recall from Eq. (4.28) that the lock characteristic is given by

$$\Omega(\theta) = \frac{1}{T_{\text{inj}}} \int_{T_{\text{inj}}} \tilde{\Gamma}\left(\omega_{\text{inj}} t + \theta\right) i_{\text{inj}}(t)\, dt. \tag{B.1}$$

The invariance of the averaging operation with respect to the time scale allows us to rewrite the lock characteristic as

$$\Omega(\theta) = \frac{1}{T_0} \int_{T_0} \tilde{\Gamma}(\omega_0 t + \theta)\, i_{\text{inj},0}(\omega_0 t)\, dt. \tag{B.2}$$

This equation exposes the intuition behind the SPIR, which is formally defined as the phase shift $\Psi(\theta)$ induced by a single period of the injection $i_{\text{inj},0}(\omega_0 t)$, time-scaled to the free-running period T_0 and at a relative phase $-\theta$ with respect to the (unperturbed) oscillation waveform. In effect, the SPIR *attempts* to simulate the

lock characteristic (multiplied by T_0) directly:

$$\Psi(\theta) \stackrel{?}{=} \int_{T_0} \tilde{\Gamma}(\omega_0 t + \theta)\, i_{\text{inj},0}(\omega_0 t)\, dt. \tag{B.3}$$

Assuming this is correct, we arrive at the following lock characteristic and lock range in terms of the SPIR [77]:

$$\Delta\omega \stackrel{?}{=} \frac{\Psi(\theta)}{T_0} \tag{B.4}$$

and

$$\omega_L^{\pm} \stackrel{?}{=} \frac{\Psi_{\text{max/min}}}{T_0}. \tag{B.5}$$

Also, observe that because the SPIR is essentially an approximation of the lock characteristic, it can also be used to predict the transient behavior of an injection-locked oscillator.[1]

However, carefully note that during the course of the injection, the accumulated phase shift $\phi(t)$ becomes part of the oscillator's total phase $\varphi(t)$, and should therefore be included in the argument of the ISF. To see this, recall the original differential equation Eq. (4.15) for the oscillator's excess phase $\phi(t)$, which we derived from first principles earlier:

$$\frac{d\phi}{dt} = \tilde{\Gamma}[\varphi(t)]\, i_{\text{inj}}(t). \tag{B.6}$$

Assuming without loss of generality that the injection $i_{\text{inj}}(t) = i_{\text{inj},0}(\omega_0 t)$ occurs from $t = 0$ to $t = T_0$, and that the oscillator's phase at the *start* of the injection is equal to θ, observe that the SPIR $\Psi(\theta)$ is actually the solution $\phi(t)$ evaluated at $t = T_0$:

$$\phi(t) = \int_0^t \tilde{\Gamma}[\omega_0 \tau + \theta + \phi(\tau)]\, i_{\text{inj},0}(\omega_0 \tau)\, d\tau. \tag{B.7}$$

Consequently,

$$\begin{aligned} \phi(t) &\neq \int_0^t \tilde{\Gamma}[\omega_0 \tau + \theta + \cancel{\phi(\tau)}]\, i_{\text{inj},0}(\omega_0 \tau)\, d\tau \\ &= \int_0^t \tilde{\Gamma}(\omega_0 t + \theta)\, i_{\text{inj},0}(\omega_0 t)\, dt. \end{aligned} \tag{B.8}$$

Therefore, the SPIR does not have the direct correspondence with the lock characteristic postulated in Eq. (B.3):

$$\implies \Psi(\theta) = \phi(T_0) \neq \int_{T_0} \tilde{\Gamma}(\omega_0 t + \theta)\, i_{\text{inj},0}(\omega_0 t)\, dt. \tag{B.9}$$

[1] Note that equations (29) and (30) in [77] are wrong: f_{inj} should be replaced with the free-running oscillation frequency f_0. This is because the jitter-tracking bandwidth ω_{TB}, which is the pull-in frequency from Section 7.4, is equal to $\omega_{\text{TB}} = -\partial\Delta\omega/\partial\theta|_{\theta=\theta_{\text{ss}}} \stackrel{?}{=} -\Psi'(\theta_{\text{ss}}) \cdot f_0$.

In other words, the SPIR approach to modeling injection locking neglects this "phase accumulation" term and is therefore fundamentally flawed from a mathematical standpoint. Intuitively, the SPIR can be thought of as the oscillator's *transient* response to a single period of the injection current. However, the actual phase shift per period that the injection produces in a locked oscillator is a *steady-state* phenomenon. In the latter scenario, there is no "extra" phase accumulation to account for, as the oscillator's phase must always experience a total change of 2π per injection period.

One aspect of the SPIR we wanted to demonstrate is its invariance with respect to the injection current's *absolute* phase, which can be thought of as the particular single-period "window" of the injection under use. As we demonstrated analytically using our linear periodically time-varying model, $\Psi(\theta)$ depends only on the *relative* phase θ between the injection and oscillation waveforms. In other words, the two approaches of varying θ shown in Figures B.1a and B.1b should lead to identical results. These simulations lend further credence to the accuracy of our model—the slight variations in the phase of the resultant waveform are invariably due to nonlinearities in the oscillator's response to the injection current. Figs. B.3 depicts this for a ring oscillator and an LC oscillator.

Another major limitation of the single-period injection response is that the incurred phase shift is technically restricted to the range $[-\pi, \pi]$. In other words, phase shifts "beyond" $\pm\pi$ cannot be unambiguously resolved, as a phase shift of $4\pi/3$, for example, is mathematically identical to a phase shift of $-2\pi/3$. Consequently, the lock range predicted by the SPIR through Eq. (B.5) is bounded by $\omega_L \leq \omega_0/2$. This issue can be empirically addressed to a certain extent by arguing that the incurred phase shift for a given θ should be continuous with respect to the injection strength, and so one can *unwrap* the SPIR with respect to the injection strength in order to resolve ambiguities that arise in the incurred phase. However, note that this issue does not appear when simulating the ISF because such simulations consist of small injections which induce phase shifts that are $|\Delta\phi| \ll 2\pi$. Furthermore, the inaccuracy of the SPIR model due to neglecting phase accumulation usually already precludes its usage when the injection is so strong that the incurred phase shift is close to $\pm\pi$.

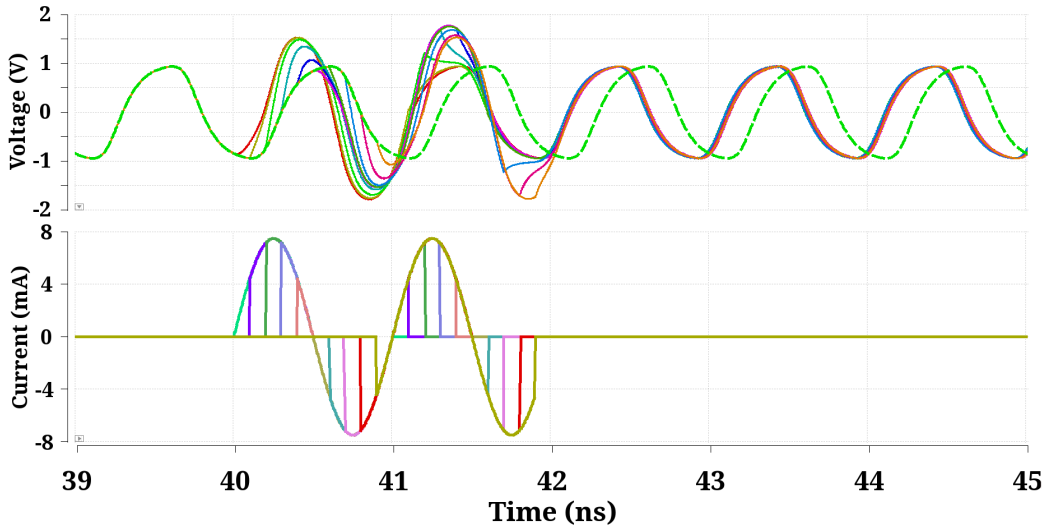

(a) Invariance of the SPIR to the injection window for a 6-stage differential ring oscillator under a 7.5 mA sinusoidal injection.

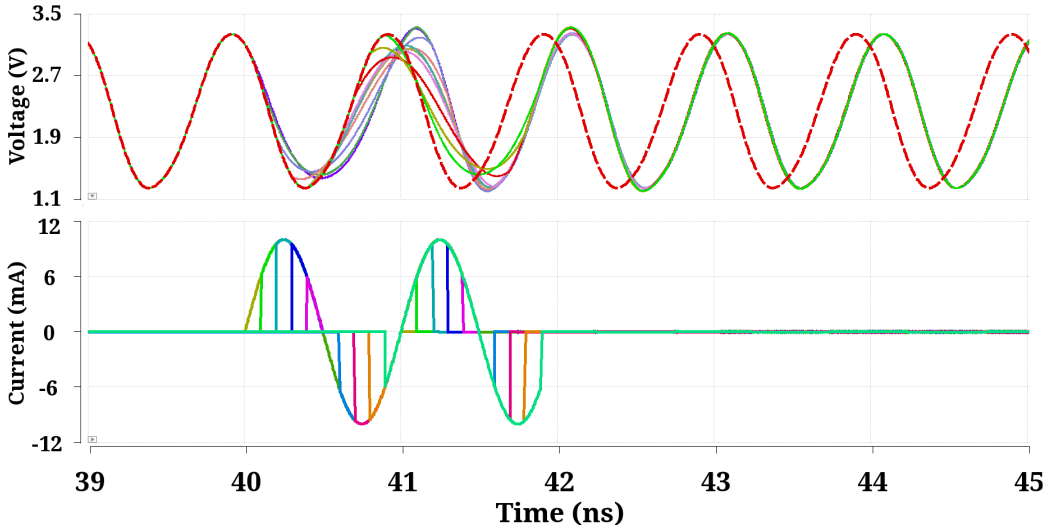

(b) Invariance of the SPIR to the injection window for a bipolar Colpitts oscillator under a 10 mA sinusoidal injection.

Figure B.3: Demonstration that the SPIR depends only on the relative phase θ and not on the absolute phase of the injection. For each simulation, both the oscillator's phase at which the injection takes place and the injection's phase are shifted by the same amount.

Let us compare the predictions made by the SPIR model of Eq. (B.4) against those from our ISF-based model as well as Spectre injection locking simulation results for several illustrative examples. For the ideal Bose oscillator, Figure B.4 depicts a surface plot of the SPIR vs. the oscillator phase θ and the injection strength,

examines the lock range as a function of the injection strength, and shows the lock characteristic for two different injection strengths. Note that we unwrapped the SPIR with respect to the injection strength as mentioned above, thereby allowing $|\Psi(\theta)|$ to exceed π. Also, observe that as θ increases from 0 to 2π, $\Psi(\theta)$ starts out negative and decreases to its minimum value, begins increasing and crosses 0, and then increases to its maximum positive value before returning to $\Psi(2\pi) = \Psi(0)$. Finally, the SPIR prediction of the lock range is shown by overlaying the SPIR (normalized by T_0) over all phases θ and looking at the minimum and maximum for each injection current, leading to the "envelope" of the SPIR points as shown.

For the Bose oscillator, the ISF model follows the simulated lock characteristic follows the ISF model much more closely than the SPIR model does, particularly as the injection strength increases. But the SPIR model is not always inferior; it fares rather well for long ring oscillators. Figure B.5 depicts the same set of analyses for a 17-stage single-ended ring oscillator (from Figure 4.12), where one can see that the simulated lock characteristic for large injections is more closely captured by the SPIR model for frequencies below f_0, leading to much better predictions of the lower lock range compared to the ISF model. This fortuity does not extend to all ring oscillators, however. Consider the 6-stage differential ring oscillator (from Figure 4.14), whose plots are shown in Figure B.6. Although the SPIR is capable of predicting the lock range somewhat more accurately than the ISF for large injections, the shape of the SPIR deviates much more significantly from the simulated lock characteristic than does the ISF model. As a more extreme example, the differential NMOS astable multivibrator (from Figure 4.17) is analyzed in Figure B.7, where both the ISF and SPIR models fail to capture the severely nonlinear behavior invoked by large injection currents.

In closing, we wanted to point out a distinct advantage of the SPIR over the ISF-based model, which is its ability to capture subharmonic injection locking. As we saw from Section 6.5, our model requires the M^{th} harmonics of the injection to appear explicitly in the injection current $i_{\text{inj}}(t)$, whereas these harmonics are usually generated within the oscillator internally through mixing. The SPIR-based model inherently captures this phenomenon by directly simulating the oscillator's response to a disturbance which lasts M times the free-running period. Indeed, a number of applications involving subharmonic injection-locked oscillators have already emerged based on the SPIR framework [18], [77], [78].

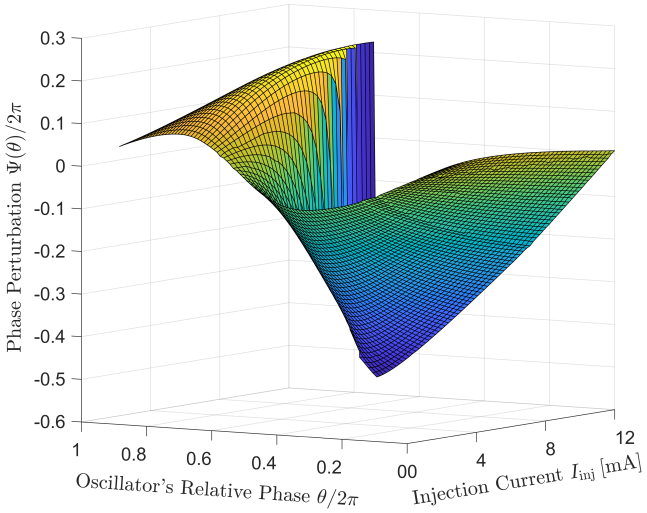

(a) SPIR surface plot.

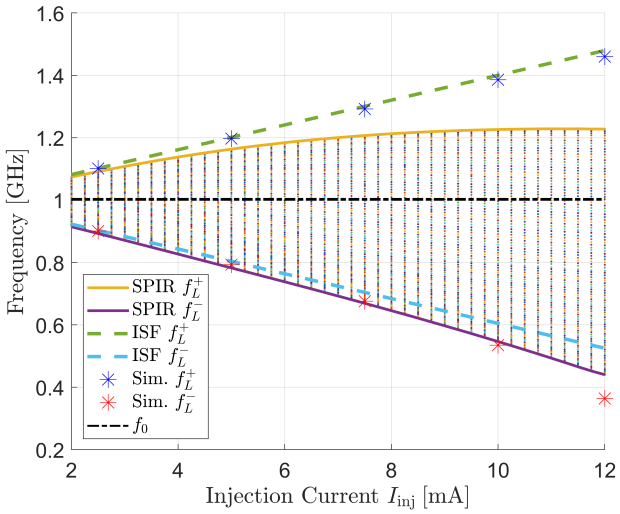

(b) Sinusoidal lock range.

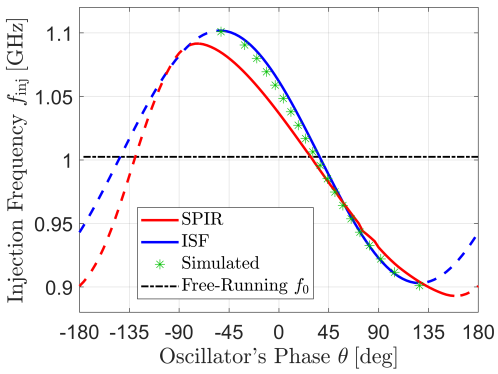

(c) Lock characteristic for $I_{\text{inj}} = 2.5$ mA.

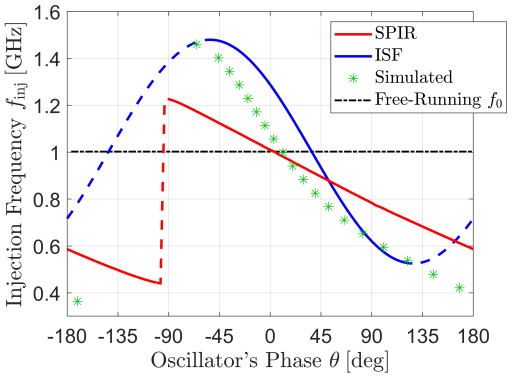

(d) Lock characteristic for $I_{\text{inj}} = 12$ mA.

Figure B.4: Bose oscillator SPIR analysis.

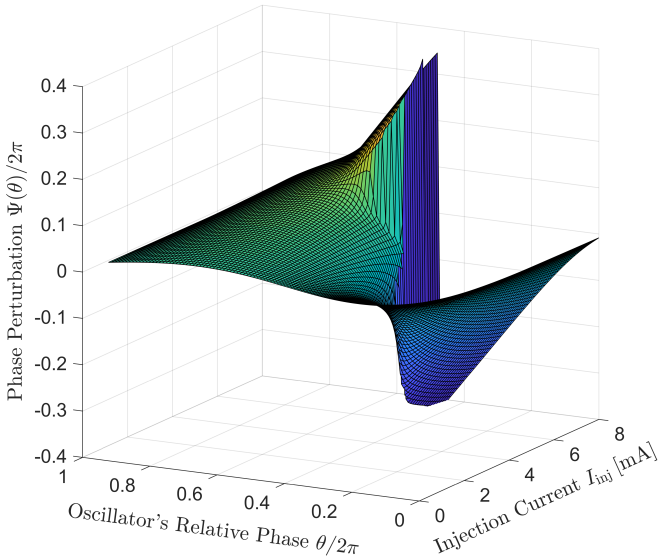

(a) SPIR surface plot.

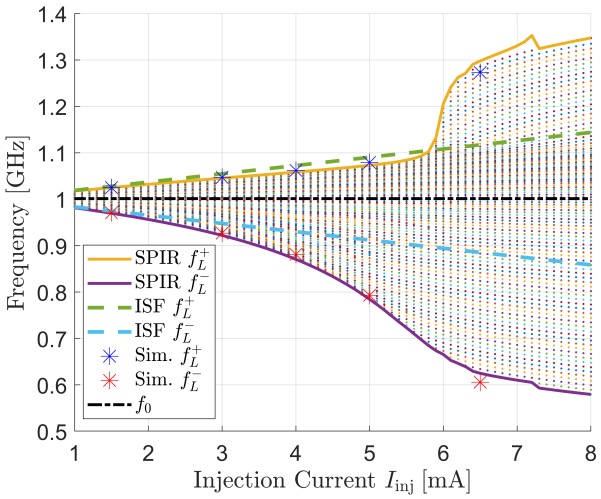

(b) Sinusoidal lock range.

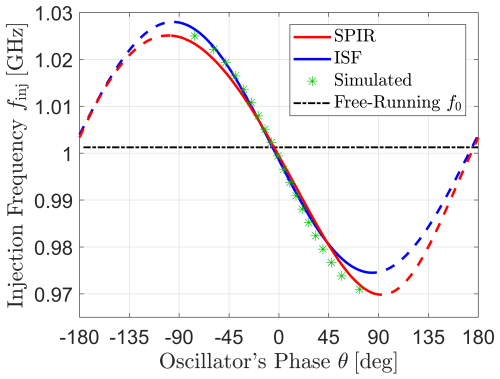

(c) Lock characteristic for $I_{\text{inj}} = 1.5$ mA.

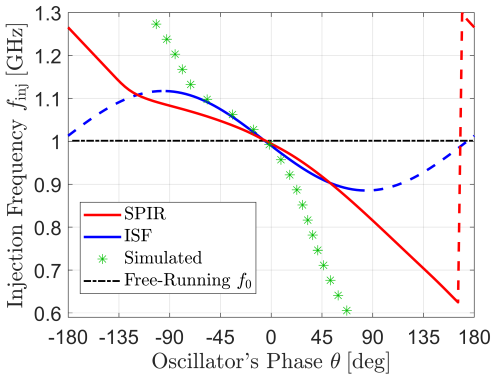

(d) Lock characteristic for $I_{\text{inj}} = 6.5$ mA.

Figure B.5: 17-stage single-ended ring oscillator SPIR analysis.

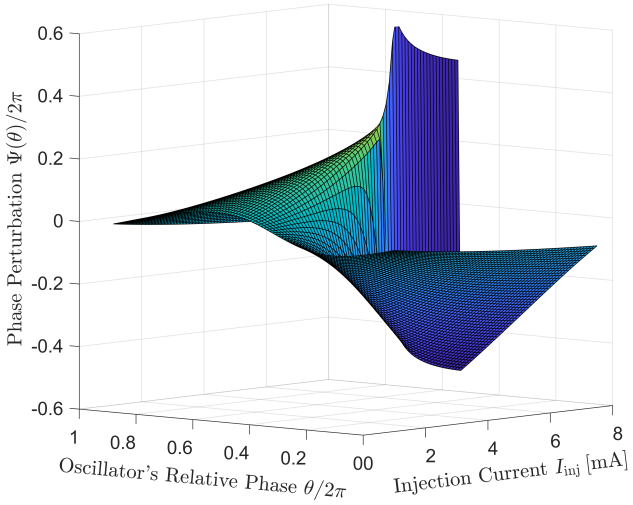

(a) SPIR surface plot.

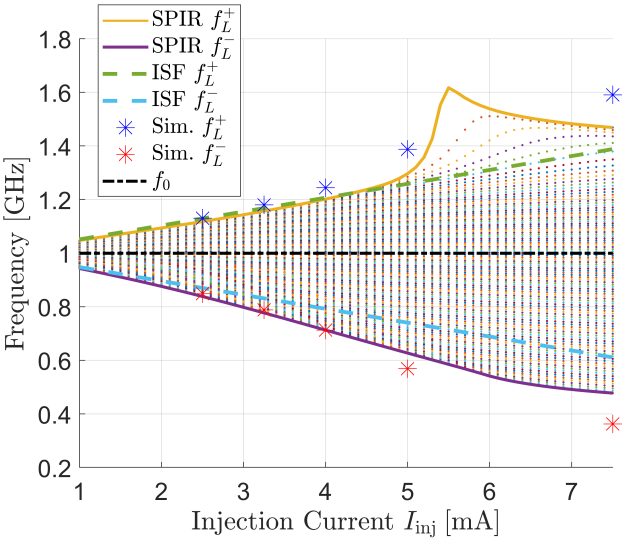

(b) Sinusoidal lock range.

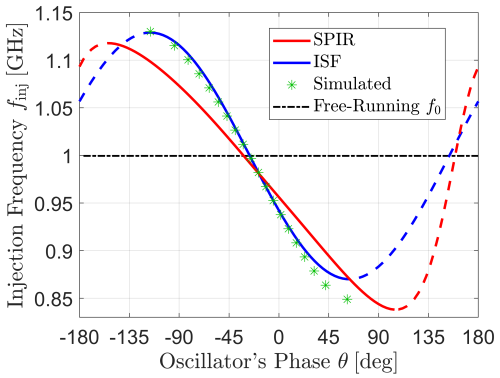

(c) Lock characteristic for $I_{\text{inj}} = 2.5$ mA.

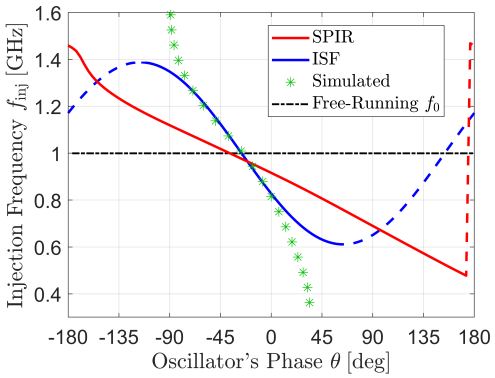

(d) Lock characteristic for $I_{\text{inj}} = 7.5$ mA.

Figure B.6: 6-stage differential ring oscillator SPIR analysis.

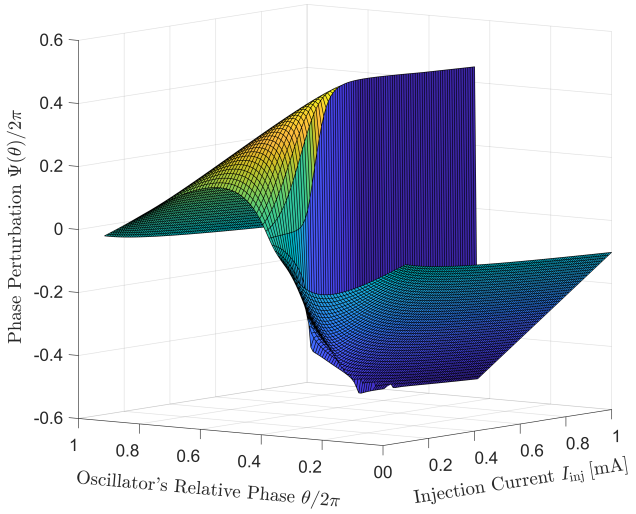

(a) SPIR surface plot.

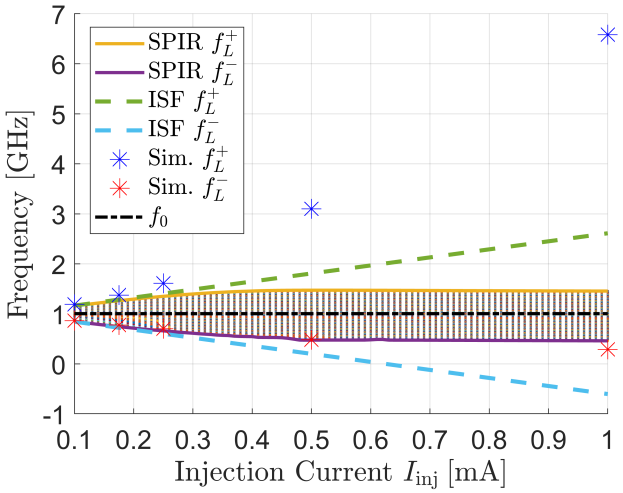

(b) Sinusoidal lock range.

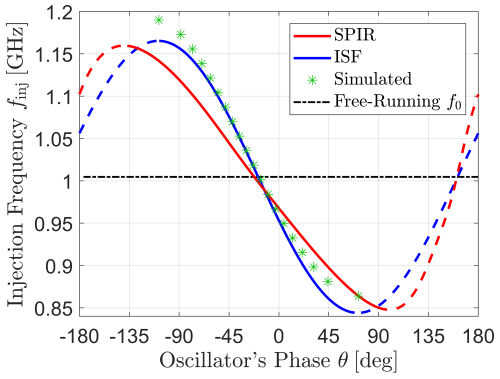

(c) Lock characteristic for $I_{\text{inj}} = 0.1$ mA.

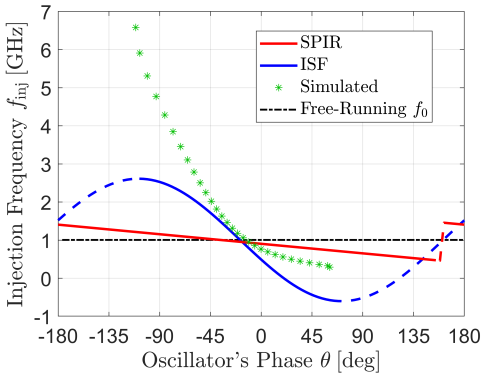

(d) Lock characteristic for $I_{\text{inj}} = 1$ mA.

Figure B.7: NMOS astable multivibrator SPIR analysis.

Appendix C

MISCELLANEOUS MATHEMATICAL FACTS

C.1 Some Standard Integrals

For $|a| > 1$, we have the following antiderivatives:

$$\int \frac{dx}{a + \cos x} = \frac{2}{\sqrt{a^2 - 1}} \tan^{-1}\left[\frac{a-1}{\sqrt{a^2-1}} \tan\left(\frac{x}{2}\right)\right] + C \tag{C.1}$$

$$\int \frac{dx}{a + \sin x} = \frac{2}{\sqrt{a^2 - 1}} \tan^{-1}\left[\frac{a \tan\left(\frac{x}{2}\right) + 1}{\sqrt{a^2-1}}\right] + C, \tag{C.2}$$

where C is an integration constant.

For $|a| < 1$, we can appeal to Euler's identity, which allows us to derive the relation $\tan^{-1}(ix) = i \tanh^{-1}(x)$. This yields the following antiderivatives:[1]

$$\int \frac{dx}{a + \cos x} = \frac{2}{\sqrt{1 - a^2}} \tanh^{-1}\left[\frac{1-a}{\sqrt{1-a^2}} \tan\left(\frac{x}{2}\right)\right] + C \tag{C.3}$$

$$\int \frac{dx}{a + \sin x} = -\frac{2}{\sqrt{1 - a^2}} \tanh^{-1}\left[\frac{a \tan\left(\frac{x}{2}\right) + 1}{\sqrt{1-a^2}}\right] + C. \tag{C.4}$$

C.2 Proof of Claim 8.4.1

Claim. *Consider the infinite-dimensional vector space of square-summable complex sequences $\ell^2(\mathbb{C})$. The map $\langle \cdot, \cdot \rangle : \ell^2(\mathbb{C}) \times \ell^2(\mathbb{C}) \to \mathbb{R}$, defined for any choice of $\mathbf{u}, \mathbf{v} \in \ell^2(\mathbb{C})$ as*

$$\langle \mathbf{u}, \mathbf{v} \rangle \coloneqq \mathrm{Re}\{\mathbf{u}^H \mathbf{v}\} \equiv \mathrm{Re}\left\{\sum_n \overline{u_n} v_n\right\}, \tag{C.5}$$

is an inner product for $\ell^2(\mathbb{C})$ over the field of real numbers $\mathbb{R}$. Furthermore, the norm induced by this inner product is the same as that for the usual Euclidean complex inner product $\mathbf{u}^H \mathbf{v}$.

[1] The careful reader might wonder if these integral formulas are consistent, given the fact that $\sin x = \cos(x - \pi/2)$. Here, we point out that if one utilizes this identity, the formulas given in Eqs. (C.1) and (C.2), or in Eqs. (C.3) and (C.4), will be "off by a constant" (which is absorbed by the integration constant C anyways).

Proof:

We will rely on the fact that $\mathbf{u}^H\mathbf{v}$ is itself an inner product over $\mathbb{C}$.

- *Symmetry:*

  For any $\mathbf{u}, \mathbf{v} \in \ell^2(\mathbb{C})$,

$$\begin{aligned} \langle \mathbf{u}, \mathbf{v} \rangle &= \mathrm{Re}\{\mathbf{u}^H\mathbf{v}\} \\ &= \mathrm{Re}\{\overline{\mathbf{v}^H\mathbf{u}}\} \\ &= \mathrm{Re}\{\mathbf{v}^H\mathbf{u}\} \\ &= \langle \mathbf{v}, \mathbf{u} \rangle . \end{aligned} \tag{C.6}$$

- *Linearity in the first argument:*

  For any $\mathbf{u}, \mathbf{v}, \mathbf{w} \in \ell^2(\mathbb{C})$ and $\alpha \in \mathbb{R}$,

$$\begin{aligned} \langle \alpha\mathbf{u}, \mathbf{v} \rangle &= \mathrm{Re}\{\alpha\mathbf{u}^H\mathbf{v}\} \\ &= \alpha \cdot \mathrm{Re}\{\mathbf{u}^H\mathbf{v}\} \\ &= \alpha \langle \mathbf{u}, \mathbf{v} \rangle . \end{aligned} \tag{C.7}$$

  and

$$\begin{aligned} \langle \mathbf{u} + \mathbf{v}, \mathbf{w} \rangle &= \mathrm{Re}\{(\mathbf{u} + \mathbf{v})^H\mathbf{w}\} \\ &= \mathrm{Re}\{\mathbf{u}^H\mathbf{w} + \mathbf{v}^H\mathbf{w}\} \\ &= \mathrm{Re}\{\mathbf{u}^H\mathbf{w}\} + \mathrm{Re}\{\mathbf{v}^H\mathbf{w}\} \\ &= \langle \mathbf{u}, \mathbf{w} \rangle + \langle \mathbf{v}, \mathbf{w} \rangle . \end{aligned} \tag{C.8}$$

- *Positive-definiteness:*

  For any $\mathbf{u} \in \ell^2(\mathbb{C})$,

$$\langle \mathbf{u}, \mathbf{u} \rangle = \mathrm{Re}\{\mathbf{u}^H\mathbf{u}\} = \mathrm{Re}\left\{ \sum_n \overline{u_n} u_n \right\} = \sum_n |u_n|^2 \geq 0. \tag{C.9}$$

  It is trivial to see that equality is achieved if and only if $u_n = 0 \, \forall n \Leftrightarrow \mathbf{u} = \mathbf{0}$.

- *Induced norm:*

  For any $\mathbf{u} \in \ell^2(\mathbb{C})$, it is straightforward to see that $\mathbf{u}^H\mathbf{u}$ is real. Therefore, the norm induced by this inner product is

$$\|\mathbf{u}\| \equiv \sqrt{\langle \mathbf{u}, \mathbf{u} \rangle} = \sqrt{\mathbf{u}^H\mathbf{u}}, \tag{C.10}$$

  which is the same norm induced by the standard Euclidean inner product $\mathbf{u}^H\mathbf{v}$ defined for all $\mathbf{u}, \mathbf{v} \in \ell^2(\mathbb{C})$.

Appendix D

CORRECTION TO "A STUDY OF INJECTION LOCKING AND PULLING IN OSCILLATORS" BY RAZAVI

We would like to take this opportunity to rectify a small error we noticed in Razavi's prominent paper[1] [38]. The equation in Section III, Subsection C on the 4th line from the bottom of the 2nd column on page 1419 should actually be

$$\frac{\left(\omega_0 - \omega_{\text{inj}}\right)^2}{{\omega_L}^2} = \frac{1}{1 - (1/n^2)}. \tag{D.1}$$

Therefore, contrary to the claim made in the last paragraph of this subsection of [38], it is *indeed* possible for a sideband to appear at ω_0 when ω_{inj} is outside of the lock range, provided an integer solution to Eq. (D.1) exists for n.

There does not appear to be a *physical* reason why a sideband at ω_0 cannot exist. The reason we say the oscillator is "pulled" from its natural frequency is not because the oscillator output $V_{\text{osc},p}$ contains no components at ω_0 as [38] states, but rather because the *largest* component of $V_{\text{osc},p}$ does not appear at ω_0 [104].

To see this, let us elucidate where exactly the largest component of the oscillator output $V_{\text{osc},p}$ falls, which we will denote as ω_{main}. That is, ω_{main} is the "oscillation frequency" of an injection-pulled oscillator. Note from Eq. (D.1) that $|n| > 1$, and so only a sideband at least twice the beat frequency away from ω_{inj} can coincide with ω_0. This should also be evident from the fact that the distance between adjacent tones, known as the beat frequency [38], is $\omega_b = \sqrt{\Delta\omega^2 - {\omega_L}^2} < |\Delta\omega|$, which is less than the distance between ω_{inj} and ω_0. Hence, ω_0 always lies more than a sideband away from ω_{inj}. It is convenient here to define a parameter known as the "pulling strength" [104]:

$$\zeta := \frac{\omega_L}{|\omega_0 - \omega_{\text{inj}}|}. \tag{D.2}$$

If $\zeta \geq 1$, then the oscillator is injection locked; unity ζ corresponds to the edge of the lock range. We consider the case where $\zeta < 1$ and the oscillator is injection pulled. It is easily shown from [104] that if $\zeta > \sqrt{4/5}$ (approximately 0.9), then the pulled oscillator "oscillates" at the injection frequency $\left(\omega_{\text{main}} = \omega_{\text{inj}}\right)$ and we can say that the oscillator is "quasi-locked" as per the vocabulary in [38]; whereas if $\zeta < \sqrt{4/5}$,

[1] Archived at: `https://perma.cc/42RP-YF2F`

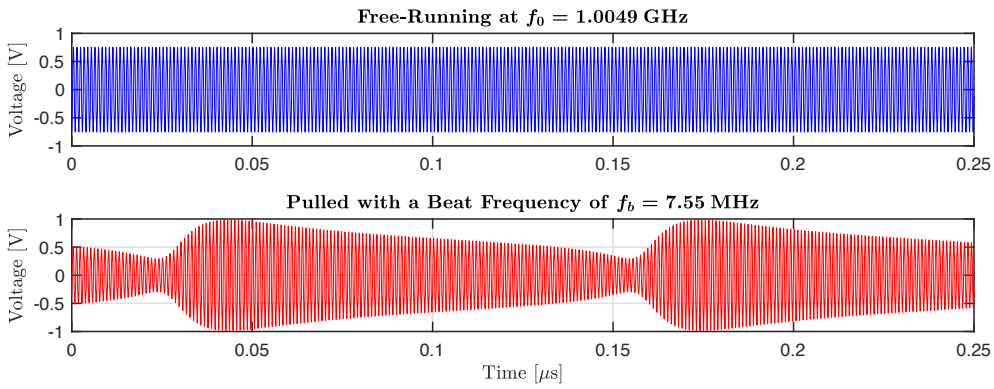

(a) Time Domain

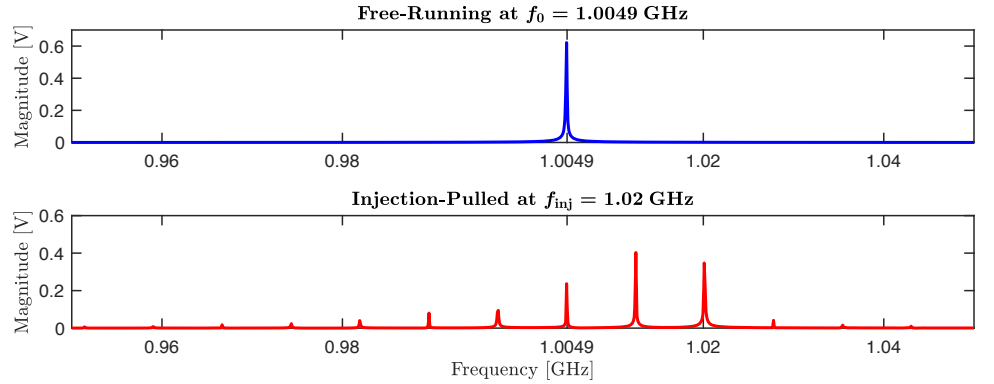

(b) Frequency Spectrum

Figure D.1: Transient simulation of an injection-pulled cross-coupled differential LC oscillator composed on a 65-nm bulk CMOS process with $Q = 15.088$, $I_{osc} = (4/\pi)$ mA, and $f_0 = 1.0049$ GHz. At an injection current of $I_{inj} = 0.5$ mA, the lock range is roughly $f_L = 13.077$ MHz. Pulling the oscillator from an injection frequency of $f_{inj} = 1.02$ GHz leads to a beat frequency of $f_b = 7.55$ MHz, which positions the second sideband from the injection frequency right at f_0.

then $\omega_{main} = \omega_{inj} \pm \omega_b$.[2] (Again, the sign in front of ω_b here is the same as the sign of $(\omega_0 - \omega_{inj})$, since ω_{main} is pulled away from ω_0 towards ω_{inj}.) Therefore, the claim is verified: the oscillation frequency ω_{main} of a pulled oscillator is no longer at its free-running value ω_0 but instead is at either the injection frequency ω_{inj} or is one sideband toward ω_0 away from the injection frequency at $\omega_{inj} \pm \omega_b$.

We show a simulated example of a scenario where one of the sidebands of an injection-pulled LC oscillator falls at ω_0 in Figure D.1.

[2] If $\zeta = \sqrt{4/5}$, then the components at ω_{inj} and at $\omega_{inj} \pm \omega_b$ contain equal amounts of power. It is easily computed that the remaining sidebands carry the remaining $\sqrt{5} - 2$ (roughly $1/4$) of the total output power.